PARTICLE MECHANICS AND CONTINUUM APPROACHES TO MODELING PERMANENT DEFORMATIONS IN CONFINED PARTICULATE SYSTEMS

by

Ankit Agarwal

A Dissertation

Submitted to the Faculty of Purdue University

In Partial Fulfillment of the Requirements for the degree of

Doctor of Philosophy

School of Mechanical Engineering

West Lafayette, Indiana

August 2020

THE PURDUE UNIVERSITY GRADUATE SCHOOL
STATEMENT OF THESIS APPROVAL

Dr. Marcial Gonzalez, Chair

School of Mechanical Engineering

Dr. Carl Wassgren

School of Mechanical Engineering

Dr. Ganesh Subbarayan

School of Mechanical Engineering

Dr. Rodrigo Salgado

Lyles School of Civil Engineering

Approved by:

Dr. Nicole Key

Associate Head for Graduate Studies

Dedicated to my beloved parents

ACKNOWLEDGMENTS

This research was supported by the National Science Foundation through Grant No. CMMI-1538861, and by the Air Force Research Laboratory through Grant No. FA8651-16-0287 entitled "Near-Resonant Thermomechanics of Energetic and Mock Energetic Composite Materials", Grant No. FA8651-16-D-0287 entitled "Near-Resonant Thermomechanics of Energetic and Mock Energetic Composite Materials, Part II", and Grant No. FA8651-17-S-0003 entitled "Exploring the Thermomechanics of Energetic and Mock Energetic Composite Materials Under Quasi-Static and Near-Resonant Excitations". I'd also like to acknowledge the support received from Purdue University through the Frederick N. Andrews Fellowship.

I'd like to extend my heartiest gratitude to my advisor, Professor Marcial Gonzalez, for his guidance, support and incredible patience throughout the course of my doctoral studies. His intuitive and creative thinking, persistence and insightful ideas made this research possible, and I hope to follow his teachings and guidance in the future. My special thanks to Professor Patricia Davies, Professor Jeff Rhoads, Professor Steve Son, Professor Stuart Bolton, Dr. Jelena Paripovic, Dr. Allison Range, Nick Cummock, and Tim Manship for their feedback and interesting discussions through the numerous weekly project meetings. I'd also like to express my profound gratitude to Professor Ganesh Subbarayan, Professor Carl Wassgren and Professor Rodrigo Salgado for serving in my advisory committee and providing their valuable feedback and suggestions for enhancing this work.

During my time as a graduate student, I've had the privilege of working alongside some of the brightest minds that constituted our research group. I'd like to thank Yasasvi, Pedro, Caroline, Abhishek, Muhammad and Nathan for their help, motivation and constructive feedback on my work.

I'd also like to specially acknowledge and thank Dr. Dhananjay Pai, who, during his time as the Lab Manager of the Center of Particulate Products and Processes (CP3), provided his immense support and guidance with operating the lab equipment and performing experiments.

Finally, I'd like to thank my family for their perpetual support and encouragement to follow my dreams and career aspirations. My loving parents are the backbone of my life and the guiding force behind my endeavors. Their consistent motivation during times of failure and appreciation during periods of success have kept me going, and I hope to receive their blessings and comfort for many more years to come.

TABLE OF CONTENTS

Page

Page

LIST OF TABLES

LIST OF FIGURES

Figure Page

Figure Page

Figure Page

Figure Page

Figure Page

Figure Page

Figure Page

ABSTRACT

Author: Agarwal, Ankit. PhD
Institution: Purdue University
Degree Received: August 2020
Title: Particle Mechanics and Continuum Approaches to Modeling Permanent Deformations in Confined Particulate Systems
Committee Chair: Marcial Gonzalez

The research presented in this work addresses open questions regarding (i) the fundamental understanding of powder compaction, and (ii) the complex mechanical response of particle-binder composites under large deformations. This work thus benefits a broad range of industries, from the pharmaceutical industry and its recent efforts on continuous manufacturing of solid tablets, to the defense and energy industries and the recurrent need to predict the performance of energetic materials. Powder compacts and particle-binder composites are essentially confined particulate systems with significant heterogeneity at the meso (particle) scale. While particle mechanics strategies for modeling evolution of mesoscale microstructure during powder compaction depend on the employed contact formulation to accurately predict macroscopic quantities like punch and die wall pressures, modeling of highly nonlinear, strain-path dependent macroscopic response without a distinctive yield surface, typical of particle-binder composites, requires proper constitutive modeling of these complex deformation mechanisms. Moreover, continued loading of particle-binder composites over their operational life may introduce significant undesirable changes to their microstructure and mechanical properties. These challenges are addressed with a combined effort on theoretical, modeling and experimental fronts, namely, (a) novel contact formulations for elasto-plastic particles under high levels of confinement, (b) a multi-scale experimental procedure for assessing changes in microstructure and mechanical behavior of particle-binder composites due to cyclic loading and time-recovery, and (c) a finite strain nonlinear elastic, endochronic plastic constitutive formulation for particle-binder composites.

CHAPTER 1. INTRODUCTION

1.1 Motivation

Confined particulate systems, particularly powder compacts and densely loaded particulate composites, are one of the most commonly used type of materials, with extensive applications in manufacturing processes of critical industries like pharmaceuticals, ceramics, energy, automotive, construction, food and metallurgy (Figure 1.1). The versatility, manipulability and applicability of these materials have made them a subject of active scientific research, particularly in the area of predictive modeling of meso and macroscopic behavior of these materials under confinement. While the development of predictive and computationally efficient models capable of accurately describing the behavior of confined granular media would positively impact manufacturability, waste reduction, quality and price of the end product, the same for particle-binder composites such as energetics would significantly reduce the risks associated with handling, storage and transportation of these materials.

1.2 Background

1.2.1 Deformation Mechanisms

Both powder compacts and particle-binder composites have been found to contain significant heterogeneity at the meso (particle) scale, which has a fundamental impact on their macroscopic behavior. Powder compacts consist of a disordered blend of powder particles with different particle size distributions. Macroscopic compaction pressure in these materials is supported by contact and deformation of the particles as forces get transmitted throughout the system, forming a heterogeneous contact network of force chains (Majmudar & Behringer, 2005; Makse et al., 2000; Blair et al., 2001; Chan & Ngan, 2005). Concurrently, particulate composites, or particle-binder composites, consist of hard particles or fillers (carbon, tungsten carbide, silica, etc.) embedded in the matrix of a soft material (polymers, soft

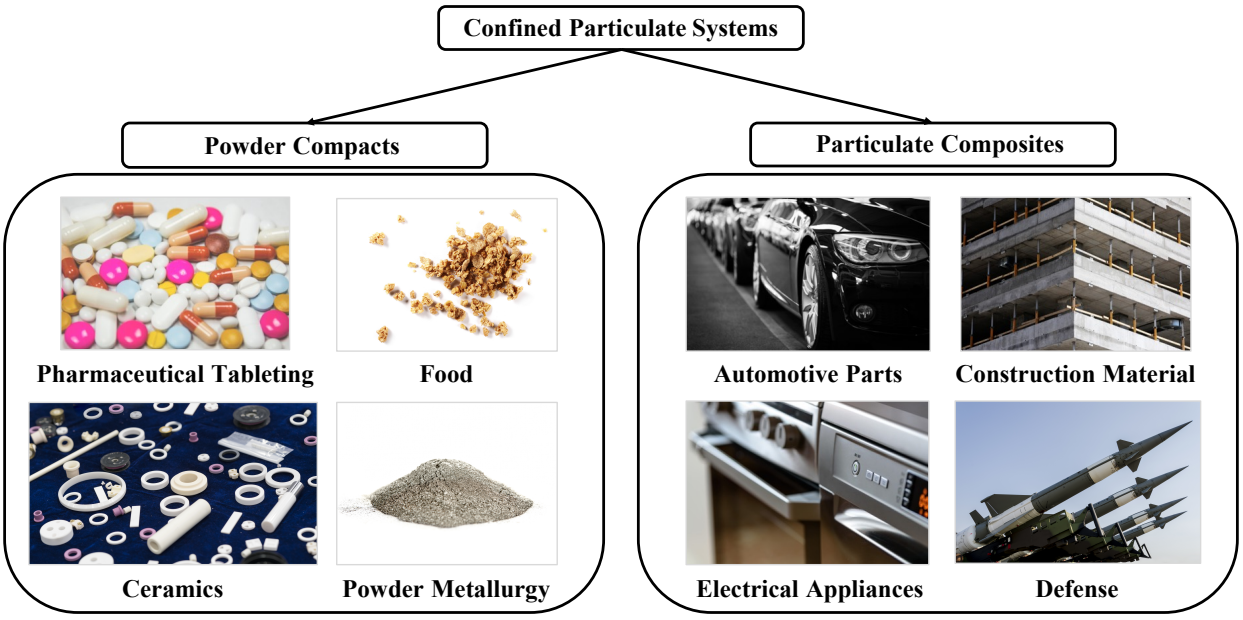

Figure 1.1. The applications of confined particulate systems. Images are allowed for reuse under their respective licenses. Image sources: Pexels (http://www.pexels.com/) and Adobe Stock (©Author Name - http://stock.adobe.com/).

metals, etc.). Under mechanical load, the main load bearing mechanism is the contact force chain network formed by the filler particles, while the matrix has a bulk effect on the load transfer (Liu et al., 2014a; Topin et al., 2007) and a confining effect on the initial rearrangement of the filler particles. Additionally, the presence of filler particles introduces significant inelastic phenomenon in the macroscopic mechanical response of particle-binder composites (Dargazany et al., 2014). For example, filled elastomers (Bergström & Boyce, 1998; Miehe & Keck, 2000) typically exhibit stress-softening or Mullins effect (Mullins, 1948, 1969) and hysteresis (Netzker et al., 2010) under the application of cyclic load.

1.2.2 Multi-scale Modeling Strategy

In conformity with the evident complexity of the microstructural evolution and macroscopic deformation mechanisms of these materials, a multi-scale modeling strategy for confined particulate systems has been identified in the current literature (Figure 1.2). Each of the modeling techniques in this strategy is discussed separately in the coming sections.

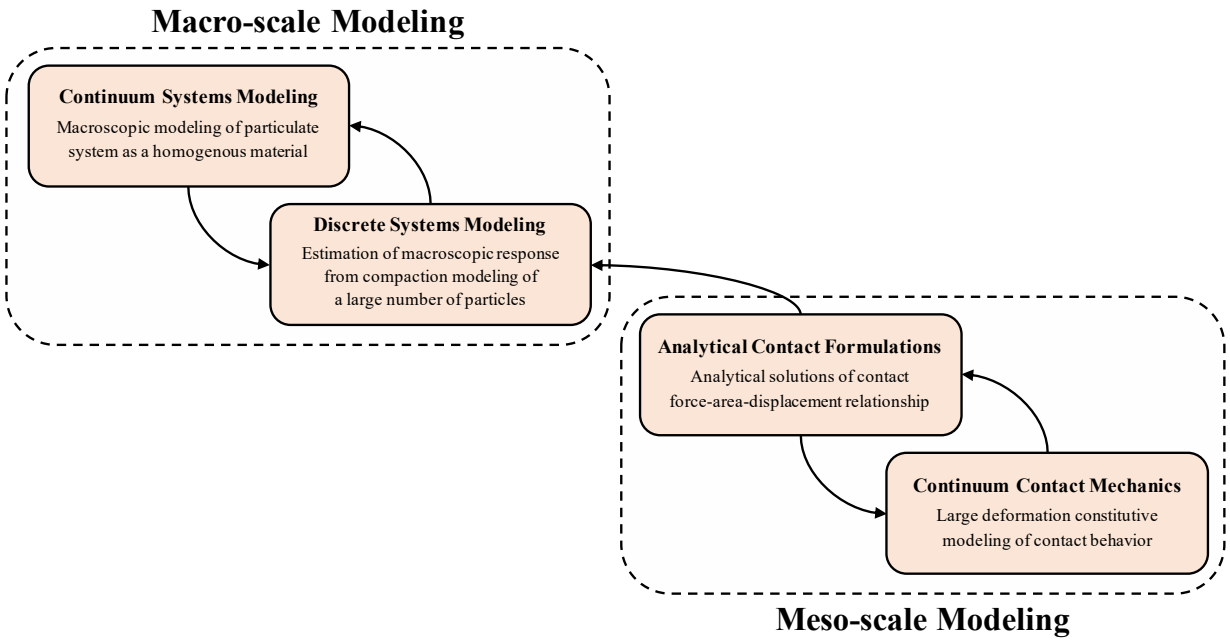

Figure 1.2. Multi-scale modeling strategy for confined particulate materials.

Continuum Contact Mechanics

At the meso-scale, the most fundamental modeling procedures involve the application of continuum contact mechanics, where individual particles are treated as bulk material and their contact behavior is modeled using large deformation continuum mechanics. Models proposed in this category typically utilize computer simulation techniques such as the Finite Element Method (FEM). For confined granular systems, finite element models for the compaction of two dimensional (Gethin et al., 2002; Procopio & Zavaliangos, 2005) and three dimensional (Chen et al., 2007; Frenning, 2008; Harthong et al., 2009, 2012) granular packings using discrete meshed spherical particles have been proposed, collectively known as the Meshed Distinct Element Method (Harthong et al., 2009). For particle-binder composites, models based on the framework of Cohesive Finite Element Method (CFEM) (Zhong & Knauss, 1997; X. Allan Zhong, 2000; Matouš & Geubelle, 2006; Barua & Zhou, 2011) have been proposed to capture inter-particle contact interactions and damage nucleation due to particle-binder interfacial dewetting under both quasi-static and dynamic impact loading. For the specific case of energetic Polymer-Bonded Explosives (PBXs), these models are capa-

ble of predicting the formation of local hotspots due to frictional heating at particle-particle and particle-binder interfaces, which is important for efficient design of the detonation mechanism of these materials.

While meso-scale continuum contact mechanics is the most accurate predictive modeling technique for large deformation response of confined particulate materials, it suffers from the prohibitive limitations of the computational cost of performing finite element simulations. For instance, MDEM-based models are at most capable of simulating the macroscopic response of an assembly of a few hundred particles (Harthong et al., 2009). Therefore, it is not suitable for performing simulations of a realistic representative volume of particulate systems such as pharmaceutical tablets, which may contain a packing of millions of particles.

Analytical Contact Formulations

To enable large-scale simulations of realistic granular packings, meso-scale analytical contact formulations have been developed, which essentially are closed-form solutions of the relationship between three important physical quantities representing particle-particle contact, i.e.

1. Contact displacement (γ), which is the displacement of centers of mass of the contacting particles

2. Contact force (P), which is the force due to pressure developed at the contact between the particles, and

3. Contact radius (a), which is the radius of the approximately circular contact developed between the contacting particles.

Analytical contact formulations, or contact laws, are developed by taking several simplifying assumptions with regards to particle and contact geometry, material's mechanical properties, loading configuration, and boundary conditions. Therefore, the predictions of these formulations may not be as accurate as those of models based on continuum contact mechanics. Nevertheless, their computational efficiency due to being closed-form expressions enables them to be applicable to discrete simulations of a realistically large number of particles.

The foundational concepts of analytical contact formulations were pioneered by Hertz (1882), who proposed a contact law for linear-elastic spherical particles by solving an approximate problem for frictionless contact between paraboloids of revolution, where the contacting surfaces are assumed as elastic half-spaces. For this assumption to hold, the deformations at the contact are assumed to be small as compared to the the dimensions of the contacting bodies and the relative radii of curvature of the contacting surfaces. By assuming an ellipsoidal pressure distribution over the circular contact area, Hertz derived closed-form expressions for relating the three physical quantities P, a and γ, given by

$$P = \eta_{\mathrm{H}} \gamma^{3/2} \tag{1.1}$$

where $\eta_{\mathrm{H}} = \frac{4}{3}\left(\frac{1-\nu_1}{E_1} + \frac{1-\nu_2}{E_2}\right)^{-1}\left(\frac{1}{R_1} + \frac{1}{R_2}\right)^{-1/2}$, and

$$a = \left(\frac{1}{R_1} + \frac{1}{R_2}\right)^{-1/2} \gamma^{1/2} \tag{1.2}$$

In the above expressions, R_1 and R_2 are the radii of the two spheres and (E_1, ν_1) and (E_2, ν_2) are their respective elastic mechanical properties (Young's modulus and Poisson's ratio).

Since its development in 1882, the Hertz theory is one of the most commonly applied contact laws to model normal contact between elastic solids of revolution, with extensive applications in mechanical characterization of nano and micro particles using single particle compression experiments (King & Bourgeois, 1993; Liu et al., 1998; Wang et al., 2005; Egholm et al., 2006; Zhang et al., 2007; Yan et al., 2009; Marigo et al., 2014; Portnikov & Kalman, 2014), made possible with fairly recent nanoindentation and micro-compression testing technology. However, in the context of confined particulate systems where multiple particles form a heterogeneous contact network, the predictions of Hertz theory are limited by its *local* character (Argatov et al., 2017), i.e., the multiple contacts on a single particle are treated as independent of each other, with contact force and area determined from the local deformation at each contact. For dense granular packings with high relative densities (typically $\sim$0.9 for pharmaceutical tablets according to Hancock et al. (2003)), this characteristic is found to be untrue due to significant contact interactions at large deformations

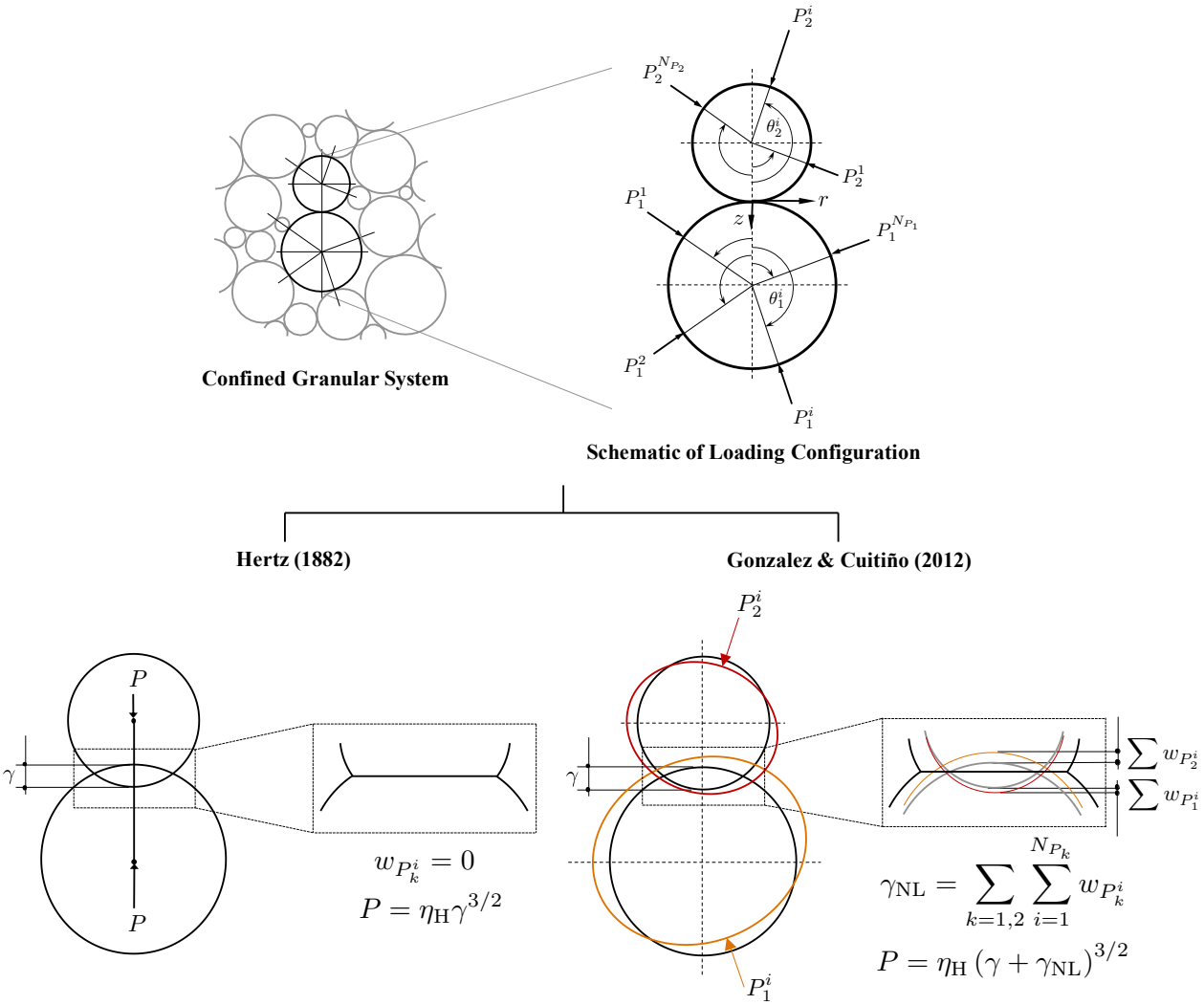

Figure 1.3. Comparison of Hertz (1882) theory and the nonlocal contact formulation by Gonzalez & Cuitiño (2012) for confined granular systems.

(Mesarovic & Fleck, 2000). This limitation was overcome by Gonzalez & Cuitiño (2012), who proposed the *nonlocal* contact formulation to provide an accurate description of the force-deformation behavior at contacts of particles pressed to high relative densities. The formulation is a direct extension of the Hertz theory and follows the work of Tatara (1989) to express the total deformation at a particle contact as the sum of *local* (Hertz) applied deformation and *nonlocal* deformations resulting from the other contacts on the same particle. Since the material behavior is assumed to be purely elastic, the principle of superposition allows the sum of deformations to be applied at each contact.

Figure 1.3 shows a comparison the Hertz (1882) theory and the nonlocal contact formulation (Gonzalez & Cuitiño, 2012) in the context of confined granular systems. It is evident that any two particles in contact within the heterogeneous contact network are additionally in contact with their immediate neighboring particles. Therefore, if the two contacting particles are isolated, they are assumed to be subjected to a general configuration of contact forces acting at the centers of each contact. According to the Hertz (1882) theory, each of the contact forces evolve independently of one another as a function of the local deformation at each contact. Therefore, the contact force P is given by Equation (1.1), which is a function of the local contact displacement γ and the mechanical properties and geometry of the contacting particles. Conversely, the nonlocal contact formulation (Gonzalez & Cuitiño, 2012) considers the nonlocal contributions to the contact displacement by each force P_k^i ($k = 1, 2$, $i = 1, ..., N_{P_k}$), denoted by $w_{P_k^i}$ and estimated from the Boussinesq solution (Johnson, 1985; Timoshenko & Goodier, 1970) for a point load on an elastic half space. The final solution to $w_{P_k^i}$ is given by

$$w_{P_k^i} \simeq \frac{(1+\nu_k)P_k^i}{4\pi R_k E_k} \frac{\left[-2(1-\nu_k) - 2(1-2\nu_k)\sin\left(\theta_k^i/2\right) + (7-8\nu_k)\sin^2\left(\theta_k^i/2\right)\right]}{\sin\left(\theta_k^i/2\right)} \tag{1.3}$$

According to the above equation, $w_{P_k^i}$ for each force P_k^i is a function of the material properties (E_k, ν_k) and geometry (R_k) of the particle k, as well as the angular distance θ_k^i of the force from the considered contact. By invoking the principle of superposition, the total nonlocal displacement γ_{NL} at the contact between the two particles is given by

$$\gamma_{\mathrm{NL}} = \sum_{k=1,2} \sum_{i=1}^{N_{P_k}} w_{P_k^i} \tag{1.4}$$

and thus the contact force P is given by

$$P = \eta_{\mathrm{H}} \left(\gamma + \gamma_{\mathrm{NL}}\right)^{3/2} \tag{1.5}$$

Figure 1.4 shows the applied load vs. deformation plots for the contacts of a single rubber sphere of radius $R = 10$ mm pressed between two rigid plates. In the figure, experimental

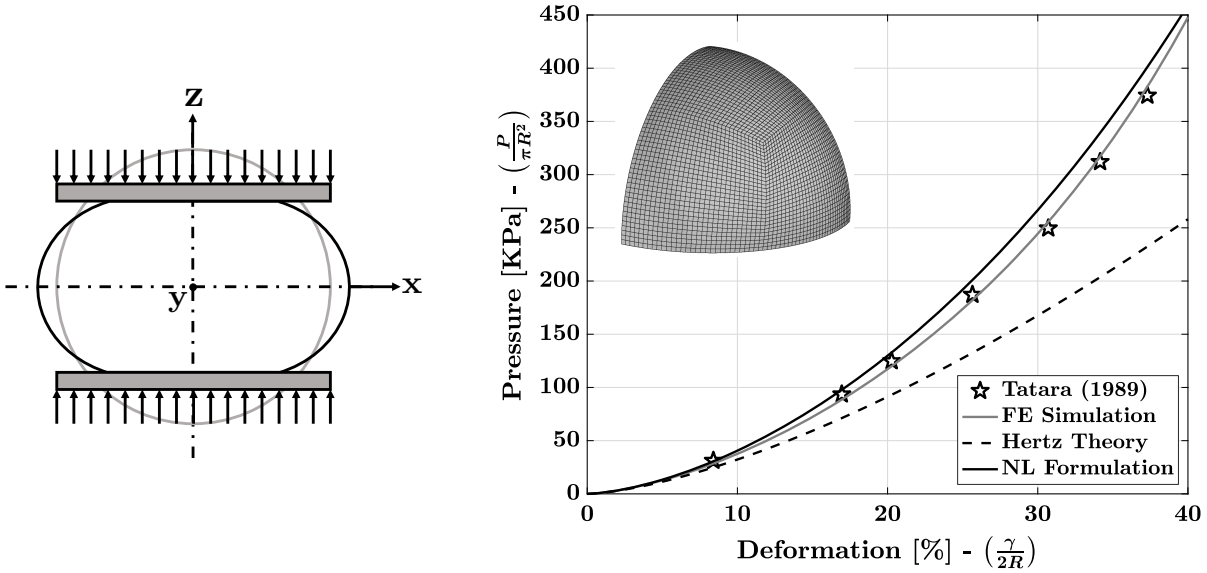

Figure 1.4. Comparison of Hertz (1882) theory and the nonlocal contact formulation by Gonzalez & Cuitiño (2012) for confined granular systems.

results reported by Tatara (1989) are compared with the analytical predictions of the Hertz theory and the nonlocal contact formulation, as well as numerical results from FE simulation of the compression performed on $(1/8)^{\text{th}}$ of the sphere (owing to geometric and loading symmetries). The FE model of the sphere was meshed with 500,000 hexahedral elements of type C3D8R with 515,201 nodes. The material properties for analytical formulations were taken as $E = 1.85$ MPa and $\nu = 0.48$ (Tatara, 1989; Tatara et al., 1991), while a compressible Neo-Hookean hyperelastic material assumption with material constants corresponding to these material properties was applied in the FE simulation to adequately model large nonlinear elastic deformations.

From the figure, it is evident the Hertz theory predictions deviate from the experimental and FE results at very small deformations ($\sim$5%), while the predictions of the nonlocal contact formulation are in excellent agreement for deformations ranging up to 40% (equivalent to relative density of $\sim$0.9 in confined granular systems). Moreover, the NLC formulation predictions were obtained within a few seconds, compared to about 5 hours taken ti obtain the FE results. This demonstrates the high computational efficiency of closed-form analytical contact formulations as compared to models based on continuum contact mechanics,

as well as their applicability towards performing large-scale simulations involving granular packings of a realistic number of particles.

While predictive analytical contact models for elastic particles provide essential insight into the microstructure evolution and large deformation macroscopic behavior of confined particulate systems, key progress in this regard entails the development of closed-form contact formulations for particles exhibiting elasto-plastic behavior, since most particulate materials undergo large permanent deformations under confined conditions. However, the contact response of elasto-plastic particles is found to be highly complex and spanning multiple distinct deformation regimes. From finite element study of the compression of elasto-plastic spheres, Mesarovic & Fleck (2000) and Tsigginos et al. (2015) showed that the contact between two spheres primarily undergoes four distinct deformation modes: (1) fully elastic at small deformations, (2) elasto-plastic or 'contained plastic' mode, (3) fully plastic or 'uncontained plastic' mode, and (4) large deformation plasto-elastic mode.

For small elastic deformations, the Hertz (1882) theory is sufficient to model the contact response. For elasto-plastic contact deformations, where the plastically deforming zone is 'contained' below the contact, spherical cavity expansion models have been proposed using small-strain approximation for elastic-perfectly plastic (Johnson, 1985; Studman et al., 1977; Hardy et al., 1971) and elastic-plastic power law hardening materials (Gao et al., 2006; Mata et al., 2006). These models assume that a hemispherical region directly beneath the contact area can be approximated by a hemispherical core of radius a (equal to the contact radius) which is subjected to the hydrostatic component of stress, $\bar{p}$. A plastically deforming hemispherical shell surrounds the core, the boundary of which is at a state of stress that satisfies the von-Mises yield criterion. Rest of the material outside the plastic shell deforms elastically. For small-strain models, by assuming a radial symmetry of stresses and displacements outside the hydrostatic core, the mean contact pressure and subsequently the force-displacement relationship have been obtained from the solutions of spherical shell expansion by Hill (1950).

For deformations in the fully plastic regime, where the plastically deforming zone breaks out to the contact and the surrounding free surface ('uncontained' mode), Biwa and Storåkers (Biwa & Storåkers, 1995; Storåkers et al., 1997) formulated an analytical contact model

by reducing the moving boundary contact problem of a curved rigid indenter deforming a half space to a stationary one, where the dependence of particle velocities and strain rates on the indentation magnitude (i.e., the contact radius) is removed through appropriate transformations. This approach makes the solution self-similar (Spence & Temple, 1968), and therefore the contact model is commonly known as the *similarity solution*. The solution, however, assumes small-strain kinematics and rigid-plastic power law hardening behavior (stress $\sigma = \kappa\epsilon^{1/m}$, where κ is a representative strength and m is the hardening exponent) without consideration of particle elasticity, thus limiting its application to small-deformations within the fully plastic regime.

With the onset of finite deformation plasticity, multiple contacts on a particle in confined particulate systems cannot be treated as independent due to significant contact interactions (Mesarovic & Fleck, 2000), and, therefore, local contact laws such as the similarity solution and others developed by Thornton & Ning (1998), Vu-Quoc et al. (1999), Brake (2012, 2015) and Rathbone et al. (2015) are no longer applicable. Additionally, at high relative densities close to 1, the plastic incompressibility causes the particles to support stress through elastic compression. This stage, referred to as the 'low compressibility' regime (Tsigginos et al., 2015), is characterized by dominant contact interactions and rising compaction pressure. In the context of a general loading configuration, the systematic development of an analytical contact formulation capable of predicting these contact interactions at later stages of compaction remains an open problem. However, initial progress was made by Harthong et al. (2009, 2012), who proposed a semi-empirical contact model for rigid-plastic power law hardening spheres based on MDEM results of the compaction of spherical particles in a simple cubic lattice. The model presents the contact force as the product of a stiffness and the contact displacement, where the stiffness consists of two terms. The first term describes the contact stiffness for the case of unconfined compression of a single particle between two rigid plates, or equivalently, the simple contact of two particles. The second, singular term is dependent on the relative density of the particle within its voronoi cell (Gellatly & Finney, 1982) as it is compressed by its immediate neighbors, and describes the plastic incompressibility of the particles at high relative densities by approaching infinity as the relative density approaches 1. Frenning (2013) proposed a contact model for a particle under a general configuration

of contact forces, albeit limited in applicability to moderate deformations. By following the work of Fischmeister & Arzt (1983) and Montes et al. (2006), he proposed that the deformed configuration of a sphere with multiple contacts can be approximated by a truncated sphere of a radius larger than that of the initial, undeformed particle. The radius of the truncated sphere is estimated by equating the average pressure on the particle due to the contact forces to the average volumetric pressure due to elastic compression. With the evaluated radius R, the contact force P_i on each contact i is given by $P_i = H\pi\left[R^2 - (R_o - \gamma_i/2)^2\right]$, where H is the material's hardness (Tabor, 1951), R_o is the initial particle radius and γ_i is the displacement at the i^{th} contact. The model, however, is limited to moderate deformations due to inability to describe contact areas after contact impingement (Harthong et al., 2012) and the large contact pressures during the 'low compressibility' regime. Later, Frenning (2015) extended this model to include these physical deformation mechanisms, albeit for the particular case of hydrostatic triaxial compaction.

For particle-binder composites, analytical contact laws capable of describing particle-binder-particle interactions, as well as particle-particle contact behavior when surrounded by a binder, are currently under development (Baker & Gonzalez, 2020).

Discrete Systems Modeling

As discussed previously, the main objective behind development of analytical contact laws is to enable large-scale simulations of the compaction of a realistic number of particles, and to predict the macroscopic response of confined particulate systems by scaling up their meso-scale contact behavior. Such simulations are performed by utilizing discrete numerical methods capable of modeling the static and dynamic behavior of granular materials. One of the most common and rapidly developing numerical technique is the Discrete Element Method (DEM), which is a Lagrangian approach for tracking the motion and effect of a large number of particles in time. Since its initial development by Cundall & Strack (1979), the method has been widely accepted and extensively employed to study particle rearrangement, microstructure evolution and macroscopic densification process during powder compaction (Sheng et al., 2002; Martin et al., 2003; Martin & Bouvard, 2003; Martin et al., 2006; Skrinjar

& Larsson, 2004; Belheine et al., 2009; Harthong et al., 2009; Jerier et al., 2011; Rojek et al., 2016). Advantages of this method include flexibility towards incorporating variety of contact behavior, including normal and tangential (frictional) contact, formation and breakage of solid bridges and attractive forces such as cohesion and adhesion, as well as the capability to consider non-spherical particle shapes. However, being a dynamic solver, DEM employs a time integrator (Rougier et al., 2004) to solve for the position and velocity of each particle during a particular time step, and therefore, suffers from a conditional numerical stability that imposes a limitation on the size of the time step (Burns et al., 2019). The solution instability also increases with higher compaction, thus requiring very small time steps at large deformations which increases the computational cost of the simulation. Additionally, to simulate a quasi-static compaction process, the requirement of a small strain-rate usually results in a significantly long simulation time (Sheng et al., 2004). Consequently, most DEM simulations of large granular packings are solvable up to a relative density of about 0.8, which is not sufficient to obtain a typical powder compact.

Recently, another discrete modeling technique, referred to as the particle mechanics approach (Gonzalez & Cuitiño, 2016; Yohannes et al., 2016, 2017; Gonzalez et al., 2018; Poorsolhjouy & Gonzalez, 2018; Gonzalez, 2019) has been developed to predict the microstructure evolution of granular packings of spherical particles. It is a highly computationally efficient numerical technique that describes each individual particle in the powder bed, and the collective rearrangement and deformation of particles that results in a compacted specimen. The approach considers rate-independent material behavior and models the compaction process as sequence of quasi-static loading steps. During each load step, a set of nonlinear equations for the equilibrium configuration of each particle is defined by a suitable analytical contact formulation and solved by a computationally efficient optimization approach based on the trust region method (Coleman & Li, 1996; Conn et al., 2000) (for more details on the implementation of trust-region based optimization, please ref. Gonzalez & Cuitiño (2016) and Gonzalez (2019)). Being an inherent time-independent quasi-static approach, particle mechanics calculations provide complete control over the size of the loading step, thus allowing the solution to be stable at large deformations. Consequently, particle mechanics simulations

are solvable up to a relative density close to 1, which is sufficient to study the macroscopic response of any powder compaction process.

Continuum Systems Modeling

Constitutive models based on small and large deformation continuum mechanics have been been the conventional methods used for describing the macroscopic response of confined particulate systems. Continuum-based models assume the particle media as homogeneous material and define the stress-state at every material point by constitutive equations that relate stress with the applied strain. Although these models neglect mesoscopic deformation mechanisms, they have been extensively used to model densification and macroscopic stress response for industrial powder compaction processes and to predict the mechanical response of particle-binder composites under variety of loading conditions.

For confined granular systems, the framework of many continuum mechanical models has been developed from models proposed originally to study geological materials, such as Drucker-Prager (Drucker & Prager, 1952), Cam-Clay plasticity (Schofield & Wroth, 1968) and Cap plasticity (Drucker et al., 1957) models. For instance, the Drucker-Prager Cap (DPC) plasticity model (DiMaggio & Sandler, 1971) has been developed by adding a cap yield surface to the Drucker-Prager model to allow for material hardening and dilatancy control during inelastic deformation. Often implemented in Finite Element (FE) codes, the DPC model has been used extensively for analysis of metal (Coube & Riedel, 2000; Almanstötter, 2015), ceramic (Aydin et al., 1996) and pharmaceutical (Michrafy et al., 2002; Sinka et al., 2003; Cunningham et al., 2004; Sinka et al., 2004; Wu et al., 2005; Han et al., 2008; Sinha et al., 2010) powder compaction. For compaction of metal powders, where plasticity effects may show very early during the loading process (Häggblad, 1991), models based on yield-surface free endochronic plasticity (Khoei et al., 2002; Bakhshiani et al., 2002, 2004) have been proposed. The endochronic theory (Valanis, 1970) considers material behavior during the entire load path as elasto-plastic, thus eliminating the requirement of a yield surface that classical plasticity theories employ to describe the onset and evolution of a material's plastic behavior.

For particle-binder composites, many constitutive models have been developed over the years in the context of large deformation continuum mechanics (Miehe & Keck, 2000; Laiarinandrasana et al., 2003; Ayoub et al., 2014; Dargazany et al., 2014; Österlöf et al., 2016; Raghunath et al., 2016; Plagge & Klppel, 2017; Guo et al., 2018a,b). The efficacy of a constitutive model for these materials in particular lies in the capability to account for inelastic phenomenon such as irreversible molecular slipping at the filler-binder interface (Kaliske & Rothert, 1998; Netzker et al., 2010), micro-cracking and interfacial debonding, cyclic stress-softening or Mullins effect (Mullins, 1948, 1969), hysteresis, and permanent deformations. To model such material behavior, nonlinear rheological models have been frequently employed. For instance, a zener-type viscoelastic rheological model was developed by Ayoub et al. (2014) for filled rubber-type materials based on the network alteration theory (Marckmann et al., 2002; Chagnon et al., 2006). To capture rate-independent plasticity effects of filled rubbers, multi-yield-surface models based on a parallel combination of Prandtl elements (Kaliske & Rothert, 1998) and yield-surface-free endochronic plasticity model (Netzker et al., 2010) have been proposed.

1.3 Identifying Research Gaps

As discussed in the previous section, the nonlocal contact formulation for elastic confined granular systems (Gonzalez & Cuitiño, 2012) is an accurate and efficient analytical tool for predicting the force-deformation behavior at the contacts of particles in a highly confined environment. However, it still has wide scope for improvement in the context of predicting the complete contact behavior and further relaxing the limiting assumptions of the Hertz theory. A successful description of inter-particle contact response entails prediction of both contact force and contact area. Since the nonlocal deformations also affect inter-particle contact boundaries, they must be accounted for in the contact radius-displacement relationship. Additionally, the limiting assumption of parabolic contacting profiles is also incorporated in the nonlocal contact formulation due to it being a direct extension of the Hertz theory. This assumption is mathematically defined as a one-term truncation of the Taylor series expansion of the undeformed contacting profiles. Therefore, the associated error in calculation of the

contact pressure distribution can be reduced by adding higher-order terms of the Taylor series to increase the accuracy of the profile function.

With regard to availability of predictive contact formulations for elasto-plastic confined granular systems, it is found that the current state-of-the-art contact formulations, such those developed by Harthong et al. (2009) and Frenning (2013, 2015), lack a consistent material or loading-condition dependence. For instance, the singular stiffness term in the contact law developed by Harthong et al. (2009) does not consider elastic compressibility, thus predicting very high contact forces at relative densities close to 1 for all material types regardless of their elastic behavior. On the other hand, the contact formulation proposed by Frenning (2013, 2015) does consider elastic compressibility, although solely for the specific case of hydrostatic compaction.

In the context of particle-binder composites, efforts are focused specifically on understanding the growing need of the defense and energy sector to develop the capability of predicting the performance and safety of energetic composite materials, particularly Plastic Bonded Explosives (PBX) that are commonly used in ammunition and warheads. These materials have explosive crystals embedded in a polymeric binder, where the binder provides structural integrity to the ammunition and protection from weak impact loads. Due to the hazardous nature of these materials, they must be designed to detonate and perform under a very specific external stimulus. However, due to a variety of loading conditions that these materials intermittently undergo during handling, storage and transportation over their operational life, undesirable changes in their mechanical behavior and microstructure may render them unpredictable and therefore, unsafe. While a number of independent experimental (Funk et al., 1996; Idar et al., 1998; Wiegand, 2000; Thompson et al., 2002; Idar et al., 2002; Grantham et al., 2004; Wiegand & Reddingius, 2005; Williamson et al., 2007; Drodge & Williamson, 2016) and constitutive modeling (Bardenhagen et al., 1998; Le et al., 2010; Yang et al., 2018) studies have been conducted over the years to understand and predict the mechanical response of energetic materials to different loading conditions, the current open literature lacks a systematic experimental and modeling procedure to understand and quantify the microstructural evolution of PBX and changes in their mechanical behavior due

to periodic application of mechanical load while allowing a time period of material recovery and aging.

1.4 Thesis Goal and Objectives

The goal of this thesis is to address the identified research gaps and challenges in predicting the microstructural evolution and mechanical behavior of confined particulate materials through experimental, particle mechanics and continuum constitutive modeling techniques. The specific objectives of the proposed thesis research are:

1. Develop closed-form analytical formulations to correct the elastic nonlocal contact formulation by including nonlocal and curvature corrections to the inter-particle contact area and profile functions of the contacting surfaces.

2. Develop contact formulations for elasto-plastic confined granular systems that are predictive at high relative densities and applicable to particle mechanics simulations.

3. Develop a systematic and reproducible experimental procedure to visualize and quantify the evolution of mesoscale microstructure and mechanical properties of particle-binder composites due to repeated quasi-static cyclic loading followed by time-recovery or aging.

4. Complement the experimental efforts by developing a large deformation constitutive model to characterize and predict the mechanical stress-strain response of particle-binder composites.

CHAPTER 2. CONTACT RADIUS AND CURVATURE CORRECTIONS TO THE NONLOCAL CONTACT FORMULATION ACCOUNTING FOR MULTI-PARTICLE INTERACTIONS IN ELASTIC CONFINED GRANULAR SYSTEMS

This chapter and associated appendices A and B were published in the International Journal of Engineering Science, Volume 133, Ankit Agarwal and Marcial Gonzalez, Contact radius and curvature corrections to the nonlocal contact formulation accounting for multi-particle interactions in elastic confined granular systems, pages 26-46, Copyright Elsevier (2018).

2.1 Introduction

The extensive applications of powder compaction, especially in manufacturing processes of critical industries like pharmaceutics, ceramic, energy, food, and metallurgy, make it a subject of intense research in the scientific community. Development of predictive and computationally efficient models that could accurately describe the behavior of granular media during compaction would directly impact optimality in manufacturing, waste reduction, and price and quality of the end product.

Macroscopic behavior of confined granular systems has been conventionally described by *continuum-based models*, which consider granular media as a continuous system, and hence have minimal emphasis on the behavior at particle scale. Many of these models were originally developed for analyzing the behavior of geological materials, such as Drucker & Prager (1952), Cam-Clay plasticity and Cap plasticity models. More recently, the Drucker-Prager Cap (DPC) plasticity model (DiMaggio & Sandler, 1971), where a cap yield surface is added to the Drucker & Prager model to allow for material hardening and dilatancy control during inelastic deformation, has been used for analysis of metal, ceramic and pharmaceutical powder compaction. Although requiring an elaborate mechanical testing procedure for calibration of model parameters (Cunningham, Sinka & Zavaliangos, 2004), the DPC model is widely used due to its adaptability to finite element method (Sinka, Cunningham & Zavaliangos, 2004). However, accuracy of the model response, especially during the decompression

(unloading) phase, relies heavily on the design of calibration experiments (Sinha, Curtis, Hancock & Wassgren, 2010) and proper elastic constitutive modeling (Han, Elliott, Bentham, Mills, Amidon & Hancock, 2008). In order to incorporate microstructural properties of the granular system into its global behavior, *discrete models* have been proposed, where contact behavior of individual particles is taken into account. Numerical methods in this category, such as dynamic discrete element methods (Cundall & Strack, 1979; Zhu, Zhou, Yang & Yu, 2008) and quasi-static particle mechanics approaches (Gonzalez & Cuitiño, 2016; Yohannes, Gonzalez, Abebe, Sprockel, Nikfar, Kiang & Cuitiño, 2016; Gonzalez, Poorsolhjouy, Thomas, Liu & Balakrishnan, 2018), are used in combination with a suitable contact formulation to predict the macroscopic behavior of compacted granular systems and, thus, predictability is heavily dependent on the contact law involved. The Hertz (1882) contact law for linear-elastic materials and similarity solution by Storåkers, Biwa & Larsson (1997) for viscous-plastic power law hardening materials are fairly predictable at small deformations and low relative densities of powder compacts. However, due to the occurrence of contact interactions at higher deformations, as pointed out by Mesarovic & Fleck (2000) in their study of elasto-plastic spheres, their predictions become increasingly deviant due to the assumption of independent contacts. This was partially overcome by introducing a local relative density parameter in contact laws curve-fitted to finite element simulations of small three-dimensional packings (Harthong, Jérier, Dorémus, Imbault & Donzé, 2009). Finally, a systematic and mechanistic connection between macroscopic and particle level behaviors, using continuum and discrete models respectively, was recently proposed (Poorsolhjouy & Gonzalez, 2018) to capture the anisotropic evolution of a die-compacted systems.

Several efforts towards experimental characterization of confined granular systems have also been made to understand the deformation behavior at granular scale, and to provide an efficient validation tool for the analytical contact formulations. Of particular interest is the mechanical response of single particles under confined conditions, most commonly studied using uniaxial compression experiments (Liu, Williams & Briscoe, 1998; Lu, Tung, Hung, Shiau & Hwang, 2001; Shima, Tatara, Iio, Shu & Lucero, 1993; Tatara, Shima & Lucero, 1991; Topuz & Okay, 2009; Zhang, Kristiansen & Liu, 2007). Recently, an apparatus has been developed for triaxial testing of single particles (Jonsson, Gråsjö, Nordström, Johansson

& Frenning, 2015), providing a more realistic insight into the behavior of individual particles during powder compaction.

For elastic confined granular systems, relaxing the underlying assumptions of the Hertz contact theory that limit its applicability to small deformations could be the key to achieving predictability at moderate to large deformations. Significant efforts in this direction have been made by Zhupanska (2011), who relaxed the small-strain Hertz assumption of considering contacting surfaces as elastic half spaces by proposing an analytical solution to the boundary value problem of an elastic sphere subject to contact stresses on a finite region of its surface and supported at its center. The results showed that the Hertz pressure distribution remained accurate for relatively large contact areas. Recently, Argatov et al. (2017) explored the concept of far points in Hertz contact problems, emphasizing the limitations of the "local character" of Hertz predictions. A major contribution in this regard is the nonlocal contact formulation for confined granular systems by Gonzalez & Cuitiño (2012), which provides an accurate and mechanistic description of the force-deformation behavior at contacts of a linear-elastic spherical particle subject to multiple contact forces, a typical configuration in particulate systems compressed to high relative densities. It follows the work of Tatara (1989) and relaxes the classical contact mechanics assumption of independent contacts by invoking the principle of superposition to express the deformation at a particular contact as a sum of local (i.e., Hertzian) deformation and nonlocal deformations generated by other contact forces acting on the same particle. The nonlocal contact formulation has recently been employed successfully to study the die-compaction of large frictionless non-cohesive granular systems comprising weightless elastic spherical particles (Gonzalez & Cuitiño, 2016).

A complete description of the inter-particle contact behavior in confined granular systems includes determination of both contact force and area with respect to particle deformation. While critical macroscopic quantities like compaction pressure and the reaction from die walls are directly related to inter-particle contact forces, the prediction of contact area is needed to estimate strength formation in the compacted solid (Gonzalez, 2019). In addition, the evolution of contact area is associated with contact impingement, i.e., with the merger of neighboring contacts. Since the assumption of circular contacts no longer remains valid after contact impingement, the predictions of a contact formulation may not be representative

of real contact behavior beyond the occurrence of this phenomenon, making an accurate determination of contact areas ever so important.

In the context of the nonlocal contact formulation (Gonzalez & Cuitiño, 2012), nonlocal mesoscopic deformations are derived from the Boussinesq solution (Johnson, 1985; Timoshenko & Goodier, 1970) of an elastic half-space under a concentrated force. The components of these deformations normal to the contact surface constitute the nonlocal contribution to the contact displacement, for which a closed-form solution has been obtained (Gonzalez & Cuitiño, 2012). However, the derivation of an analytical solution for nonlocal components radial to the contact center, that contribute to the evolution of contact radius, remains an open problem. Therefore, part of the work presented in this chapter is concerned with the development of an analytical framework for predicting nonlocal effects in the evolution of inter-particle contact area. The analysis presented is in the spirit of Tatara's (1991) work on expanded contact radius during uniaxial compression of rubber spheres.

An important aspect of this nonlocal contact formulation is that it is a direct extension of the classical Hertz contact theory. When nonlocal effects are neglected, the formulation reduces to Hertz theory. Therefore, any correction introduced in the Hertz solution should, in turn, improve the accuracy of the formulation. The second analysis presented in this chapter is concerned with the improvement of the formulation using contact pressures of higher accuracy. A solution of higher accuracy is obtained by correcting the description of the profiles of contacting surfaces through higher order terms in the Taylor series expansion of the profile functions. This methodology, termed curvature correction, is similar to the one reported by Cattaneo (1947) for solids of revolution and Luo (1958) for general solids. Closed form solutions of contact force and radius in terms of displacement are obtained for two-, three- and four-term curvature corrections.

Finally, a validation of the two proposed corrections is performed by comparison of the analytical predictions of contact force and radius versus deformation for compression of rubber spheres under various loading configurations with finite element simulations and experimental measurements.

The chapter is organized as follows. The deformation of an elastic sphere in a confined granular system under the action of multiple contact forces is discussed in Section 2.2. The

analytical formulation for predicting nonlocal effects in the evolution of the contact radius is then presented in Section 2.3. In Section 2.4, a curvature corrected nonlocal contact formulation is discussed. Section 2.5 presents a numerical and experimental validation of contact radius and curvature corrections. Finally, a summary and concluding remarks are presented in Section 2.6.

2.2 Deformation of an Elastic Sphere in a Confined Granular System under the action of a Distributed Surface Pressure

The deformation of a linear elastic sphere with radius R, Young's modulus E and Poisson's ratio ν is considered under the action of a distributed pressure and a general loading configuration of multiple contact forces. By approximating the deformation with an axially symmetric field, a cylindrical coordinate system defined in Figure 2.1 is adopted. The reference coordinates are denoted by $\mathbf{X} : (r, z)$, while the deformed coordinates are denoted by $\mathbf{x} : (r', z')$. The general loading configuration is represented by (P_i, θ_i), where P_i are the forces acting on the sphere's surface and θ_i are their angular distances with respect to z or z' axis.

A spherical cap of base radius a deforms to a flat circular surface of radius a' under the action of an ellipsoidally distributed pressure p proposed by Hertz (1882) and given by

$$p(r) = \bar{p}_m \sqrt{1 - \frac{r^2}{a^2}} \tag{2.1}$$

where $\bar{p}_m = 3P/2\pi a^2$ is the maximum value of the pressure and P is the effective contact force. The displacement of the elastic cap is represented by a deformation mapping $\boldsymbol{\varphi}(\mathbf{X})$, given by

$$\begin{Bmatrix} r' \\ z' \end{Bmatrix} = \boldsymbol{\varphi}(\mathbf{X}) = \begin{Bmatrix} r + u(r) + \sum_{i=1}^{N_P} u_{P_i}(r) \\ R - \sqrt{R^2 - r^2} + w(r) - \sum_{i=1}^{N_P} w_{P_i}(r) \end{Bmatrix} \tag{2.2}$$

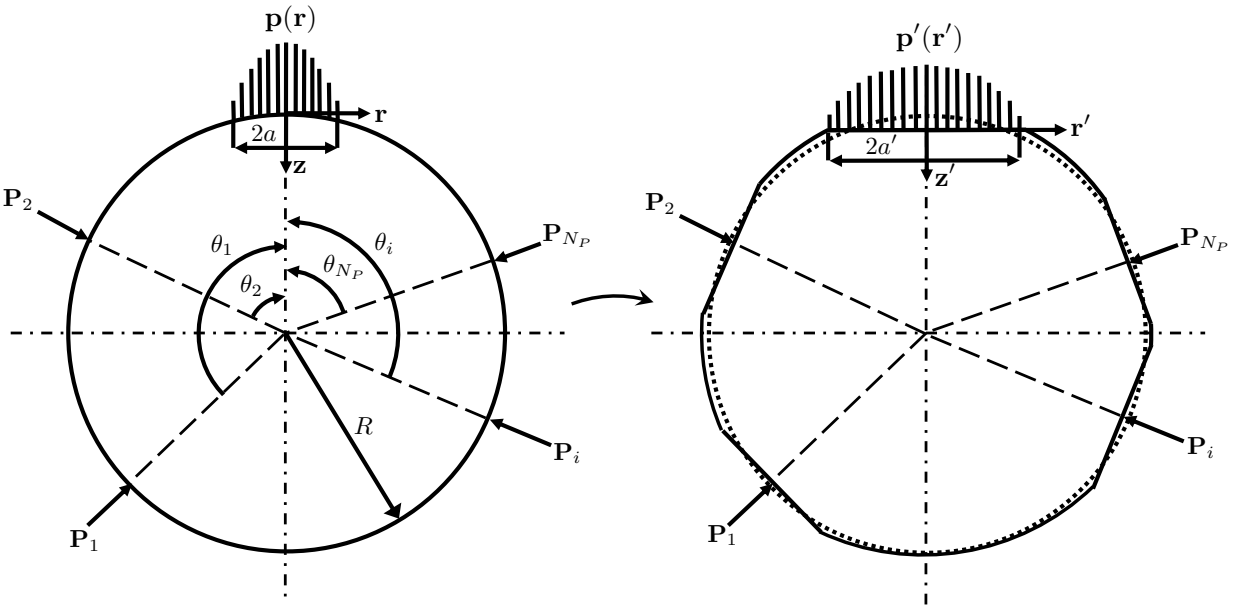

Figure 2.1. Depiction of deformation of an elastic sphere under the action a general configuration of contact forces, due to a distributed surface pressure p acting on its surface. The figure on the left denotes the configuration before deformation (reference configuration) while the figure on the right denotes the deformed configuration.

where $z = R - \sqrt{R^2 - r^2}$ is used, thus enabling the deformation mapping of surface points solely in terms of r. Quantities $w(r)$ and $u(r)$ are the vertical and radial displacements of the cap's surface points due to local pressure $p(r)$, which can be approximated by means of Boussinesq solution (Johnson, 1985; Timoshenko & Goodier, 1970), i.e., by

$$w(r) = \frac{3P(1-\nu^2)}{8a^3E}(2a^2 - r^2) \tag{2.3}$$

and, according to Tatara (1991), by

$$u(r) = \frac{(1+\nu)P}{4\pi E r}\left[\frac{r}{\sqrt{2}R}\sqrt{1+\sqrt{1-\frac{r^2}{R^2}}} - 2(1-2\nu)\left(1 - \frac{1}{\sqrt{2}}\sqrt{1-\sqrt{1-\frac{r^2}{R^2}}}\right)\right] \tag{2.4}$$

Quantities $u_{P_i}(r)$ and $w_{P_i}(r)$ are the nonlocal contributions to radial and vertical displacements induced by the concentrated forces P_i acting on the surface of the sphere. As a

valid approximation, Gonzalez & Cuitiño (2012) have represented $w_{P_i}(r)$ by the value of w_{P_i} at the contact center, i.e., by

$$w_{P_i}(r) \simeq w_{P_i}(0) \simeq \frac{(1+\nu)P_i}{4\pi RE}\left[\frac{-2(1-\nu)-2(1-2\nu)\sin(\theta_i/2)+(7-8\nu)\sin^2(\theta_i/2)}{\sin(\theta_i/2)}\right] \tag{2.5}$$

The determination of nonlocal radial displacements $u_{P_i}(r)$ is addressed in the next section and it is a major contribution of this work. It is worth noting that if both local and nonlocal radial displacements are assumed to be negligible, the nonlocal contact formulation proposed by Gonzalez & Cuitiño (2012) is recovered.

From the above particle deformation analysis, an important conclusion can be drawn. Although physical quantities, such as pressure and contact radius, compatibility conditions and equilibrium are defined in the deformed configuration, it is more convenient to work in the reference configuration. Physical quantities can be easily converted to spacial quantities by using the deformation mapping $\boldsymbol{\varphi}(\mathbf{X})$ and push-forward operations. This understanding will be used in the analysis performed in subsequent sections.

2.3 Nonlocal effects in the Evolution of Inter-Particle Contact Area

Now, the evolution of contact surface between two elastic spherical particles i and j of radius R_i and R_j, and material properties E_i, ν_i and E_j, ν_j respectively is considered. The particles are being pressed together in a general configuration of particles simulating a confined granular system (Figure 2.2). It is proposed that the particles deform to accommodate a flat contact surface of effective radius a'_{ij}, given by

$$a'_{ij} = a_{ij} + \frac{1}{2}\left[\frac{P_{ij}}{m^{\mathrm{L}}_{ij}(a_{ij})} + \sum_{h\in\mathcal{N}_i, h\neq j}\frac{P_{ih}}{m^{\mathrm{NL}}_{jih}(\mathbf{x}_j,\mathbf{x}_i,\mathbf{x}_h)} + \sum_{k\in\mathcal{N}_j, k\neq i}\frac{P_{jk}}{m^{\mathrm{NL}}_{ijk}(\mathbf{x}_i,\mathbf{x}_j,\mathbf{x}_k)}\right] \tag{2.6}$$

where a_{ij} is the contact radius in the reference configuration, $\mathbf{x}_i$ and $\mathcal{N}_i$ are the position and neighbors of particle i, and P_{ij} is the effective contact force between particles i and j. The factor of $1/2$ signifies an average of the radial deformations at the contact due to particles i and j and their respective neighbors.

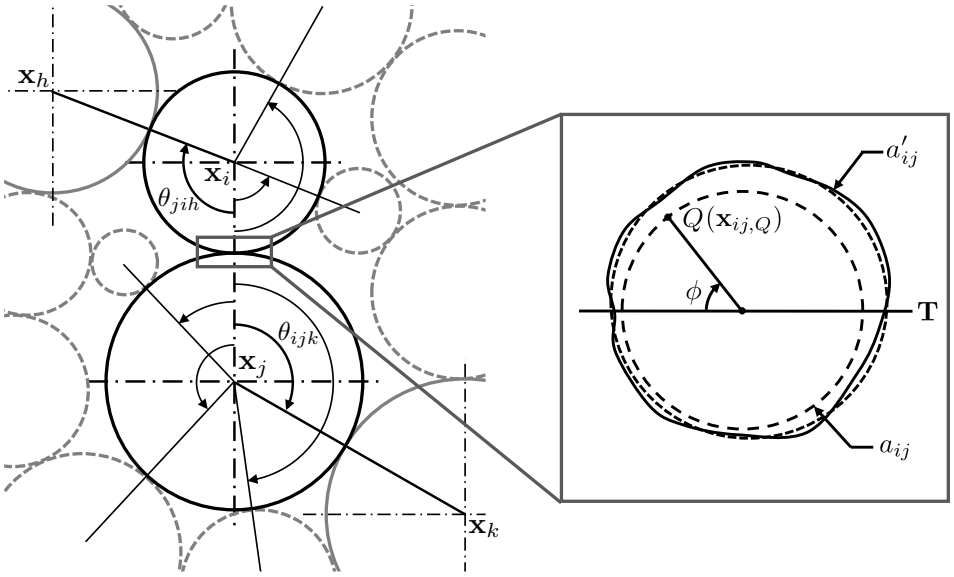

Figure 2.2. Depiction of nonlocal effects on the contact area between two dissimilar particles being compressed by a general loading configuration. The figure shows a schematic of the loading configuration, and the contact configuration without (long dashed curve) and with (solid curve) nonlocal correction. The contact with effective nonlocal correction is depicted by a short dashed curve, with radius a'_{ij}.

Term m_{ij}^{L} corresponds to the local contribution to radial deformation of the contact boundary. Using Equation (2.4) for $r = a_{ij}$, it can be expressed as

$$\begin{aligned}\frac{1}{m_{ij}^{\mathrm{L}}} = \sum_{l=i,j} \frac{1+\nu_l}{4\pi E_l R_l} \Bigg[& \frac{1}{\sqrt{2}} \sqrt{1+\sqrt{1-\frac{a_{ij}^2}{R_l^2}}} \\ & -2(1-2\nu_l)\left(\frac{R_l}{a_{ij}}\right)\left(1-\frac{1}{\sqrt{2}}\sqrt{1-\sqrt{1-\frac{a_{ij}^2}{R_l^2}}}\right)\Bigg]\end{aligned} \tag{2.7}$$

Term m_{jih}^{NL} corresponds to the nonlocal contribution to the radial deformation of the contact boundary, given by

$$\frac{1}{m_{jih}^{\mathrm{NL}}} = \frac{1}{2\pi}\int_0^{2\pi} \frac{\mathrm{d}\phi}{m_{jih,Q}^{\mathrm{NL}}(\mathbf{x}_j, \mathbf{x}_i, \mathbf{x}_h, \phi)} \tag{2.8}$$

where $m_{jih,Q}^{\mathrm{NL}}$ corresponds to a particular point Q on the contact boundary, given by its angular position ϕ with respect to the plane $\mathbf{T}$ given by the equation $[(\mathbf{x}_i - \mathbf{x}_j) \times (\mathbf{x}_i - \mathbf{x}_h)] \cdot (\mathbf{x} -$

$\mathbf{x}_i) = \mathbf{0}$ (the plane shown in Figure 2.2). Specifically, $m^{\mathrm{NL}}_{jih,Q}$ is mathematically represented by

$$\frac{1}{m^{\mathrm{NL}}_{jih,Q}} = \frac{1+\nu_i}{2\pi E_i R_i}\left[\frac{\sin\theta_{jih}\cos\phi\,\{\sin(\theta_{jih}/2)-\sin(\beta_{jih,Q}/2)\}\times\{\sin(\theta_{jih}/2)\sin(\beta_{jih,Q}/2)-2+2\nu_i\}}{2\sin(\theta_{jih}/2)\sin(\beta_{jih,Q}/2)}\right.$$
$$+\sqrt{1-\sin^2\theta_{jih}\cos^2\phi}\left[\frac{\cos(\beta_{jih,Q}/2)-\cos(\theta_{jih}/2)}{2}\right. \tag{2.9}$$
$$\left.\left.-(1-2\nu_i)\left\{\frac{1-\sin(\beta_{jih,Q}/2)}{\sin\beta_{jih,Q}}-\frac{\cos(\theta_{jih}/2)}{2\sin(\theta_{jih}/2)(1+\sin(\theta_{jih}/2))}\right\}\right]\right]$$

where $\beta_{jih,Q} = \widehat{\mathbf{x}_{ij,Q}\mathbf{x}_i\mathbf{x}_h}$ is the angle between point Q and position coordinates of particles i and h, given by

$$\beta_{jih,Q} = \cos^{-1}\left[\cos\left|\theta_{jih}-\sin^{-1}\left(\frac{a_{ij}}{R_i}\right)\right| - \left(\frac{a_{ij}}{R_i}\right)(1-\cos\phi)\sin\theta_{jih}\right] \tag{2.10}$$

and $\theta_{jih} = \widehat{\mathbf{x}_j\mathbf{x}_i\mathbf{x}_h}$ is the angle between position coordinates of particles j, i and h. A detailed derivation of $m^{\mathrm{NL}}_{jih,Q}$ is presented in Appendix A. It essentially entails the calculation of the radial displacement of point Q on the boundary of the deforming surface due to one of the forces P_i depicted in Figure 2.1.

In Equation (2.8), m^{NL}_{jih} is calculated by taking an average of the radial displacements due to nonlocal forces exerted by particles h on particle i across the contact boundary between particles i and j. Such averaging is necessary due to the fact that the nonlocal radial contribution due to a particular force is asymmetric over the contact boundary due to dependence on variable angle ϕ. By averaging over ϕ, the assumed symmetry in the deformation field is recovered and thus the deformed contact surface is approximated by a circular surface, although resulting in a shift in the position of its center which will be neglected in this work (see insert in Figure 2.2 and Appendix A, Equation (A.10)). It was found that the integral in Equation (2.8) does not have an exact closed-form solution, however its numerical integration is convergent and is used in further analysis.

To identify a closed-form approximate solution for m_{jih}^{NL} amenable to a computationally tractable implementation, a Taylor series expansion of $1/m_{jih,Q}^{\mathrm{NL}}$ about $a_{ij}/R_i = 0$ is obtained

$$\frac{1}{2\pi}\int_0^{2\pi}\frac{\mathrm{d}\phi}{m_{jih,Q}^{\mathrm{NL}}(\mathbf{x}_j,\mathbf{x}_i,\mathbf{x}_h,\phi)} = \frac{1+\nu_i}{16\pi E_i R_i}\left[\frac{\cos^2\left(\theta_{jih}/2\right)\left(4\nu_i - 3 - \cos\theta_{jih}\right)}{\sin\left(\theta_{jih}/2\right)}\right]\left(\frac{a_{ij}}{R_i}\right) + \mathcal{O}\left(\left(\frac{a_{ij}}{R_i}\right)^2\right) \tag{2.11}$$

Similarly, a Taylor expansion of $1/m_{jih,Q}^{\mathrm{NL}}$ about $\theta_{jih} = \pi$ is also obtained

$$\frac{1}{2\pi}\int_0^{2\pi}\frac{\mathrm{d}\phi}{m_{jih,Q}^{\mathrm{NL}}(\mathbf{x}_j,\mathbf{x}_i,\mathbf{x}_h,\phi)} = \frac{1}{m_{jih,\pi}^{\mathrm{NL}}} - \frac{(1+\nu_i)(1+2\nu_i)}{16\pi E_i R_i}(\pi - \theta_{jih}) + \mathcal{O}\left((\pi-\theta_{jih})^2\right) \tag{2.12}$$

where $m_{jih,\pi}^{\mathrm{NL}}$ corresponds to the analytical solution of Equation (2.8) for $\theta_{jih} = \pi$, that is

$$\frac{1}{m_{jih,\pi}^{\mathrm{NL}}} = \frac{1+\nu_i}{4\pi E_i R_i}\left[\frac{1}{\sqrt{2}}\sqrt{1-\sqrt{1-\frac{a_{ij}^2}{R_i^2}}} - 2(1-2\nu_i)\left(\frac{R_i}{a_{ij}}\right)\left(1-\frac{1}{\sqrt{2}}\sqrt{1+\sqrt{1-\frac{a_{ij}^2}{R_i^2}}}\right)\right] \tag{2.13}$$

Figure 2.3 presents a comparison of the two approximate analytical solutions obtained from truncated Taylor expansions at $a_{ij}/R_i = 0$ (Equation (2.11)) and $\theta_{jih} = \pi$ (Equation (2.12)) with the numerical solution of Equation (2.8), by plotting the dimensionless quantity $E_i R_i/m_{jih}^{\mathrm{NL}}$ with respect to θ_{jih} for all possible values of $\theta_{jih} \in \left(\sin^{-1}\left(a_{ij}/R_i\right), \pi\right]$. To gain a better insight into the non-linear dependency of the expressions on a_{ij}/R_i and ν_i, graphs for three different values of ν_i (= 0.15, 0.3 and 0.45) are shown, with each graph having plots evaluated at three different values of a_{ij}/R_i (= 0.25, 0.5 and 0.75). Analysis of the plots suggests that the numerical solution is fairly represented by Equation (2.11) until it shifts to positive values near $\theta_{jih} = 3\pi/4$. Thereafter, the numerical solution is well represented by Equation (2.12).

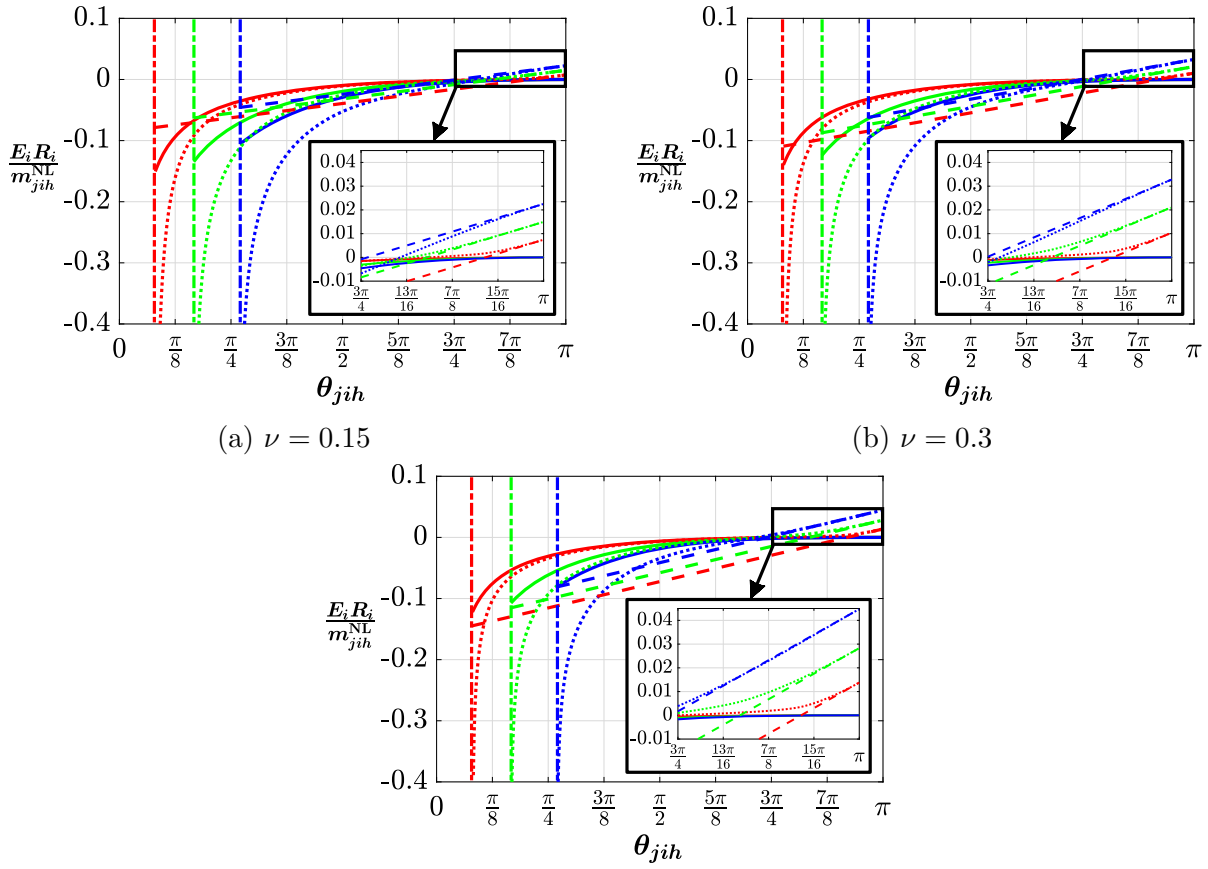

(a) $\nu = 0.15$ (b) $\nu = 0.3$

(c) $\nu = 0.45$

Figure 2.3. Plots of $E_i R_i / m_{jih}^{\mathrm{NL}}$ obtained from truncated Taylor series expansion at $a_{ij}/R_i = 0$ (Equation (2.11), solid curves) and $\theta_{jih} = \pi$ (Equation (2.12), dashed curves) versus angular distance θ_{jih}, compared with numerical solution of Equation (2.8) (dotted curves). Graphs for three different values of ν_i equal to (a) 0.15, (b) 0.3 and (c) 0.45 are presented, with plots for each evaluated at three different values of a_{ij}/R_i (red curves for $a_{ij}/R_i = 0.25$, green for $a_{ij}/R_i = 0.5$ and blue for $a_{ij}/R_i = 0.75$). The lower bound of $\theta_{jih} = \sin^{-1}(a_{ij}/R_i)$ (dashed-dotted lines) for evaluation of nonlocal contributions has also been delineated in each of the graphs.

Accordingly, a piecewise continuous function is proposed to represent m_{jih}^{NL}, given by

$$\frac{1}{m_{jih}^{\mathrm{NL}}} \simeq \begin{cases} \dfrac{1+\nu_i}{16\pi E_i R_i}\left[\dfrac{\cos^2(\theta_{jih}/2)(4\nu_i - 3 - \cos\theta_{jih})}{\sin(\theta_{jih}/2)} - \dfrac{\cos^2(\theta_{jih}^{\mathrm{c}}/2)(4\nu_i - 3 - \cos\theta_{jih}^{\mathrm{c}})}{\sin(\theta_{jih}^{\mathrm{c}}/2)}\right]\left(\dfrac{a_{ij}}{R_i}\right) & \theta_{jih} \le \theta_{jih}^{\mathrm{c}} \\ \dfrac{1}{m_{jih,\pi}^{\mathrm{NL}}} - \dfrac{(1+\nu_i)(1+2\nu_i)}{16\pi E_i R_i}(\pi - \theta_{jih}) & \theta_{jih} > \theta_{jih}^{\mathrm{c}} \end{cases} \tag{2.14}$$

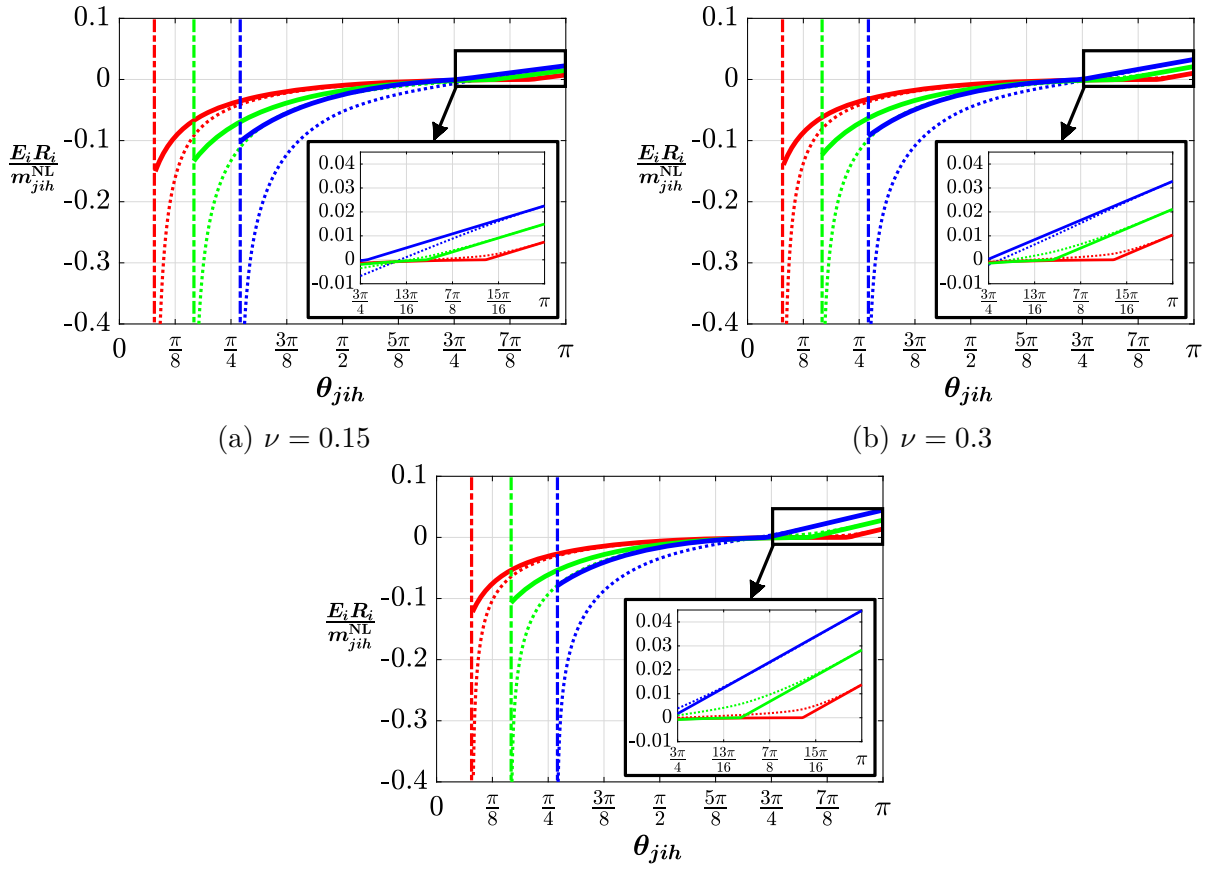

(a) $\nu = 0.15$ (b) $\nu = 0.3$

(c) $\nu = 0.45$

Figure 2.4. Plots of $E_i R_i / m_{jih}^{\mathrm{NL}}$ obtained by piece-wise approximate solution Equation (2.14) (bold solid curves) versus angular distance θ_{jih}, compared with numerical solution of Equation (2.8) (dotted curves). The values of ν_i and a_{ij}/R_i are the same as in figure 2.3.

where $\theta_{jih}^{\mathrm{c}}$ is the critical value of angular distance at which $1/m_{jih}^{\mathrm{NL}} = 0$, given by

$$\theta_{jih}^{\mathrm{c}} = \pi - \frac{16\pi E_i R_i}{(1+\nu_i)(1+2\nu_i) m_{jih,\pi}^{\mathrm{NL}}} \tag{2.15}$$

Figure 2.4 shows a comparison of the numerical solution of $1/m_{jih}^{\mathrm{NL}}$ and the proposed piece-wise continuous approximate solution, using the same values of a_{ij}/R_i and ν_i as in Figure 2.3. The accuracy of the closed-form approximate solution is acceptable and the computational tractability of the formulation is attained.

2.4 Curvature correction to the Nonlocal Contact Formulation

In this problem, the contact of two elastic spheres i and j being pressed together by a general configuration of concentrated forces (Figure 2.2) is considered again. According to the nonlocal contact formulation (Gonzalez & Cuitiño, 2012), any point within the contact area satisfies the following compatibility equation

$$\gamma_{ij} = R_i - \sqrt{R_i^2 - r_{ij}^2} + R_j - \sqrt{R_j^2 - r_{ij}^2} + w_i(r_{ij}) + w_j(r_{ij}) - \gamma_{ij}^{\mathrm{NL}} \tag{2.16}$$

where γ_{ij} is the relative displacement of $\mathbf{x}_i$ and $\mathbf{x}_j$ along the direction $\mathbf{z}_{ij} = (\mathbf{x}_i - \mathbf{x}_j)/||\mathbf{x}_i - \mathbf{x}_j||$, r_{ij} is the radial coordinate from axis $\mathbf{z}_{ij}$ of surface points in the reference configuration, and $w_i(r_{ij})$ and $w_j(r_{ij})$ are the vertical displacements of surface points located at r_{ij} on spheres i and j. The last term in the equation, $\gamma_{ij}^{\mathrm{NL}}$, is the total nonlocal contribution to vertical displacements induced by all neighbors of the two particles, i.e.,

$$\gamma_{ij}^{\mathrm{NL}} = \sum_{h \in \mathcal{N}_i, h \neq j} \frac{P_{ih}}{n_{jih}^{\mathrm{NL}}(\mathbf{x}_j, \mathbf{x}_i, \mathbf{x}_h)} + \sum_{k \in \mathcal{N}_j, k \neq i} \frac{P_{jk}}{n_{ijk}^{\mathrm{NL}}(\mathbf{x}_i, \mathbf{x}_j, \mathbf{x}_k)} \tag{2.17}$$

with n_{jih}^{NL} derived from Equation (2.5) (Gonzalez & Cuitiño, 2012)

$$\frac{1}{n_{jih}^{\mathrm{NL}}} = \frac{(1+\nu_i)}{4\pi R_i E_i} \left[\frac{-2(1-\nu_i) - 2(1-2\nu_i)\sin(\theta_{jih}/2) + (7-8\nu_i)\sin^2(\theta_{jih}/2)}{\sin(\theta_{jih}/2)} \right] \tag{2.18}$$

An important assumption of the Hertz theory is that the profile of the undeformed spherical contact surface is replaced by the first term of its Taylor series expansion, i.e.

$$R_i - \sqrt{R_i^2 - r_{ij}^2} = R_i \left[\frac{r_{ij}^2}{2R_i^2} + \mathcal{O}\left(\frac{a_{ij}^4}{R_i^4} \right) \right] \simeq \frac{r_{ij}^2}{2R_i} \tag{2.19}$$

This approximation largely deviates from the exact solution for moderate to high mesoscopic deformations. However, the error can be controlled by including more terms in the series to further correct the profile curvature; for example, the first four terms are given by

$$R_i - \sqrt{R_i^2 - r_{ij}^2} = R_i \left[\frac{r_{ij}^2}{2R_i^2} + \frac{r_{ij}^4}{8R_i^4} + \frac{r_{ij}^6}{16R_i^6} + \mathcal{O}\left(\frac{a_{ij}^8}{R_i^8} \right) \right] \simeq \frac{r_{ij}^2}{2R_i} + \frac{r_{ij}^4}{8R_i^3} + \frac{r_{ij}^6}{16R_i^5} + \frac{5r_{ij}^8}{128R_i^7} \tag{2.20}$$

Therefore, by adopting a four-term curvature correction, Equation (2.16) simplifies to

$$w_i(r_{ij}) + w_j(r_{ij}) = (\gamma_{ij} + \gamma_{ij}^{\mathrm{NL}}) - \frac{r_{ij}^2 \mathbb{A}_{ij}}{2} - \frac{r_{ij}^4 \mathbb{B}_{ij}}{8} - \frac{r_{ij}^6 \mathbb{C}_{ij}}{16} - \frac{5 r_{ij}^8 \mathbb{D}_{ij}}{128} \tag{2.21}$$

where

$$\mathbb{A}_{ij} = \frac{1}{R_i} + \frac{1}{R_j} \qquad \mathbb{B}_{ij} = \frac{1}{R_i^3} + \frac{1}{R_j^3} \qquad \mathbb{C}_{ij} = \frac{1}{R_i^5} + \frac{1}{R_j^5} \qquad \mathbb{D}_{ij} = \frac{1}{R_i^7} + \frac{1}{R_j^7}$$

Next, the pressure distribution p_{ij} compatible with Equation (2.21), over the circular contact region $\mathcal{Q}_{ij}$ of contact radius a_{ij} in the reference configuration (Figure 2.5) is determined. Specifically, for a pressure $p_{ij}(q_{ij}, \omega_{ij})$ acting over an elemental region B of area $q_{ij}\, dq_{ij}\, d\omega_{ij}$, the vertical displacement field according to the theory of elasticity (Johnson, 1985, pg. 53) is given by

$$w_i(r_{ij}) + w_j(r_{ij}) = \left(\frac{1 - \nu_i^2}{\pi E_i} + \frac{1 - \nu_j^2}{\pi E_j} \right) \int \int_{\mathcal{Q}_{ij}} p_{ij}(q_{ij}, \omega_{ij}) dq_{ij} d\omega_{ij} \tag{2.22}$$

and thus, by using Equation (2.22) in Equation (2.21), one gets

$$\begin{aligned} \left(\frac{1 - \nu_i^2}{\pi E_i} + \frac{1 - \nu_j^2}{\pi E_j} \right) \int \int_{\mathcal{Q}_{ij}} p_{ij}(q_{ij}, \omega_{ij}) dq_{ij} d\omega_{ij} = (\gamma_{ij} + \gamma_{ij}^{\mathrm{NL}}) - \frac{r_{ij}^2 \mathbb{A}_{ij}}{2} - \frac{r_{ij}^4 \mathbb{B}_{ij}}{8} \\ - \frac{r_{ij}^6 \mathbb{C}_{ij}}{16} - \frac{5 r_{ij}^8 \mathbb{D}_{ij}}{128} \end{aligned} \tag{2.23}$$

The pressure distribution p_{ij} is readily available by following the method reported by Luo (1958), which involves taking an approximate form of p_{ij} to solve the integral, followed by comparing coefficients of like powers of r_{ij} on both sides of the equation. For reference, the solution method is described in Appendix B. Using the pressure distribution functions, contact radius-force-displacement relationships for two-term, three-term and four-term curvature corrections are presented next in turn.

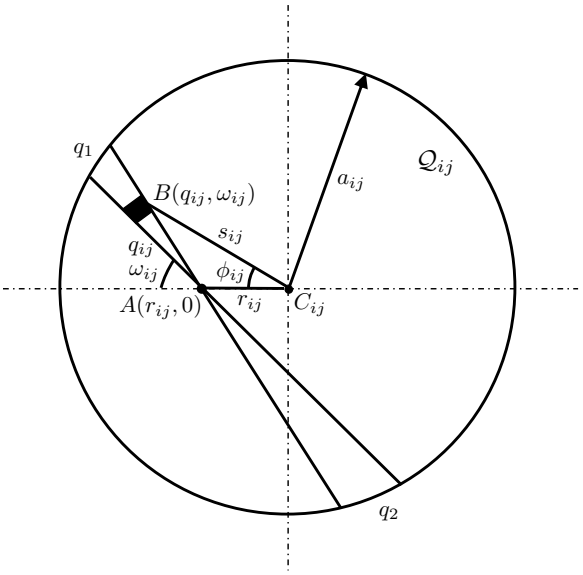

Figure 2.5. Depiction of the circular contact region $\mathcal{Q}_{ij}$ of contact radius a_{ij} under the action of a distributed contact pressure, with $B(q_{ij},\omega_{ij})$ being an elemental region on which the pressure distribution is considered.

2.4.1 Two-Term Curvature Correction

Pressure distribution (Appendix B.1, Equation (B.20)):

$$p_{ij}(r_{ij}) = \frac{2a_{ij}}{\pi}\left(\frac{1-\nu_i^2}{E_i}+\frac{1-\nu_j^2}{E_j}\right)^{-1}\left(1-\frac{r_{ij}^2}{a_{ij}^2}\right)^{1/2}\left[\mathbb{A}_{ij}+\frac{2a_{ij}^2\mathbb{B}_{ij}}{9}\left(1+2\frac{r_{ij}^2}{a_{ij}^2}\right)\right] \tag{2.24}$$

Contact radius-displacement relationship (Appendix B.1, Equation (B.19)):

$$a_{ij}^4\left(\frac{\mathbb{B}_{ij}}{3}\right)+a_{ij}^2\mathbb{A}_{ij}-(\gamma_{ij}+\gamma_{ij}^{\mathrm{NL}})=0 \tag{2.25}$$

which yields only one real and positive solution given by

$$a_{ij}=\left[\frac{3}{2\mathbb{B}_{ij}}\left(\sqrt{\frac{4\mathbb{B}_{ij}}{3}(\gamma_{ij}+\gamma_{ij}^{\mathrm{NL}})+\mathbb{A}_{ij}^2}-\mathbb{A}_{ij}\right)\right]^{1/2} \tag{2.26}$$

Contact force-radius-displacement relationship:

$$P_{ij}=\int_0^{a_{ij}} p_{ij}(r_{ij})2\pi r_{ij}dr_{ij}=\frac{4E_{ij}^*}{3}a_{ij}(\gamma_{ij}+\gamma_{ij}^{\mathrm{NL}})^3\left[\mathbb{A}_{ij}+\frac{2a_{ij}(\gamma_{ij}+\gamma_{ij}^{\mathrm{NL}})^2\mathbb{B}_{ij}}{5}\right] \tag{2.27}$$

where

$$\frac{1}{E_{ij}^*} = \frac{1-\nu_i^2}{E_i} + \frac{1-\nu_j^2}{E_j}$$

and $a_{ij}(\gamma_{ij} + \gamma_{ij}^{\mathrm{NL}})$ is given by Equation (2.26).

2.4.2 Three-Term Curvature Correction

Pressure distribution(Appendix B.2, Equation (B.30)):

$$p_{ij}(r_{ij}) = \frac{2a_{ij}}{\pi}\left(\frac{1-\nu_i^2}{E_i} + \frac{1-\nu_j^2}{E_j}\right)^{-1}\left(1 - \frac{r_{ij}^2}{a_{ij}^2}\right)^{1/2}\left[\mathbb{A}_{ij} + \frac{2a_{ij}^2\mathbb{B}_{ij}}{9}\left(1 + 2\frac{r_{ij}^2}{a_{ij}^2}\right) + \frac{a_{ij}^4\mathbb{C}_{ij}}{25}\left(3 + 4\frac{r_{ij}^2}{a_{ij}^2} + 8\frac{r_{ij}^4}{a_{ij}^4}\right)\right] \tag{2.28}$$

Contact radius-displacement relationship (Appendix B.2, Equation (B.29)):

$$\gamma_{ij} + \gamma_{ij}^{\mathrm{NL}} = a_{ij}^2\mathbb{A}_{ij} + \frac{a_{ij}^4}{3}\mathbb{B}_{ij} + \frac{a_{ij}^6}{5}\mathbb{C}_{ij} \tag{2.29}$$

which yields only one real and positive solution given by

$$a_{ij} = \left[\frac{\left[(\mathbb{Q}_{ij}^2 + 4\mathbb{R}_{ij}^3)^{1/2} + \mathbb{Q}_{ij}\right]^{1/3}}{9(2)^{1/3}\mathbb{C}_{ij}} - \frac{(2)^{1/3}\mathbb{R}_{ij}}{9\mathbb{C}_{ij}\left[(\mathbb{Q}_{ij}^2 + 4\mathbb{R}_{ij}^3)^{1/2} + \mathbb{Q}_{ij}\right]^{1/3}} - \frac{5\mathbb{B}_{ij}}{9\mathbb{C}_{ij}}\right]^{1/2} \tag{2.30}$$

where

$$\mathbb{Q}_{ij} = 2025\mathbb{A}_{ij}\mathbb{B}_{ij}\mathbb{C}_{ij} - 250\mathbb{B}_{ij}^3 + 3645\mathbb{C}_{ij}^2(\gamma_{ij} + \gamma_{ij}^{\mathrm{NL}})$$

$$\mathbb{R}_{ij} = 135\mathbb{A}_{ij}\mathbb{C}_{ij} - 25\mathbb{B}_{ij}^2$$

Contact force-radius-displacement relationship:

$$P_{ij} = \frac{4E_{ij}^*}{3}a_{ij}(\gamma_{ij} + \gamma_{ij}^{\mathrm{NL}})^3\left[\mathbb{A}_{ij} + \frac{2a_{ij}(\gamma_{ij} + \gamma_{ij}^{\mathrm{NL}})^2\mathbb{B}_{ij}}{5} + \frac{9a_{ij}(\gamma_{ij} + \gamma_{ij}^{\mathrm{NL}})^4\mathbb{C}_{ij}}{35}\right] \tag{2.31}$$

where $a_{ij}(\gamma_{ij} + \gamma_{ij}^{\mathrm{NL}})$ is given by Equation (2.30).

2.4.3 Four-Term Curvature Correction

Pressure distribution (Appendix B.3, Equation (B.42)):

$$p_{ij}(r_{ij}) = \frac{2a_{ij}}{\pi}\left(\frac{1-\nu_i^2}{E_i}+\frac{1-\nu_j^2}{E_j}\right)^{-1}\left(1-\frac{r_{ij}^2}{a_{ij}^2}\right)^{1/2}\left[\mathbb{A}_{ij}+\frac{2a_{ij}^2\mathbb{B}_{ij}}{9}\left(1+2\frac{r_{ij}^2}{a_{ij}^2}\right)\right.$$
$$\left.+\frac{a_{ij}^4\mathbb{C}_{ij}}{25}\left(3+4\frac{r_{ij}^2}{a_{ij}^2}+8\frac{r_{ij}^4}{a_{ij}^4}\right)+\frac{4a_{ij}^6\mathbb{D}_{ij}}{245}\left(5+6\frac{r_{ij}^2}{a_{ij}^2}+8\frac{r_{ij}^4}{a_{ij}^4}+16\frac{r_{ij}^6}{a_{ij}^6}\right)\right] \tag{2.32}$$

Contact radius-displacement relationship (Appendix B.3, Equation (B.41)):

$$\gamma_{ij}+\gamma_{ij}^{\mathrm{NL}} = a_{ij}^2\mathbb{A}_{ij}+\frac{a_{ij}^4}{3}\mathbb{B}_{ij}+\frac{a_{ij}^6}{5}\mathbb{C}_{ij}+\frac{a_{ij}^8}{7}\mathbb{D}_{ij} \tag{2.33}$$

which yields only one real and positive solution given by

$$a_{ij} = \left[\frac{1}{2}\sqrt{\frac{147\mathbb{C}_{ij}^2}{100\mathbb{D}_{ij}^2}-\frac{14\mathbb{B}_{ij}}{3\mathbb{D}_{ij}}-\mathbb{S}_{ij}-\frac{1}{4\sqrt{\mathbb{S}_{ij}}}\left(\frac{196\mathbb{B}_{ij}\mathbb{C}_{ij}}{15\mathbb{D}_{ij}^2}-\frac{343\mathbb{C}_{ij}^3}{125\mathbb{D}_{ij}^3}-\frac{56\mathbb{A}_{ij}}{\mathbb{D}_{ij}}\right)}\right.$$
$$\left.-\frac{\sqrt{\mathbb{S}_{ij}}}{2}-\frac{7\mathbb{C}_{ij}}{20\mathbb{D}_{ij}}\right]^{1/2} \tag{2.34}$$

where

$$\mathbb{S}_{ij} = \frac{7(2)^{1/3}\mathbb{S}_{ij}^{(1)}}{9\mathbb{D}_{ij}\left[\mathbb{S}_{ij}^{(2)}+\sqrt{{\mathbb{S}_{ij}^{(2)}}^2-171500{\mathbb{S}_{ij}^{(1)}}^3}\right]^{1/3}}+\frac{\left[\mathbb{S}_{ij}^{(2)}+\sqrt{{\mathbb{S}_{ij}^{(2)}}^2-171500{\mathbb{S}_{ij}^{(1)}}^3}\right]^{1/3}}{45(2)^{1/3}\mathbb{D}_{ij}}$$
$$+\frac{49\mathbb{C}_{ij}^2}{100\mathbb{D}_{ij}^2}-\frac{14\mathbb{B}_{ij}}{9\mathbb{D}_{ij}}$$
$$\mathbb{S}_{ij}^{(1)} = 35\mathbb{B}_{ij}^2-189\mathbb{A}_{ij}\mathbb{C}_{ij}-540\mathbb{D}_{ij}(\gamma_{ij}+\gamma_{ij}^{\mathrm{NL}})$$
$$\mathbb{S}_{ij}^{(2)} = 4465125\mathbb{A}_{ij}^2\mathbb{D}_{ij}-694575\mathbb{A}_{ij}\mathbb{B}_{ij}\mathbb{C}_{ij}+85750\mathbb{B}_{ij}^3$$
$$+(3969000\mathbb{B}_{ij}\mathbb{D}_{ij}-1250235\mathbb{C}_{ij}^2)(\gamma_{ij}+\gamma_{ij}^{\mathrm{NL}})$$

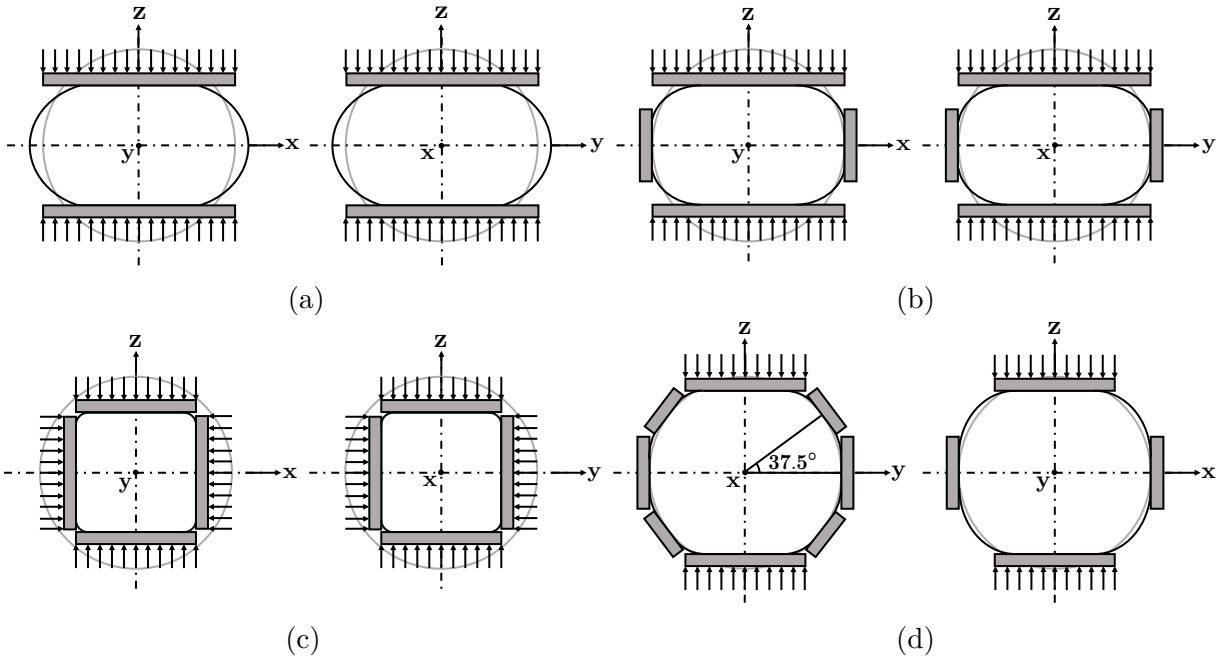

Figure 2.6. Schematic of the loading configurations considered for validation of contact radius and curvature corrections to the nonlocal contact formulation. (a) Simple Compression, (b) Die Compression, (c) Hydrostatic Compaction and (d) Die compression with four additional walls at an angle of 37.5° from lateral walls in the y-direction. For each loading configuration, views in x-z and y-z plane are provided for clarity.

Contact force-radius-displacement relationship:

$$P_{ij} = \frac{4E^*_{ij}}{3} a_{ij}(\gamma_{ij} + \gamma^{\mathrm{NL}}_{ij})^3 \left[\mathbb{A}_{ij} + \frac{2a_{ij}(\gamma_{ij} + \gamma^{\mathrm{NL}}_{ij})^2 \mathbb{B}_{ij}}{5} + \frac{9a_{ij}(\gamma_{ij} + \gamma^{\mathrm{NL}}_{ij})^4 \mathbb{C}_{ij}}{35} + \frac{4a_{ij}(\gamma_{ij} + \gamma^{\mathrm{NL}}_{ij})^6 \mathbb{D}_{ij}}{21} \right] \tag{2.35}$$

where $a_{ij}(\gamma_{ij} + \gamma^{\mathrm{NL}}_{ij})$ is given by Equation (2.34).

2.5 Validation of Contact Radius and Curvature Corrections

Validation of contact radius and curvature corrections to the nonlocal contact formulation was performed by considering four types of loading configurations (Figure 2.6), three of which simulate the compaction of particles in a simple cubic lattice, namely simple compression (sphere pressed between two rigid plates, figure 2.6a), die compaction (sphere compressed

between rigid plates and constrained laterally by rigid walls, figure 2.6b) and hydrostatic compaction (sphere compressed triaxially by rigid plates, figure 2.6c). The fourth configuration consists of four additional walls perpendicular to the y-z plane between the plates and lateral walls of a die compaction configuration (Figure 2.6d). Analytical predictions for all the configurations were compared with detailed finite element simulations, analytical results obtained from the original nonlocal contact formulation (Gonzalez & Cuitiño, 2012), and the classical Hertz predictions. For the case of simple compression, predictions were also compared with experimental measurements (Tatara, 1989; Tatara et al., 1991).

The finite element simulations were performed in ABAQUS on one-eighth of a sphere, owing to geometric and loading symmetries. Finite deformations were considered and the material was characterized as compressible Neo-Hookean with energy density of the form

$$W(\lambda_1, \lambda_2, \lambda_3) = \frac{\mu}{2}\left[J^{-2/3}(\lambda_1^2 + \lambda_2^2 + \lambda_3^2) - 3\right] + \frac{\lambda}{2}(J-1)^2 \tag{2.36}$$

where λ_1, λ_2 and λ_3 are the principle material stretches, $J = \det(\mathbf{F}) = \lambda_1\lambda_2\lambda_3$ and μ and λ are the Lamé constants. In ABAQUS, $C_{10} = \frac{\mu}{2}$ and $D_1 = \frac{2}{\lambda}$ are the input parameters The elastic constants used in the simulations correspond to the values of $E = 1.85$ MPa and $\nu = 0.48$ reported for rubber (Tatara, 1989; Tatara et al., 1991). Following a mesh convergence study, mesh comprising of 500,000 elements of type C3D8R (8-node linear hexahedral) and 515,201 nodes was chosen. For illustration purposes, a course mesh of 108,000 elements is depicted in Figure 2.7.

One of the most important factors to be considered while comparing analytical predictions with numerical simulations, other than the evolution of contact force and contact radius, is the occurrence of contact impingement. This is a phenomenon that causes the contacts to no longer remain circular and, thereby, restricts the applicability of the nonlocal contact formulation. Figure 2.8 provides a geometrical description of the impingement of two contacts in a spherical particle under a general loading configuration. From the figure, the angular distance θ_{12} between the two contacts at the inception of impingement is given by

$$\theta_{12} = \tan^{-1}\left(\frac{a_1'}{R - (\gamma_1/2)}\right) + \tan^{-1}\left(\frac{a_2'}{R - (\gamma_2/2)}\right) \tag{2.37}$$

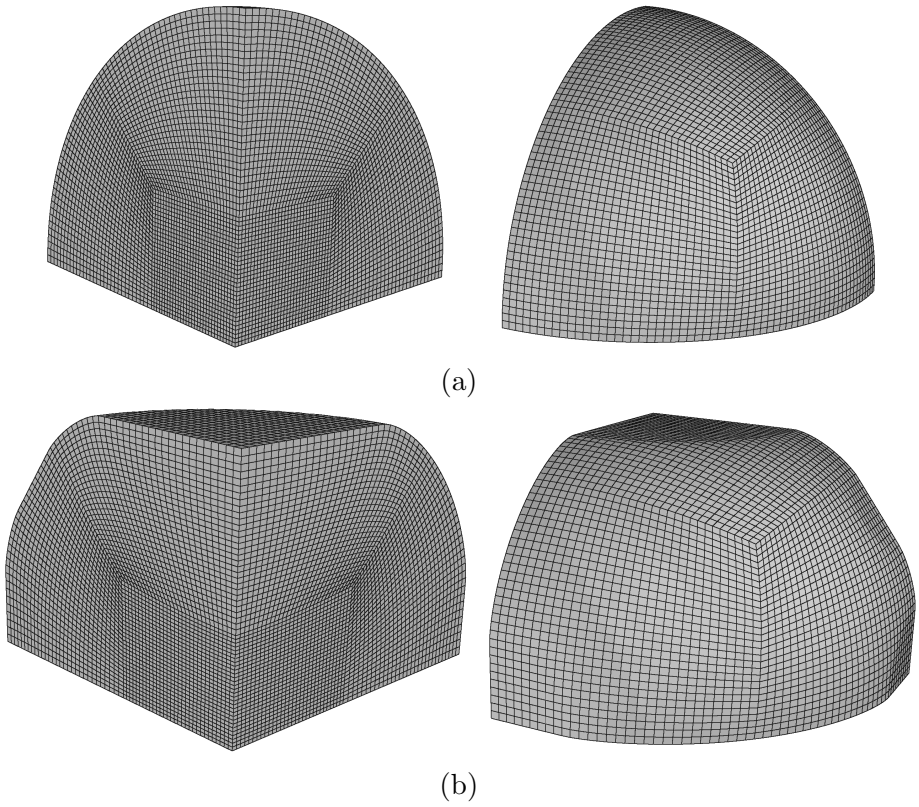

Figure 2.7. Finite-element mesh of one-eighth of a sphere created in ABAQUS. The depicted mesh is coarser than the final converged mesh, and consists of 108,000 hexahedral elements and 113,521 nodes. (a) Initial undeformed mesh. (b) Deformed mesh for the fourth loading configuration of die compression with four additional oblique walls.

Figures 2.9-2.12 present the validation results in form of load-versus-deformation ($F/\pi R^2$ versus $\gamma/2R$) and contact radius-versus-deformation (a'/R versus $\gamma/2R$) plots. The figures also show the values of deformation at which contact impingement occurs for each finite-element simulation (except simple compression where impingement does not occur)—this information is extracted by using the contact radius and displacement values obtained from the simulations in Equation (2.37). It is interesting to note that for all loading configurations except simple compression, the analytical predictions show an apparent strain-hardening or stiffening at various deformation levels. This is an artifact of the formulation, which possibly results from various modeling assumptions made for evaluation of γ^{NL} (Gonzalez & Cuitiño, 2012), that limits the range of applicability of the nonlocal contact formulation. Such limited

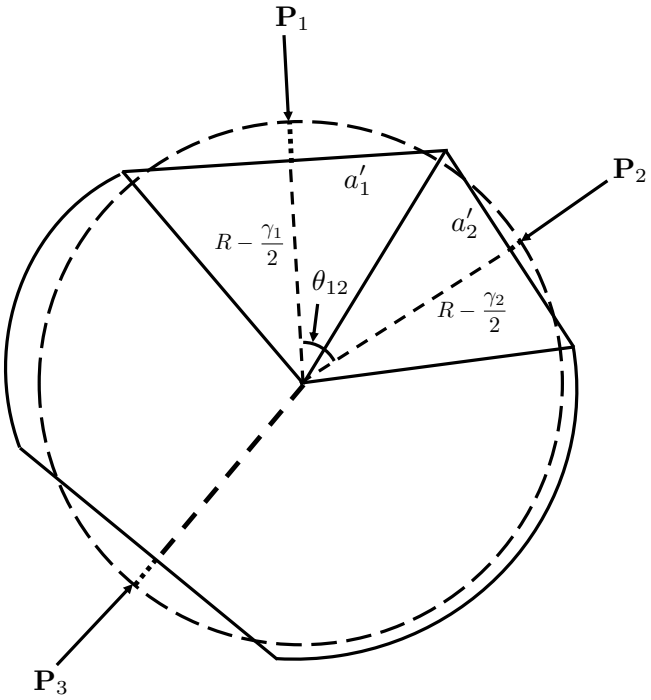

Figure 2.8. Impingement of two contacts of radii a_1' and a_2' at distances $\left(R - \frac{\gamma_1}{2}\right)$ and $\left(R - \frac{\gamma_2}{2}\right)$ respectively from the center of a particle of radius R, separated by an angular distance θ_{12}.

range of applicability exists for simple compression as well, albeit at deformations greater than 80% that are beyond the scope of this study.

Analysis of the plots suggests that the proposed contact radius and curvature corrections increase the range of applicability of the nonlocal contact formulation, thereby enabling predictions at higher levels of deformation. Further improvement is observed with increase in the order of curvature correction until convergence, which is achieved with a four-term correction. Quantitatively, the range of applicability of the formulation is increased by roughly 5% for die compaction, 2% for hydrostatic compaction and 6% for die compaction with additional walls is observed. Additionally, the corrections enable predictions closer to the geometric contact impingement, marked by dotted straight lines in the graphs. This is well represented in the graphs for die compaction, where predictions continue right until the impingement of vertical and lateral contacts, and for die compaction with additional walls, where predictions continue until the impingement of vertical and lateral contacts in the x-direction. Interestingly, the analytical predictions for the fourth configuration are remarkably accurate even

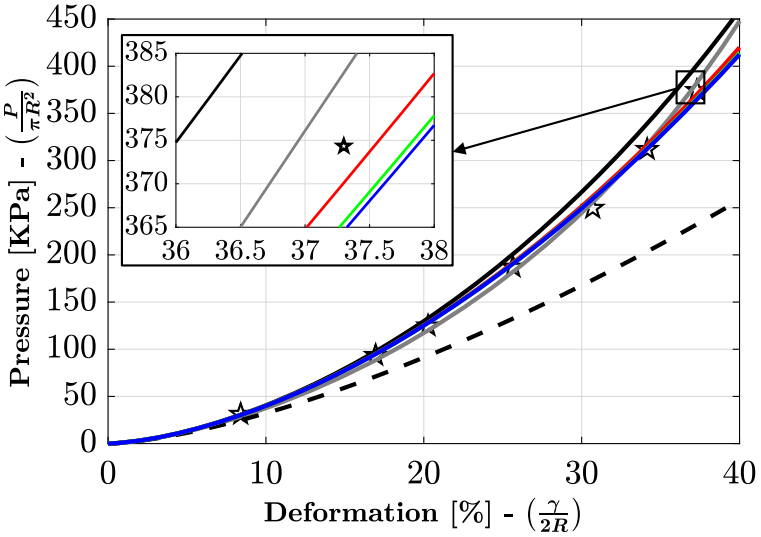

(a)

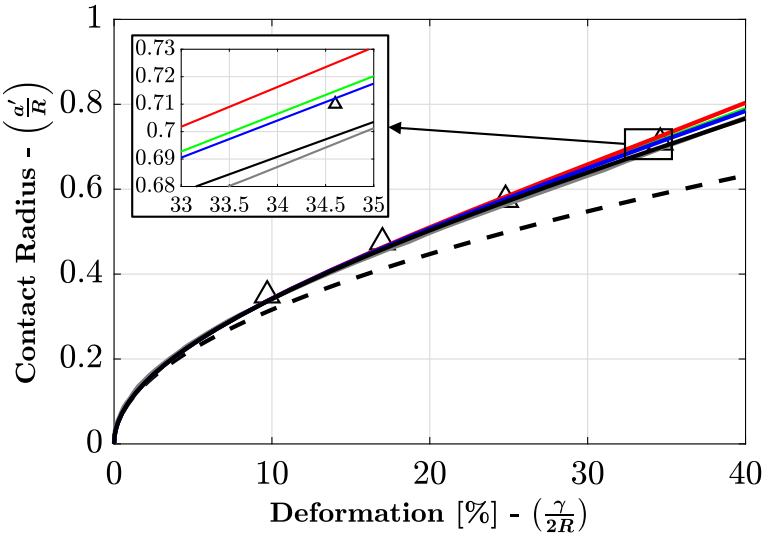

(b)

Figure 2.9. (a) Load - deformation and (b) contact radius - deformation curves for simple compression of a rubber sphere. Hertz theory predictions (black-dashed curves), nonlocal contact formulation results without contact radius and curvature corrections (black curves), with contact radius and two- (red curves), three- (green curves) and four- (blue curves) term corrections, finite element solution (gray curves), and experimental measurements (Tatara, 1989; Tatara et al., 1991) (five-pointed stars and triangles) are presented. The convergence of predictions at a four-term correction is shown in the inserts.

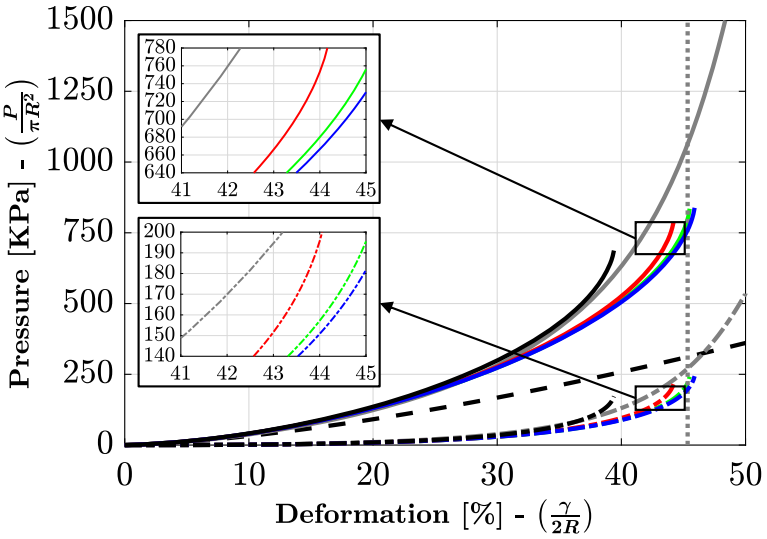

(a)

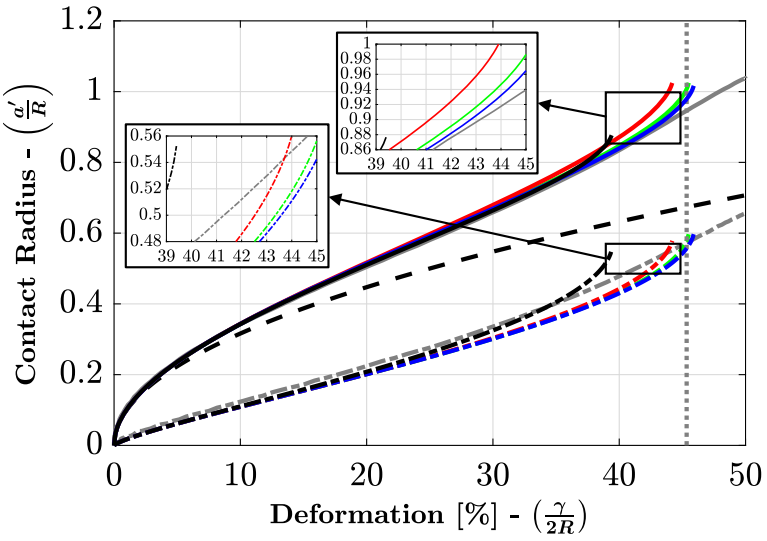

(b)

Figure 2.10. (a) Load - deformation and (b) contact radius - deformation curves for die compression of a rubber sphere. Predictions for vertical loaded contacts are given by solid curves while predictions for lateral constrained contacts are given by dashed-dotted curves. Hertz theory predictions (black-dashed curves), nonlocal contact formulation results without contact radius and curvature corrections (black curves), with contact radius and two- (red curves), three- (green curves) and four- (blue curves) term corrections, and finite element solution (gray curves) are presented. The deformation at geometrical contact impingement of vertical and lateral contacts is marked by a gray dotted line. The convergence of predictions at a four-term correction is shown in the inserts.

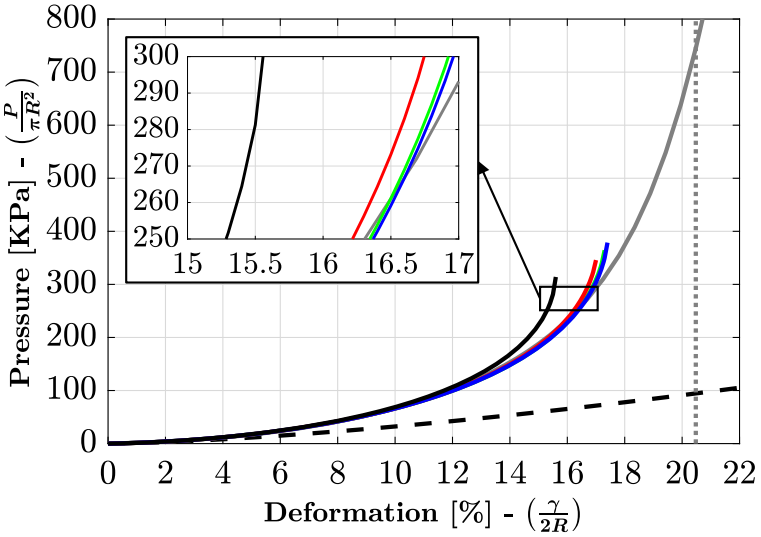

(a)

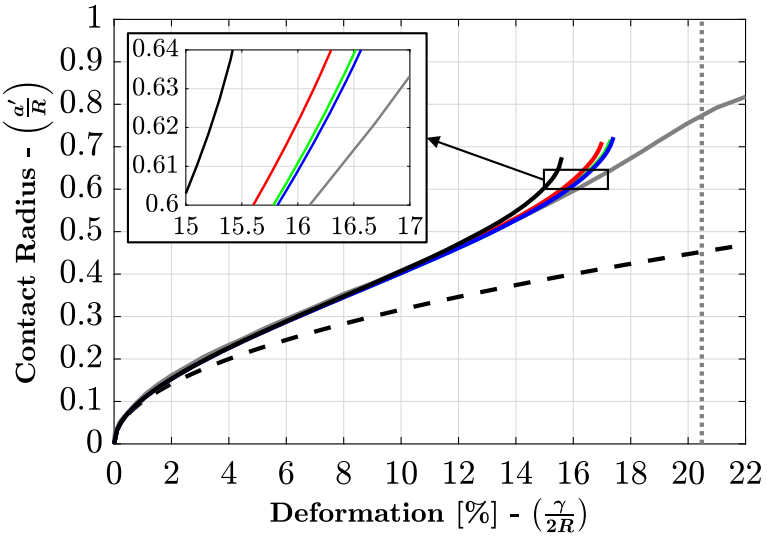

(b)

Figure 2.11. (a) Load - deformation and (b) contact radius - deformation curves for hydrostatic compression of a rubber sphere. Hertz theory predictions (black-dashed curves), nonlocal contact formulation results without contact radius and curvature corrections (black curves), with contact radius and two- (red curves), three- (green curves) and four- (blue curves) term corrections, and finite element solution (gray curves)) are presented. The deformation at geometrical contact impingement of contacts is marked by a gray dotted line. The convergence of predictions at a four-term correction is shown in the inserts.

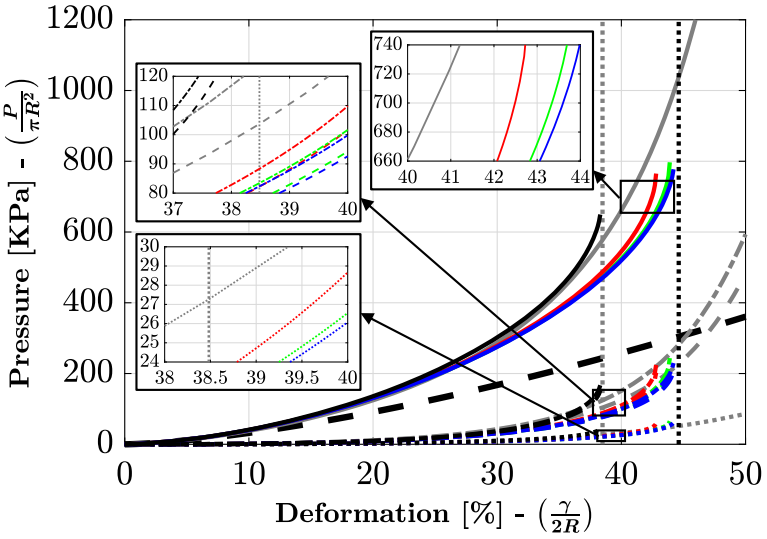

(a)

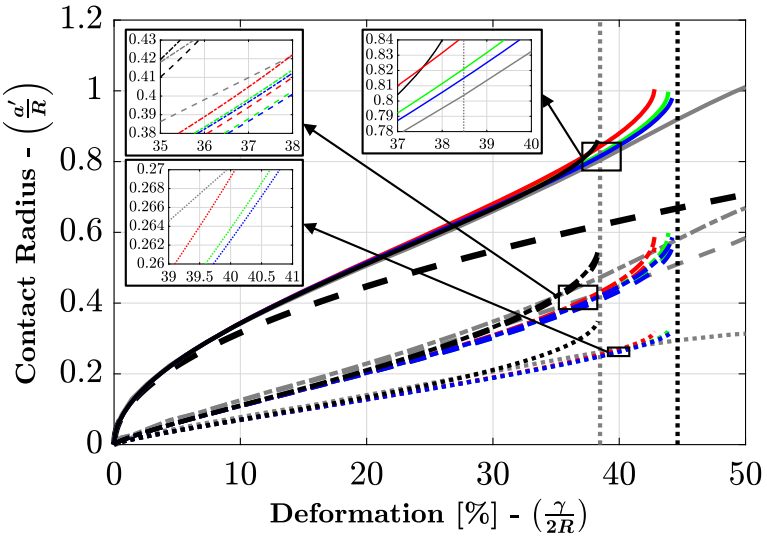

(b)

Figure 2.12. (a) Load - deformation and (b) contact radius - deformation curves for compression of a rubber sphere according to the loading configuration depicted in Figure 2.6d. Predictions are represented by solid curves for vertical loaded contacts, dashed-dotted curves for lateral constrained contacts in x-direction, dashed curves for lateral constrained contacts in y-direction, and dotted curves for oblique contacts. Hertz theory predictions (bold black-dashed curves), nonlocal contact formulation results without contact radius and curvature corrections (black curves), with contact radius and two- (red curves), three- (green curves) and four- (blue curves) term corrections, and finite element solution (gray curves) are presented. The deformation at geometrical contact impingement of vertical, oblique and lateral (y-direction) contacts is marked by a gray dotted line, and that of vertical contacts and lateral contacts in x-direction by a black dotted line. The convergence of predictions at a four-term correction is shown in the inserts.

after the impingement of vertical, oblique and lateral (y-direction) contacts (gray dotted line), indicating that predictions of the extended nonlocal contact formulation are accurate until impingement of all the particle contacts. As for the case of simple compression, an overall improvement in the representation of experimental measurements for both contact force and radius is observed, which again converges at the four-term curvature correction.

2.6 Summary and Discussion

An analytical framework has been developed for contact radius correction to nonlocal contact formulations, which accounts for local and nonlocal contributions to the radial deformation of contact boundaries due to multiple contact forces acting on a single particle. Furthermore, a method of curvature correction has been proposed to relax the traditional assumption of one-term Taylor series representation of undeformed contacting surfaces. For definiteness, attention has been restricted to elastic spheres in the absence of gravitational forces, adhesion or friction. Hence, a notable feature of the nonlocal formulation presented here is that, when no contact radius and curvature corrections are accounted for, it reduces to the nonlocal contact formulation presented by Gonzalez & Cuitiño (2012) and thus, when all nonlocal effects and corrections are neglected, it reduces to Hertz theory. A salient feature of the proposed formulation is that it increases the range of applicability of the nonlocal contact formulation (Gonzalez & Cuitiño, 2012) and, consequently, it enables accurate predictions of contact behavior until contact impingement for confined loading configurations. Specifically, investigation of four different loading conditions (namely simple compression, die compression within four walls and within six walls, and hydrostatic compaction) have successfully validated the predictions of the proposed nonlocal formulation with respect to experimental and detailed finite-element simulation results of rubber particles.

To conclude this chapter, future research directions and possible approaches for extension of the formulation are mentioned below.

First, the work presented in this chapter together with the nonlocal contact formulation by Gonzalez & Cuitiño (2012) serves as the foundation for conceiving an analytical elasto-plastic nonlocal contact formulation. Similar to elastic particles, the assumption of

independent contacts is not valid for particles deforming predominantly plastically in the range of moderate to high mesoscopic deformations (Mesarovic & Fleck, 2000). Recently, finite element simulations of linear elastic-perfectly plastic particles (Tsigginos, Strong & Zavaliangos, 2015) have shown contact interactions at moderate deformations physically manifesting as coalescence of local plastically deforming zones around individual contacts, with further deformation leading to the development of a low-compressibility regime when the contact deformations become predominantly elastic. The systematic investigation of these interaction effects is a worthwhile direction of future research.

Second, although the work presented in this chapter is a contribution to predictive modeling of confined granular systems, considerable effort is required for modeling of contact behavior beyond contact impingement. Finite element simulations presented in this chapter show an almost linear increase in contact force with deformation after impingement of all contacts, indicating a linear force-displacement relationship in this deformation regime. However, a rigorous analysis of such linear correlation is desirable, if beyond the scope of this study.

CHAPTER 3. SEMI-MECHANISTIC CONTACT LAWS FOR LARGE DEFORMATION UNIAXIAL AND TRIAXIAL COMPRESSION OF ELASTO-PLASTIC PARTICLES

The content of this chapter and associated appendices C, D and E has been submitted to the International Journal of Solids and Structures, and it is currently under review.

3.1 Introduction

Compacted granular systems, particularly powder compacts, are one of the most commonly used types of materials, with extensive applications in manufacturing processes of critical industries like pharmaceuticals, ceramics, energy, automotive, construction, food, and metallurgy. The versatility and wide application of these materials have made them a subject of active research in the scientific community, particularly in the area of predictive modeling of meso and macroscopic behavior of these materials under confinement. Confined granular media typically consist of a disordered blend of different powder particles with different particle size distributions. During compaction, these particles deform by coming into contact with neighboring particles as forces get transmitted throughout the system, essentially forming a heterogeneous contact network of force chains (Majmudar & Behringer, 2005). The significant heterogeneity of these systems at the granular scale has, therefore, a fundamental impact on their macroscopic behavior.

Conventionally, the macroscopic behavior of confined granular systems has been described by *continuum* models such as Cam-Clay (Puri et al., 1995; Sun & Kim, 1997), Cap (Chtourou et al., 2002), Drucker-Prager Cap (DPC) (DiMaggio & Sandler, 1971; Cunningham et al., 2004; Sinka et al., 2004; Han et al., 2008; Sinha et al., 2010), and Endochronic (Khoei et al., 2002; Bakhshiani et al., 2002, 2004) plasticity models, which consider granular media as homogeneous material, thereby neglecting the critical behavior at meso (particle) scale such as particle rearrangement and non-affine deformations. More recently, macroscopic *discrete* models have been proposed. The capability of these models to incorporate microstructural

evolution and properties of the granular system into its global behavior has increased their popularity and usage in recent years. A commonly used numerical method in this category is the Discrete Element Method (DEM) proposed by Cundall & Strack (1979), which has been employed extensively to successfully study and predict densification due to particle rearrangement and particle-particle elasto-plastic deformation during powder compaction (Sheng et al., 2002; Martin et al., 2003; Martin & Bouvard, 2003; Martin et al., 2006; Skrinjar & Larsson, 2004; Belheine et al., 2009; Harthong et al., 2009; Jerier et al., 2011; Rojek et al., 2016). The discrete particle mechanics approach (Gonzalez & Cuitiño, 2016; Yohannes et al., 2016, 2017; Gonzalez et al., 2018; Poorsolhjouy & Gonzalez, 2018; Gonzalez, 2019) is another computationally efficient numerical technique for modeling of highly confined granular systems. The approach considers rate-independent material behavior and models the compaction process as a sequence of quasi-static loading steps, where a set of nonlinear equations for the equilibrium configuration of each particle is formulated and solved during each step.

While the superiority of discrete models over continuum models in describing the macroscopic behavior of confined granular systems is evident, it is worth mentioning that the predictability of discrete models relies heavily on the employed contact formulation to describe the contact force-area-deformation relationship between inter-particle contacts formed before and during the compaction process. Understanding the contact mechanics between deformable particles has been a problem of interest for several decades. While contact of elastic particles within the regime of small deformations is fairly understood, thanks to the classical work of Hertz (1882), the problem becomes more involved and complex with consideration of large deformations and inelastic material behavior. As an initial step towards formulating an analytical contact law for elasto-plastic particles under large deformations, an attempt to understand the deformation mechanisms that govern the particle response under large compression is made. Figure 3.1 represents the normalized contact force-deformation, contact radius-deformation and contact pressure-deformation responses derived from finite element simulations of a single elasto-plastic von Mises type power-law hardening spherical particle under three types of loading configurations in a simple cubic cell, namely simple axial compression, die compression (axial compression and lateral confinement between four

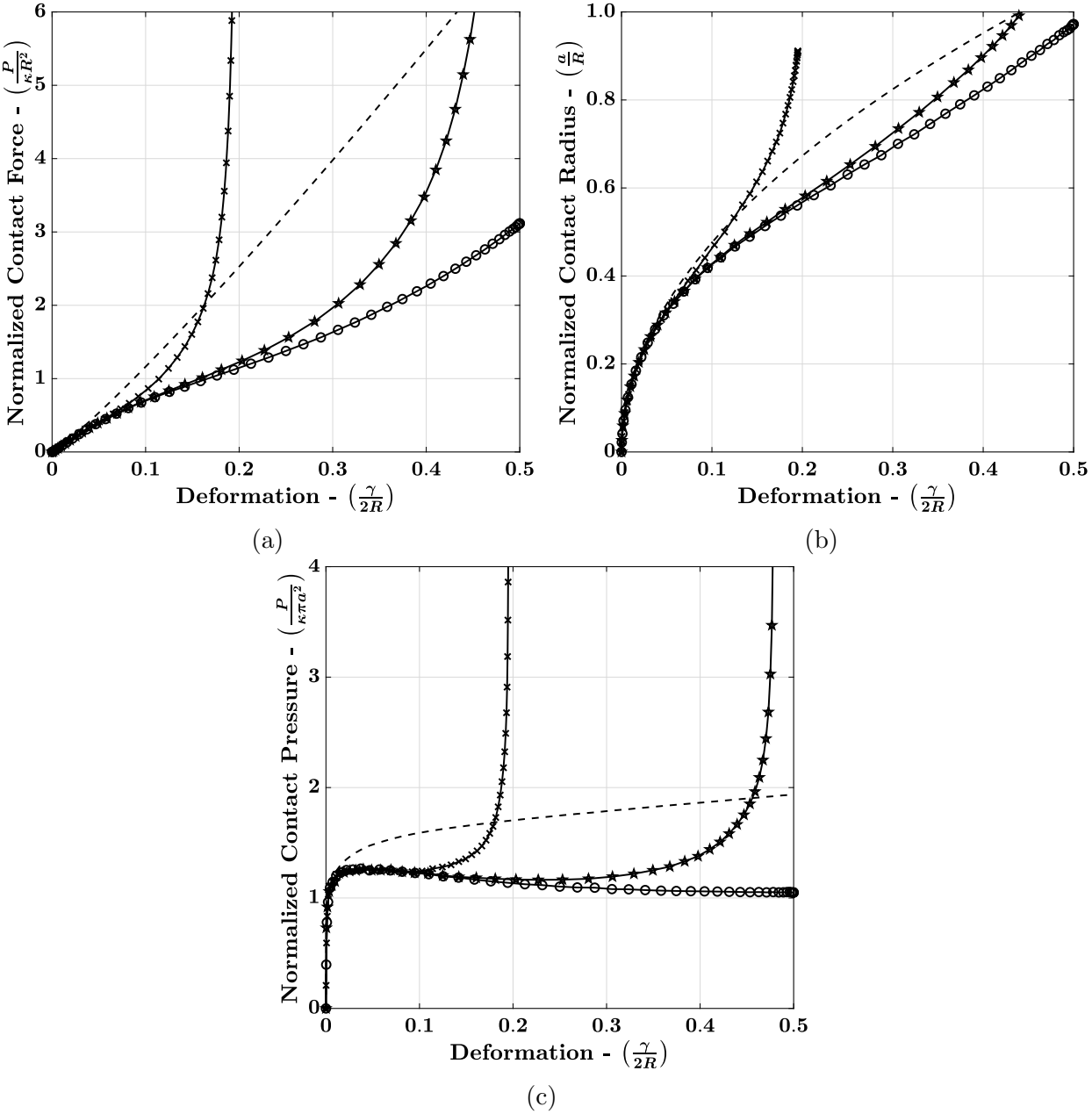

Figure 3.1. Finite element simulation results of normalized (a) contact force-deformation, (b) contact radius-deformation, and (c) contact pressure-deformation behavior of an elastic-plastic power law hardening sphere of radius $R = 10$mm under three types of loading configurations, namely simple compression (solid curve with circle markers), die compaction (solid curve with pentagram markers) and hydrostatic compaction (solid curve with cross markers). The similarity solution proposed by Biwa & Storåkers (1995) is also plotted for comparison, and is shown as dashed curve in all the plots. The material properties used here correspond to lead (Chen et al., 2007).

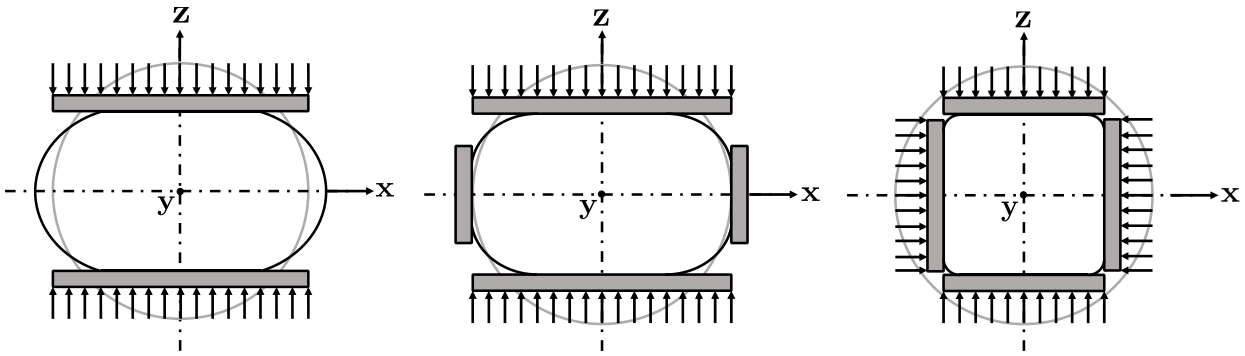

(a) Simple Compression (b) Die Compaction (c) Hydrostatic Compaction

Figure 3.2. Schematics of loading configurations considered in this study.

rigid walls) and hydrostatic compression (isostatic axisymmetric loading). Schematics of these loading configurations are depicted in Figure 3.2. The material's yield surface evolves according to the following power law (Ludwik, 1909)

$$\sigma = \sigma_y + K\epsilon_{\text{pl}}^{1/n} \tag{3.1}$$

where σ is the current stress, σ_y is the yield stress, K is a representative strength, n is the hardening exponent, and ϵ_{pl} is the plastic strain calculated as

$$\epsilon_{\text{pl}} = \epsilon - \frac{\sigma}{E} \tag{3.2}$$

where ϵ is the current strain and E is the Young's modulus. To perform the simulations, material properties corresponding to those reported by Chen et al. (2007) for lead, i.e., $K = 15.5$ MPa, $n = 2.857$, $E = 10$ GPa and $\nu = 0.435$ were used. To ensure consistency with the assumption of rigid-plastic power law hardening behavior by previous works on contact models for spherical indentation (Tabor, 1951; Biwa & Storåkers, 1995) and contact of inelastic solids of revolution (Storåkers et al., 1997), the Hollomon's power law (Hollomon, 1945) is additionally considered

$$\sigma = \kappa\epsilon^{1/m} \tag{3.3}$$

where κ is a representative strength and m is the hardening exponent. By equating power laws given by Equations (3.1) and (3.3) and adjusting the coefficient values to obtain similar response curves, Harthong et al. (2009) obtained $\kappa = 20.5$ MPa and $m = 4.167$ for lead. This value of κ was used to normalize the contact force and the contact pressure in Figure 3.1. From an observation of the contact response, it is quite apparent that the contact behavior is heavily dependent on the loading configuration, especially at moderate-to-large deformations. Particle compression causes an initial elastic deformation, followed by local plastic deformation at the vicinity of each contact where yielding occurs for the first time. Initially, the plastic zone is fully contained within the surrounding material which remains elastic, and, therefore, the contact deformation mode within this regime is termed as a 'contained' or 'elastic-plastic' deformation mode (Johnson, 1970, 1985; Stronge, 2018). On the onset of this deformation mode, the contact force and pressure curves become non-linear with a decreasing slope. The plastic zone quickly expands and breaks out to the free surface, resulting in a plastic flow of the material surrounding the contact area. This is called an 'uncontained' or 'fully plastic' mode of deformation (Johnson, 1970, 1985; Stronge, 2018). During this stage, the contact response exhibits a softening or a reduction in contact pressure with further deformation. This deformation regime has been previously studied by Frenning and co-workers (Frenning, 2013; Jonsson et al., 2017) and Tsigginos et al. (2015), who attribute the softening effect to the full mergence of plastically deforming zones around the contacts. However, the theory of Jackson, Green, and co-workers (Jackson & Green, 2003; Quicksall et al., 2004; Jackson & Green, 2006) is more intuitive, who postulated that the flattening or indentation of a sphere onto a surface causes its geometry to approach that of a compressed column, leading the contact pressure to reduce and approach the material's yield or representative strength. Until this point, the contacts can be assumed independent of each other, yielding similar force, area and pressure evolution regardless of the loading configuration, resulting in an overlap of the curves at this stage. With further deformation, the void volume around the particle gets increasingly filled by the material displaced by plastic deformation. For the case of simple compression, the lateral void volume is infinitely large. Therefore, material displacement in the lateral direction due to contact deformation does not affect the contact pressure, which continues to reduce and approach the material's

representative strength. However, for die and hydrostatic loading conditions, the void volume is finite and, therefore, the contact pressure starts increasing again with increasing particle deformation. This phenomenon, termed 'geometrical hardening' by Sundstrom & Fischmeister (1973) and 'low compressibility' regime by Tsigginos et al. (2015), has been previously studied using finite element simulations of isostatic axisymmetric loading of elastic-perfectly plastic spherical particles (Tsigginos et al., 2015). It was observed that the increase in contact pressure was the result of a significant increase in the elastic strain energy of the particle during this stage, indicating that further particle deformation is governed by elastic compressibility of the material. Due to the higher degree of confinement, void filling occurs at a faster rate during hydrostatic loading as compared to the die loading condition, resulting in the contact pressure rising at a smaller contact deformation for the hydrostatic loading configuration as compared to the die configuration. Overall, this phenomenon is observed the in form of a significant divergence of the response curves of the three cases at this stage, signifying a strong dependence on the loading configuration at large deformations.

For deformations in the 'contained' mode, spherical cavity expansion models for elasto-plastic indentation of a half space have been proposed for both small (Johnson, 1985; Studman et al., 1977; Hardy et al., 1971; Gao et al., 2006; Mata et al., 2006) and large deformations (Liu et al., 2014b). For materials undergoing negligible elastic deformations and predominant 'uncontained' plastic deformations (rigid-plastic power law hardening), Biwa and Storåkers (Biwa & Storåkers, 1995; Storåkers et al., 1997) formulated a contact model by reduction of a moving boundary contact problem to a stationary one using self-similar approach. The model was derived by first solving the fundamental contact problem of a curved rigid indenter in contact with a deformable half space (Hill et al., 1989), from which the solution of spherical indentation of a half space and more importantly, contact of two spheres of different radii and strengths but the same hardening exponent could be obtained. According to this model, for contact between two spheres (Figure 3.3) of radii R_1 and R_1, strengths κ_1 and κ_2, and plastic power-law hardening exponent m, the contact force (P)-radius (a)-displacement (γ) relationships are given by

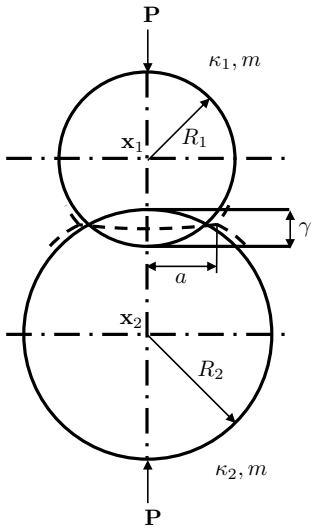

Figure 3.3. Schematic of the two-particle contact problem, depicting the contact between two spherical particles of radii R_1 and R_2. The particles are made of rigid-plastic power law hardening material with strengths κ_1 and κ_2 and a common power-law hardening exponent m. A displacement γ of the centers of mass of the particles located at positions $\mathbf{x}_1$ and $\mathbf{x}_2$ results in a contact force P and contact area of radius a.

Contact Force:

$$P = \eta_{\mathrm{P}} a^{2+\frac{1}{m}} \tag{3.4}$$

Contact Radius:

$$a = \left(\frac{2c^2}{\mathbb{A}}\right)^{1/2} \gamma^{1/2} \tag{3.5}$$

where γ is the relative displacement of the particles

$$\gamma = R_1 + R_2 - ||\mathbf{x}_1 - \mathbf{x}_2|| \tag{3.6}$$

and the geometric parameter $\mathbb{A}$ and plastic law coefficient η_{P} are given by

$$\mathbb{A} = \frac{1}{R_1} + \frac{1}{R_2} \tag{3.7}$$

$$\eta_{\mathrm{P}} = \pi k \mathbb{A}^{1/m} \left(\frac{1}{\kappa_1^m} + \frac{1}{\kappa_2^m}\right)^{-1/m} \tag{3.8}$$

with $k = 3 \times 6^{-1/m}$ and $c^2 = 1.43\mathrm{e}^{-0.97/m}$ (Storåkers & Larsson, 1994). To illustrate the applicability of the contact law, it is plotted for the properties of lead in Figure 3.1 (dashed curves). It can be seen that the solution is independent of the loading configuration, and diverges from the response curves at small deformations ($\sim 2 - 3\%$). This is consistent with the assumption of small strain kinematics and independent contacts employed for the derivation of the similarity contact law.

The formulation of an analytical contact law capable of describing the contact behavior at later stages of compression is particularly challenging due to the inapplicability of the assumptions of independent contacts and small strain kinematics. Besides, the contact formulation must account for complex phenomena such as softening at moderate strains and the significant increase in contact pressure evident at large strains for confined loading conditions. Initial progress in this regard was made by Harthong et al. (2009, 2012), who proposed a semi-mechanistic contact law for spherical particles with rigid plastic power-law hardening material behavior through curve fitting of force-deformation FE data of particle compression under simple, die and hydrostatic loading conditions. The model is based on a local relative density-dependent stiffness parameter, which is added to the stiffness of the contact under simple compression to represent the rise in contact force for die and hydrostatic loading conditions due to plastic incompressibility at large deformations. While the model is highly predictive at large deformations, it is limited to the force-deformation relationship and neglects elastic deformations, leading to infinite force as the relative density tends to unity. Frenning (2013) proposed a truncated sphere model applicable for small-to-moderate deformations of a spherical particle under a general loading configuration. The model utilizes the plastic incompressibility assumption to relate the average pressure in the particle due to elastic volumetric strain to the mean pressure generated at the particle contacts. For the specific case of hydrostatic loading condition, Frenning (2015) later extended the model to account for contact impingement and low compressibility at large deformations. Olsson & Larsson (2013a,b, 2016) proposed semi-analytical contact laws for elasto-plastic spherical particles under simple loading configuration that are predictive at large deformations. Their formulation is based on the work of Johnson (1970) on the correlation of indenta-

tion tests performed on elasto-plastic materials to a single master curve dependent on a non-dimensional material and contact geometry parameter.

While the development of a closed-form analytical formulation for large deformation contact behavior of elasto-plastic confined granular systems remains an open problem, valuable progress towards achieving this goal can be made by developing the capability to predict the complete contact behavior, i.e., contact force and contact area, for particles under unconfined and confined compression in a simple cubic packing. In this chapter, a semi-mechanistic contact formulation for an elastic-perfectly plastic spherical particle under simple, die and hydrostatic loading configurations is presented. Contact laws for the evolution of contact pressure and contact radius with deformation are proposed, which enable the determination of contact force as the product of pressure and area. The contact radius is derived as a three-term expansion of the curvature-corrected (Agarwal & Gonzalez, 2018) similarity contact law, where each term corresponds to the contact response under a specific deformation regime (small, moderate and large deformations). The contact pressure is described in each deformation regime by distinct contact laws that are continuous and differentiable at the transition from one regime to another. The proposed laws are both material and loading condition-dependent, accounting for initial elastic and elasto-plastic deformations and limited elastic compressibility for confined loading conditions (die and hydrostatic) at large deformations. This is accomplished by calibrating the various model parameters to a sufficiently large set of finite element simulations, where the set of elasto-plastic material properties used to perform the simulations is obtained through a space-filling design, thus ensuring sufficient diversity of the considered material behavior.

The chapter is organized as follows. Section 3.2 describes the space-filling design problem for acquiring mechanical properties used in the finite element simulations. The finite element analysis and results are then presented and discussed in Section 3.3. A detailed description of the semi-mechanistic contact formulation is presented in Section 3.4, followed by its validation through a comparison of model predictions with the finite element results in Section 3.5. A preliminary semi-mechanistic analysis of the lateral contacts in the die loading configuration is presented in Section 3.6. Finally, a summary and concluding remarks are presented in Section 3.7.

3.2 Space-Filling Design of Experiments for acquiring Mechanical Properties and Loading Configurations

To obtain a diverse set of elasto-plastic material properties for our finite element simulations, the mechanical properties and loading configurations are modeled as variables of a space-filling design problem (Santner et al., 2013). Therefore, independent variables are the mechanical properties, i.e. Young's modulus (E), Poisson's ratio (ν) and uniaxial yield stress (σ_y), and the loading configurations, i.e. simple, die and hydrostatic loading. Another material-dependent quantity worthy of consideration is either one of the ratios $E/(1-\nu^2)\sigma_y$ (Mesarovic & Fleck, 2000) and E/σ_y (Tsigginos et al., 2015), which have been numerically shown to influence the contact behavior significantly during the initial stages of compression. Although $E/(1-\nu^2)\sigma_y$ is a more appropriate choice considering the fact that it incorporates all the properties that influence stiffness, yield and compression behavior of the material, E/σ_y is chosen as the final independent variable to ensure minimal nonlinearity in the constraints and acquisition of a broader range of material properties. Table 3.1 provides bounds for the considered independent variables in the space-filling design. The bounds are selected to encompass the observed mechanical properties of most elasto-plastic materials (thermoplastic polymers, metals, alloys, pharmaceutical powders, etc.).

Although the mechanical properties E, ν and σ_y, and the ratio E/σ_y are modeled as separate variables, there is an evident relationship between them. This relationship is incorporated into the design problem as a nonlinear constraint, given by

$$\left|\frac{x_1/x_2 - x_3}{x_1/x_2}\right| < \text{TOL} \tag{3.9}$$

Table 3.1. Bounds for the independent variables (mechanical properties) considered in the space-filling design problem.

	Minimum Value	Maximum Value
E (MPa)	2000	200000
σ_y (MPa)	1	500
ν	0.2	0.48
E/σ_y	100	5000

where $x_1 \rightarrow E$, $x_2 \rightarrow \sigma_y$ and $x_3 \rightarrow E/\sigma_y$. According to this constraint, the relative difference between the ratio of variables E and σ_y and the variable E/σ_y should be lower than a specified tolerance. In this study, a tolerance of TOL $= 0.005$ (0.5%) is assumed.

The formulated design problem was solved in the statistical software JMP®, Version 14 (2018) using the Fast Flexible Filling (FFF) algorithm, which is capable of incorporating nonlinear constraints. According to the software's Design of Experiments documentation (SAS Institute Inc., 2018), the FFF algorithm starts by balancing the total number of design points across the total number of combinations of levels n of the categorical variables. For the given problem, only one categorical variable (loading configurations) is defined with 3 levels (simple, die and hydrostatic), which implies that for a total of K design points, $K/3$ points are allocated to each level. For this study, a total of $K = 51$ FE simulations were performed. Therefore, 17 points were allocated to each level, i.e., 17 simulations were performed for each loading configuration.

Next, a large number of points within the design space defined by the continuous variables (E, σ_y, ν and E/σ_y) are generated, which are then grouped into $K/3\,(= 17)$ primary clusters using a fast Ward's algorithm (Ward Jr., 1963). Each of the primary clusters are then further clustered into $n\,(= 3)$ sub-clusters. Within each primary cluster, a design point is calculated for each of the sub-clusters by minimizing a Maximum Projection (MaxPro) criterion (Joseph et al., 2015), which, for the given problem with $p = 4$ continuous variables and $K = 51$ total clusters is defined as

$$C_{\text{MaxPro}} = \sum_{i}^{50} \sum_{j=i+1}^{51} \left[\prod_{k=1}^{4} (x_{ik} - x_{jk})^2 \right]^{-1} \tag{3.10}$$

By minimizing the above criterion, product of the distance between potential design points is maximized in a way that involves all variables, which results in a good space-filling design. Finally, for each of the $K/3\,(= 17)$ primary clusters, one of the $n\,(= 3)$ categorical levels is randomly assigned to each of the $n\,(= 3)$ sub-cluster design points, yielding the total of $K\,(= 51)$ design points.

Figure 3.4 provides scatter plots of the design points obtained for the three symmetric loading configurations, while Table 3.2 provides a complete list of the mechanical properties

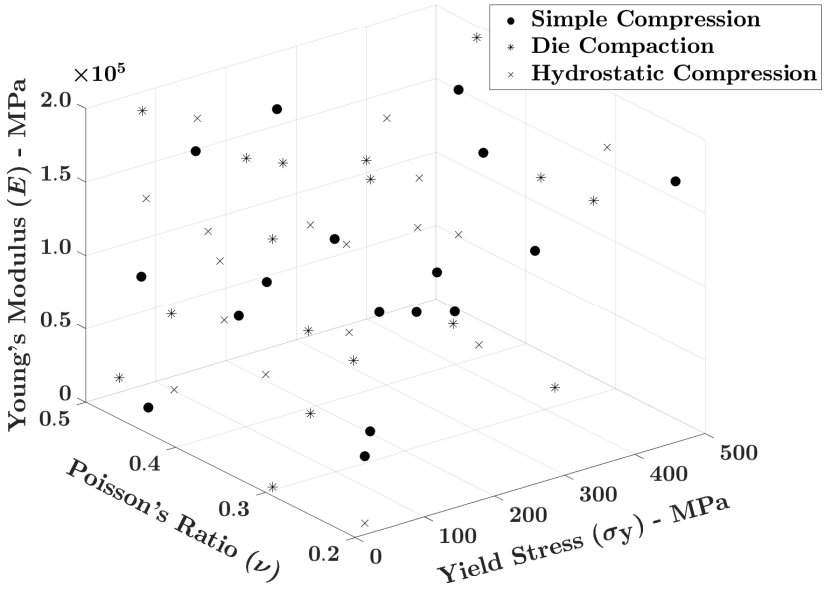

Figure 3.4. Scatter plot of the design points obtained from the space-filling design of mechanical properties and loading configurations for the FEA study.

obtained by solving the design problem. It is quite evident that the points are fairly-spaced, and hence, the obtained mechanical properties can be used further to set-up the FE simulations.

Table 3.2. : List of mechanical properties (arranged in the increasing order of E/σ_y ratio) and corresponding loading configurations obtained from the solution of the space-filling design problem.

Loading Condition	E (MPa)	ν	σ_y (MPa)	E/σ_y
Simple	36961.79	0.4130	361.11	102.36
Compression	20639.45	0.2993	148.54	138.95
	84752.72	0.3524	452.13	187.45
	150500.27	0.4739	499.21	301.48
	172086.58	0.2115	472.34	364.32
	101785.47	0.2643	225.81	450.75
	190003.52	0.2939	304.09	624.83
	75517.00	0.4019	92.86	813.25
	196617.68	0.4270	178.85	1099.37
	161529.29	0.2046	123.92	1303.46
	114577.91	0.3579	76.34	1500.97
	88565.10	0.4709	42.09	2104.13

Continued on next page

Table 3.2 – *Continued from previous page*

Loading Condition	E (MPa)	ν	σ_y (MPa)	E/σ_y
	139990.73	0.2161	54.84	2552.68
	52841.85	0.2003	13.95	3786.85
	178811.38	0.2582	45.49	3930.52
	16555.89	0.4328	3.48	4756.54
	193549.09	0.4078	39.13	4946.77
Die Compaction	49200.85	0.2251	317.80	154.82
	57221.17	0.3899	176.03	325.06
	146900.23	0.3247	424.97	345.67
	199028.86	0.4392	480.79	413.96
	180937.93	0.2001	341.00	530.61
	41573.92	0.3058	71.21	583.84
	141078.40	0.4640	234.62	601.32
	118951.98	0.2124	156.49	760.11
	184270.83	0.3440	199.86	922.02
	21959.27	0.4749	16.08	1365.37
	199785.29	0.2841	129.76	1539.61
	190786.67	0.3829	78.68	2424.75
	5314.12	0.2933	2.01	2643.37
	78547.20	0.4264	28.38	2767.69
	198038.19	0.4772	51.91	3815.19
	160754.07	0.3213	37.41	4297.29
	110376.78	0.2204	23.42	4713.79
Hydrostatic Compaction	2958.14	0.2099	26.39	112.08
	57840.71	0.4623	483.90	119.53
	65157.56	0.2831	283.64	229.72
	135501.57	0.3973	345.15	392.59
	194137.98	0.2418	413.75	469.22
	79402.31	0.4792	164.35	483.14
	198495.80	0.3652	256.71	773.23
	143839.36	0.3178	138.24	1040.50
	61598.96	0.3370	47.86	1286.97
	187812.04	0.4654	114.89	1634.70
	131429.64	0.4187	70.02	1876.91
	197086.03	0.2014	92.22	2137.09
	174002.47	0.2976	61.27	2839.88
	34338.87	0.4100	11.20	3065.39
	123218.19	0.2344	35.71	3451.00
	147336.69	0.4576	31.83	4628.58
	95689.98	0.3607	19.17	4992.44

3.3 Finite Element Analysis

On the account of geometric and loading symmetries, finite-element simulations were performed on one-eighth of a sphere of radius $R = 10$mm in ABAQUS. As mentioned before, the material was characterized as elastic-ideal plastic (hardening exponent $m \to \infty$), satisfying the following constitutive law

$$\sigma = \begin{cases} E\epsilon & \epsilon \leq \epsilon_y \\ \sigma_y & \epsilon > \epsilon_y \end{cases} \tag{3.11}$$

Following a mesh convergence study, a mesh comprising of 500,000 linear hexahedral elements of type C3D8R and 515,201 nodes was chosen for our analysis. For representational purposes, a courser mesh of 62,500 elements and 66,351 nodes is depicted in Figure 3.5. A total of 51 FE simulations were performed with this model, 17 for each loading configuration (simple, die and hydrostatic) using the material properties obtained from the space-filling design.

To simulate the extensive particle deformation conditions during powder compaction process, the contact response for simple compression was evaluated until 50% deformation. For hydrostatic and die configurations, a state of complete closure of porosity is achieved with continued particle deformation and material flow. This stage is termed as the zero porosity limit (Tsigginos et al., 2015), following which the stresses required for further deformation

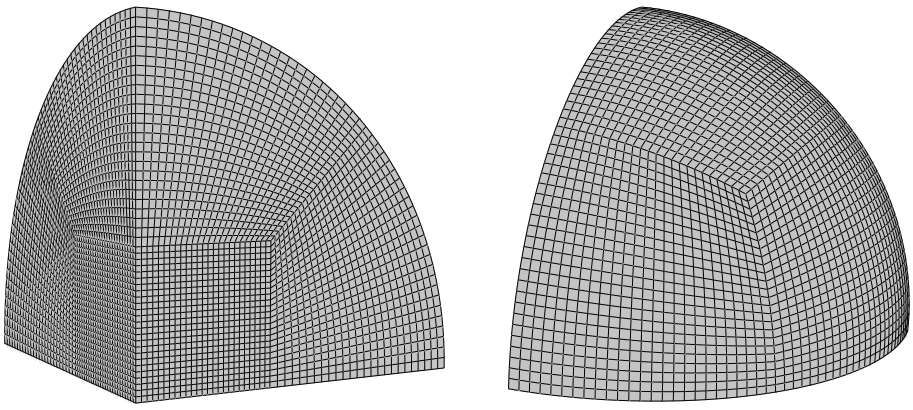

Figure 3.5. Finite element mesh consisting of linear hexahedral elements of type C3D8R, created for one-eighth of a sphere in ABAQUS. The depicted mesh is coarser than the final converged mesh, and consists of 62,500 elements and 66,351 nodes.

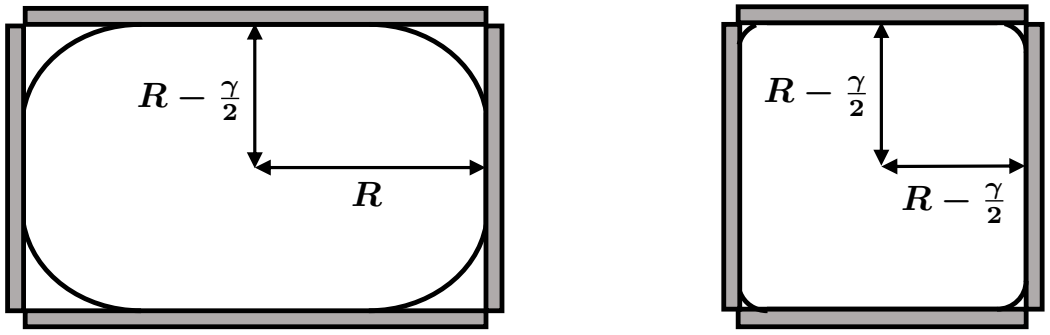

(a) Die Compaction (b) Hydrostatic Compaction

Figure 3.6. Schematic of the voronoi cell for (a) die and (b) hydrostatic loading conditions.

are very high and are governed by the bulk modulus of the material. At this stage, the volume of the particle's radical voronoi cell (Gellatly & Finney, 1982; Aurenhammer, 1987), which is the polyhedron formed by the rigid contact planes of the particle, becomes equal to the particle volume. For hydrostatic and die configurations, this limit can be geometrically computed if the elastic volume reduction during initial stages of particle compression is neglected. Considering the voronoi cell dimensions presented in Figure 3.6, the zero porosity limits are calculated below:

Die Compaction:

$$\begin{aligned} V_p &= \frac{4}{3}\pi R^3 = 8R^2\left(R - \frac{\gamma}{2}\right) \\ \implies \frac{\gamma}{2R} &= 1 - \frac{\pi}{6} \simeq \mathbf{0.476} \end{aligned} \tag{3.12}$$

Hydrostatic Compaction:

$$\begin{aligned} V_p &= \frac{4}{3}\pi R^3 = 8\left(R - \frac{\gamma}{2}\right)^3 \\ \implies \frac{\gamma}{2R} &= 1 - \left(\frac{\pi}{6}\right)^{1/3} \simeq \mathbf{0.194} \end{aligned} \tag{3.13}$$

To fully represent this final stage of particle compression and to account for small elastic volume reduction during the course of particle compression, contact response was evaluated until a small deformation beyond the attainment of zero porosity, i.e., 48% for die and 19.5% for hydrostatic loading configuration.

Figures 3.7, 3.8, 3.9 and 3.10 show the normalized contact pressure, contact radius and contact force response of the particles plotted against contact deformation, for simple, hydrostatic and die loading configurations respectively. Contact response is plotted for 5 out of the 17 material property sets for each configuration, with the ratio $E/(1-\nu^2)\sigma_y$ (referred to as parameter λ in the rest of this chapter) ranging from minimum to the maximum value obtained from the space-filling design. Observation of contact pressure response of the particle under simple loading configuration (Figure 3.7a) indicates a dependence of the response on material properties during elastic and elasto-plastic regimes of particle compression, where higher response stiffness and larger maximum contact pressure values are observed with increasing λ. Although, the response curves tend to converge at higher values of λ, indicating an asymptotic relationship with respect to material properties. Following the onset of a fully plastic regime, the gradual decreasing trend of contact pressure is observed to be fairly independent of material properties. Similar observations are made in the contact radius (Figure 3.7b) and contact force (Figure 3.7c) response, with the response stiffness rising asymptotically with increasing λ for small-to-moderate particle deformation ($\sim$ 20%) and converging to a single response curve for larger deformation. The effect of material properties becomes increasingly apparent in the contact response for hydrostatic loading configuration, where the contact pressure response (Figure 3.8a) follows the trend of simple loading until about 15% deformation, following which the contact pressure increases rapidly with increasing particle confinement. Elasticity becomes relevant again during this regime of particle compression, evident from increasing stiffness of the response and higher values of pressure with increasing λ, although an asymptotic relationship with respect to the material parameter is also evident. Similar observations are made again in the contact radius (Figure 3.8b) and contact force (Figure 3.8c) response, where noticeable dependence on the value of λ is observed during initial and final compression stages, with the response stiffness increasing asymptotically with increasing value of the parameter.

For the case of die loading configuration, contact response is plotted for both axially loaded (or primary) contacts (Figure 3.9) and lateral walled (or secondary) contacts (Figure 3.10). The primary contacts exhibit a response similar to the contacts in hydrostatic loading configuration, with the exception of a higher level of deformation at which the contact

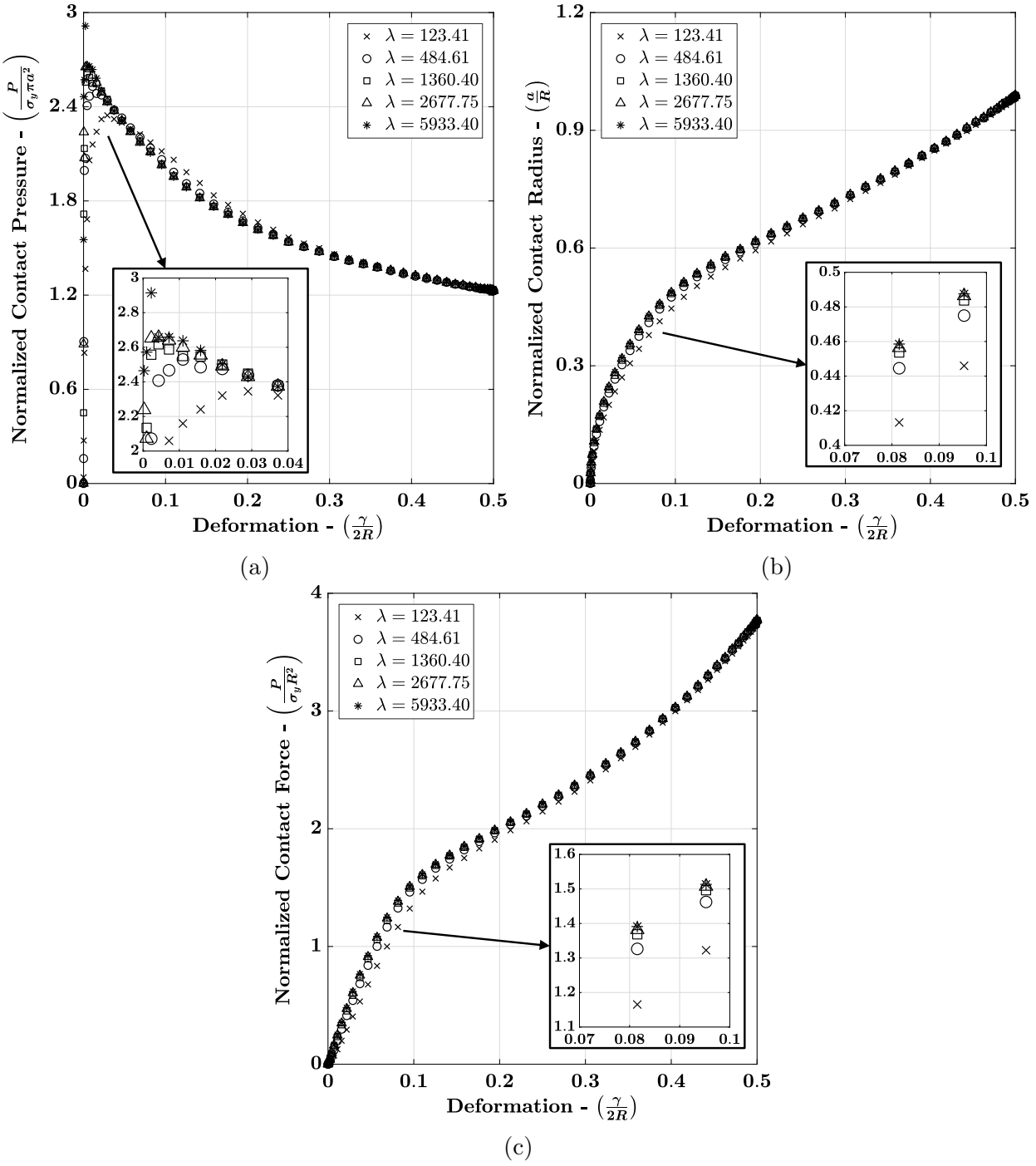

Figure 3.7. Finite element simulation results of normalized (a) contact pressure-deformation, (b) contact radius-deformation, and (c) contact force-deformation behavior of an elastic-perfectly plastic sphere of radius $R = 10$mm under simple compression. Contact response is depicted with corresponding $\lambda = E/(1-\nu^2)\sigma_y$ values for 5 material properties, ranging from minimum to maximum value of λ among the 17 property values obtained from the space-filling design.

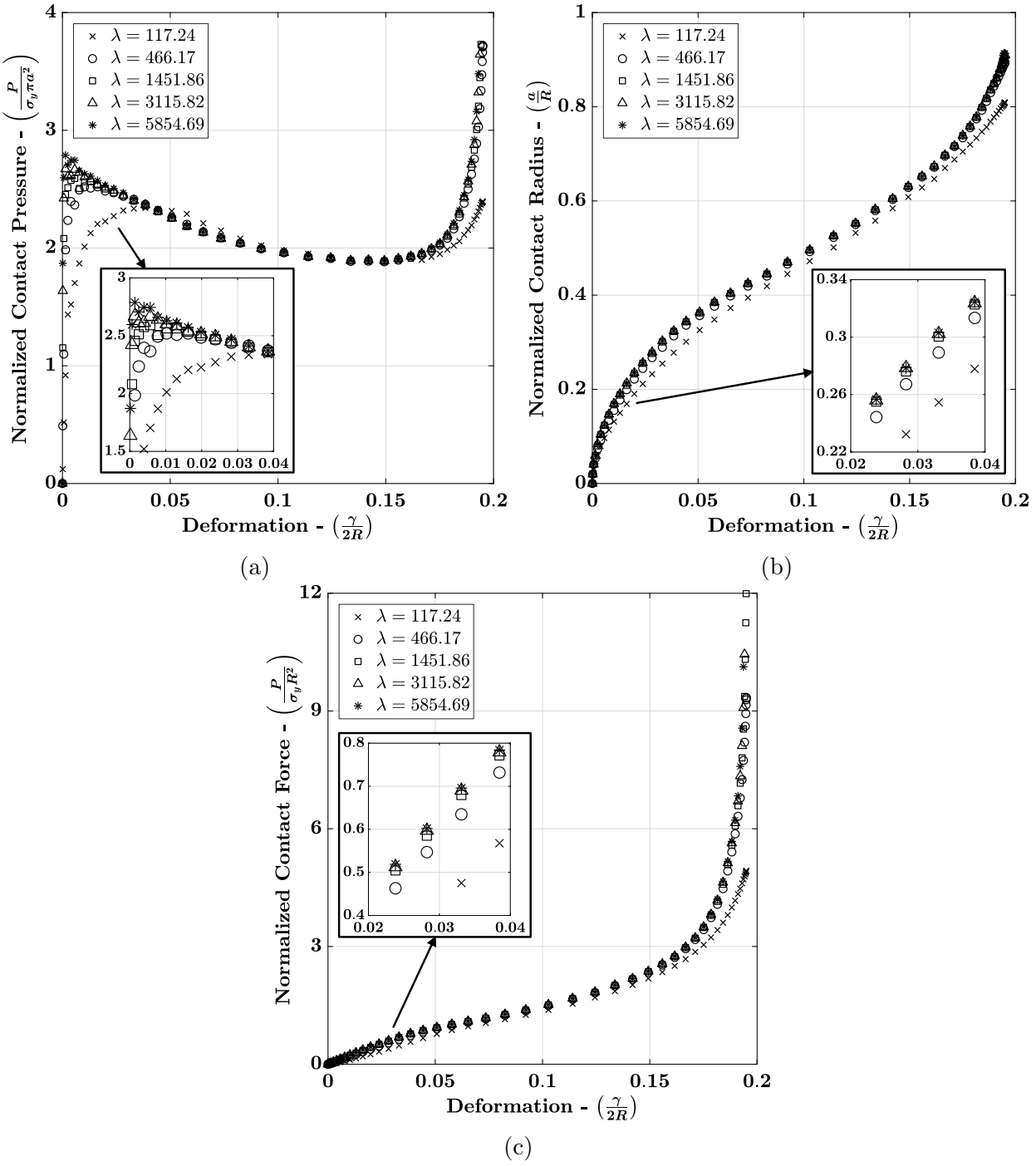

Figure 3.8. Finite element simulation results of normalized (a) contact pressure-deformation, (b) contact radius-deformation, and (c) contact force-deformation behavior of an elastic-perfectly plastic sphere of radius $R = 10$mm under hydrostatic compaction. Contact response is depicted with corresponding $\lambda = E/(1-\nu^2)\sigma_y$ values for 5 material properties, ranging from minimum to maximum value of λ among the 17 property values obtained from the space-filling design.

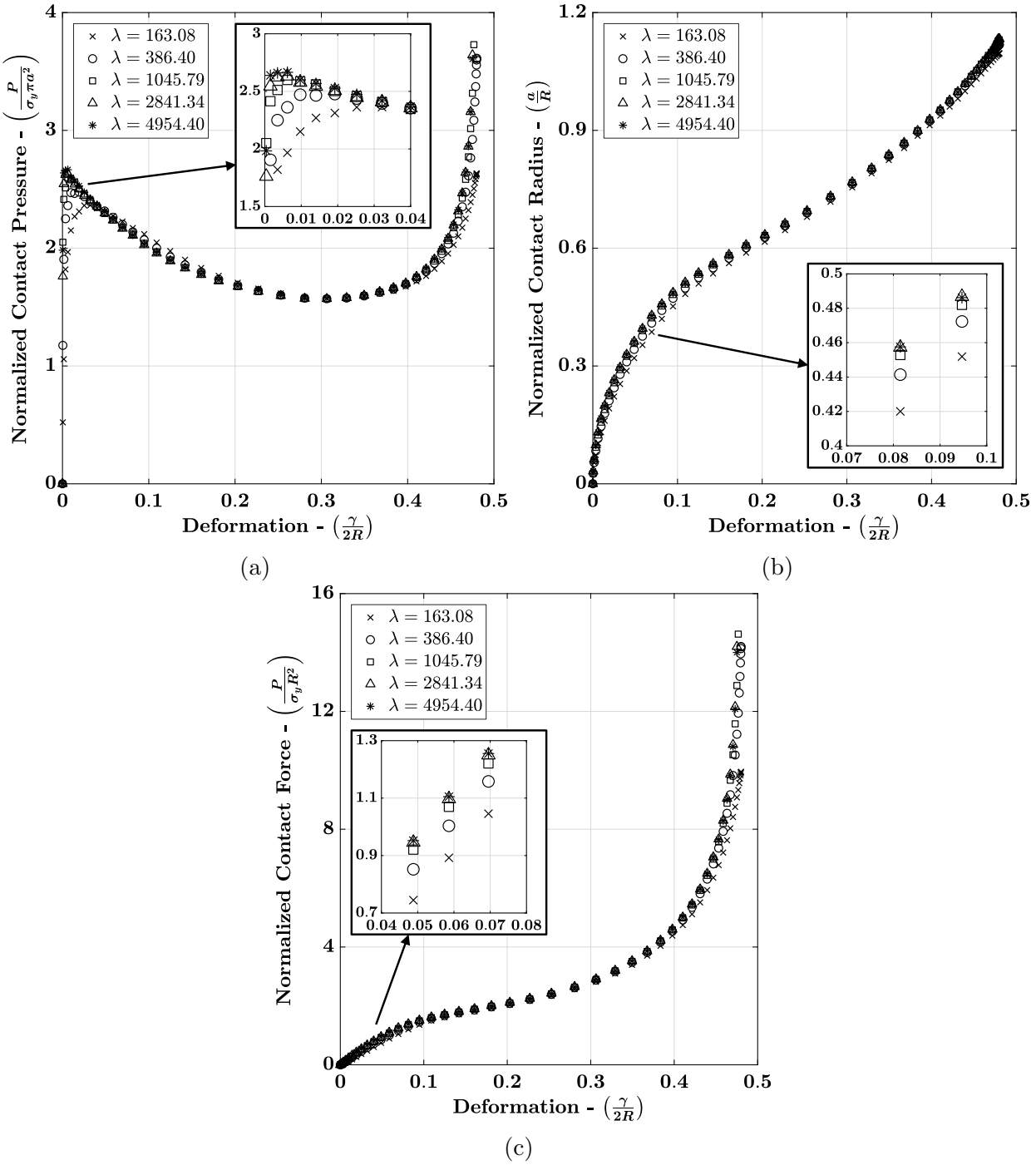

Figure 3.9. Finite element simulation results of normalized (a) contact pressure-deformation, (b) contact radius-deformation, and (c) contact force-deformation behavior at the primary (axial) contacts of an elastic-perfectly plastic sphere of radius $R = 10$mm under die compression. Contact response is depicted with corresponding $\lambda = E/(1-\nu^2)\sigma_y$ values for 5 material properties, ranging from minimum to maximum value of λ among the 17 property values obtained from the space-filling design.

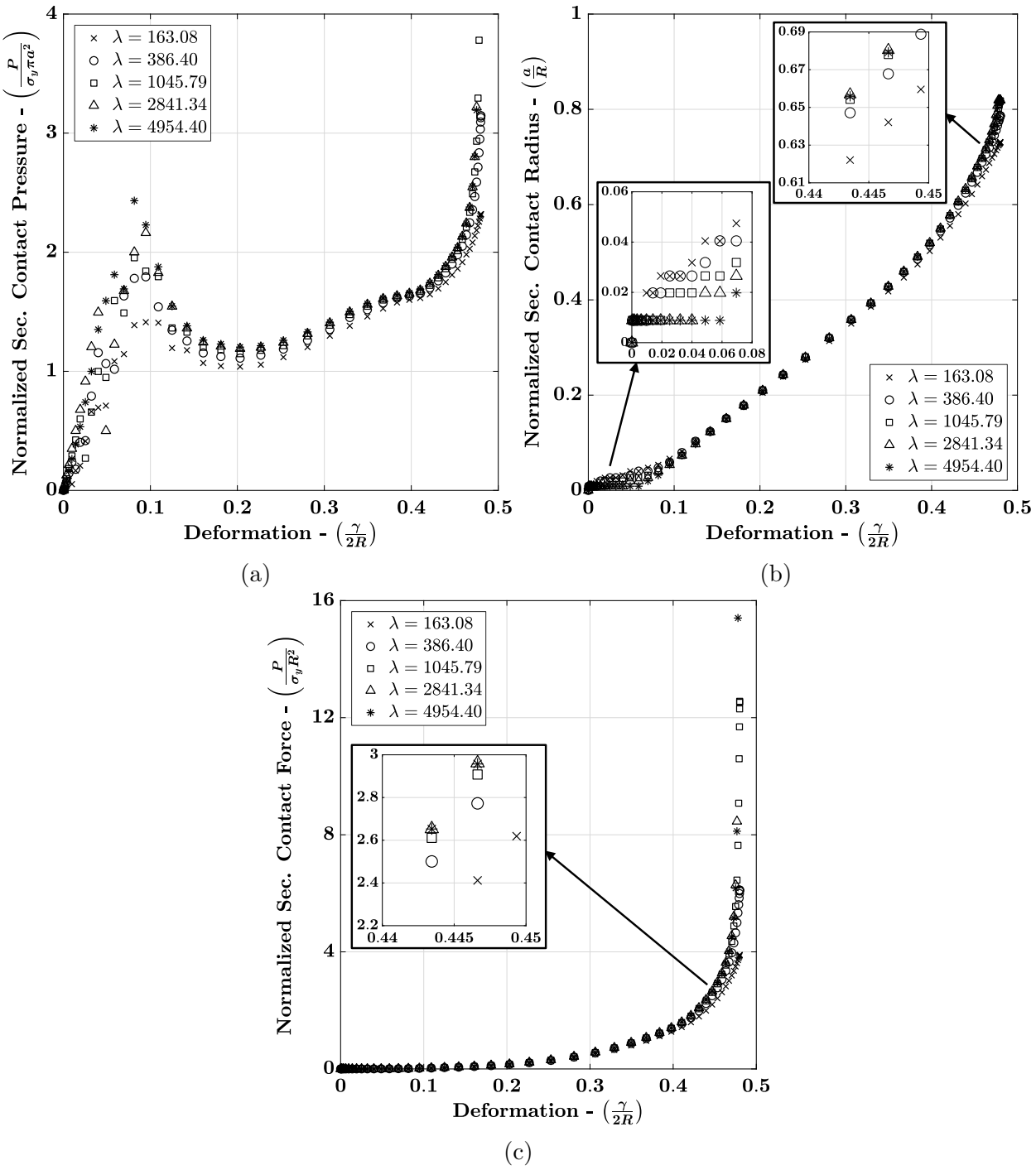

Figure 3.10. Finite element simulation results of normalized (a) contact pressure-deformation, (b) contact radius-deformation, and (c) contact force-deformation behavior at the secondary (lateral) contacts of an elastic-perfectly plastic sphere of radius $R = 10$mm under die compression. Contact response is depicted with corresponding $\lambda = E/(1-\nu^2)\sigma_y$ values for 5 material properties, ranging from minimum to maximum value of λ among the 17 property values obtained from the space-filling design.

pressure starts rising again ($\sim 30\%$) due to a lower degree of confinement. The secondary contacts, despite not being subjected to any applied deformation, exhibit an evolution of contact pressure, area, and force with increasing deformation of the primary contact. Interestingly, they exhibit levels of contact pressure and force similar to the primary contacts at later stages of compression. Such contact behavior is not predictable by a local contact formulation (for example, the similarity contact law) which treats contacts to be independent of each other, but a nonlocal contact formulation (ref. Gonzalez & Cuitiño (2012, 2016) and Agarwal & Gonzalez (2018) for an elastic nonlocal contact formulation) that is capable of predicting the nonlocal lateral deformation in the secondary contacts as a function of the applied deformation at the primary contacts. While the systematic development of a nonlocal contact formulation for elasto-plastic particles is currently being pursued by the authors, a foundational semi-mechanistic analysis of the secondary contacts is presented in one of the later sections of this chapter.

Figure 3.11 shows a magnified view of the contact pressure response of hydrostatic and die (both primary and secondary contacts) loading configurations during the 'low compressibility' regime. As already explained in the previous sections, particle deformation during this regime for confined loading conditions is mainly governed by elastic compressibility of the material, leading to rising contact pressure values during the final stages of compression. Therefore, the contact response in Figure 3.11 is plotted with respect to material parameter $\zeta = B/\sigma_y$, where B is the Bulk Modulus of the material. An apparent asymptotic relationship of the contact pressure with respect to ζ is observed in all the plots, with the response stiffness and pressure values rising rapidly with increasing ζ and converging to a single curve for larger values of ζ.

This section is concluded by pointing out the evident asymptotic relationship between the contact response and material properties (parameters λ and ζ) during the initial and final stages of particle compression. This observation provides key insight into the material dependence of the contact behavior in confined granular systems, which is essential for the development of accurate and predictive contact models.

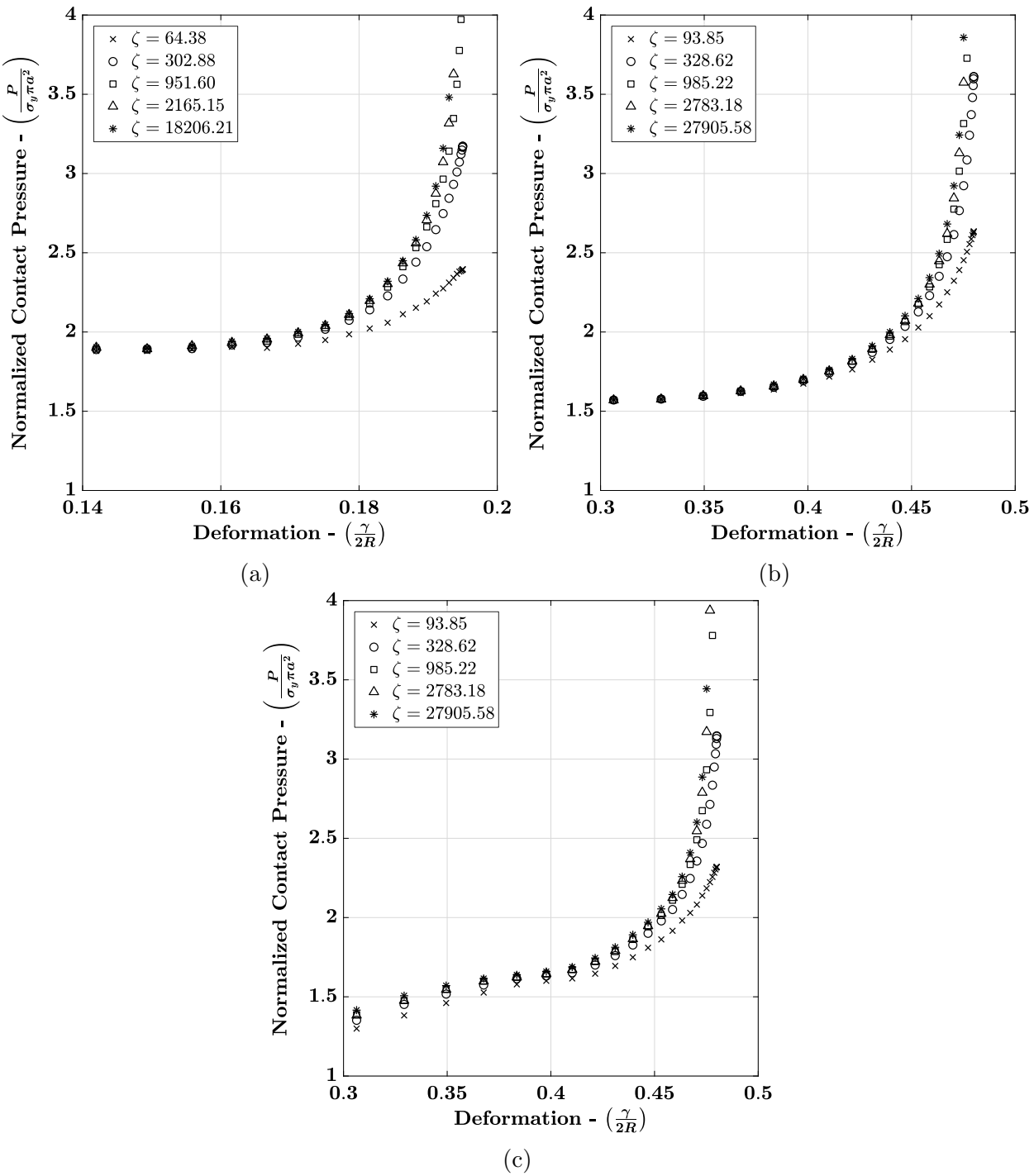

Figure 3.11. Finite element simulation results of normalized contact pressure-deformation behavior of an elastic-perfectly plastic sphere of radius $R = 10$mm during 'low compressibility' regime (Tsigginos et al., 2015), under (a) hydrostatic compaction, (b) die compression (primary contacts) and (c) die compression (secondary contacts). Contact response is depicted with corresponding $\zeta = B/\sigma_y$ values for 5 material properties, ranging from minimum to maximum value of ζ among the 17 property values obtained from the space-filling design for each loading configuration.

3.4 Formulation of a Semi-Mechanistic Contact Law

To develop a semi-mechanistic contact law for the large-deformation, material and loading configuration-dependent contact behavior of elastic-ideally plastic spherical particles in confined granular systems, the two-particle contact problem described by the similarity solution explained in section 3.1 is reconsidered. For the case of an ideally plastic material ($m \to \infty$), the solution for contact force (Equation (3.4)) reduces to

$$P = 3\sigma_y \pi a^2 \tag{3.14}$$

This solution corresponds to the definition of material's hardness, or the average contact pressure during indentation of a deformable flat surface with a rigid indenter. Hardness, as defined by Brinell (1900), is the contact force divided by the contact surface area, i.e. $P/\pi a^2$. According to the similarity solution, this hardness H is given by

$$H = \frac{P}{\pi a^2} = 3\sigma_y = \bar{H}\sigma_y \tag{3.15}$$

Therefore, the hardness is obtained as a coefficient $\bar{H}$, often termed as the normalized hardness (Olsson & Larsson, 2013a,b, 2016), equal to 3 times the yield strength of the material. This result is in good agreement with the empirical findings of Tabor (1951), who proposed the hardness of materials from Brinell indentation tests to given by $2.84\sigma_y$. However, observation of the normalized contact pressure vs. deformation plots obtained from the FE simulations suggests that the proposed value of hardness is higher than the numerically obtained value for the majority of the particle compression process. Additionally, the proposed hardness is independent of the loading configuration and material properties, which is not true, as is evident from the observed dependence of the contact response on material parameters λ and ζ, and its contrasting evolution for simple, die and hydrostatic loading configurations. Considering these observations, the following contact law is proposed

$$P(\gamma; \lambda, \zeta, \mathrm{LC}) := \bar{H}(\gamma; \lambda, \zeta, \mathrm{LC})\sigma_y \pi \{a(\gamma; \lambda, \mathrm{LC})\}^2 \tag{3.16}$$

where LC corresponds to the loading configuration. In the next sections, semi-mechanistic functional relationships for contact radius a and normalized hardness $\bar{H}$ are proposed from an analytical framework based on the similarity contact law and the data obtained from FE simulations.

3.4.1 Semi-Mechanistic Formulation for the Contact Radius

In addition to small-strain kinematics, one of the important limiting assumptions of the similarity contact law is an approximation of the spherical profile of the contacting surfaces by paraboloids of revolution. This is done by replacing the profile surface functions by the first term of their Taylor series expansion. A similar approximation is also assumed for derivation of the Hertz contact law (Hertz, 1882) for elastic spherical particles. This assumption was relaxed by Agarwal & Gonzalez (2018), who proposed the method of curvature correction to re-derive the Hertz solution after considering higher order terms in the Taylor series expansion of the profile functions. While the method was proposed to improve the predictions of Hertz law for large deformations, it is utilized in this study to obtain the analytical framework for a semi-mechanistic contact radius formulation. A detailed derivation of a 2-term curvature corrected similarity solution is presented in Appendix C. Considering the first three terms of the Taylor expansion of this solution (ref. Equation (C.25) in Appendix C), the following contact law is proposed:

$$a = \mathcal{D}_1 \left(\frac{1}{\mathbb{A}^{1/2}} \right) \gamma^{1/2} - \mathcal{D}_3 \left(\frac{\mathbb{B}}{\mathbb{A}^{5/2}} \right) \gamma^{3/2} + \mathcal{D}_5 \left(\frac{\mathbb{B}^2}{\mathbb{A}^{9/2}} \right) \gamma^{5/2} \tag{3.17}$$

where $\mathbb{A}$ is given by Equation (3.7) and

$$\mathbb{B} = \frac{1}{R_1^3} + \frac{1}{R_2^3} \tag{3.18}$$

According to the above law, the contact radius a is a nonlinear function of the contact displacement γ between two spherical particles of radii R_1 and R_2, with material and loading configuration described by parameters $\mathcal{D}_1$, $\mathcal{D}_3$, and $\mathcal{D}_5$. The proposed law is similar to the stress-strain contact model proposed for large unconfined compression of microcrystalline

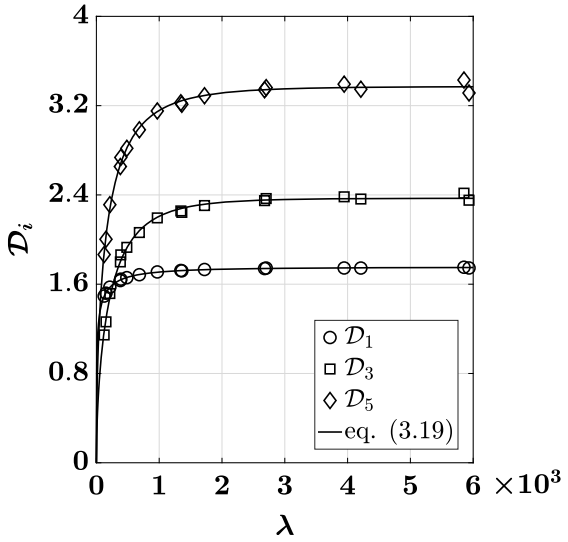

Figure 3.12. Estimation of parameters $\mathcal{D}_1$, $\mathcal{D}_3$, and $\mathcal{D}_5$ for simple loading configuration. Plotted discrete values correspond to the values calibrated from FE data, while solid curves correspond to $\mathcal{D}_i - \lambda$ relationships obtained from curve fitting.

cellulose particles by Bommireddy et al. (2019), and is composed of three terms; the first term corresponds to the small deformation behavior and is similar to the $a - \gamma$ relationship derived from self-similarity approach by Biwa & Storåkers (1995). The second term describes the contact response during moderate deformations under the fully plastic regime, where the overall response undergoes a softening and a dip in the slope of $a - \gamma$ curve is observed. The third term describes the large deformation contact response during the 'low compressibility' regime in confined loading conditions, where the slope of $a - \gamma$ curve starts rising again. For the simple loading condition, the third term models the slight increase in slope of the $a - \gamma$ curve in the large deformation fully plastic regime.

The material and loading condition parameters $\mathcal{D}_1$, $\mathcal{D}_3$, and $\mathcal{D}_5$ are given by

$$\mathcal{D}_i = \left(b_i^{\mathrm{LC}}\right)^{\frac{i}{2}} \left[\alpha_i \tanh\left(\beta_i \lambda^{\delta_i}\right)\right] \quad (i = 1, 3, 5) \tag{3.19}$$

where each parameter $\mathcal{D}_i\,(i = 1, 3, 5)$ is expressed as the product of two nonlinear functions; a power function of loading condition parameter b_i^{LC} raised to the power of $i/2$, and an asymptotic material function of parameter λ with constant α_i, coefficient β_i and exponent δ_i. Simple compression (SC), being the most fundamental loading configuration where the

Table 3.3. Estimated values of material function constants α_i, β_i and δ_i.

i	α_i	β_i	δ_i
1	1.7527	0.3540	0.2633
3	2.3702	0.0411	0.5366
5	3.3715	0.0634	0.4766

Table 3.4. Estimated values of loading condition parameters b_i^{LC} for simple (SC), die (DC) and hydrostatic (HC) loading configurations.

	SC	DC	HC
b_1^{LC}	1	1.048 ± 0.00477	1.1701 ± 0.0276
b_3^{LC}	1	1.1818 ± 0.00873	2.4002 ± 0.096
b_5^{LC}	1	1.2352 ± 0.00641	2.9376 ± 0.0452

particle remains unconfined, is assigned a loading condition parameter value of $b_i^{\mathrm{SC}} = 1\,(i = 1, 3, 5)$. Consequently, the material function constants α_i, β_i and δ_i are estimated by fitting the material function to $\mathcal{D}_i$ values calibrated from FE simulation data of the simple loading case (Figure 3.12). The estimated values of these constants are listed in Table 3.3. It is interesting to note that the limiting value of parameter $\mathcal{D}_1 = \alpha_1 = 1.7527$ is very close to the value of an equivalent coefficient $\sqrt{2c^2} = 1.6911$ for perfectly plastic materials in the $a - \gamma$ relationship derived from self-similar approach (Equation (3.5)), which makes the small deformation predictions of the proposed contact law consistent with predictions of the similarity contact law as the material behavior approaches rigid plasticity ($\lambda \to \infty$).

Once the material function constants are known, the values of loading condition parameters for die (b_i^{DC}) and hydrostatic (b_i^{HC}) compression are estimated from FE simulation data of the respective loading configurations. The estimated values within 95% confidence interval are listed in Table 3.4. It is interesting to note that all the parameter values for the hydrostatic loading condition are higher than those for the die loading condition, which validates the relationship of the proposed loading condition parameters with the degree of confinement.

3.4.2 Semi-Mechanistic Formulation for the Normalized Hardness

As already discussed in the previous sections, particle contacts undergo four major deformation regimes during large compression: elastic, elasto-plastic, fully plastic and 'low compressibility' (for confined loading configurations). Since the evolution of normalized hardness $\bar{H}$ is found to be significantly different in each of these regimes, we propose distinct contact laws for each regime in a way that C^1 continuity is maintained at the transition from one regime to another. Hence, the proposed semi-mechanistic formulation is continuous and differentiable at any given level of particle deformation.

During the elastic regime at small deformations, the well-known Hertz contact theory (Hertz, 1882) is capable of sufficiently describing the contact response. According to the theory, normalized hardness $\bar{H}$ for contact between particles of radii R_1 and R_2 and material parameter λ as a function of displacement γ is given by

$$\bar{H}^{\mathrm{e}} = \frac{2}{3\pi}\lambda \mathbb{A}^{1/2}\gamma^{1/2} \tag{3.20}$$

where $\mathbb{A}$ is given by Equation (3.7), and the superscript "e" is used to denote the elastic regime. Using Equation (3.20), the slope of $\bar{H}$ with respect to γ, i.e., $\partial\bar{H}/\partial\gamma$ in the elastic regime is given by

$$\frac{\partial \bar{H}^{\mathrm{e}}}{\partial \gamma} = \frac{1}{3\pi}\lambda \mathbb{A}^{1/2}\gamma^{-1/2} \tag{3.21}$$

The elastic regime transitions to the elasto-plastic regime when yield occurs at a point beneath the contact surface at $\bar{H} = 1.1$ (Johnson, 1985). Using Equation (3.20), the contact displacement at yield, γ_y, is given by

$$\gamma_y = \frac{1}{\mathbb{A}}\left(\frac{3.3\pi}{2\lambda}\right)^2 \tag{3.22}$$

During the elasto-plastic regime, the non-linear evolution of $\bar{H}$ with respect to displacement γ is well-represented by the following relationship

$$\bar{H}^{\text{ep}} = \bar{H}_{\max} - c_1 \left[\ln \left(\frac{\gamma|_{\bar{H}_{\max}}}{\gamma} \right) \right]^{c_2} \tag{3.23}$$

where the superscript "ep" is used to denote the elasto-plastic regime. The proposed relationship is in spirit of a similar formulation proposed by Olsson & Larsson (2013b) for the elasto-plastic regime, where $\bar{H}$ is represented as a function of the Johnson's parameter (Johnson, 1970). In the above equation, $\bar{H}_{\max}$ and $\gamma|_{\bar{H}_{\max}}$ are, respectively, the maximum value of normalized hardness and the contact displacement observed at the transition between elasto-plastic and fully plastic regimes. Figure 3.13 shows these values plotted against material parameter λ for all 51 FE simulations. Evidently, $\bar{H}_{\max}$ has an asymptotic increasing trend, while $\gamma|_{\bar{H}_{\max}}$ has an asymptotic decreasing trend with respect to the parameter. From fitting of the plotted values, we propose the following relationships for $\bar{H}_{\max}$ and $\gamma|_{\bar{H}_{\max}}$ with λ

$$\bar{H}_{\max} = 3.101 \tanh \left\{ 0.6746 \lambda^{0.0829} \right\} \tag{3.24}$$

$$\gamma|_{\bar{H}_{\max}} = (R_1 + R_2) \left[\exp \left(\frac{0.7073}{\lambda^{0.6547}} \right) - 1 \right] \tag{3.25}$$

The proposed relationships are also plotted in Figure 3.13 (solid curves), and provide very good estimates of the values obtained from FE simulations.

Additionally, the elasto-plastic $\bar{H}$ formulation comprises a coefficient c_1 and an exponent c_2, both of which are determined from the condition of C^1 continuity at the transition between elastic and elasto-plastic regimes. Using Equation (3.23), the slope of $\bar{H}$ with respect to γ in the elasto-plastic regime is given by

$$\frac{\partial \bar{H}^{\text{ep}}}{\partial \gamma} = \frac{c_1 c_2}{\gamma} \left[\ln \left(\frac{\gamma|_{\bar{H}_{\max}}}{\gamma} \right) \right]^{c_2 - 1} \tag{3.26}$$

which gives the condition $c_2 \geq 1$ for the slope given by the above equation to be equal to zero at $\gamma = \gamma|_{\bar{H}_{\max}}$. By equating the values of $\bar{H}$ given by Equations (3.20) and (3.23), and its first derivatives with respect to displacement γ given by Equations (3.21) and (3.26) at the

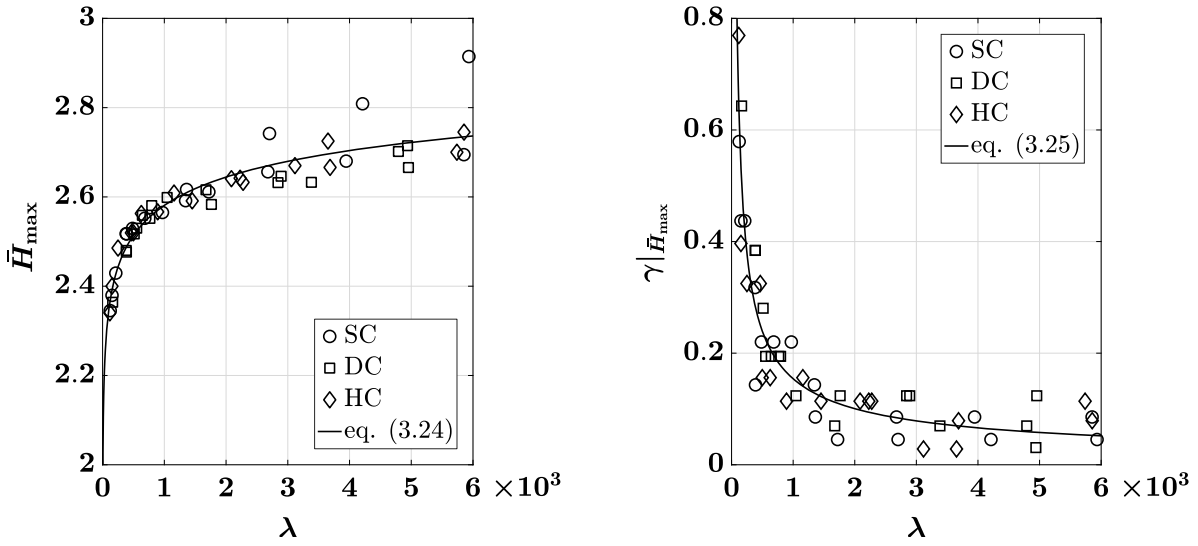

(a) (b)

Figure 3.13. Estimation of (a) $\bar{H}_{\max}$ and (b) $\gamma|_{\bar{H}_{\max}}$ as functions of parameter λ. Plotted discrete values correspond to values obtained from FE data, while solid curves correspond to relationships obtained from curve fitting.

transition displacement γ_y given by Equation (3.22) to achieve C^1 continuity for evolution of $\bar{H}$ between elastic and elasto-plastic regimes, two equations are obtained with two unknowns c_1 and c_2. By solving the equations, we get

$$c_2 = \ln\left(\frac{\gamma|_{\bar{H}_{\max}}}{\gamma_y}\right)\left[\frac{\lambda \mathbb{A}^{1/2}\gamma_y^{1/2}}{3\pi(\bar{H}_{\max}-1.1)}\right] \tag{3.27}$$

and

$$c_1 = (\bar{H}_{\max}-1.1)\left[\ln\left(\frac{\gamma|_{\bar{H}_{\max}}}{\gamma_y}\right)\right]^{-c_2} \tag{3.28}$$

To determine the permissible values of material parameter λ for the fulfillment of condition $c_2 \geq 1$, we substitute the expressions for γ_y, $\bar{H}_{\max}$ and $\gamma|_{\bar{H}_{\max}}$ given by Equations (3.22), (3.24) and (3.25) in the expression for c_2 given by Equation (3.27) to obtain

$$c_2 = \frac{0.1774\ln\left[0.0372\mathbb{A}(R_1+R_2)\lambda^2\exp\left(\frac{0.7073}{\lambda^{0.6547}}-1\right)\right]}{\tanh\left\{0.6746\lambda^{0.0829}\right\}-0.3547} \geq 1 \tag{3.29}$$

For contacting particles of equal radii ($R_1 = R_2 = R$), which is the case for our considered loading configurations, $\mathbb{A} = 1/2R$ and $R_1 + R_2 = 2R$ cancel out each other, making Equation (3.29) a nonlinear equation in λ. Using Newton Raphson's method, the solution to the equation is determined to be $\lambda \geq 22.08$. Therefore, the elasto-plastic $\bar{H} - \gamma$ relationship given by Equation (3.23), and thus the proposed semi-mechanistic contact formulation, is valid for material parameter λ values greater than or equal to 22.08.

On the onset of a fully plastic regime, the normalized hardness $\bar{H}$ starts decreasing gradually from its previously achieved maximum value of $\bar{H}_{\max}$. While we acknowledge that a number of contact models have been proposed to predict the evolution of hardness in this regime (see Ghaednia et al. (2017) and references therein), we propose a contact formulation that incorporates dependence on material properties and loading configuration while maintaining C^1 continuity with other deformation regimes. With this consideration, the normalized hardness in the fully plastic regime is given by

$$\bar{H}^{\text{fp}} = \bar{H}_{\max} - p\left[\tanh\left\{q\left(\frac{\gamma - \gamma|_{\bar{H}_{\max}}}{R_1 + R_2}\right)\right\}\cos\left\{\left(\frac{\gamma - \gamma|_{\bar{H}_{\max}}}{R_1 + R_2}\right) - s(\gamma|_{\bar{H}_{\min}}, q)\right\}\right]^r \tag{3.30}$$

where

$$s(\gamma|_{\bar{H}_{\min}}, q) = \left(\frac{\gamma|_{\bar{H}_{\min}} - \gamma|_{\bar{H}_{\max}}}{R_1 + R_2}\right) - \tan^{-1}\left[2q\,\text{csch}\left\{2q\left(\frac{\gamma|_{\bar{H}_{\min}} - \gamma|_{\bar{H}_{\max}}}{R_1 + R_2}\right)\right\}\right] \tag{3.31}$$

In the above equations, $\gamma|_{\bar{H}_{\min}}$ is the value of contact displacement at the minimum value of normalized hardness, i.e., $\bar{H}_{\min}$, while p, q, and r are positive model parameters. According to the proposed equations, the value of $\bar{H}^{\text{fp}}$ at $\gamma = \gamma|_{\bar{H}_{\max}}$ is equal to $\bar{H}_{\max}$, while its slope with respect to γ, given by

$$\begin{aligned}\frac{\partial \bar{H}^{\text{fp}}}{\partial \gamma} = &-\left(\frac{pr}{R_1 + R_2}\right)\left[\tanh\left\{q\left(\frac{\gamma - \gamma|_{\bar{H}_{\max}}}{R_1 + R_2}\right)\right\}\cos\left\{\left(\frac{\gamma - \gamma|_{\bar{H}_{\max}}}{R_1 + R_2}\right) - s(\gamma|_{\bar{H}_{\min}}, q)\right\}\right]^{r-1} \\ &\times\left[q\,\text{sech}^2\left\{q\left(\frac{\gamma - \gamma|_{\bar{H}_{\max}}}{R_1 + R_2}\right)\right\}\cos\left\{\left(\frac{\gamma - \gamma|_{\bar{H}_{\max}}}{R_1 + R_2}\right) - s(\gamma|_{\bar{H}_{\min}}, q)\right\}\right. \\ &\left.-\tanh\left\{q\left(\frac{\gamma - \gamma|_{\bar{H}_{\max}}}{R_1 + R_2}\right)\right\}\sin\left\{\left(\frac{\gamma - \gamma|_{\bar{H}_{\max}}}{R_1 + R_2}\right) - s(\gamma|_{\bar{H}_{\min}}, q)\right\}\right]\end{aligned} \tag{3.32}$$

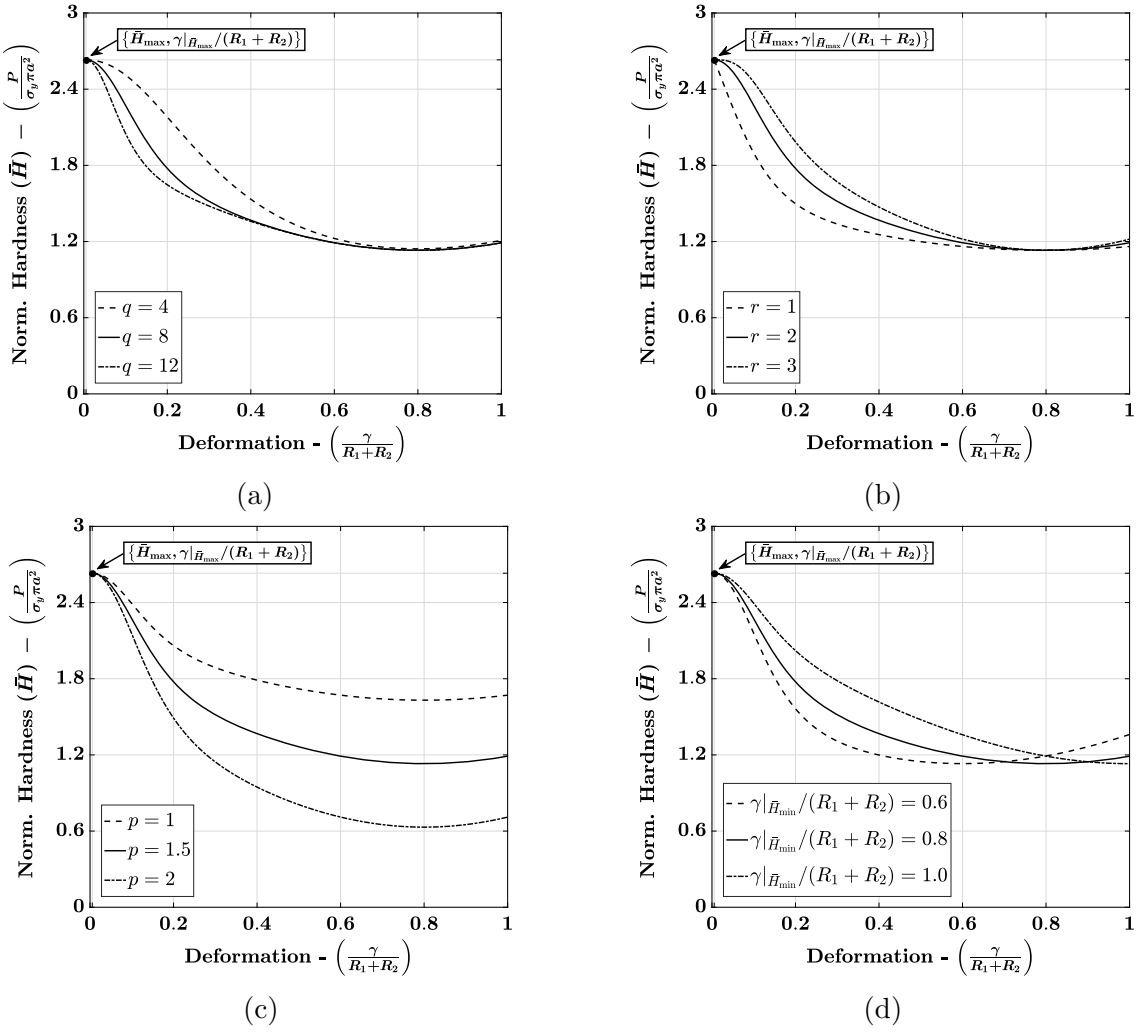

Figure 3.14. Analysis of the influence of model parameters (a) q, (b) r, (c) p and (d) $\gamma|_{\bar{H}_{\min}}$ on $\bar{H}^{\text{fp}}$ model response. Solid curves correspond to the reference curve obtained by setting $q = 8$, $r = 2$, $p = 1.5$ and $\gamma|_{\bar{H}_{\min}}/(R_1 + R_2) = 0.8$, while the other curves (dashed-dotted and dashed) correspond to those obtained by perturbing one of the parameter values while keeping other values constant. The value of $\bar{H}_{\max}$ and $\gamma|_{\bar{H}_{\max}}/(R_1 + R_2)$ corresponds to $\lambda = 1721.55$.

is equal to zero at $\gamma = \gamma|_{\bar{H}_{\max}}$ for $r \geq 1$. Therefore, when the condition $r \geq 1$ is true, the $\bar{H}^{\text{fp}} - \gamma$ relationship given by Equations (3.30) and (3.31) is C^1 continuous with the $\bar{H}^{\text{ep}} - \gamma$ relationship given by Equation (3.23).

Figure 3.14 shows the influence of model parameters q, r, p and $\gamma|_{\bar{H}_{\min}}$ on the response of $\bar{H}^{\text{fp}}$. In all figures, the reference model curve (solid line) is obtained by setting $p = 1.5$, $q = 8$, $r = 2$ and $\gamma|_{\bar{H}_{\min}}/(R_1 + R_2) = 0.8$. The other curves (dashed and dashed-dotted lines) are

obtained by perturbing one of the parameter values while keeping the other values constant. The value of $\bar{H}_{\max}$ and $\gamma|_{\bar{H}_{\max}}/(R_1+R_2)$ in the plots is obtained by setting $\lambda = 1721.55$, which corresponds to the material properties with $E/\sigma_y = 1500.97$ for simple loading case obtained from the space-filling design (ref. Table 3.2). From the study, it is evident that parameters q and r predominantly influence the rate of softening of $\bar{H}$, with r mainly controlling the rate at the onset of the fully plastic regime and q governing the rate of descent thereafter until the attainment of a minimum. Parameter $\gamma|_{\bar{H}_{\min}}$, as per its definition, predominantly influences the level of deformation at the minimum, while p regulates the value of $\bar{H}_{\min}$. It is important to note that the proposed equation models the evolution of $\bar{H}$ until the point of minimum, following which the loading condition effects predominate and another formulation is required to predict the rising pressure values for confined loading configurations.

From the observations of normalized hardness versus deformation data obtained from FE simulations, it is quite evident that the initial softening response from the onset of the fully plastic regime is primarily dependent on the material properties and fairly independent of the loading configuration. Therefore, parameters q and r are identified to be material-dependent parameters. However, the minimum value of $\bar{H}$ and the level of deformation at the minimum is heavily dependent on the loading configuration as well as the initial rate of softening. Therefore, $\gamma|_{\bar{H}_{\min}}$ and p are identified to be both material and loading condition-dependent parameters.

For the case of a simple loading configuration, it is theorized that the contact response softens until contact pressure approaches the material's yield strength as the particle geometry approaches that of a flat disk at $\gamma \to R_1 + R_2 = 2R$. Therefore, we obtain $\gamma^{\mathrm{SC}}|_{\bar{H}_{\min}} = R_1 + R_2 = 2R$. For confined loading configurations, the contact pressure rises again during the 'geometric hardening' regime due to void filling, as well as occupation of the voronoi cell faces by the contact surfaces. While void filling causes the elastic energy of the particle to increase due to material compression, the voronoi cell faces limit the evolution of contact areas, both of which lead to the increase in pressure. In accordance with this analysis, we propose the following condition to be true at the minimum:

$$\rho_V^{\mathrm{LC,contact}} \rho_S^{\mathrm{LC,contact}} = \Gamma \tag{3.33}$$

Table 3.5. Expressions for various volume and surface quantities in the minimum $\bar{H}$ condition given by Equation (3.33) for all contacts under hydrostatic and primary contacts under die loading configuration.

	DC	HC
$V_{\text{voro}}^{\text{LC}}$	$8R^2\left(R-\gamma/2\right)$	$8\left(R-\gamma/2\right)^3$
$V_{\text{contact}}^{\text{LC}}$	$(4/3)R^2\left(R-\gamma/2\right)$	$(4/3)\left(R-\gamma/2\right)^3$
$S_{\text{face}}^{\text{LC}}$	$4R^2$	$4\left(R-\gamma/2\right)^2$

Thus, for a particular contact of a particle under a given loading condition, the product of relative volume density ($\rho_V^{\text{LC,contact}}$) and relative surface area density ($\rho_S^{\text{LC,contact}}$) is equal to a parameter Γ at the minimum. The relative volume density for a contact is given by

$$\rho_V^{\text{LC,contact}} = \rho_V^{\text{LC}}\left(\frac{V_{\text{contact}}^{\text{LC}}}{V_{\text{voro}}^{\text{LC}}}\right) = \left(\frac{V_{\text{particle}}}{V_{\text{voro}}^{\text{LC}}}\right)\left(\frac{V_{\text{contact}}^{\text{LC}}}{V_{\text{voro}}^{\text{LC}}}\right) \tag{3.34}$$

where $\rho_V^{\text{LC}} = \left(V_{\text{particle}}/V_{\text{voro}}^{\text{LC}}\right)$ is the relative density of the particle's voronoi cell (Harthong et al., 2009), $V_{\text{particle}} = (4/3)\pi R^3$ is the volume of the spherical particle, $V_{\text{voro}}^{\text{LC}}$ is the volume of the voronoi cell, and $V_{\text{contact}}^{\text{LC}}$ is a section of the voronoi cell volume associated with the contact, which is estimated as the volume of a pyramid with the base as the contact's voronoi cell face and apex as the particle's center of mass. The relative surface area density is given by

$$\rho_S^{\text{LC,contact}} = \frac{S_{\text{contact}}^{\text{LC}}}{S_{\text{face}}^{\text{LC}}} \tag{3.35}$$

where $S_{\text{contact}}^{\text{LC}}$ is the contact area and $S_{\text{face}}^{\text{LC}}$ is the area of the contact's voronoi cell face. Table 3.5 provides expressions for $V_{\text{voro}}^{\text{LC}}$, $V_{\text{contact}}^{\text{LC}}$ and $S_{\text{face}}^{\text{LC}}$ in terms of particle radius R and contact displacement γ for all contacts under hydrostatic loading and primary contacts under die loading configuration.

Figure 3.15 shows the values of Γ obtained from FEA simulations of die (primary contacts) and hydrostatic loading conditions, plotted against material parameter λ. From the figure, it is evident that Γ has a weak dependence on both material properties and loading condition, which results from the material and loading dependence of the contact area. These weak

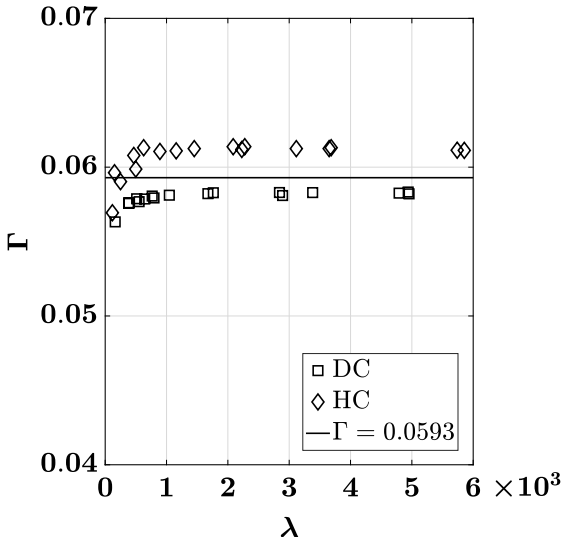

Figure 3.15. Plot of Γ values against material parameter λ for die (primary contacts) and hydrostatic loading conditions. Discrete values correspond to values obtained from FE data, while the solid plot corresponds to the average Γ value determined for the confined loading conditions.

effects are neglected by proposing a value of Γ averaged across all the obtained numerical values for die and hydrostatic loading conditions, which is $\Gamma = 0.0593$.

Using Equation (3.33), a detailed derivation of the solution of $\gamma|_{\bar{H}_{\min}}$ for primary contacts of die ($\gamma^{\mathrm{DC}}|_{\bar{H}_{\min}}$) and all contacts of hydrostatic ($\gamma^{\mathrm{HC}}|_{\bar{H}_{\min}}$) conditions is presented in Appendix D. It essentially entails substituting various volume and surface quantities (V_{particle}, $V^{\mathrm{LC}}_{\mathrm{voro}}$, $V^{\mathrm{LC}}_{\mathrm{contact}}$ and $S^{\mathrm{LC}}_{\mathrm{face}}$), and contact area $S^{\mathrm{LC}}_{\mathrm{contact}} = \pi a^2$ in Equation (3.33) with their respective expressions for die and hydrostatic conditions to finally obtain a solvable quintic in terms of the unknown variable $\gamma|_{\bar{H}_{\min}}$.

As discussed previously, the parameter p governs the minimum value of normalized hardness, i.e., $\bar{H}_{\min}$. For the case of simple loading configuration, the contact pressure approaches material's yield strength, and hence $\bar{H}^{\mathrm{SC}}_{\min} = 1$ at $\gamma^{\mathrm{SC}}|_{\bar{H}_{\min}} = R_1 + R_2 = 2R$. Consequently, using Equations (3.30) and (3.31), we have

$$\bar{H}^{\mathrm{SC}}_{\min} = \bar{H}_{\max} - p^{\mathrm{SC}} \left[\tanh\left\{ q\left(1 - \frac{\gamma|_{\bar{H}_{\max}}}{2R}\right)\right\} \cos\left\{ \left(1 - \frac{\gamma|_{\bar{H}_{\max}}}{2R}\right) - s(2R, q)\right\}\right]^r = 1 \quad (3.36)$$

Rearranging the above equation, we get

$$p^{\mathrm{SC}} = \frac{\bar{H}_{\max} - 1}{\left[\tanh\left\{q\left(1 - \frac{\gamma|_{\bar{H}_{\max}}}{2R}\right)\right\}\cos\left\{\left(1 - \frac{\gamma|_{\bar{H}_{\max}}}{2R}\right) - s(2R,q)\right\}\right]^r} \tag{3.37}$$

For die and hydrostatic loading conditions, determination of $\bar{H}_{\min}$ is not straightforward, since the contact pressure starts rising at $\gamma = \gamma^{\mathrm{LC}}|_{\bar{H}_{\min}}$ (LC→{DC, HC}) before reaching the material's yield strength. However, two prospective values of $\bar{H}_{\min}$ can be obtained from different analysis. The first value is determined as the value of $\bar{H}$ for the simple loading case at $\gamma^{\mathrm{LC}}|_{\bar{H}_{\min}}$, i.e.

$$\begin{aligned}\bar{H}^{\mathrm{LC}}_{\min,1} = \bar{H}_{\max} - p^{\mathrm{SC}}&\left[\tanh\left\{q\left(\frac{\gamma^{\mathrm{LC}}|_{\bar{H}_{\min}} - \gamma|_{\bar{H}_{\max}}}{2R}\right)\right\}\right.\\ &\left.\times\cos\left\{\left(\frac{\gamma^{\mathrm{LC}}|_{\bar{H}_{\min}} - \gamma|_{\bar{H}_{\max}}}{2R}\right) - s(2R,q)\right\}\right]^r\end{aligned} \tag{3.38}$$

Considering that the initial evolution of normalized hardness during the fully plastic regime is similar for all loading conditions, a second prospective value of $\bar{H}_{\min}$ can be evaluated by determining an intermediate value of p^{LC}, such that the slope of $\bar{H}^{\mathrm{LC}}$ for die and hydrostatic cases is equal to the slope of $\bar{H}^{\mathrm{SC}}$ for the simple case at their points of inflection, i.e. at the point where the second derivative of $\bar{H}$ with respect to $\gamma/(R_1 + R_2)$ $(= \gamma/2R)$ is zero. This inflection point is evident in the $\bar{H}$ vs. $\gamma/2R$ curves obtained from FE simulations for all loading conditions (Figures 3.7a, 3.9a and 3.8a) during the initial softening response, when the curve changes from *concave downward* to *concave upward*. A detailed approximate solution for this point, denoted by the contact deformation $\gamma^{\mathrm{LC}}|_{\bar{H}''=0}/2R$ (LC→{SC, DC, HC}) at the point, is presented in Appendix E, where the highly nonlinear equation $\bar{H}'' = 0$ is solved using Taylor series expansion. The approximate solution is obtained as

$$\begin{aligned}\frac{\gamma^{\mathrm{LC}}|_{\bar{H}''=0}}{2R} \simeq \frac{\gamma|_{\bar{H}_{\max}}}{2R} + \frac{3r\tan\left\{s(\gamma^{\mathrm{LC}}|_{\bar{H}_{\min}},q)\right\} + \left[3(2q^2+3)(r-1)(2r+1)\right.}{(2q^2+3)(2r+1) + 3(r+1)\tan^2\left\{s(\gamma^{\mathrm{LC}}|_{\bar{H}_{\min}},q)\right\}}\\ \left.+9(2r^2-1)\tan^2\left\{s(\gamma^{\mathrm{LC}}|_{\bar{H}_{\min}},q)\right\}\right]^{1/2}\end{aligned} \tag{3.39}$$

By equating the slope of $\bar{H}^{\mathrm{LC}}$ (LC→{DC, HC}) at $\gamma^{\mathrm{LC}}|_{\bar{H}''=0}/2R$ to the slope of $\bar{H}^{\mathrm{SC}}$ at $\gamma^{\mathrm{SC}}|_{\bar{H}''=0}/2R$, and rearranging the equation, we obtain the intermediate value of p^{LC} (LC→{DC, HC}), denoted by p_o^{LC}, as

$$p_o^{\mathrm{LC}} = p^{\mathrm{SC}} \left[\frac{\begin{array}{c} 2q\mathrm{csch}\left\{2q\left(\frac{\gamma^{\mathrm{SC}}|_{\bar{H}''=0}-\gamma|_{\bar{H}_{\max}}}{2R}\right)\right\} \\ -\tan\left\{\left(\frac{\gamma^{\mathrm{SC}}|_{\bar{H}''=0}-\gamma|_{\bar{H}_{\max}}}{2R}\right) - s(2R,q)\right\} \end{array}}{\begin{array}{c} 2q\mathrm{csch}\left\{2q\left(\frac{\gamma^{\mathrm{LC}}|_{\bar{H}''=0}-\gamma|_{\bar{H}_{\max}}}{2R}\right)\right\} \\ -\tan\left\{\left(\frac{\gamma^{\mathrm{LC}}|_{\bar{H}''=0}-\gamma|_{\bar{H}_{\max}}}{2R}\right) - s(\gamma^{\mathrm{LC}}|_{\bar{H}_{\min}},q)\right\} \end{array}} \right] \times \left[\frac{\begin{array}{c} \tanh\left\{q\left(\frac{\gamma^{\mathrm{SC}}|_{\bar{H}''=0}-\gamma|_{\bar{H}_{\max}}}{2R}\right)\right\} \\ \times\cos\left\{\left(\frac{\gamma^{\mathrm{SC}}|_{\bar{H}''=0}-\gamma|_{\bar{H}_{\max}}}{2R}\right) - s(2R,q)\right\} \end{array}}{\begin{array}{c} \tanh\left\{q\left(\frac{\gamma^{\mathrm{LC}}|_{\bar{H}''=0}-\gamma|_{\bar{H}_{\max}}}{2R}\right)\right\} \\ \times\cos\left\{\left(\frac{\gamma^{\mathrm{LC}}|_{\bar{H}''=0}-\gamma|_{\bar{H}_{\max}}}{2R}\right) - s(\gamma^{\mathrm{LC}}|_{\bar{H}_{\min}},q)\right\} \end{array}} \right]^r \tag{3.40}$$

The second value of $\bar{H}_{\min}$ at $\gamma^{\mathrm{LC}}|_{\bar{H}_{\min}}$ is then given by

$$\bar{H}^{\mathrm{LC}}_{\min,2} = \bar{H}_{\max} - p_o^{\mathrm{LC}} \left[\tanh\left\{q\left(\frac{\gamma^{\mathrm{LC}}|_{\bar{H}_{\min}} - \gamma|_{\bar{H}_{\max}}}{2R}\right)\right\} \times\cos\left\{\left(\frac{\gamma^{\mathrm{LC}}|_{\bar{H}_{\min}} - \gamma|_{\bar{H}_{\max}}}{2R}\right) - s(\gamma^{\mathrm{LC}}|_{\bar{H}_{\min}},q)\right\}\right]^r \tag{3.41}$$

Figure 3.16 shows the plots of $\bar{H}^{\mathrm{LC}}_{\min}$ for die and hydrostatic loading conditions against material parameter λ. The discrete values (square plots for die and diamond plots for hydro) are obtained from FE simulation data, while $\bar{H}^{\mathrm{LC}}_{\min,1}$ (dashed curve) and $\bar{H}^{\mathrm{LC}}_{\min,2}$ (dashed-dotted curve) are plotted using Equations (3.38) and (3.41) respectively for permissible values of $\lambda \geq 22.08$. From the figure, it is evident that $\bar{H}^{\mathrm{LC}}_{\min,1}$ underpredicts the numerical values of $\bar{H}^{\mathrm{LC}}_{\min}$, while $\bar{H}^{\mathrm{LC}}_{\min,2}$ overpredicts the values. An average of the two prospective values, plotted as a solid curve in the figure, accurately predicts the minimum normalized hardness for both confined loading conditions. Therefore, we represent $\bar{H}^{\mathrm{LC}}_{\min}$ as

$$\bar{H}^{\mathrm{LC}}_{\min} = \frac{\bar{H}^{\mathrm{LC}}_{\min,1} + \bar{H}^{\mathrm{LC}}_{\min,2}}{2} \tag{3.42}$$

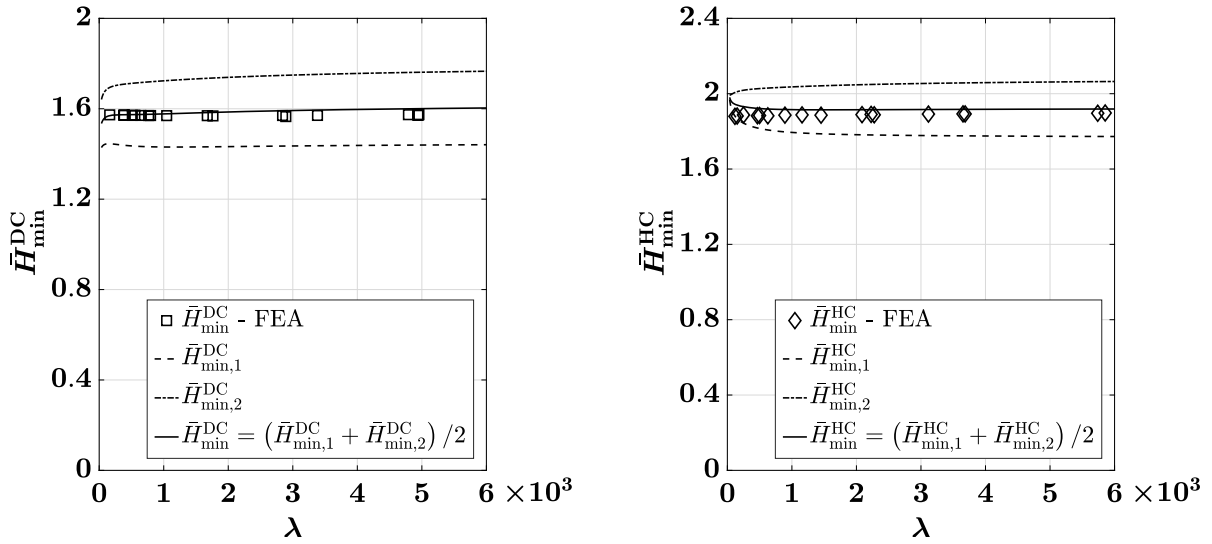

Figure 3.16. Plots of $\bar{H}^{\mathrm{LC}}_{\mathrm{min}}$ against material parameter λ for (a) die and (b) hydrostatic loading conditions. Discrete plots (squares for die and diamonds for hydrostatic) represent values obtained from FE simulation data. $\bar{H}^{\mathrm{LC}}_{\mathrm{min,1}}$ and $\bar{H}^{\mathrm{LC}}_{\mathrm{min,2}}$ are represented by dashed and dashed-dotted curves respectively. The analytical value of $\bar{H}^{\mathrm{LC}}_{\mathrm{min}}$, given by the average of $\bar{H}^{\mathrm{LC}}_{\mathrm{min,1}}$ and $\bar{H}^{\mathrm{LC}}_{\mathrm{min,2}}$, is represented by a solid curve.

Consequently, using Equations (3.30) and (3.31), parameter p^{LC} (LC$\rightarrow${DC, HC}) is given by

$$p^{\mathrm{LC}} = \frac{\bar{H}_{\max} - \bar{H}^{\mathrm{LC}}_{\mathrm{min}}}{\left[\tanh\left\{q\left(\frac{\gamma^{\mathrm{LC}}|_{\bar{H}_{\min}} - \gamma|_{\bar{H}_{\max}}}{2R}\right)\right\}\cos\left\{\left(\frac{\gamma^{\mathrm{LC}}|_{\bar{H}_{\min}}\gamma|_{\bar{H}_{\max}}}{2R}\right) - s(\gamma^{\mathrm{LC}}|_{\bar{H}_{\min}}, q)\right\}\right]^r} \tag{3.43}$$

The remaining parameters q and r, determined to be material-dependent parameters, are calibrated from the $\bar{H}$ vs. $\gamma/2R$ FE simulation data of the simple loading case. Figure 3.17 shows the plots of calibrated q and r values against material parameter λ. From fitting of the plotted values, we propose the following relationships for q and r with λ

$$q = 14.1819\tanh\left(0.3729\lambda^{0.1013}\right) \tag{3.44}$$

$$r = \exp\left(\frac{1.6199}{\lambda^{0.3232}}\right) \tag{3.45}$$

For confined loading conditions, following the attainment of a minimum normalized hardness $\bar{H}^{\mathrm{LC}}_{\mathrm{min}}$ at contact deformation $\gamma^{\mathrm{LC}}|_{\bar{H}_{\mathrm{min}}}$, the contact pressure rises steadily during the 'low

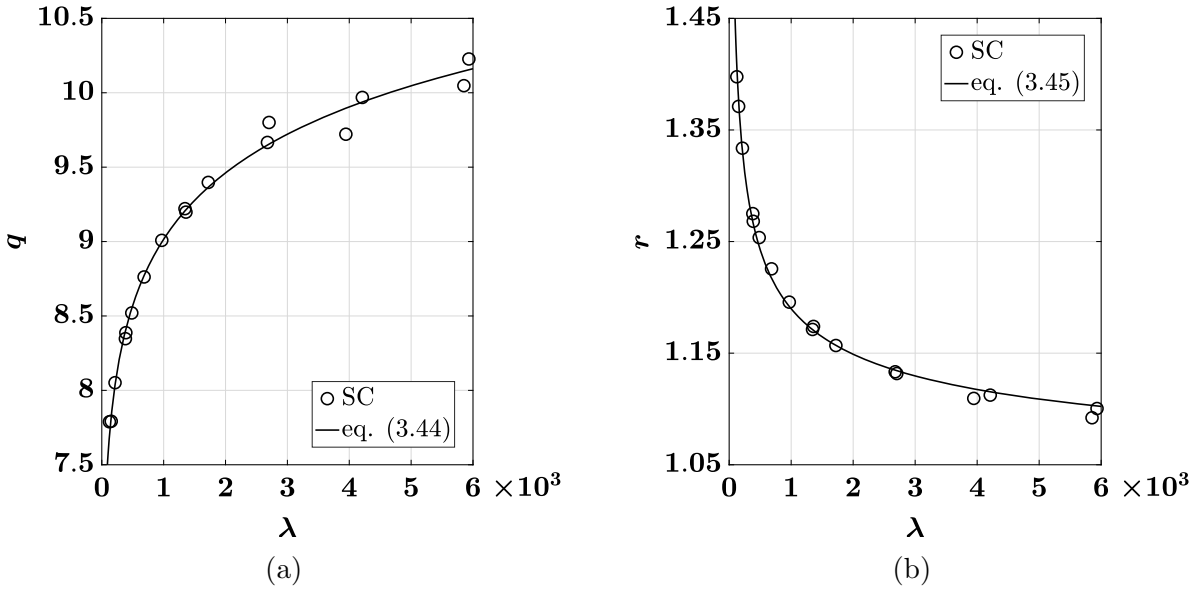

Figure 3.17. Estimation of material-dependent parameters (a) q and (b) r as functions of parameter λ for normalized hardness $\bar{H}^{\text{fp}}$ in the fully plastic regime. Plotted discrete values correspond to values obtained from FE data, while solid curves correspond to relationships obtained from curve fitting.

compressibility' regime. During this regime, contact behavior is heavily dependent on the loading condition due to significant contact interactions. Therefore, contacts in this regime cannot be treated independent of each other; rather, the contact behavior should be directly related to the overall particle response under compression. With this consideration, we propose to model contact response in this regime as a function of the relative density of the voronoi cell, ρ_V^{LC}, where the normalized hardness $\bar{H}$ is given by

$$\bar{H}^{\text{lc}} = \bar{H}_{\text{min}}^{\text{LC}} - u \ln \left\{ 1 - l \left(\frac{\chi^{\text{LC}} - \chi^{\text{LC}}|_{\bar{H}_{\text{min}}}}{\chi_{\text{zp}}^{\text{LC}} - \chi^{\text{LC}}|_{\bar{H}_{\text{min}}}} \right)^2 \right\} \tag{3.46}$$

where the superscript "lc" denotes the 'low compressibility' regime, u and l are the model parameters and $\chi^{\text{LC}} = 1/\rho_V^{\text{LC}} = \left(V_{\text{voro}}^{\text{LC}}/V_{\text{particle}}\right)$ is the inverse of the relative density. Using the expressions for $V_{\text{voro}}^{\text{LC}}$ in terms of particle radius R and contact displacement γ from Table

3.5, and $V_{\text{particle}} = (4/3)\pi R^3$, the contact deformation $\gamma^{\text{LC}}/2R$ ($\text{LC} \rightarrow \{\text{DC}, \text{HC}\}$) in terms of χ^{LC} is given by

$$\frac{\gamma^{\text{DC}}}{2R} = 1 - \frac{\pi\chi^{\text{DC}}}{6} \ , \quad \frac{\gamma^{\text{HC}}}{2R} = 1 - \left(\frac{\pi\chi^{\text{HC}}}{6}\right)^{1/3} \tag{3.47}$$

Additionally, $\chi^{\text{LC}}|_{\bar{H}_{\text{min}}}$ is the value of χ attained at $\bar{H}^{\text{LC}}_{\text{min}}$, while $\chi^{\text{LC}}_{\text{zp}}$ is the value of χ attained at the zero porosity limit (Tsigginos et al., 2015), which is the limit of full closure of porosity and beyond which the contact pressure is governed by the particle's elastic volume compressibility. It is given by

$$\chi^{\text{LC}}_{\text{zp}} = \frac{V_{\text{particle}} - V^{\text{LC}}_{\text{el}}}{V_{\text{particle}}} \tag{3.48}$$

where $V^{\text{LC}}_{\text{el}}$ is the elastic reduction in particle volume until the zero porosity limit is reached. It is important to note that the normalized hardness given by Equation (3.46) attains its minimum value equal to $\bar{H}^{\text{LC}}_{\text{min}}$ at $\chi^{\text{LC}} = \chi^{\text{LC}}|_{\bar{H}_{\text{min}}}$, making it C^1 continuous with the normalized hardness in the fully plastic regime given by Equation (3.30).

The contact pressure beyond the zero porosity limit is given by the elastic volumetric stress on the particle. Therefore, the normalized hardness in this regime is given by

$$\bar{H}^{\text{ev}} = \frac{B}{\sigma_y}\left(1 - \frac{V_{\text{voro}}}{V_{\text{particle}}}\right) = \zeta(1 - \chi^{\text{LC}}) \tag{3.49}$$

where the superscript "ev" denotes the elastic volumetric regime. By equating the value and slope of $\bar{H}^{\text{gh}}$ given by Equation (3.46) and $\bar{H}^{\text{ev}}$ given by (3.49) at $\chi^{\text{LC}} = \chi^{\text{LC}}_{\text{zp}}$ to achieve C^1 continuity between the contact formulations for $\bar{H}$ in the 'low compressibility' and elastic volumetric regimes, we obtain the following relationships between model parameters u and l and elastic volume reduction $V^{\text{LC}}_{\text{el}}$

$$u = \frac{V_{\text{particle}}\bar{H}^{\text{LC}}_{\text{min}} - \zeta V^{\text{LC}}_{\text{el}}}{V_{\text{particle}}\ln(1-l)} \tag{3.50}$$

$$V^{\text{LC}}_{\text{el}} = \frac{V_{\text{particle}}\left\{2l\bar{H}^{\text{LC}}_{\text{min}} + \zeta(1 - \chi^{\text{LC}}|_{\bar{H}_{\text{min}}})(1-l)\ln(1-l)\right\}}{\zeta\left\{2l + (1-l)\ln(1-l)\right\}} \tag{3.51}$$

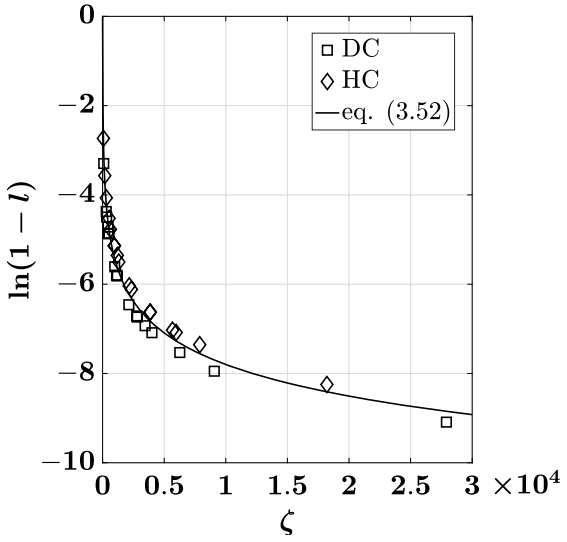

Figure 3.18. Estimation of model parameter l as a function of material parameter ζ for normalized hardness $\bar{H}^{\text{gh}}$ in the 'geometrical hardening' regime. Plotted discrete values correspond to $\ln(1-l)$ values obtained from calibration of FE data, while the solid curve represents the relationship obtained from curve fitting.

From the above equations, it is evident that u and $V_{\text{el}}^{\text{LC}}$ can be evaluated from a known value of l. Figure 3.18 shows a plot of the natural log of $(1-l)$ against material parameter ζ, where the l values are calibrated from $\bar{H}$ vs. $\gamma/2R$ FE simulation data of die and hydrostatic loading cases. It is interesting to note that the parameter l is independent of the loading condition, since the $\ln(1-l)$ values for both die and hydrostatic loading conditions fall on a single trend curve that is a function of ζ. Therefore, it is fair to conclude that l is a material-dependent parameter.

From curve fitting of the plotted values, we propose the following relationship between l and ζ

$$\begin{aligned} \ln(1-l) &= \ln\left(\frac{1}{1+0.1985\zeta^{1.0222}}\right) \\ \implies l &= 1-\left(\frac{1}{1+0.1985\zeta^{1.0222}}\right) \end{aligned} \tag{3.52}$$

To conclude the analysis, we provide below a summarized form of the semi-mechanistic contact law for the normalized hardness $\bar{H}$

$$\bar{H} = \begin{cases} = \bar{H}^{\mathrm{e}} = \frac{2}{3\pi}\lambda\mathbb{A}^{1/2}\gamma^{1/2} & \gamma \in [0, \gamma_y] \\ = \bar{H}^{\mathrm{ep}} = \bar{H}_{\max} - c_1\left[\ln\left(\frac{\gamma|_{\bar{H}_{\max}}}{\gamma}\right)\right]^{c_2} & \gamma \in (\gamma_y, \gamma|_{\bar{H}_{\max}}] \\ = \bar{H}^{\mathrm{fp}} = \bar{H}_{\max} - p^{\mathrm{LC}}\left[\tanh\left\{q\left(\frac{\gamma-\gamma|_{\bar{H}_{\max}}}{2R}\right)\right\}\right. & \gamma \in \left(\gamma|_{\bar{H}_{\max}}, \gamma^{\mathrm{LC}}|_{\bar{H}_{\min}}\right] \\ \qquad \left.\times\cos\left\{\left(\frac{\gamma-\gamma|_{\bar{H}_{\max}}}{2R}\right) - s(\gamma^{\mathrm{LC}}|_{\bar{H}_{\min}}, q)\right\}\right]^r & \mathrm{LC} \to \{\mathrm{SC}, \mathrm{DC}, \mathrm{HC}\} \\ = \bar{H}^{\mathrm{lc}} = \bar{H}^{\mathrm{LC}}_{\min} - u\ln\left\{1 - l\left(\frac{\chi^{\mathrm{LC}} - \chi^{\mathrm{LC}}|_{\bar{H}_{\min}}}{\chi^{\mathrm{LC}}_{\mathrm{zp}} - \chi^{\mathrm{LC}}|_{\bar{H}_{\min}}}\right)^2\right\} & \gamma \in \left(\gamma^{\mathrm{LC}}|_{\bar{H}_{\min}}, \gamma^{\mathrm{LC}}_{\mathrm{zp}}\right] \\ & \mathrm{LC} \to \{\mathrm{DC}, \mathrm{HC}\} \\ = \bar{H}^{\mathrm{ev}} = \zeta(1 - \chi^{\mathrm{LC}}) & \gamma \in \left(\gamma^{\mathrm{LC}}_{\mathrm{zp}}, \infty\right) \\ & \mathrm{LC} \to \{\mathrm{DC}, \mathrm{HC}\} \end{cases} \tag{3.53}$$

3.5 Validation of the Semi-Mechanistic Contact Law

The semi-mechanistic contact formulation developed in the previous section was validated by comparing the contact law predictions of normalized contact radius (a/R), normalized contact pressure or hardness ($\bar{H} = P/\sigma_y\pi a^2$) and normalized contact force ($P/\sigma_y\pi R^2$) with data obtained from FE simulations. Figures 3.19, 3.20 and 3.21 present this comparison for simple, die (primary contacts) and hydrostatic loading configurations respectively. To validate the material property dependence of the contact formulation, comparative plots for all loading configurations are provided for the lowest and the highest value of material parameter λ obtained from the space-filling design. The figures show an excellent agreement between the numerical FEA data and the analytical contact law predictions, with an accurate representation of material and loading condition - dependence of the contact behavior.

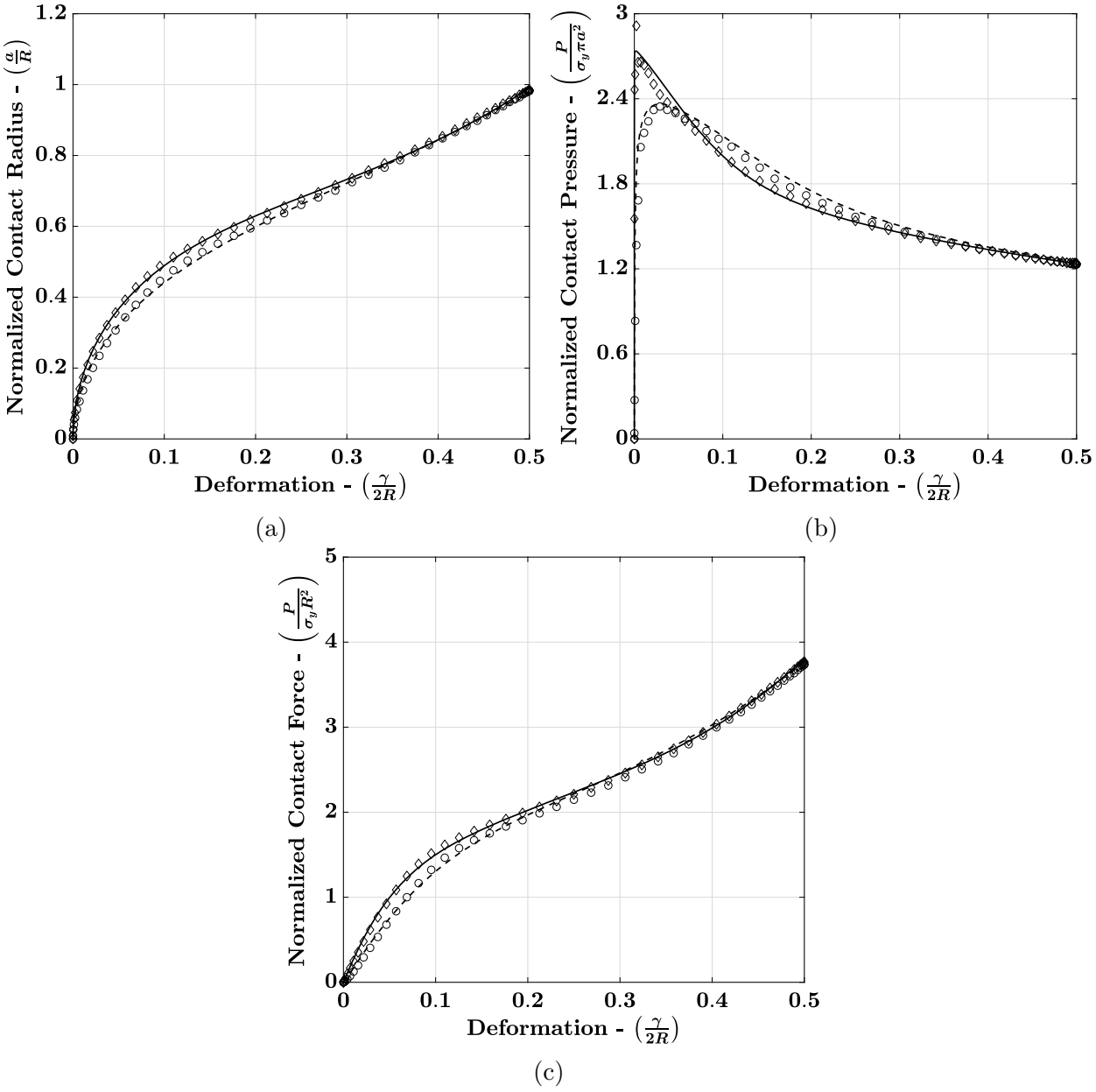

Figure 3.19. Comparison of the predictions of proposed semi-mechanistic contact formulation with FE simulation data for a particle under simple compression. Plots of normalized (a) contact radius-deformation, (b) contact pressure-deformation, and (c) contact force-deformation are depicted. FE data for the lowest value of $\lambda = 123.41$ obtained from space-filling design are denoted by circles, with corresponding contact law predictions denoted by a dashed curve. FE data with the highest value of $\lambda = 5933.40$ are denoted by diamonds, with corresponding contact law predictions denoted by a solid curve.

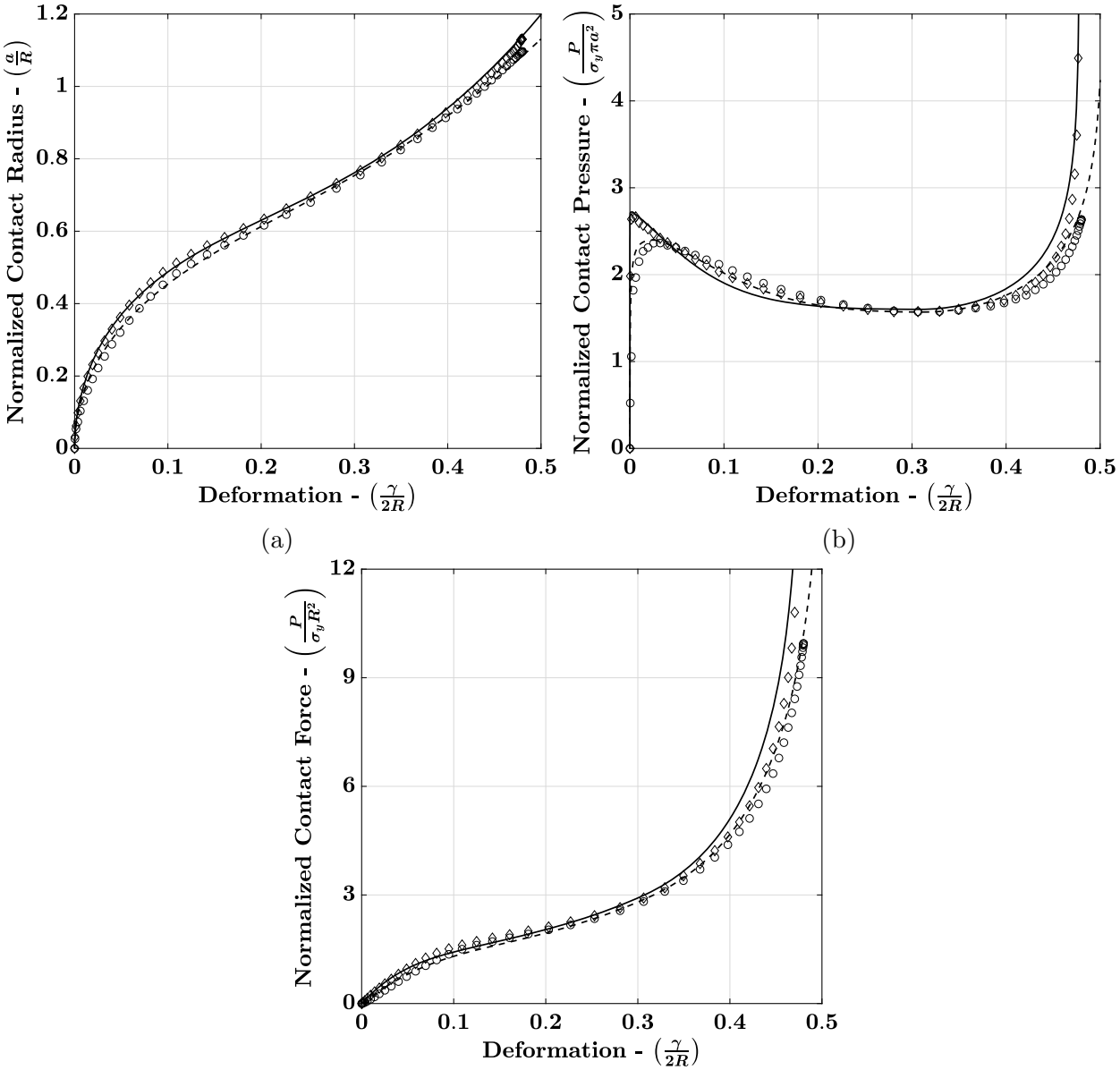

Figure 3.20. Comparison of the predictions of proposed semi-mechanistic contact formulation with FE simulation data for primary contacts of a particle under die compression. Plots of normalized (a) contact radius-deformation, (b) contact pressure-deformation, and (c) contact force-deformation are depicted. FE data for the lowest value of $\lambda = 163.08$ obtained from space-filling design are denoted by circles, with corresponding contact law predictions denoted by a dashed curve. FE data with the highest value of $\lambda = 4954.40$ are denoted by diamonds, with corresponding contact law predictions denoted by a solid curve.

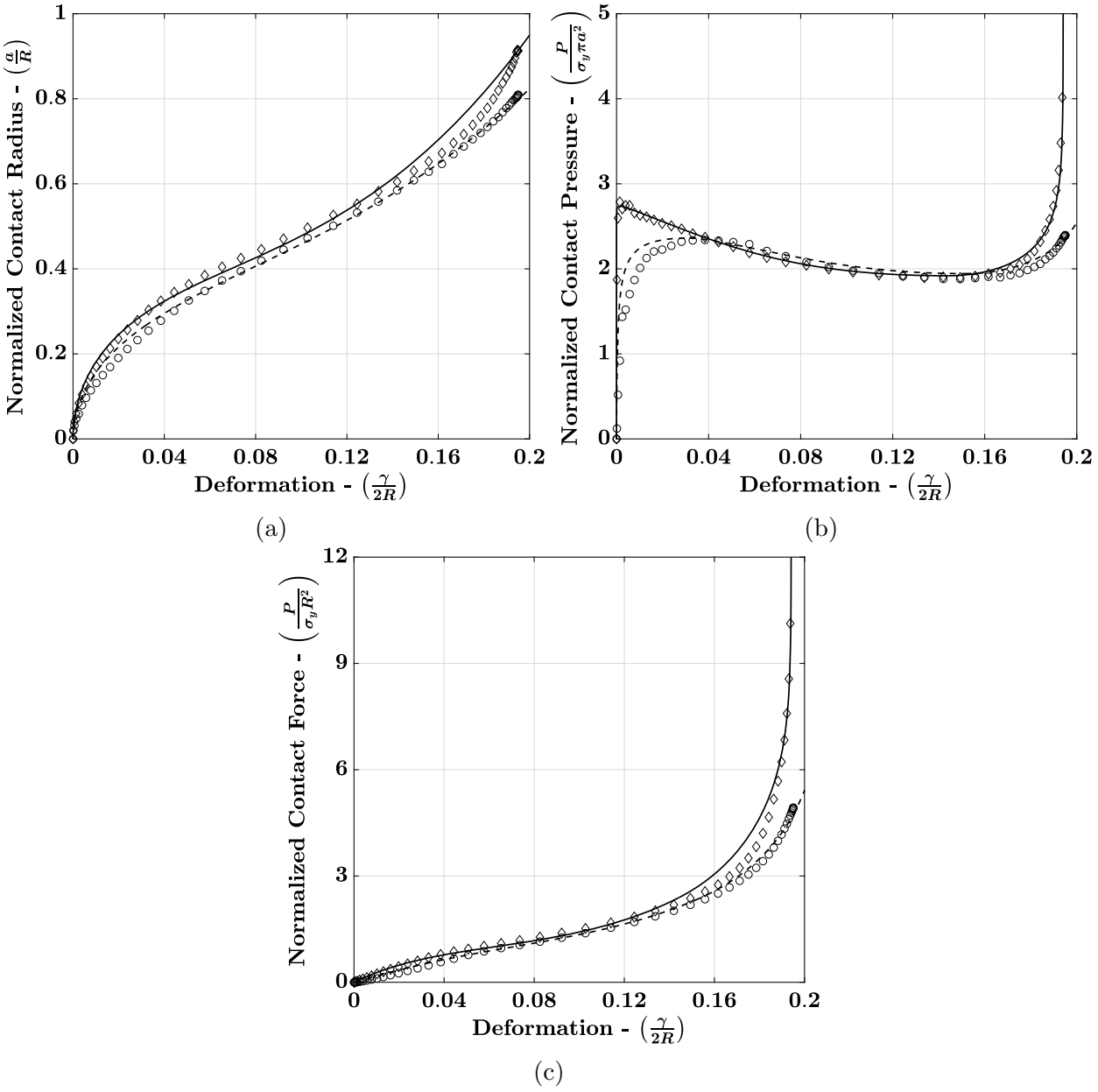

Figure 3.21. Comparison of the predictions of proposed semi-mechanistic contact formulation with FE simulation data for a particle under hydrostatic compression. Plots of normalized (a) contact radius-deformation, (b) contact pressure-deformation, and (c) contact force-deformation are depicted. FE data for the lowest value of $\lambda = 117.24$ obtained from space-filling design are denoted by circles, with corresponding contact law predictions denoted by a dashed curve. FE data with the highest value of $\lambda = 5854.69$ are denoted by diamonds, with corresponding contact law predictions denoted by a solid curve.

3.6 Preliminary semi-mechanistic analysis of the secondary contacts of die loading configuration

For the case of die loading configuration, we have shown the evolution of contact behavior at the lateral or 'secondary' contacts from the FE simulations presented in section 3.3. These contacts, despite being subjected to zero applied or 'local' deformation, develop solely due to the lateral or 'nonlocal' deformation of the particle resulting from axial compression. In this section, we attempt to lay the foundation of a nonlocal contact formulation capable of predicting such contact behavior by proposing semi-mechanistic laws relating the deformation at primary and secondary contacts.

To obtain an estimate of the lateral deformation, we utilize the FE simulations for the simple loading configuration and post-process the average nodal displacements at the lateral edge of the $(1/8)^{\text{th}}$ sphere (Figure 3.22). Therefore, for a displacement $\gamma/2$ at the particle-plate axial contact (γ for a two-particle contact), we obtain an average nodal displacement of $\gamma_s/2$ at the lateral edge, where the subscript 's' denotes the equivalent displacement at the secondary contact in the die loading configuration. It is important to note that, according to the nonlocal contact formulation (ref. Gonzalez & Cuitiño (2012, 2016) and Agarwal &

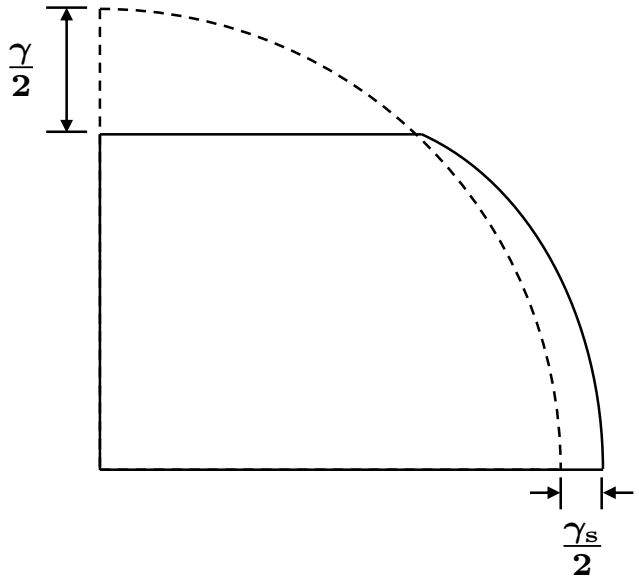

Figure 3.22. Schematic of the simple compression of $(1/8)^{\text{th}}$ sphere, showing an axial contact displacement of $\gamma/2$ resulting in a lateral edge displacement of $\gamma_s/2$.

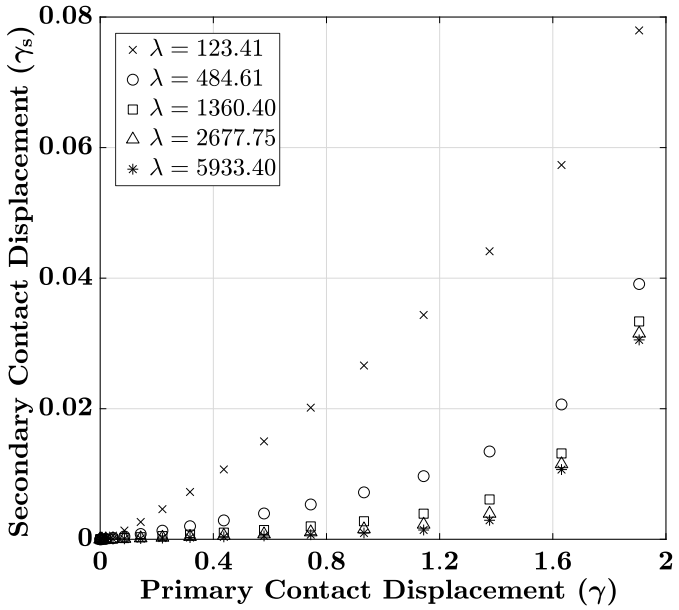

Figure 3.23. Plots of lateral secondary contact displacement (γ_s) vs. axial primary contact displacement (γ) obtained from FE simulations of the simple loading configuration. Plots are depicted for 5 out of the 17 material properties obtained from the space-filling design, ranging from minimum to maximum value of the material parameter λ. The units of displacement on both axes is millimeters (mm).

Gonzalez (2018)), each particle contact acquires nonlocal displacement contributions from all other contacts on the particle. Therefore, as the lateral secondary displacements γ_s evolve and become larger, their nonlocal contributions to the primary and other secondary contacts become significant. Since the development of a complete nonlocal contact formulation for elasto-plastic particles is beyond the scope of this chapter, we restrict our estimation of the secondary displacements to the small deformation regime to safely neglect any nonlocal contributions from the secondary contacts.

From the observation of FE simulation results of normalized hardness for secondary die contacts (Figure 3.10a), we find that the contact behavior remains within the small deformation elasto-plastic regime until the primary contact deformation $\gamma/2R$ reaches 0.1. Therefore, the lateral secondary displacements are evaluated until the primary contact displacement reaches $\gamma = 0.1 \times 2R = 2$mm for $R = 10$mm. The obtained displacements are plotted in Figure 3.23 for 5 out of the 17 material properties for simple configuration obtained from the space filling design, ranging from minimum to the maximum value of material parameter

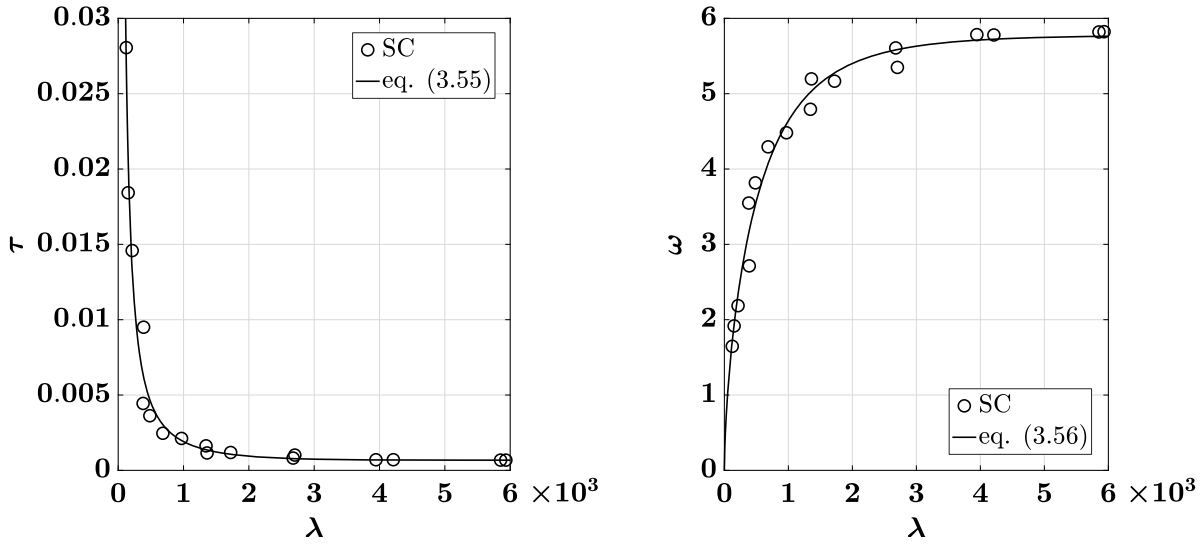

(a) (b)

Figure 3.24. Estimation of material-dependent parameters (a) τ and (b) ω as functions of parameter λ for the relationship between secondary and primary contact displacements γ_s and γ. Plotted discrete values correspond to the values obtained from FE data, while solid curves correspond to relationships obtained from curve fitting.

λ. From the figure, we observe that the evolution of lateral displacement follows a power law, with the rate of evolution increasing with increasing material compliance (decreasing λ). Accordingly, we propose the following relationship between the secondary and primary contact displacement

$$\gamma_s = \tau \gamma^{\omega} \tag{3.54}$$

where τ and ω are material-dependent parameters. Figure 3.24 shows a plot of the discrete values of these parameters against material parameter λ, obtained by fitting the above relationship to the secondary vs. primary displacement data for all 17 material properties. From curve fitting of these calibrated values, we propose the following relationship for τ and ω with λ

$$\tau = \frac{1}{1480.8863 \tanh\left\{(5.0261 \times 10^{-5}) \cdot (\lambda^{1.2889})\right\}} \tag{3.55}$$

$$\omega = 5.7775 \tanh\left\{0.0159\left(\lambda^{0.6146}\right)\right\} \tag{3.56}$$

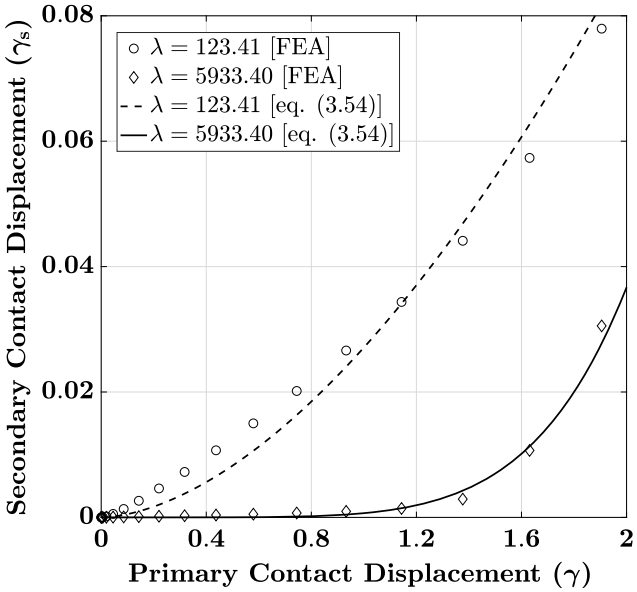

Figure 3.25. Comparison of secondary displacement (γ_s) vs. primary displacement (γ) obtained from the power law given by Equation (3.54) and FE simulations of the simple loading configuration. Plots are depicted for minimum and maximum value of λ obtained from the space-filling design. The units of displacement on both axes is millimeters (mm).

The above relationships are also plotted in Figure 3.24, and provide excellent estimates of the calibrated parameter values. Finally, by using these relationships in the $\gamma_s - \gamma$ power law given by Equation (3.54), the evaluated secondary displacements are plotted and compared with the FE values for the minimum and maximum λ in Figure 3.25. The figure confirms the accuracy of the proposed power law, with an excellent agreement obtained between the modeled and FE results.

The secondary contact displacement model from Equation (3.54) can now be used to obtain the contact radius (Equation (3.17)), normalized hardness (Equation (3.20) for elastic and Equation (3.23) for elasto-plastic regime) and contact force (Equation (3.16)) until the primary contact deformation reaches 0.1, which denotes the limit of elasto-plastic regime for the secondary contacts.

Additionally, we have proposed in the previous section that during the 'low compressibility' regime, the contact response is a function of the overall particle compression due to significant contact interactions. Therefore, it is fair to assume that beyond the 'low compressibility' regime, all particle contacts are subjected to the same pressure, which is given

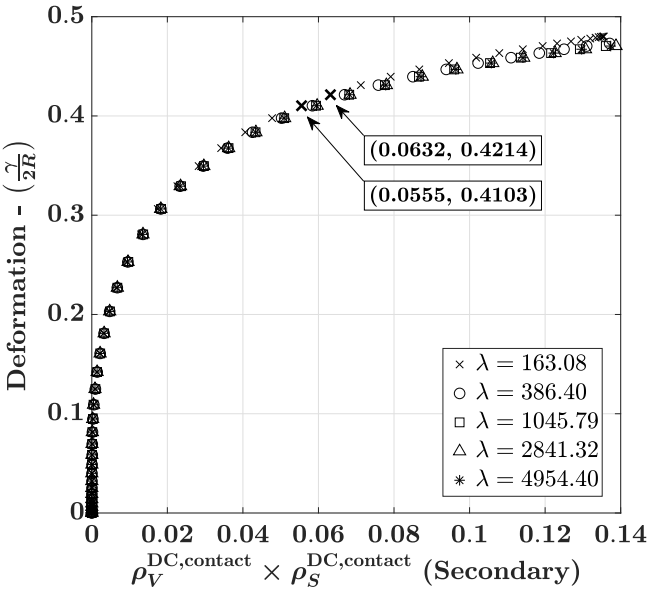

Figure 3.26. Plot of primary deformation ($\gamma/2R$) vs. the product of volume and surface relative densities $\rho_V^{\mathrm{DC,contact}} \times \rho_S^{\mathrm{DC,contact}}$ for the secondary contacts of die loading configuration. Plots are depicted for 5 out of 17 material properties for die configuration, ranging from minimum to maximum value of λ. The marked points (bold cross markers) correspond to the points between which the value of $\gamma/2R$ at $\rho_V^{\mathrm{DC,contact}} \rho_S^{\mathrm{DC,contact}} = \Gamma = 0.0593$ is interpolated for $\lambda = 163.08$.

by Equation (3.46) in the 'low compressibility' regime and Equation (3.49) in the elastic volumetric regime. For the secondary contacts, the onset of 'low compressibility' regime is predicted by using the minimum hardness condition given by Equation (3.33), where the product of volume and surface relative densities is given by

$$\begin{aligned}
\rho_V^{\mathrm{DC,contact}} \times \rho_S^{\mathrm{DC,contact}} &= \left(\frac{V_{\mathrm{particle}}}{V_{\mathrm{voro}}^{\mathrm{DC}}}\right)\left(\frac{V_{\mathrm{contact}}^{\mathrm{DC}}}{V_{\mathrm{voro}}^{\mathrm{DC}}}\right)\left(\frac{S_{\mathrm{contact}}^{\mathrm{DC}}}{S_{\mathrm{face}}^{\mathrm{DC}}}\right) \\
&= \frac{\frac{4}{3}\pi R^3}{8R^2\left(R-\frac{\gamma}{2}\right)} \times \frac{\frac{4}{3}R^2\left(R-\frac{\gamma}{2}\right)}{8R^2\left(R-\frac{\gamma}{2}\right)} \times \frac{S_{\mathrm{contact}}^{\mathrm{DC}}}{4R\left(R-\frac{\gamma}{2}\right)} \\
&= \frac{\pi S_{\mathrm{contact}}^{\mathrm{DC}}}{144R^2\left(1-\frac{\gamma}{2R}\right)^2}
\end{aligned} \tag{3.57}$$

The value of primary deformation $\gamma/2R$ at the onset can be obtained by interpolating the $\gamma/2R$ vs. $\rho_V^{\mathrm{DC,contact}} \times \rho_S^{\mathrm{DC,contact}}$ data generated by using FE values of the secondary contact area $S_{\mathrm{contact}}^{\mathrm{DC}}$. Figure 3.26 presents this data for 5 out of the 17 material properties for die configuration, ranging from minimum to maximum λ. According to Equation (3.33), the

Table 3.6. Values of primary contact deformation $\gamma/2R$ at the onset of 'low compressibility' regime for secondary die contacts. Values are provided for 5 out of the 17 material properties for die loading configuration.

λ	$\gamma/2R$ (Low Compressibility)
163.08	0.4159
386.40	0.4115
1045.79	0.4102
2841.32	0.41
4954.40	0.4098

'low compressibility' regime starts when the product of volume and surface relative densities equals $\Gamma = 0.0593$. The deformation values at the fulfillment of this condition are obtained by cubic interpolation between points on either side of the Γ value, and are listed in Table 3.6 for the five plotted material properties.

Observation of the large deformation normalized contact pressure response of secondary die contacts from finite element simulations (Figure 3.11c) suggests that while the normalized hardness $\bar{H}$ at the onset of 'low compressibility' regime ($\gamma/2R \sim 0.41$ from Table 3.6) does not attain a minimum value, it does fall on an inflection point, following which the evolution of contact pressure is visibly similar to that of the primary contacts (Figure 3.11b). This observation confirms the accuracy of our predictions of the onset of the 'low compressibility' regime for secondary die contacts.

Figure 3.27 presents a comparison of the predicted evolution of normalized secondary contact radius and contact force in the small-deformation (elastic and elasto-plastic) regime with the finite element simulation results. Additionally, Figure 3.28 shows the predicted vs. FE results of the evolution of normalized hardness in both small and large (beyond 'low compressibility') deformation regimes. Comparative plots are provided for the minimum and the maximum value of λ for die configuration. Even though an excellent agreement is not achieved, the predicted results at small deformations are still comparable with the FE data and of the same order of magnitude. Concurrently, a good agreement between the predicted and FE results is obtained for normalized hardness in the large deformation regime.

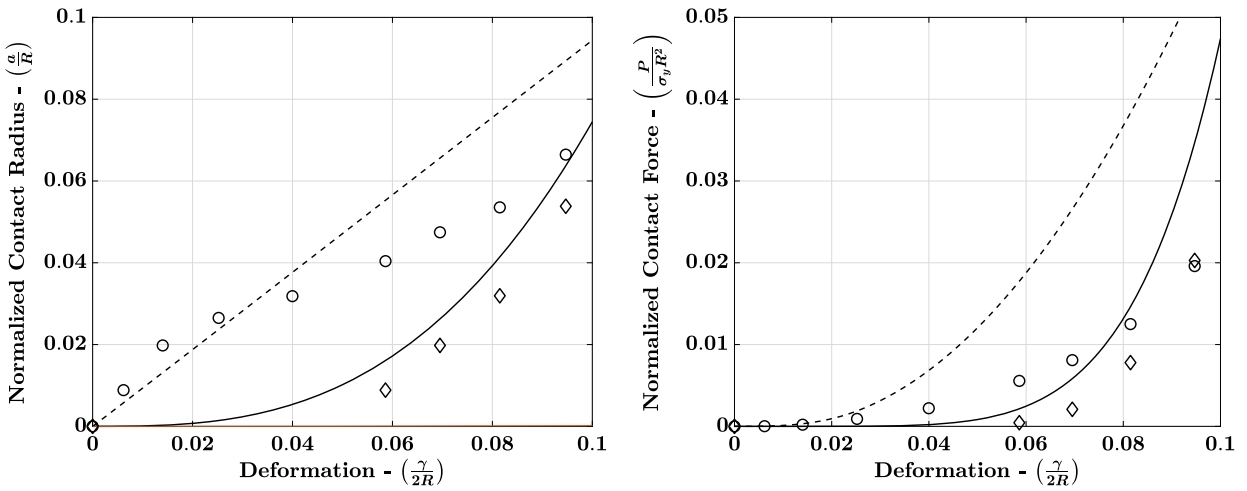

(a) (b)

Figure 3.27. Comparison of the predictions of small-deformation normalized (a) contact radius (Equation (3.17)) and (b) contact force (Equation (3.16)) evolution at the secondary contacts with respect to primary contact deformation with FE simulation data for a particle under die compression. FE data for the lowest value of $\lambda = 163.08$ are denoted by circles, with corresponding contact law predictions denoted by a dashed curve. FE data with the highest value of $\lambda = 4954.40$ are denoted by diamonds, with corresponding contact law predictions denoted by a solid curve.

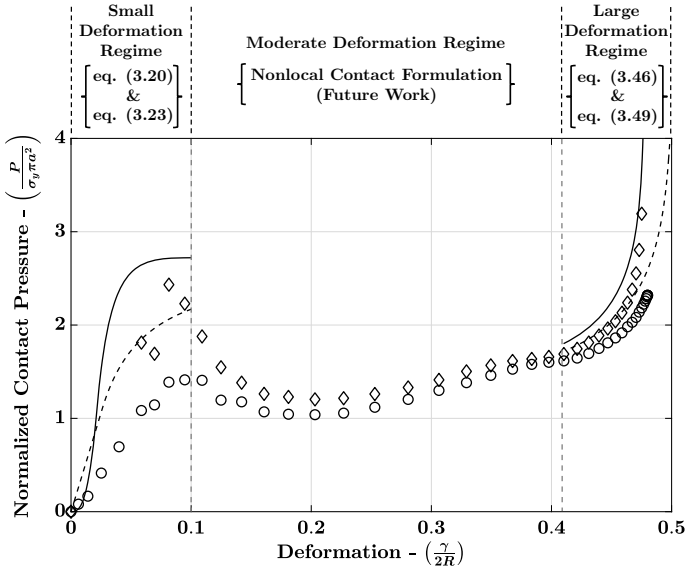

Figure 3.28. Comparison of the predictions of small and large deformation normalized hardness evolution at the secondary contacts with respect to primary contact deformation with FE simulation data for a particle under die compression. FE data for the lowest value of $\lambda = 163.08$ are denoted by circles, with corresponding contact law predictions denoted by a dashed curve. FE data with the highest value of $\lambda = 4954.40$ are denoted by diamonds, with corresponding contact law predictions denoted by a solid curve.

3.7 Summary and Discussion

A semi-mechanistic contact formulation has been developed for material and loading condition-dependent contact behavior of an elastic-perfectly plastic spherical particle, as it is compressed in a simple cubic packing under unconfined (simple axial compression) or confined (die and hydrostatic compression) loading conditions. Contact laws for the evolution of contact radius and normalized contact pressure (or hardness) have been proposed, while the contact force is efficiently determined from the product of contact pressure and area. The material-dependence is systematically incorporated in the formulation through calibration of model parameters to a set of 51 single-particle finite element simulations (17 for each of simple, die and hydrostatic loading conditions), where the diverse set of material properties is obtained from a space-filling design.

The contact radius is determined as a three-term nonlinear function of the contact displacement, where each term corresponds to the evolution of contact area during a specific deformation regime, i.e., small, moderate and large deformations. The analytical framework for the three-term function is obtained by applying the method of curvature-correction to the small-deformation similarity contact law. The normalized hardness, due to its complex and distinct evolution in each deformation regime, is modeled as a piece-wise differentiable function, with distinct contact laws proposed for each regime in a way that the function remains continuous and differentiable with respect to the contact deformation at all stages of particle compression. A salient feature of the proposed contact law is its capability to predict the rise in contact pressure for confined loading conditions during the 'geometrical hardening' or 'low compressibility' regime as a function of the particle's elastic compressibility, thus unraveling critical material-dependent behavior at large deformations. The capabilities of the contact formulation are successfully validated by attainment of an excellent agreement between the model and finite element predictions of the evolution of contact radius, pressure and force with contact deformation for the three considered loading configurations.

Finally, a foundational semi-mechanistic analysis of the lateral walled (secondary) contacts in the die loading configuration is presented. The secondary contacts, despite not being subjected to any applied deformation, evolve as a result of the lateral expansion of

the axially compressed particle. The induced deformation at the secondary contacts, termed as nonlocal deformation, is determined by post-processing the nodal displacements at the lateral edge of the particle from finite element simulations of the simple loading configuration. Although, this analysis is limited to small deformations to safely neglect any nonlocal contributions from the secondary contacts themselves. The relationship between primary and nonlocal secondary contact displacements is modeled as a power law, which is shown to accurately represent the material-dependent evolution of the secondary displacements. By using this relationship, the contact response is evaluated at small deformations from the proposed semi-mechanistic contact formulation. Additionally, by utilizing the assumption of equal contact pressure at all particle contacts beyond the 'low compressibility' regime, the contact pressure at large deformations for the secondary contacts is determined from the proposed normalized hardness law. A comparison of the model and finite element predictions of the secondary contact response shows that while an excellent agreement is not achieved, the model predicted response is comparable and of the same order of magnitude as the numerical FE data. With regard to this observation, it is worth mentioning that since the FE simulations performed in this study were set up for an accurate determination of the large deformation contact response, a separate finite element study with a finer mesh may be needed for proper convergence of contact behavior at small deformations. Such a study will enable a more reliable validation of the modeled response at the secondary contacts, and is a worthwhile direction of future research.

CHAPTER 4. EFFECTS OF CYCLIC LOADING AND TIME-RECOVERY ON MICROSTRUCTURE AND MECHANICAL PROPERTIES OF PARTICLE-BINDER COMPOSITES

This chapter was published in the ASME Journal of Applied Mechanics, Volume 87(10): 101008 (23 pages), Ankit Agarwal and Marcial Gonzalez, Effects of cyclic loading and time-recovery on microstructure and mechanical properties of particle-binder composites, Copyright ASME (2020).

4.1 Introduction

Particulate composites, or particle-binder composites, consist of hard particles, such as carbon, tungsten carbide, silica, gravel, and others, in the matrix of a soft material, such as polymers and soft metals. These materials are used across a wide range of applications in different contexts. For example, particle-reinforced composites (such as filled elastomers and concrete, i.e., gravel embedded in a cement matrix) are used to enhance the mechanical properties of the matrix. Since hard particles increase the load-bearing capacity of the material, these composites provide an improvement in strength and wear properties over single material systems. However, they also exhibit significant inelastic phenomena in their mechanical response (Dargazany et al., 2014), such as Mullins effect (Mullins, 1948, 1969) and cyclic hysteresis (Netzker et al., 2010) in filled rubbers (Bergström & Boyce, 1998; Miehe & Keck, 2000).

Plastic-bonded explosives (PBX) are another type of particle-binder composites that are widely used in ammunition for defense applications. These materials consist of explosive crystals, such as cyclotrimethylenetrinitramine (RDX) and cyclotetraminetetranitramine (HMX), in the matrix of a binder that primarily includes: (i) a soft polymer, such as hydroxyl-terminated polybutadiene (HTPB) (Akhavan, 2011) and Estane (Idar et al., 1998), (ii) a plasticizer, such as bis(2,2-dinitropropyl)acetal (BDNPA), dioctyl adipate (DOA) and bis(2,2-dinitropropyl)-formal (BDNPF), and (iii) small concentrations of antioxidants, bond-

ing agents, wetting agents, cross-linkers, stabilizers and catalysts (Daniel, 2006). The polymer acts as a safety envelope for the explosive crystals, inhibiting their movement and excitation to low amplitude loads and thus reducing their sensitivity to weak impact loads (Palmer et al., 1993; Rae et al., 2002; Rangaswamy et al., 2010). The plasticizer improves processability, mechanical properties and also lowers sensitivity (Yılmaz et al., 2014). Another major ingredient in PBX may include a metal, such as aluminum, which is often used as a fuel or booster to enhance blast effects (Prakash et al., 2004; Daniel, 2006).

Characterization and mechanistic understanding of the mechanical behavior of PBX are of particular interest to the defense community. PBXs are designed to detonate in response to a very specific external stimulus. However, these composites may be subjected to diverse loading conditions during their operational life (ranging from high to low strain-rate compression and tension, impact, mechanical vibrations and cyclic loading, among others) that in turn may alter their microstructure and their mechanical response, rendering them unpredictable and unsafe (Drodge & Williamson, 2016). Several experimental studies have been performed to analyze the mechanical response and microstructural changes in PBX under different loading conditions. The most commonly used techniques for imparting static and dynamic loads are: (i) low strain-rate uniaxial unconfined compression and tension (Funk et al., 1996; Idar et al., 1998; Thompson et al., 2002), (ii) low frequency base excitation (Paripovic & Davies, 2013, 2016), (iii) Brazilian test for measuring tensile strength (Grantham et al., 2004; Williamson et al., 2007), (iv) high strain-rate compression and impact loading using split Hopkinson pressure bars (Idar et al., 2002; Li et al., 2012; Kerschen et al., 2017), and (v) dynamic mechanical analysis (Thompson et al., 2012; Drodge & Williamson, 2016). The most common destructive and non-destructive techniques for observing microstructural changes are: (i) speckle photography (Palmer et al., 1993) and (ii) scanning electron microscopy (SEM) (Rae et al., 2002; Chen et al., 2007), that have been used to study fracture surfaces in PBX following a Brazilian test, (iii) high speed synchrotron X-ray phase contrast imaging (Hudspeth et al., 2015), which has been used to study *in-situ* deformation and failure in PBX under dynamic compression (Parab et al., 2016), and (iv) micro-computed tomography, which is an increasingly popular and sophisticated non-destructive imaging technique capable of characterizing the material in a three-dimensional (3D) space (hua YANG et al.,

2014; Al-Raoush & Papadopoulos, 2010; Koloushani et al., 2018; Mukunoki et al., 2016; Yu et al., 2018; He et al., 2013; Yermukhambetova et al., 2016). In the context of PBX, *in-situ* micro-computed tomography (micro-CT) has been used to observe microstructural changes in material specimens during large uniaxial unconfined compression (Manner et al., 2017; Chen et al., 2017), with observations of ductile plastic flow to extensive cracking and damage mechanisms like crystal-binder delamination and transgranular fracture. When coupled with optical deformation measurement techniques like digital image correlation (DIC) (Bruck et al., 1989) and digital volume correlation (DVC) (Bay et al., 1999), micro-CT has been used effectively to obtain strain fields and quantify microstructural changes in polymer-bonded sugar during large unconfined uniaxial compression (Hu et al., 2015, 2016).

The stress-strain response of particle-binder composites, specifically polymer-bonded sugar under large quasi-static monotonic compression, is typically characterized by four stages (see, e.g., Chen et al. (2017)). Initially, a nonlinear increase in the slope of the stress-strain curve is observed, which is attributed to the gradual mating of the machine platen-specimen surface. This is followed by a predominant elastic deformation of the material, where the response curve remains largely linear. The third stage commences with a nonlinear decline in the slope of the curve, attributed to predominant inelastic deformation and damage accumulation in the form of particle-binder delamination and slipping, which results in nucleation of cracks, and it continues until the material reaches its ultimate compressive strength. Subsequently, the material rapidly loses its strength, owing to an extensive transgranular crack formation during the fourth stage.

It is worth noting that, since the majority of inelastic deformation and damage accumulation without loss of structural integrity occurs within the first three stages of deformation, it is relevant to study periodic or cyclic loading within the range of moderate to high strains and to characterize its effect on microstructure and mechanical properties of particle-binder composites. Furthermore, since a material specimen may be subject to such loading conditions multiple times over its operational life, it is important to study the effect of time-recovery, degradation or aging (see, e.g., Goldrein et al. (2001)). A systematic study of the simultaneous effect of cyclic loading and time-recovery on microstructure and mechanical properties of

particle-binder composites is not available in the open literature and, thus, it is the central focus of this work.

This chapter specifically focuses on the qualitative and quantitative characterization of changes in mechanical behavior and microstructure of particle-binder composites due to the application of high amplitude quasi-static cyclic compressive loading, before and after a 4-week time-recovery or aging period. Three compositions that differ in aluminum content from the mock sugar formulation of PBXN-109 are cast into cylindrical specimens and used in this study. Microstructural changes in the spatial distribution of the primary components of the formulation, including pore space, are characterized from micro-CT images.

The chapter is organized as follows. Section 4.2 describes the experimental procedures, including specimen preparation, experimental apparatus, and the proposed cyclic testing and aging (recovery) procedure. Section 4.3 provides an analysis of the simple monotonic compressive response of mock specimens to identify optimum strain levels for cyclic loading. Section 4.4 presents a detailed analysis of cyclic loading and time-recovery effects on the mechanical response of mock specimens. Section 4.5 describes the postprocessing procedure for the identification of spatial distribution of different components in the formulation, including pore space, from micro-CT images. Section 4.6 provides a detailed quantitative analysis of changes in microstructure due to cyclic loading and time-recovery or aging. Finally, a summary and concluding remarks are presented in section 4.7.

4.2 Experimental Procedures

4.2.1 Material Preparation and Specimen Geometry

Cylindrical specimens of mock PBX material with dimensions of approximately 1-inch height and 1-inch diameter were prepared following the procedure by Range et al. (2018). *The specimens were prepared by Ms. Allison Range.*[1] The formulations used are variations of PBXN-109 formulation (Lochert et al., 2002), with sugar used as a substitute for RDX to render the specimens inert. The base formulation is summarized in Table 4.1.

[1]Allison Range, Ray W. Herrick Laboratories, Purdue University, West Lafayette, IN 47907, USA. Email: range@purdue.edu

Table 4.1. PBXN-109 formulation.

Constituent	**% w/w**
RDX	64.000
Aluminum	20.000
R45-HT (Hydroxyl-terminated Polybutadiene Resin)	7.346
Dioctyl Adipate (DOA)	7.346
Antioxidant 2246	0.100
Dantocol DHE	0.260
Triphenylbismuth	0.020
Isophorone Diisocyanate (IPDI)	0.950

The main constituents of the mock specimens are an HTPB binder with equal quantities of R45-HT resin (Cray Valley USA, LLC) and DOA plasticizer (Sigma-Aldrich USA), sucrose particles, and spherical aluminum powder (Valimet Inc, Stockton, CA, USA). The sucrose particles are sieved to a diameter range of 106–355 μm to be comparable in size to RDX particles. The aluminum powder has an average particle size of 25 μm. To prepare the specimens, a mixing and casting procedure as described by Range et al. (2018) was followed. The cast specimens were then cured in an oven for 7 days at 60°C. Experiments on the specimens were performed 1-2 months after curing.

To gain insight into the role of additive content, i.e., of aluminum powder, in the evolution of microstructure and mechanical properties during cyclic loading and aging, the base

(a) 85-00 (b) 85-15 (c) 85-30

Figure 4.1. Mock energetic material specimens.

formulation was varied to produce specimens of different formulations based on the following two parameters:

1. Solids loading, which is the weight percentage of solids (sucrose crystals and aluminum powder) in the overall mixture.

2. Additive content, which is the weight percentage of aluminum powder in the solids.

Specimens of three different formulations were studied, all of whom have 85% solids loading but differ in additive content, namely 85-00 (0% additive in solids, 0% in total, Figure 4.1a), 85-15 (15% additive in solids, 12.75% in total, Figure 4.1b) and 85-30 (30% additive in solids, 25.5% in total, Figure 4.1c). The nominal specimen heights (h), diameters (D) and test performed for 85-00, 85-15 and 85-30 are provided in Tables 4.2, 4.3 and 4.4, respectively.

Table 4.2. Test parameters for 85-00 formulation.

Specimen	**Nominal Height - h (mm)**	**Nominal Diameter - D (mm)**	**Test Performed**
85-00-01	27.17 ± 0.03	25.68 ± 0.13	Simple compressive loading
85-00-02	26.33 ± 0.01	25.71 ± 0.07	Simple compressive loading
85-00-03	27.05 ± 0.03	25.45 ± 0.12	Simple compressive loading-unloading
85-00-04	26.60 ± 0.01	25.71 ± 0.10	Simple compressive loading-unloading
85-00-05	26.32 ± 0.02	25.62 ± 0.09	Compressive cyclic

Table 4.3. Test parameters for 85-15 formulation.

Specimen	**Nominal Height - h (mm)**	**Nominal Diameter - D (mm)**	**Test Performed**
85-15-01	27.29 ± 0.01	25.66 ± 0.11	Simple compressive loading
85-15-02	26.20 ± 0.01	25.72 ± 0.11	Simple compressive loading
85-15-03	26.55 ± 0.01	25.54 ± 0.11	Simple compressive loading-unloading
85-15-04	27.25 ± 0.01	25.53 ± 0.10	Simple compressive loading-unloading
85-15-05	27.38 ± 0.01	25.52 ± 0.15	Compressive cyclic

Table 4.4. Test parameters for 85-30 formulation.

Specimen	Nominal Height - h (mm)	Nominal Diameter - D (mm)	Test Performed
85-30-01	26.70 ± 0.01	25.89 ± 0.10	Simple compressive loading
85-30-02	25.09 ± 0.03	25.54 ± 0.08	Simple compressive loading
85-30-03	26.14 ± 0.02	25.49 ± 0.14	Simple compressive loading-unloading
85-30-04	25.84 ± 0.02	25.67 ± 0.14	Simple compressive loading-unloading
85-30-05	26.33 ± 0.02	25.46 ± 0.10	Simple compressive loading-unloading
85-30-06	26.34 ± 0.02	25.52 ± 0.10	Compressive cyclic
85-30-07	26.08 ± 0.01	25.56 ± 0.07	Compressive cyclic

4.2.2 Experimental Setup

Compressive loading experiments were performed on a MTS Criterion C43 universal testing machine (Figure 4.2). The specimens were compressed between metal platens lubricated with WD-40 dry lube. Strain-controlled tests were performed at room temperature (72°F), and at a strain-rate of $0.001s^{-1}$ to produce a quasi-static loading response. A load cell of 500 N capacity was used to obtain the force measurements.

4.2.3 Micro-Computed Tomography

Micro-CT scans were performed on a Bruker Skyscan 1272 instrument (Figure 4.3). The specimens were fixed to the mounting fixture using adhesive putty, with care being taken to mount them in a straight, upright position. Table 4.5 presents the optimum scan settings identified for each of the specimen formulations. The settings were optimized for scan quality (i.e., good contrast, low beam hardening, and ring artifacts), image quality (i.e., good resolution, low noise) and scan time. Due to the specimens being larger than the detector's field of view at the selected resolution, the scan was carried out at two camera positions successively to capture the entire width of the specimens. However, the length captured was still limited by the length of the field of view. Therefore, the middle portion of the specimen

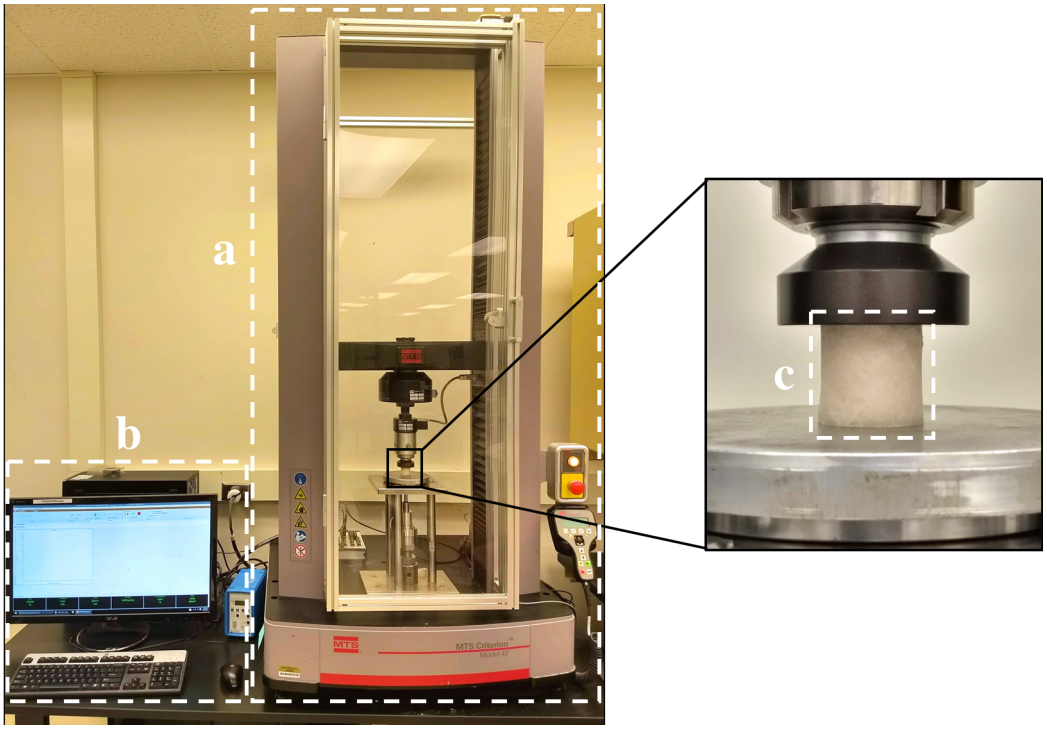

Figure 4.2. Experimental setup for compressive periodic loading tests, showing (a) MTS Criterion C43 testing frame, (b) Controlling workstation, and (c) Test specimen (85-00 shown in the figure).

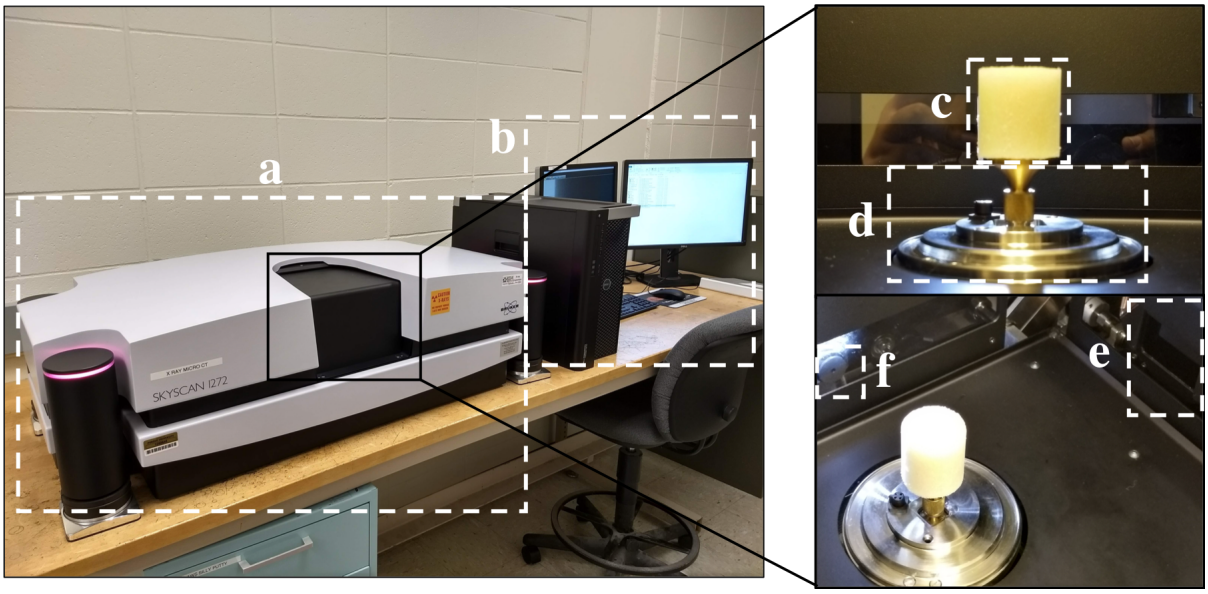

Figure 4.3. The setup for micro-computed tomography, showing (a) Bruker Skyscan 1272 instrument, (b) Controlling workstation, (c) Test specimen (85-00 shown in the figure) fixed to the (d) mounting fixture, (e) X-Ray detector, and (f) Side visual camera.

Table 4.5. Optimum micro-CT scan settings.

Scan Settings	**85-00**	**85-15**	**85-30**
Beam Voltage (kV)	70	80	100
Beam Current (μA)	142	125	100
Beam Filter	Al 1mm	Al 0.5mm + Cu 0.038mm	Cu 0.11mm
Detector Resolution	1632×1092	1632×1092	1632×1092
Voxel Size (μm)	10	10	10
Rotation Angle (degrees)	0.4	0.4	0.4
Averaging (frames)	6	6	6
Offset Scanning	Yes, with two camera positions	Yes, with two camera positions	Yes, with two camera positions
Scan duration	5 hrs 40 mins	6 hrs 15 mins	7 hrs 30 mins

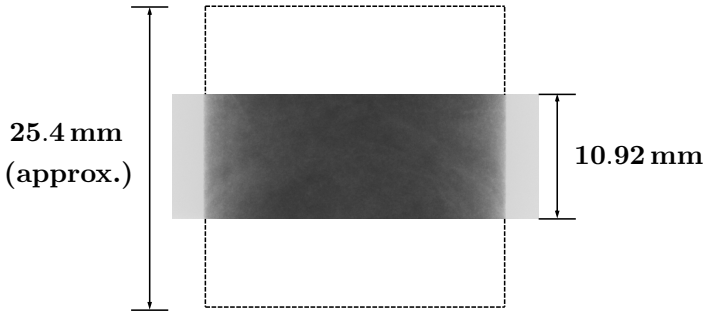

Figure 4.4. Representation of the scanned portion with respect to the entire length of the specimen.

of length 10.92 mm was scanned to adequately capture the loading and aging effects for the entire specimen (Figure 4.4).

4.2.4 Testing Procedure for assessing Cyclic Loading and Time-Recovery Effects

Figure 4.5 presents the standardized testing procedure employed to identify the dependence of mock energetic specimens on loading history and time-recovery or aging. A period of 24 hours was selected for re-scanning the specimens after cyclic compressive testing, to

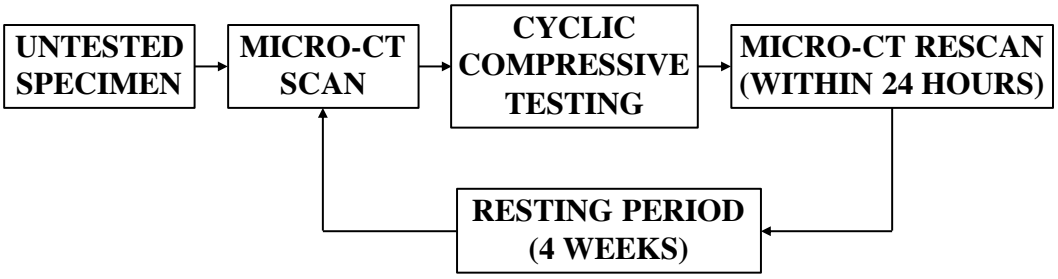

Figure 4.5. Testing procedure for assessing cyclic loading and time-recovery effects on mock energetic specimens.

allow sufficient time for scan completion, and to simultaneously capture the material's dependence on cyclic loading. Before resuming the testing cycle, a resting period of 4 weeks was allowed for the specimens to capture the aging effect, during which the specimens were stored in UV protective resealable bags in a temperature-controlled (72°F) room.

4.3 Identification of Optimal Strain Levels for Cyclic Loading

To understand the basic deformation characteristics of mock specimens, and to establish a standard procedure for identifying optimal strain levels for cyclic loading, monotonic compressive loading-unloading tests were performed for each specimen composition.

First, two specimens of each composition were compressed until a chosen maximum strain level of 30% (see Figure 4.6), and the resulting nominal stress-strain response was studied. It was observed that the 85-00 specimen exhibits (i) an initial nonlinear behavior (machine-specimen mating), followed by (ii) an approximately linear increase in stress (predominant elasticity), succeeded by (iii) a nonlinear response with decreasing slope (predominant plasticity) until a peak stress level (ultimate compressive strength), after which the (iv) stress decreases rapidly. These observations are in agreement with the previously observed behavior of polymer-bonded sugar under monotonic compression (Chen et al., 2017). In contrast, 85-15 and 85-30 specimens exhibit a predominantly nonlinear response followed by ductile plastic flow, reaching the peak stress at a much larger ultimate compressive strength; interestingly, the ultimate strength is not reached under 30% strain for 85-30 specimens. These observations are similar to those reported for aluminized explosives under high strain-rate

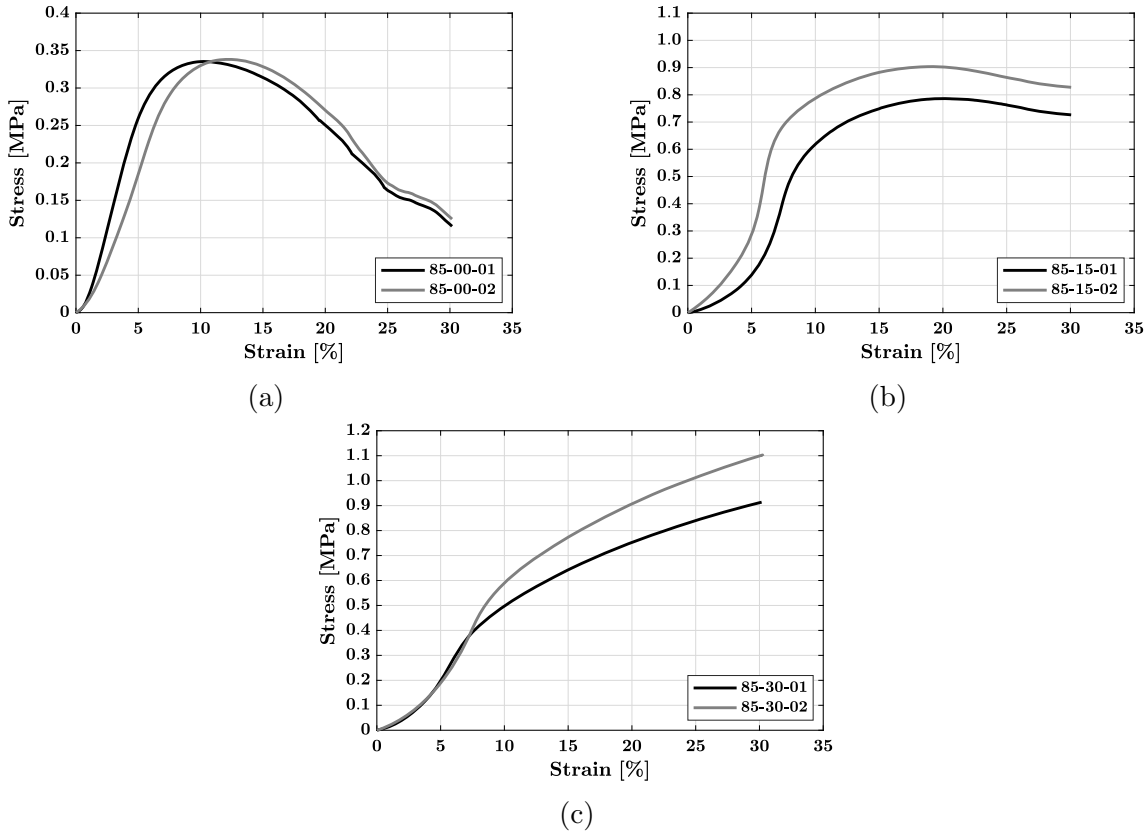

Figure 4.6. Uniaxial simple compressive stress-strain response of (a) 85-00-01 and 85-00-02, (b) 85-15-01 and 85-15-02, and (c) 85-30-01 and 85-30-02 specimens until 30% deformation.

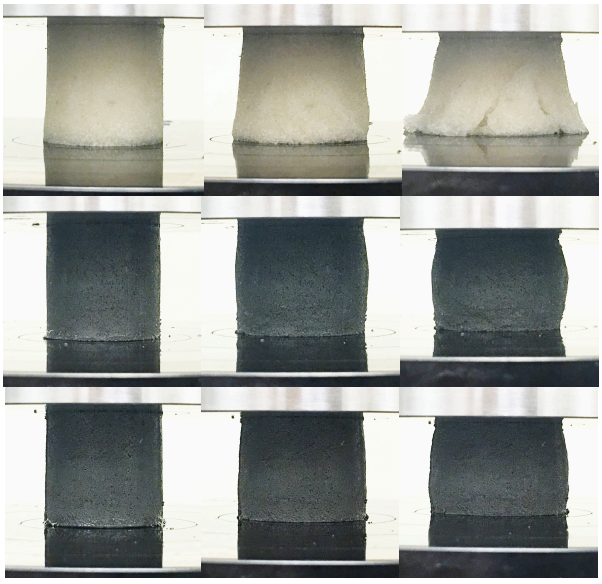

Figure 4.7. Configuration of 85-00-01 (top row), 85-15-01 (middle row) and 85-30-01 (bottom row) specimens under compression at 5%, 15% and 25% strain.

compression loading (Rumchik & Jordan, 2007). The increase in compressive strength with the addition of aluminum is attributed to an increase in inter-particle interactions and, consequently, in load-bearing capacity due to a more densely packed solid phase (i.e., crystals and aluminum powder). It is additionally noted that the presence of sucrose-aluminum contact interactions reduces sucrose-binder interfacial area, which in turn arrests extensive interfacial debonding and larger crack formation, leading to a ductile macroscopic deformation. These observations are supported by the deformed configuration of the loaded specimens (see Figure 4.7), where extensive crack formation and debonding is observed in the 85-00 specimens while lateral expansion and plastic material flow is observed in 85-15 and 85-30 specimens.

Second, optimal strain levels for cyclic loading of each specimen composition were selected on the basis of the following two principles:

1. The maximum strain level should ensure sufficient elasto-plastic deformation while preventing the material from reaching its ultimate compressive strength. Therefore, for experimental convenience, we chose the maximum stress level to be the nearest integer function of 80% of the averaged strain at ultimate compressive strength, i.e., $\epsilon_{\text{max,cyclic}} = \lfloor 0.8\ \bar{\epsilon}_{\text{ultimate}} \rceil$.

2. The minimum strain level should allow for sufficient cyclic deformation while accounting for cyclic stress softening (Mullins effect) and ensuring that the specimen remains in compression after cyclic stabilization. Therefore, we adopted an upper bound equal to two-thirds of the maximum strain level, i.e., $\epsilon_{\text{min,cyclic}} \leq 2\ \epsilon_{\text{max,cyclic}}/3$.

For 85-00 and 85-15 formulations, the values of strain at ultimate strength and the maximum cyclic strain level obtained from the tested specimens are reported in Table 4.6.

Next, two specimens each of the 85-00 and 85-15 formulations were loaded to their respective maximum strain levels and subsequently unloaded to a stress-free state (see Figure 4.8). A suitable value of the minimum strain level, lying between its upper bound (depicted by dashed-dotted lines in the figure) and the residual strain (i.e., 1% for 85-00 and 2% for 85-15), was to be chosen. We adopted a minimum strain level of 5% for 85-00 and 8% for 85-15, depicted by dotted lines in the figure. Finally, we verified (and show in the later

Table 4.6. Maximum cyclic strain values for 85-00 and 85-15 (all values in %).

Strain Type	**85-00-XX**		**85-15-XX**	
	01	02	01	02
$\epsilon_{\text{ultimate}}$	10.14	12.00	19.98	19.18
$\epsilon_{\text{max,cyclic}}$	9		16	

sections) that, for these chosen optimal strain levels, the specimens remained in compression during cyclic loading until the attainment of a stabilized cycle, despite the occurrence of stress softening.

For the 85-30 formulation, an ultimate compressive strength was not reached within 30% deformation and, therefore, the selection of optimal strain levels for cyclic loading was made based on the identification of the minimum strain level first. To this end, compressive loading-unloading tests were performed on three specimens for three different maximum strains, namely 30%, 15% and 9%. The unloading stress-strain curves for each of these tests are presented in Figure 4.9. It is evident from the figure that the specimens exhibited large residual strains; interestingly, the residual strain corresponding to a maximum strain of 30% is slightly larger than the two-thirds bound, i.e., 20%, while the residual strains for

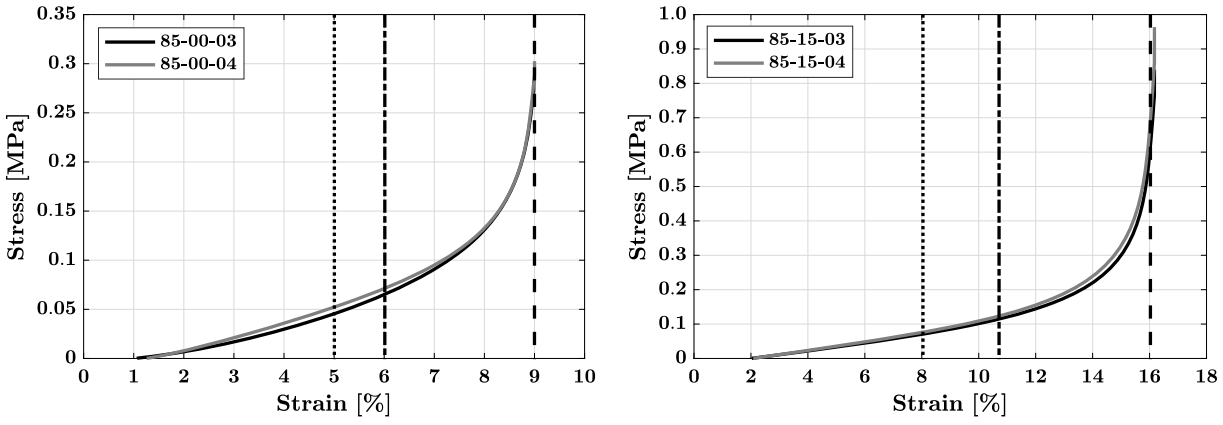

(a) (b)

Figure 4.8. Unloading stress-strain response of (a) 85-00-03 and 85-00-04, and (b) 85-15-03 and 85-15-04 specimens, with calculated maximum cyclic strain level (dashed line), upper bound on minimum cyclic strain level (dashed-dotted line) and the chosen minimum cyclic strain level (dotted line).

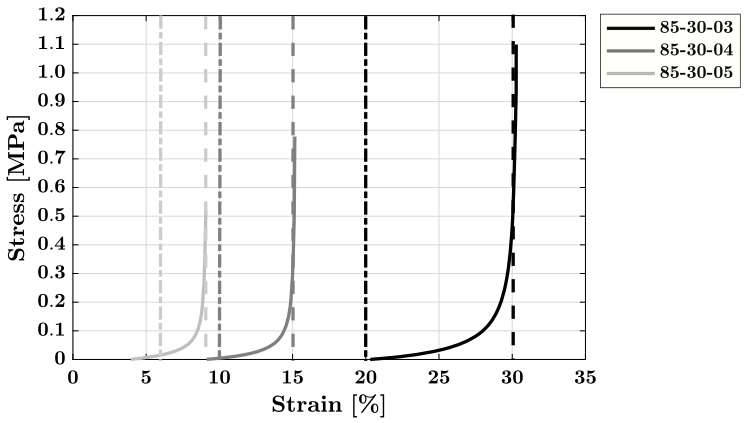

Figure 4.9. Unloading stress-strain response of 85-30-03 from 30% strain, 85-30-04 from 15% strain, and 85-30-05 from 9% strain. The maximum strains are denoted by dashed lines, while upper bounds on minimum cyclic strain level are denoted by dashed-dotted lines.

15% and 9% are slightly smaller than their respective two-thirds bounds, i.e., 10% and 6%. Consequently, cyclic compression tests were performed using 10%-15% and 6%-9% minimum-maximum strain levels (see Figure 4.10). The former test exhibited a stress-free state before cyclic stabilization, while the latter remained in compression until cyclic stabilization (see inserts in the Figure 4.10). Therefore, we adopted optimal strain levels of 6%-9% for cyclic loading of the 85-30 formulation.

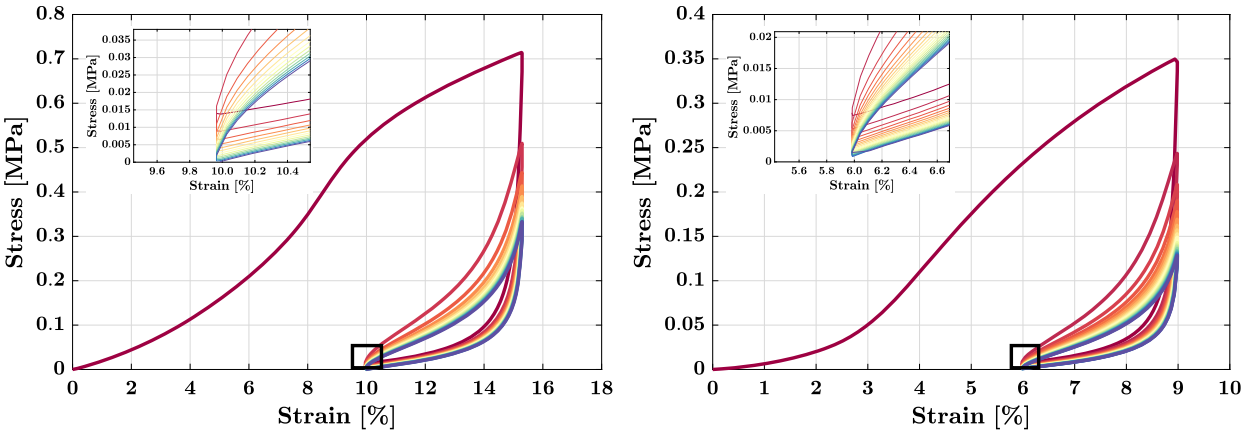

(a) (b)

Figure 4.10. Cyclic compressive response of (a) 85-30-06 specimen between 10% and 15% strain, and (b) 85-30-07 specimen between 6% and 9% strain. Graphs on the top left inset in each figure show a magnified view of the stress-strain response near the minimum cyclic strain.

A detailed analysis of the cyclic response of each mock energetic formulation is presented in the next section.

4.4 Cyclic Loading and Time-Recovery Effects on the Mechanical Response

Figure 4.12 presents the compressive cyclic nominal stress-strain response of 85-00-05, 85-15-05 and 85-30-07 specimens when loaded between the optimal strain levels selected in the previous section, i.e., 5%-9%, 8%-16% and 6%-9%, respectively. Figures 4.12a, 4.12c and 4.12e show the response during initial cyclic testing of virgin specimens, while Figures 4.12b, 4.12d and 4.12f show the response of the same specimens after a 4-week time-recovery or aging period. Nominal heights of the specimens measured before cyclic testing after the 4-week period were 26.05 ± 0.02 mm for 85-00-05, 26.95 ± 0.01 mm for 85-15-05, and 25.56 ± 0.01 mm for the 85-30-07 specimen. When compared with the nominal heights of the specimens in their virgin (untested) configuration (Tables 2, 3 and 4), a residual strain of $\sim$1% in 85-00-05, $\sim$1.57% in 85-15-05 and $\sim$2% in 85-30-07 specimen is identified after the recovery period.

Investigation of the mechanical response of the specimens suggested that all three formulations exhibited a response characterized by the following attributes: (1) highly nonlinear stress-strain response without a distinctive yield point, (2) hysteresis, and (3) cyclic stress softening with eventual stabilization, which was observed at the 20th cycle for all formulations. It is worth noting that for all compositions there are significant differences between the cyclic response before and after the time-recovery period. These differences can be quantified by the following parameters defined for a given cycle (see Figure 4.11):

1. Peak and valley stresses: the maximum $\sigma_{\max,i}$ and the minimum $\sigma_{\min,i}$ values of stress in the i^{th} $(i = 1, \ldots, 20)$ cycle. These stresses are related to the material strength.

2. Cumulative dissipated energy density: the difference between the energy supplied to the material (i.e.,the area under the loading path) and the energy recovered after a cycle (i.e., the area under the unloading path), accumulated throughout the cyclic loading. This energy quantifies cyclic hysteresis and accumulated damage in the material.

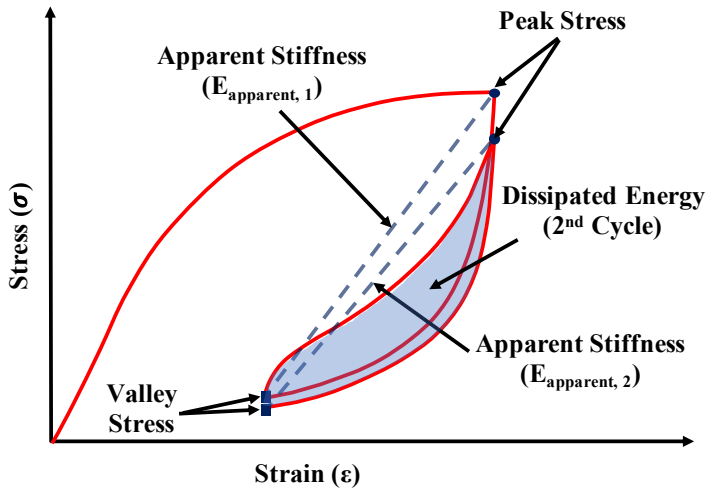

Figure 4.11. Schematic of a cyclic stress-strain curve (first two cycles shown) depicting peak and valley stresses, dissipated energy, and apparent stiffness.

3. Apparent stiffness: the slope of the line connecting peak and valley stresses in each cycle, i.e., for the i^{th} cycle, $E_{\text{apparent},i} = (\sigma_{\max,i} - \sigma_{\min,i})/(\epsilon_{\max,\text{cyclic}} - \epsilon_{\min,\text{cyclic}})$.

In the following sections, a thorough analysis of cyclic loading and time-recovery effects on the overall stress-strain response, damage, strength, and stiffness of mock energetic specimens is presented.

4.4.1 Effects on the overall Stress-Strain Response

It is interesting to note that in the cyclic stress-strain response of all specimen formulations, the first loading path of the virgin material is quite different from the subsequent reloading paths, including those recorded after the time-recovery period. Excluding the initial response (until about 3% strain) which is related to gradual mating of machine platen-specimen surface, the rate of strain hardening is observed to be decreasing with compression during the first loading path of the virgin material and increasing with compression during subsequent reloading. A similar observation has been made previously for cyclic compression of aluminized RDX-based PBX in HTPB binder (Tang et al., 2016), where the authors have described the initial loading response as *sharp oval* shaped, and the subsequent response as *crescent* shaped. This type of strain hardening has not been observed in other particle-

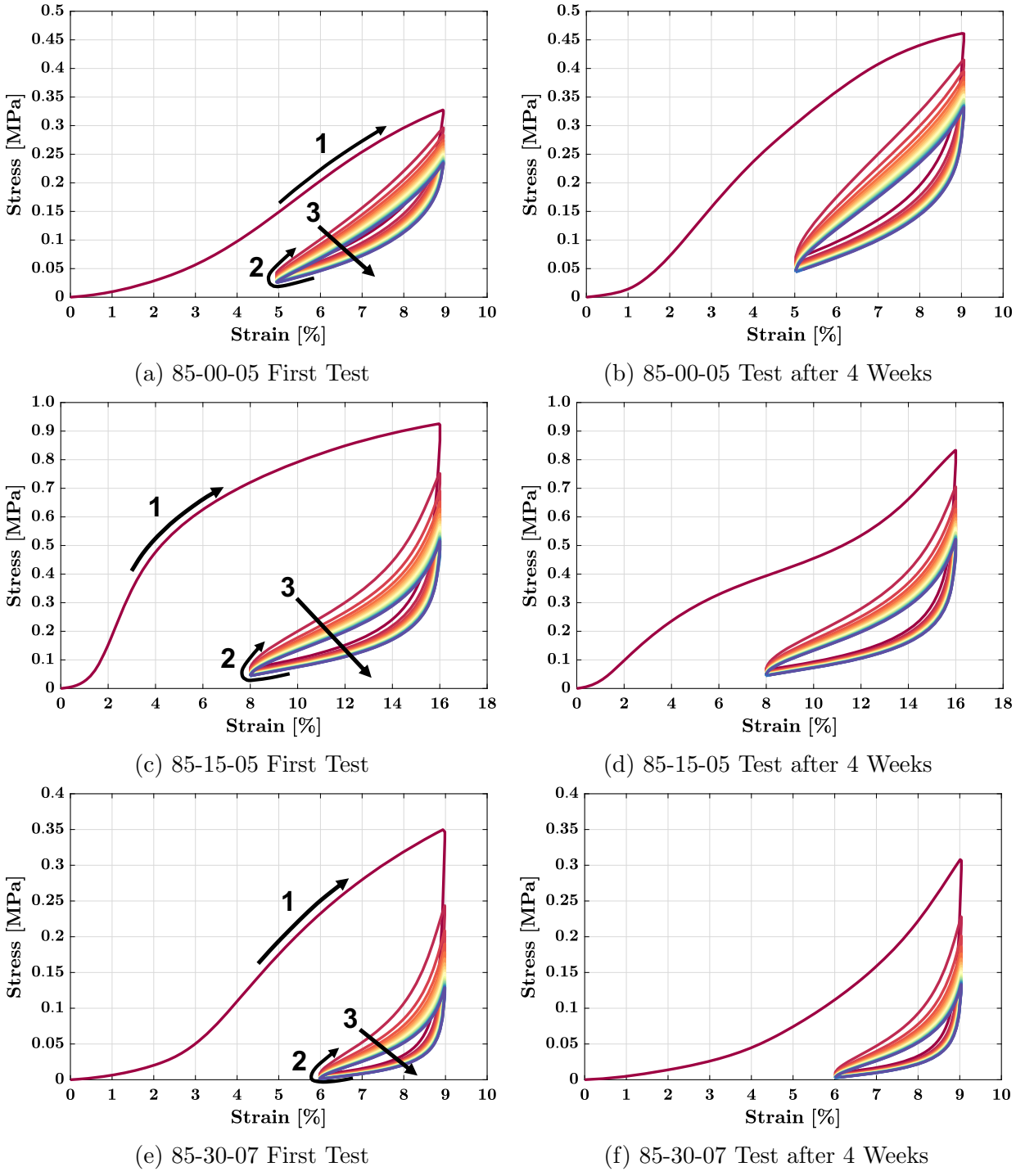

(a) 85-00-05 First Test

(b) 85-00-05 Test after 4 Weeks

(c) 85-15-05 First Test

(d) 85-15-05 Test after 4 Weeks

(e) 85-30-07 First Test

(f) 85-30-07 Test after 4 Weeks

Figure 4.12. Cyclic compressive stress-strain response of (a and b) 85-00-05, (c and d) 85-15-05 and (e and f) 85-30-07 specimens during initial testing and testing after 4 weeks. Observable response attributes include (1) highly nonlinear stress-strain response without a distinctive yield point, (2) hysteresis, and (3) cyclic stress softening with eventual stabilization (observed at the 20th cycle for all formulations).

binder composites such as filled elastomers (Bergström & Boyce, 1998; Miehe & Keck, 2000; Dargazany et al., 2014), where the initial loading response is similar to the response observed during subsequent reloading.

Another interesting observation is made regarding the effects of loading history and time-recovery on the first loading path of the aged material. For the 85-15 and 85-30 formulations, the first loading path of the aged specimen is similar in shape to both the loading response of the stabilized cycle before aging and to the subsequent reloading paths. However, for the 85-00 formulation, the shape of the first loading path of the aged specimen remains similar to the first loading path of the virgin material. This permanent change in the mechanical behavior of aluminized specimens may be attributed to the loading history memory effect observed in plastic or ductile (polycrystalline) materials (Jiang & Sehitoglu, 1994; Zhang & Jiang, 2004; Jiang & Zhang, 2008; Paul et al., 2011).

4.4.2 Effects on Damage, Strength and Stiffness

All three formulations show a nonlinear decline in peak and valley stresses (and thus in strength), and apparent stiffness with cyclic loading, for tests performed both before and after the time-recovery period (see Figures 4.13 and 4.14). The rate of decline, however, eventually reduces to zero and cyclic stabilization is observed after the 20th cycle. This weakening and softening of the material, also known as the Mullins effect, is attributed to the accumulation of damage. This accumulated damage is also evident from the evolution of cumulative dissipated energy (see Figures 4.14), and it is typically attributed to mesoscale physical processes such as bond rupture at polymer-filler interfaces (Blanchard & Parkinson, 1952), molecular slipping on the filler-particle surface (Houwink, 1956), filler aggregate rupture (Kraus et al., 1966), among others and so on (see, e.g., Diani et al. (2009) and references therein for a review of physical interpretations of the Mullins effect).

The effect of loading history and time-recovery on material behavior is evident for the 85-00 formulation. It shows a large increase in peak stress ($\sim$45%), valley stress ($\sim$66%) and apparent stiffness ($\sim$41%) consistently for all cycles, and a $\sim$100% increase in both the value of energy dissipation during the first cycle and its rate of accumulation during subsequent

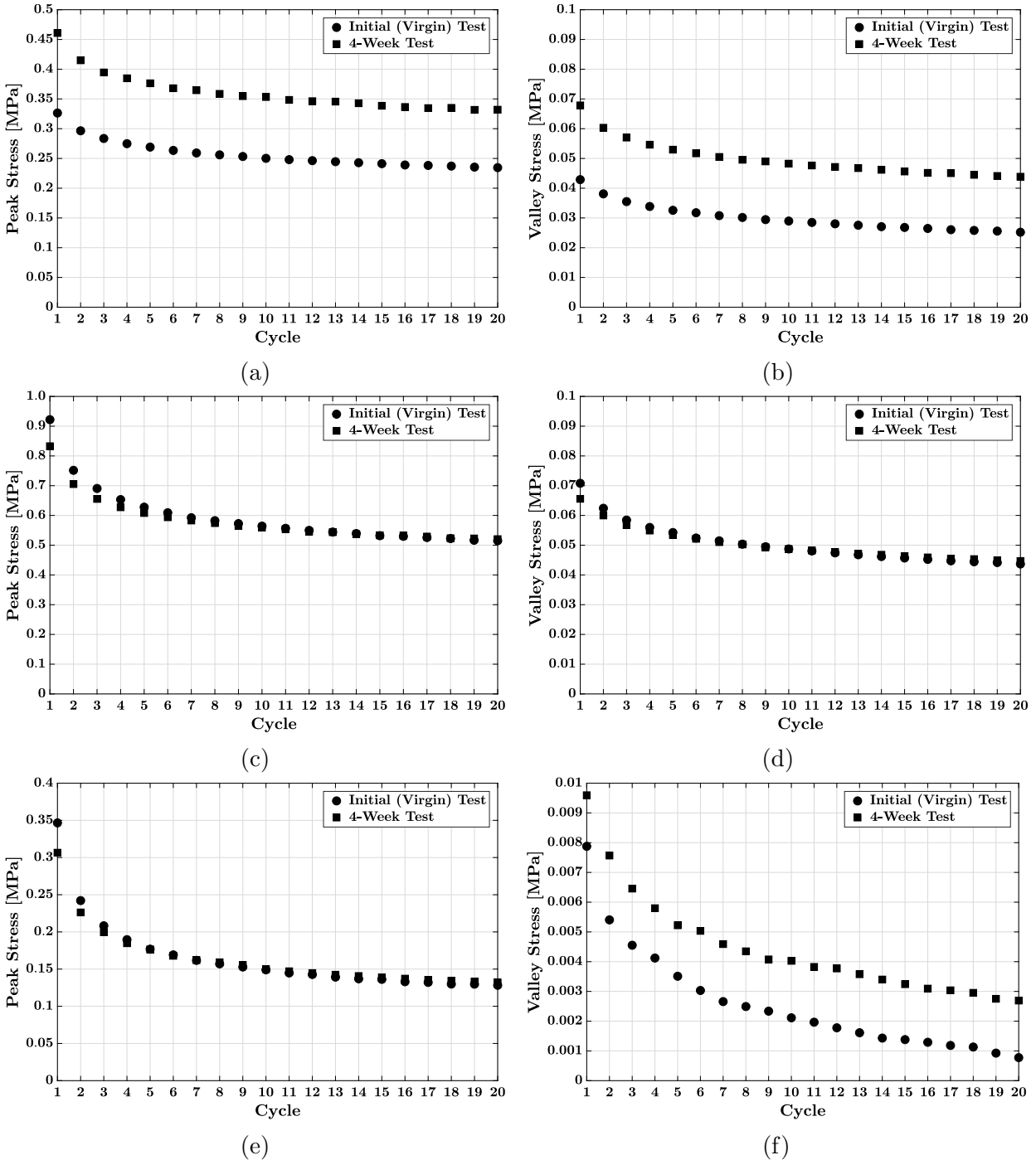

Figure 4.13. Plots depicting evolution of peak and valley stresses with cyclic loading of (a and b) 85-00-05, (c and d) 85-15-05 and (e and f) 85-30-07 specimens. Round data points indicate peak and valley stress values obtained during initial (virgin) testing, while square data points indicate values obtained during testing after 4 weeks.

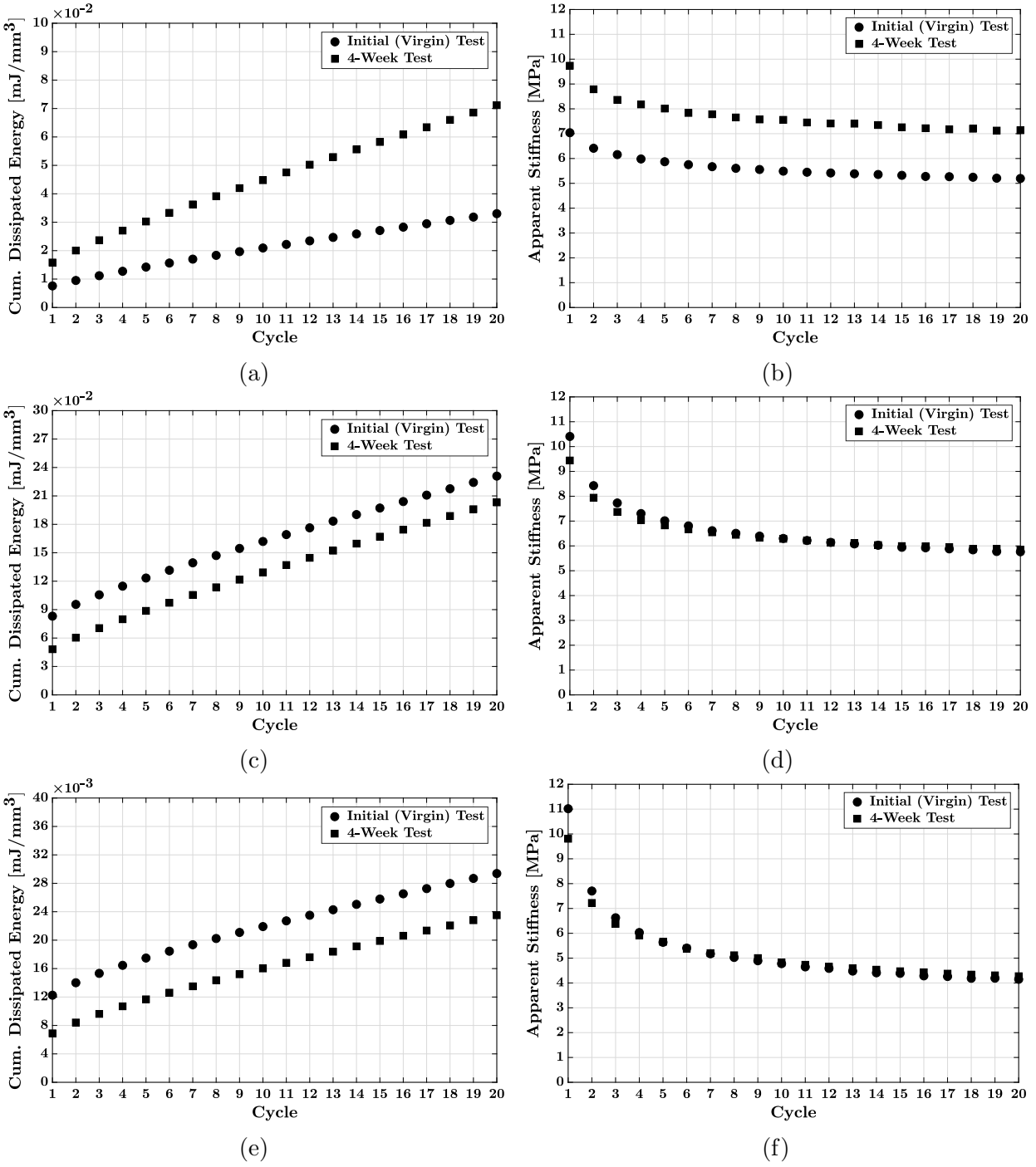

Figure 4.14. Plots depicting evolution of cumulative dissipated energy and apparent material stiffness with cyclic loading of (a and b) 85-00-05, (c and d) 85-15-05 and (e and f) 85-30-07 specimens. Round data points indicate energy and stiffness values obtained during initial (virgin) testing, while square data points indicate values obtained during testing after 4 weeks.

cycles. In contrast, aluminized formulations (i.e., 85-15 and 85-30) show a small reduction in peak stress and apparent stiffness during the initial 4-5 cycles after the time-recovery period. The 85-15 specimen also shows a small reduction in valley stress, which is consistent with observations of other values. However, the 85-30 specimen shows a consistent increase in valley stress, although the values may be too small to be captured accurately due to limitations of the load cell. Interestingly, the rates of energy dissipation before and after aging are the same, but the values are offset by a significant drop ($\sim$58% for 85-15 and $\sim$56% for 85-30) observed in the first cycle after the time-recovery period.

The observation of stiffening and strengthening of the 85-00 formulation is consistent with the proposition of an increase in sucrose particle-particle interactions during the initial loading of the virgin material. Formation of inter-particle force chains has been previously observed during high strain-rate compression of polymer-bonded sugar with high solids loading (>80%) (Ravindran et al., 2019), and during quasi-static compression of metal-matrix composites (Liu et al., 2014a). Specifically, it is argued that the force network within the filler particles is the main load-bearing mechanism under compression, while the binder matrix has a bulk effect on load transfer and a confining effect on the initial relative movement of filler particles (Liu et al., 2014a; Topin et al., 2007). Furthermore, if particle-binder interfacial debonding occurred at moderate to large deformations, then radial displacement of the soft polymer matrix would follow and, in turn, inter-particle interactions would be facilitated. Even if binder rearrangement was partially reversed during the time-recovery period, the increased proximity of the sucrose particles, as compared to the virgin material, would result in an apparent increase in load-bearing capacity due to a more densely packed solid phase. In sharp contrast, large ductile plastic flow and higher irrecoverable damage are observed for formulations with aluminum micro-sized powder, i.e., for the 85-15 and 85-30 formulations. As it was noted above, a stiffer force network is formed due to sucrose-aluminum-sucrose interactions, which results in higher material strength, but plastic irreversible deformation occurs during cyclic loading, which results in a lack of recovery during the aging period.

4.5 Identification of the Spatial Distribution of Formulation Components at the Meso-scale

A systematic procedure for identifying the spatial distribution of the primary components of each formulation, including pore space, from micro-CT scans was developed. To this end, the volumetric CT data was first reconstructed using NRecon (Bruker micro-CT) software to obtain multiple cross-sectional 8-bit gray-scale images along the length of the scanned portion of the specimen. A total of 1092 volumetric image slices (each image of 10 μm height, constituting the total scanned height of 10.92 mm) were obtained. To avoid low-quality images at the top and bottom edges due to cone-beam imaging geometry (Scarfe & Farman, 2008) of the Bruker micro-CT instrument, 68 image slices from the top and 70 image slices from the bottom were discarded; these values were recommended by the software. The effective analyzed height was then equal to 9.54 mm. The images were produced by attributing a gray value from 0-255 to each pixel depending upon its attenuation coefficient, which in turn depends on the material density. Figure 4.15 shows a schematic of the histogram of attenuation coefficient values obtained from the middle cross-section of the 85-15 specimen. From the histogram, a range of attenuation values is chosen which is mapped to the gray-scale. Limits of this range, also known as contrast limits, were chosen as follows: the lower limit was selected as 0, which is the first peak in the histogram corresponding to air, while the higher limit was selected as 4%-5% more than the maximum attenuation (density) observed in the histogram to assure complete visualization of all the material within the specimen.

In addition to choosing the contrast limits, corrections were applied to the gray-scale images to reduce the effect of tomography artifacts like beam hardening and ring artifacts, while Gaussian smoothing (Shapiro & Stockman, 2001) was applied to reduce image noise. Since these values affect the fundamental gray distribution of the images, they need to be the same for multiple scans of the same specimen for accurate qualitative and quantitative comparisons.

The gray-scale images were then further analyzed in the CT-analyzer (Bruker micro-CT) software, which is capable of performing a wide range of morphometric analyses on

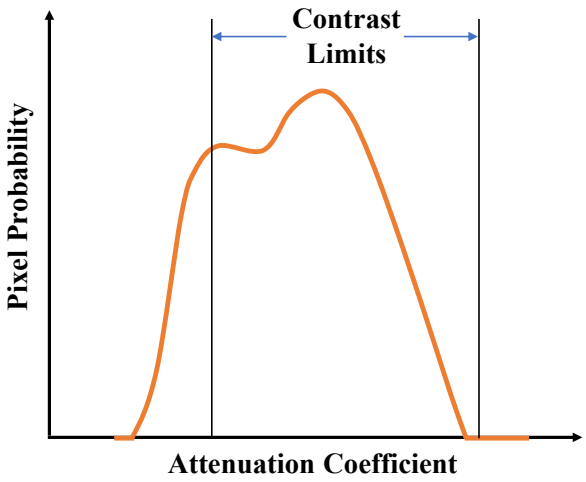

Figure 4.15. Schematic of the log-scaled histogram of the middle cross-section of the 85-15-05 specimen with respect to the attenuation coefficient of image pixels.

reconstructed scan datasets. A major function of the tool is thresholding, which is the binarization of a gray-scale image so that a certain range of gray values are assigned the value 0 (black), while the rest of the gray values are assigned the value 1 (white). Using thresholding, it is possible to distinguish materials of different densities (gray values) in the scanned image. However, automatic thresholding algorithms in CT-analyzer are at most capable of segmenting two-component material systems. Furthermore, due to partial volume effects in CT images (Wellington & Vinegar, 1987) and extensive mixing of different materials in particle-binder composites, distinct peaks corresponding to different materials are not observed in the gray-scale histogram of mock specimens, making segmentation of multiple components and porosity solely from the gray-scale histogram infeasible.

It bears emphasis that the porosity of the specimen and the volume fraction of its primary components, i.e., binder, sucrose and aluminum can be analytically computed from the measurement of specimen's weight and volume, since mass fractions and densities (binder: 0.907 g/cc, sucrose: 1.59 g/cc, aluminum: 2.7 g/cc) of the components are known. While weight could be easily measured with good accuracy using a balance, the volume was best approximated using a combination of CT-analyzer tools and physical measurements. A useful feature of the software is the ability to wrap the boundary of the Volume of Interest (VOI) tightly around the boundary of the specimen. Figure 4.16 shows the Region of Interest

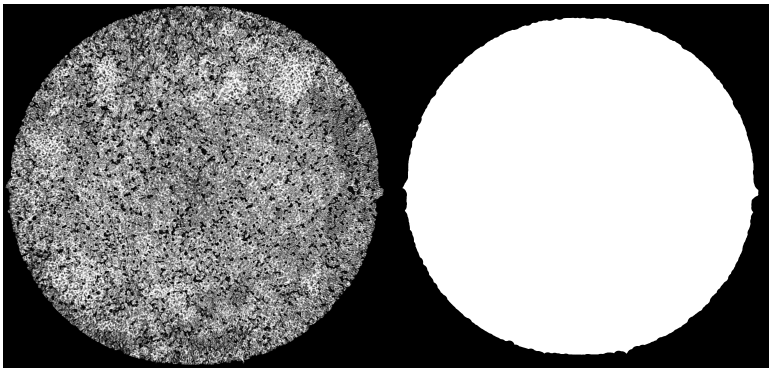

Figure 4.16. A cross-sectional image slice of the 85-15-05 specimen in gray-scale, and its corresponding ROI obtained using the "Shrink Wrap" feature available in Bruker CT-analyzer.

(ROI) obtained using this "Shrink Wrap" feature for a cross-sectional image slice of the 85-15-05 specimen. The VOI was then constructed from ROIs created along the entire length of the scanned portion, and its volume (V_{VOI}) was computed by CT-analyzer's 3D morphometric analysis tool. Volume of the entire specimen (V) was then approximated as $V = V_{\mathrm{VOI}}(h/h_{\mathrm{VOI}})$, where h is the measured specimen height and $h_{\mathrm{VOI}} = 9.54$ mm.

Once specimen porosity and volume fractions of its components were known, gray-scale ranges corresponding to the measured values were obtained from the 3D voxel gray-scale histogram available from CT-analyzer. Figure 4.17 shows representative gray-scale ranges

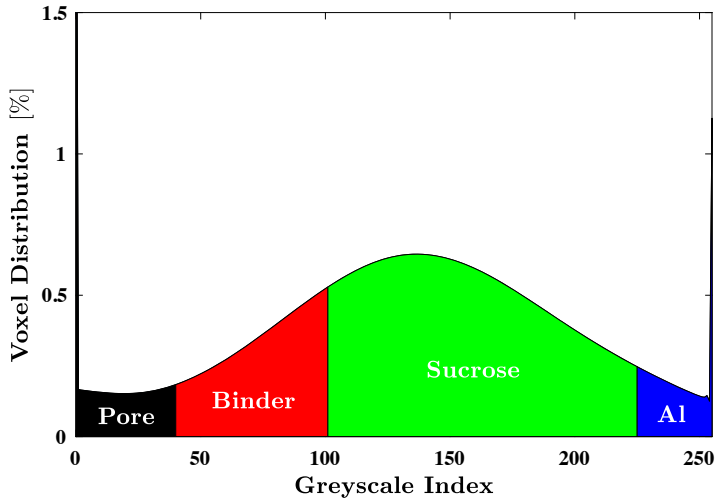

Figure 4.17. 3D voxel histogram of the 85-15-05 specimen showing representative gray-scale ranges for each specimen component.

Table 4.7. Measurements of weight, volume and comparison of measured porosity and volume fractions (VF) with values obtained from CT-analayzer voxel histogram for the three mock energetic specimens. The identified thresholding ranges are provided for reference.

Specimen	**Weight (g)**	**Volume (cm^3)**	**Component**	**Measured VF (%)**	**CT-analyzer VF (%)**	**Thresholding Range**
85-00-05	15.7524	13.6560	Porosity	19.2480	19.4842	0-33
			Binder	19.0790	19.0703	34-95
			Sucrose	61.6729	61.4454	96-255
85-15-05	18.9840	13.9674	Porosity	9.3428	9.4371	0-24
			Binder	22.4780	22.3999	25-96
			Sucrose	61.7609	61.6016	97-244
			Aluminum	6.4183	6.5614	245-255
85-30-07	20.0892	13.5762	Porosity	6.1790	6.2632	0-17
			Binder	24.4719	24.4512	18-93
			Sucrose	55.3738	55.3135	94-216
			Aluminum	13.9753	13.9721	217-255

in the 3D voxel histogram of the 85-15 specimen, arranged in the order of increasing density of components (porosity < binder < sucrose < aluminum). Table 4.7 provides weight and volume measurements, and it compares the porosity and volume fraction of each component obtained from the true density of the specimen and the CT-analyzer voxel histogram. The table also reports the threshold gray-scale ranges identified in the analysis.

Finally, the obtained gray-scale ranges were used to binarize the gray-scale images into four sets of binary images, each containing voxels representing an individual component. These binary image sets were then color-coded in MATLAB®, Version 9.4.0 (2018a), assigning a specific color to each component (porosity-black, HTPB-red, sucrose-green and aluminum-blue), and combined to obtain a single set of color-coded slices. Figure 4.18 shows a schematic of the described post-processing procedure for the identification of individual specimen components and their spatial distribution. Additionally, Figure 4.19 provides 3D rendered volume images of the gray-scale and the color-coded representations of the microstructure of each formulation.

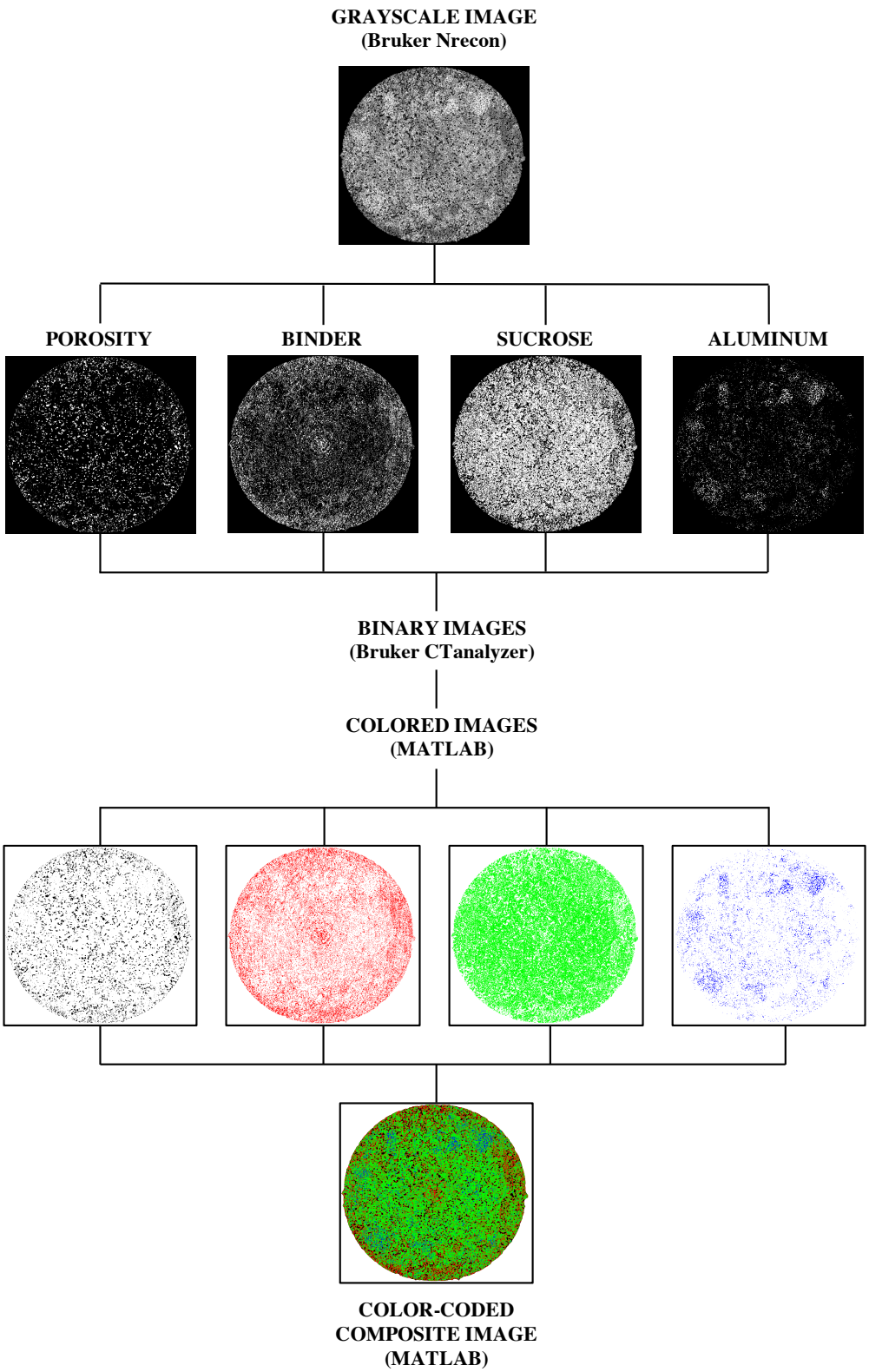

Figure 4.18. A schematic of the postprocessing procedure of micro-CT scans to reconstruct the microstructure of the specimen and the spatial distribution of its individual components.

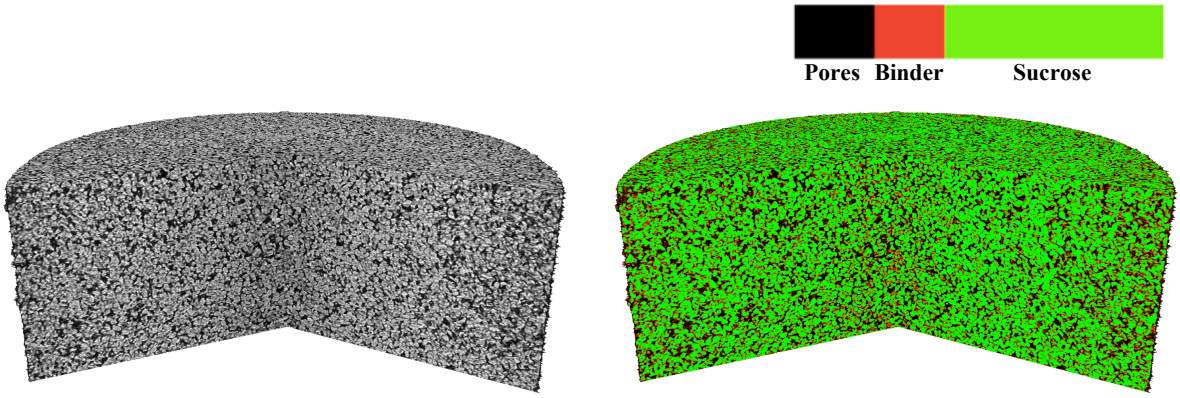

(a)

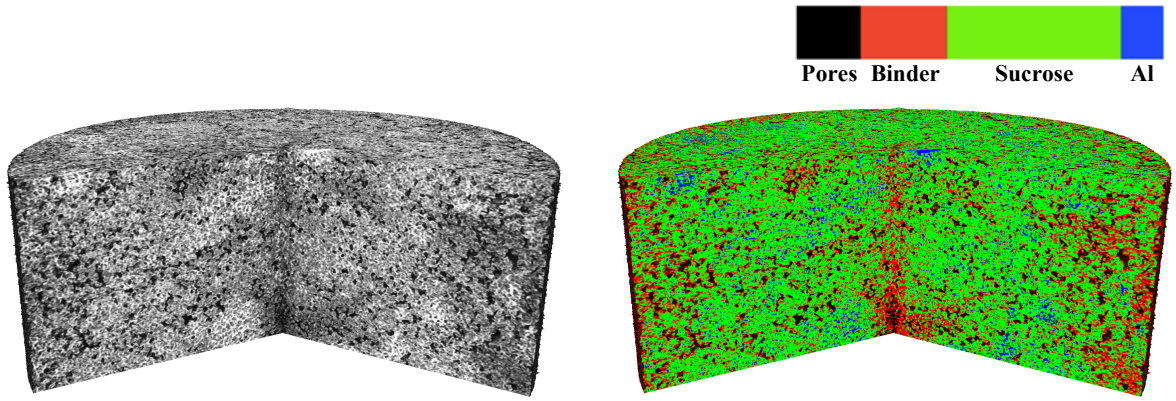

(b)

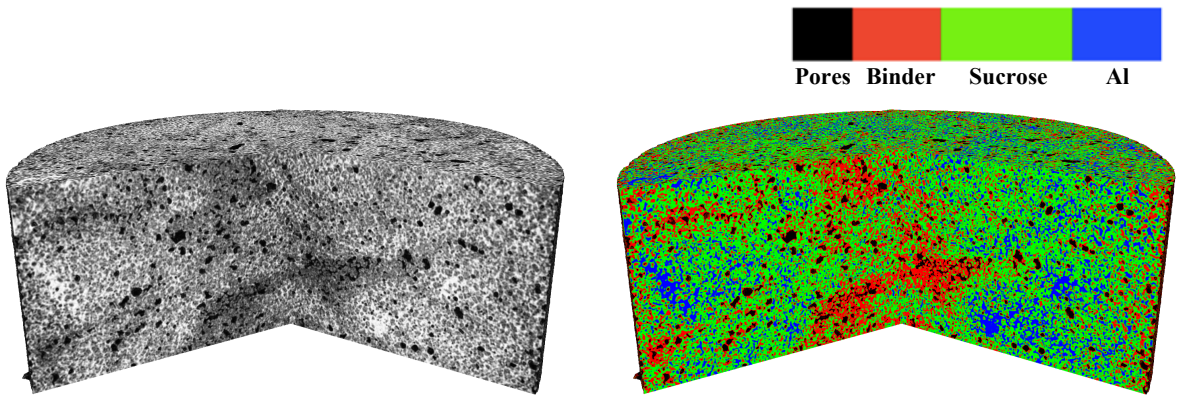

(c)

Figure 4.19. 3D rendered gray-scale and color-coded volume images of (a) 85-00-05, (b) 85-15-05 and (c) 85-30-07 mock specimens, obtained from Bruker CTvox software The color bars provide the color-code for each component, as well as a representative measure of their volume fraction.

4.6 Cyclic loading and Time-Recovery Effects on the Microstructure

In previous sections, it has been established that cyclic loading and time-recovery introduce evident and permanent changes in the macroscopic mechanical response of mock energetic materials. This behavior is attributed to mesoscale deformation and relaxation mechanisms that emerge from the presence of a hard phase (sucrose) and a soft phase (binder) in the microstructure. The soft phase becomes progressively more compliant due to accumulated damage and particle-binder interfacial debonding. It undergoes homogeneous or *affine deformation* under compressive load, it recovers during unloading, and it relaxes over time. In sharp contrast, the hard phase experiences a collective rearrangement or *non-affine deformation* under compressive loading, and it only partially recovers during unloading and over time due to the irreversible nature of this collective rearrangement. The presence of a ductile third phase (aluminum) may significantly affect these mesoscale deformation and relaxation mechanisms by forming permanent sucrose-aluminum contacts and reducing the sucrose-binder interfacial area—i.e., by arresting interfacial debonding and thus effectively stiffening the soft phase.

In this section, the proposed mesoscale deformation and relaxation mechanisms are investigated by characterizing changes in the spatial distribution of the primary components of each formulation, including pore space, before and after each cyclic test and, thus, before and after the time-recovery or aging period.

The spatial volume distribution of components in a formulation is determined from the three-dimensional color-coded micro-CT volume images (see Figure 4.19) using MATLAB®, Version 9.4.0 (2018a). Distributions in the radial direction are of primary interest, and thus the VOI is first segmented into three equal discs along its height, next into 20 angular sectors of equal volume and, lastly, into 20 radial rings (see Figure 4.20). The proposed tessellation is such that the volume of the resulting elements increases linearly with radial distance, from 0.179 mm^3 at $r = 0.6$ mm to 7.013 mm^3 at $r = 12$ mm—radial distances beyond 12 mm are excluded from the analysis to eliminate any inconsistencies that may result from imperfections in the specimen geometry. The volume fraction of sucrose, binder, aluminum and pore space within each tessellated volume, and the mean and standard deviation values

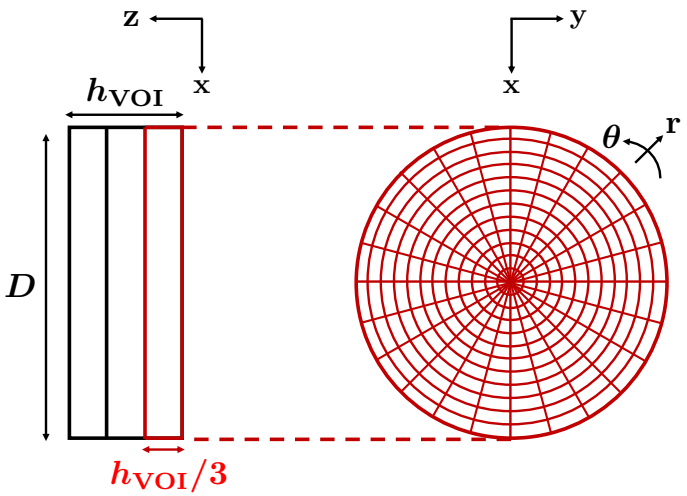

Figure 4.20. A schematic of the segmentation procedure of the volume image obtained from micro-CT into a set of elements for studying changes in volume distribution of the specimen components along the specimen's radius.

along the angular direction, are then readily available and compared for scans taken before and after virgin material testing and testing after 4 weeks in Figures 4.23-4.25, 4.26-4.29 and 4.30-4.33 for specimens 85-00-05, 85-15-05 and 85-30-07 respectively. In the figures, plots are depicted for each segmented disc (top, middle and bottom), with the volume fraction plotted against radial position, and standard deviation along the angular direction plotted as error bars. For additional qualitative comparison of microstructural changes, color-coded axial cross-sections of the specimens are provided in Figures 4.21 and 4.22. It is evident from these figures that the majority of the volumetric changes are observed near the core or center of the specimen. This observation is consistent with *in-situ* micro-CT studies in polymer-bonded sugar under quasi-static uniaxial monotonic compression (Hu et al., 2015, 2016) which show that accumulation of damage, in the form of debonding, starts from the core region and then propagates to the outer region. A detailed characterization of each formulation is presented next.

The 85-00 formulation shows an increase in the volume fraction of sucrose, and a reduction in that of binder and porosity, near the core upon the first cyclic loading test (see Figures 4.21a and 4.21b; circle (black) and square (blue) plots in Figures 4.23-4.25). This behavior is consistent with an *affine* radial deformation of the soft and debonded binder as it is compressed by stiffer sucrose crystals, and conversely, a *non-affine* longitudinal motion of

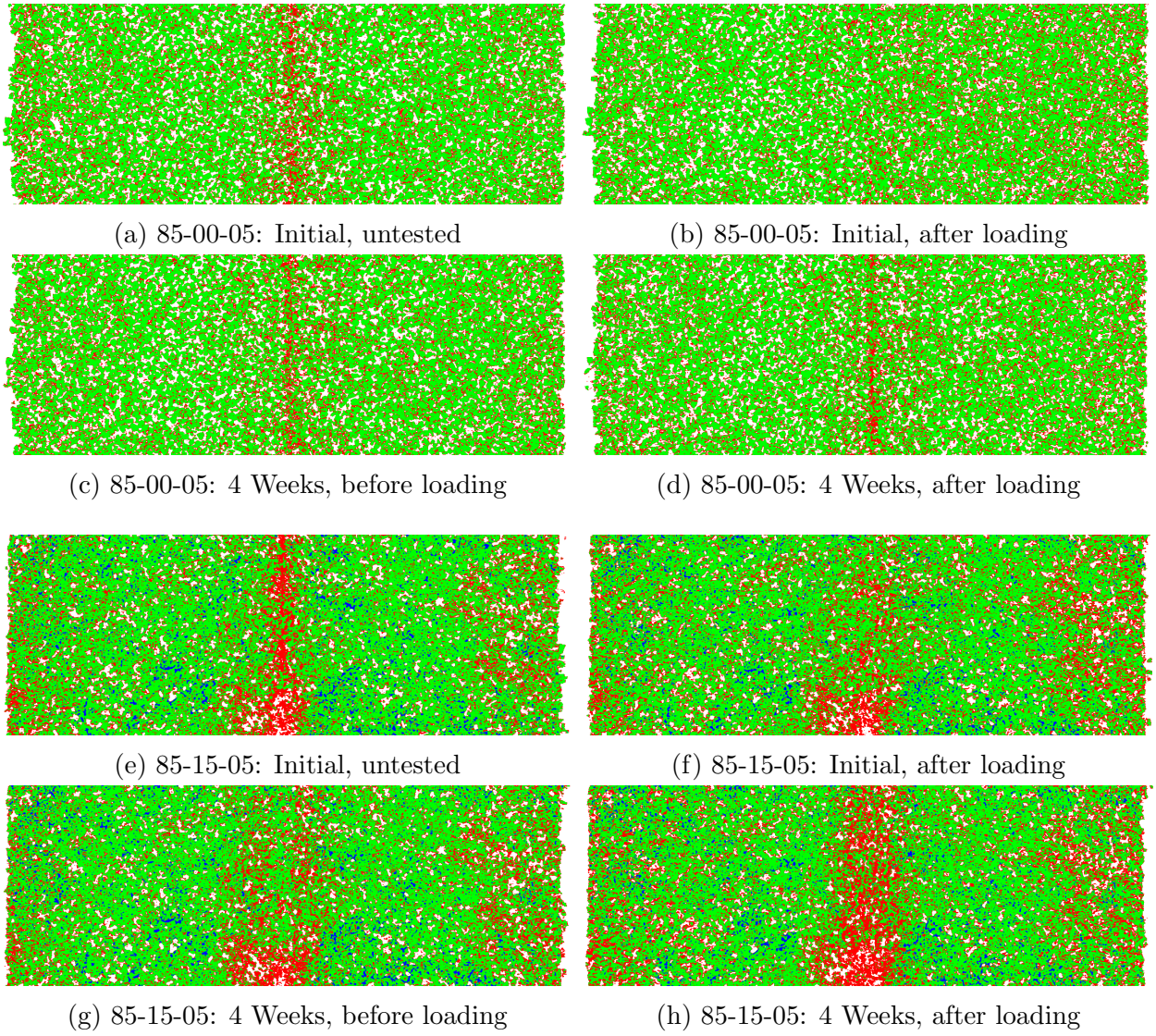

(a) 85-00-05: Initial, untested

(b) 85-00-05: Initial, after loading

(c) 85-00-05: 4 Weeks, before loading

(d) 85-00-05: 4 Weeks, after loading

(e) 85-15-05: Initial, untested

(f) 85-15-05: Initial, after loading

(g) 85-15-05: 4 Weeks, before loading

(h) 85-15-05: 4 Weeks, after loading

Figure 4.21. Central cross-sectional images along the height (z) of the spatial distribution of specimen components in the 85-00-05 (a, b, c and d) and 85-15-05 (e, f, g and h) specimens, shown for scans taken before and after virgin material testing and testing after 4 weeks. In the images, white indicates Porosity, green indicates Sucrose, red indicates Binder, while blue indicates Aluminum.

the sucrose crystals to form a denser contact network. Furthermore, this formulation exhibits a partial reversal of such microstructural rearrangement during the 4-week time-recovery or aging period (see Figures 4.21b and 4.21c; square (blue) and triangle (red) plots in Figures 4.23-4.25). This reversal or recovery is facilitated by a relaxation over time of residual strains in the binder. Finally, the second cyclic test reveals trends of binder displacement similar

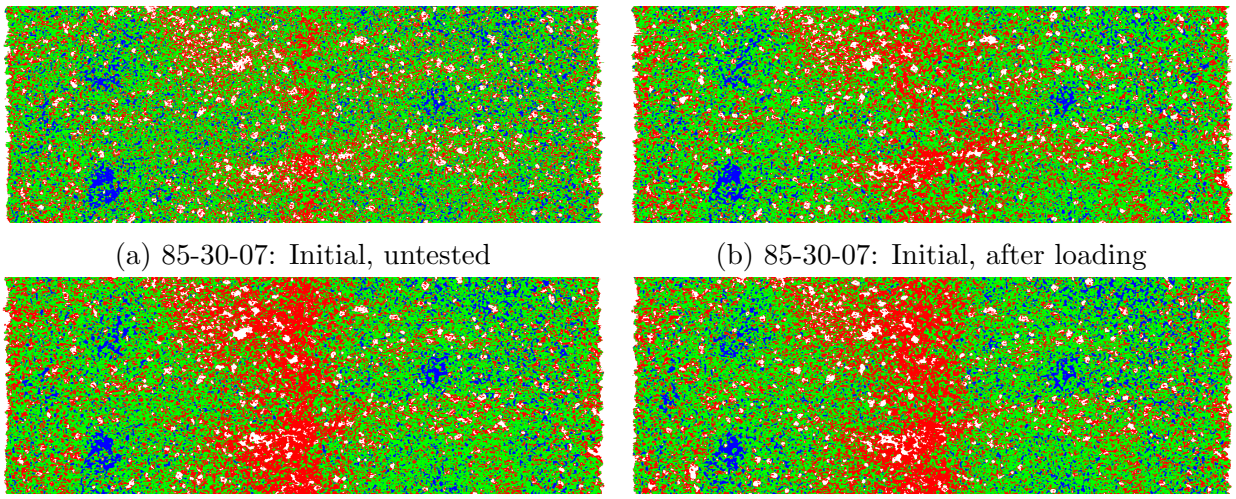

(a) 85-30-07: Initial, untested

(b) 85-30-07: Initial, after loading

(c) 85-30-07: 4 Weeks, before loading

(d) 85-30-07: 4 Weeks, after loading

Figure 4.22. Central cross-sectional images along the height (z) of the spatial distribution of specimen components in the 85-30-07 specimen, shown for scans taken before and after virgin material testing and testing after 4 weeks. In the images, white indicates Porosity, green indicates Sucrose, red indicates Binder, while blue indicates Aluminum.

to those observed during the first test but extended over a larger region, i.e., it indicates gradual propagation of damage away from the core (Chen et al., 2017) (see Figures 4.21c and 4.21d; triangle (red) and diamond (brown) plots in Figures 4.23-4.25).

In the 85-15 formulation (see Figures 4.21e and 4.21f, and Figures 4.26-4.29), the spatial distribution of specimen components is highly inhomogeneous, as observed in the radial and longitudinal distributions of sucrose and binder, and the angular distribution of aluminum and porosity. However, the average microstructural rearrangement during the first cyclic test is observed to be similar to the 85-00 formulation. Although, compared to 85-00, the increase in volume fraction of sucrose and the reduction in volume fraction of binder and porosity are observed much closer to the specimen core. This observation indicates an influence of the aluminum particles on the microstructure evolution. By forming additional contacts with sucrose, aluminum particles tend to reduce the sucrose-binder interfacial area and resist particle-binder debonding, thereby reducing the compliance of the binder. The effects of these contact interactions are observed prominently following partial recovery, where the deformation mechanisms of binder and sucrose are completely reversed during the 4-week cyclic test (see Figures 4.21g and 4.21h; triangle (red) and diamond (brown) plots in Figures

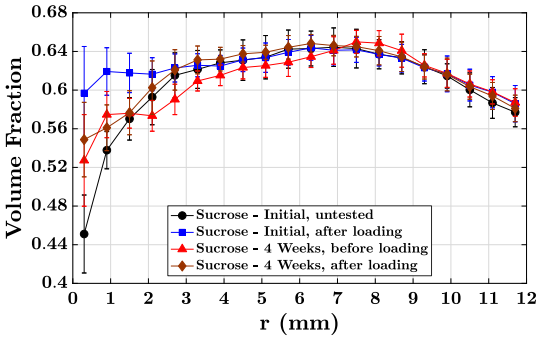

(a) 85-00-05: Sucrose (Top disc)

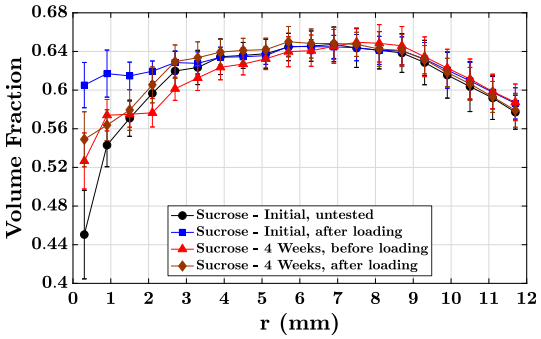

(b) 85-00-05: Sucrose (Middle disc)

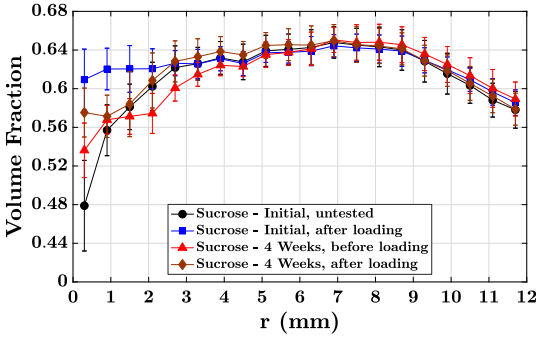

(c) 85-00-05: Sucrose (Bottom disc)

Figure 4.23. Comparison of the volume distribution of sucrose in the 85-00-05 specimen.

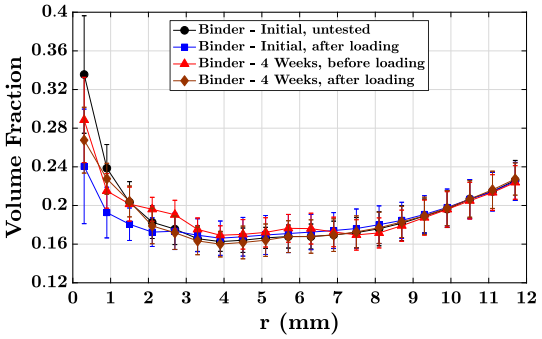

(a) 85-00-05: Binder (Top disc)

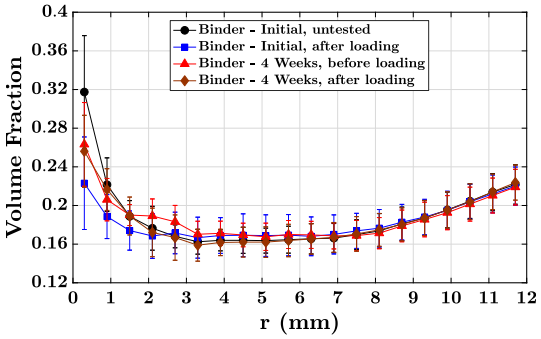

(b) 85-00-05: Binder (Middle disc)

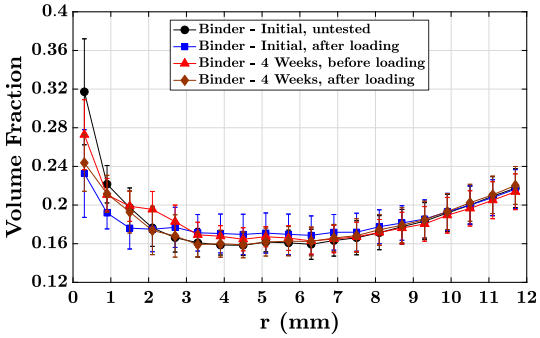

(c) 85-00-05: Binder (Bottom disc)

Figure 4.24. Comparison of the volume distribution of binder in the 85-00-05 specimen.

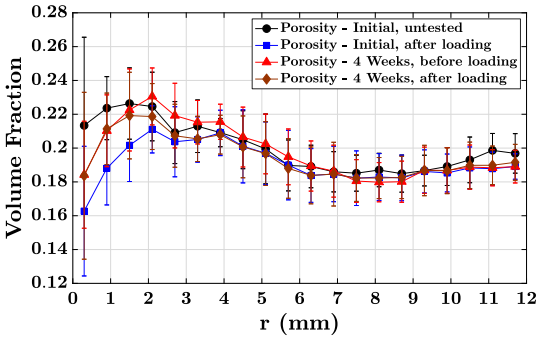

(a) 85-00-05: Porosity (Top disc)

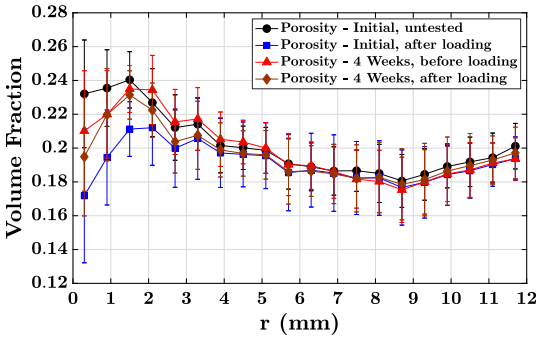

(b) 85-00-05: Porosity (Middle disc)

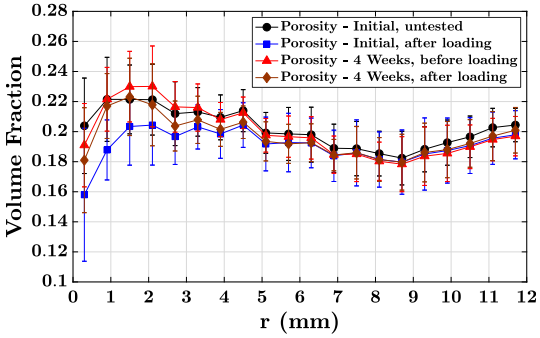

(c) 85-00-05: Porosity (Bottom disc)

Figure 4.25. Comparison of the volume distribution of porosity in the 85-00-05 specimen.

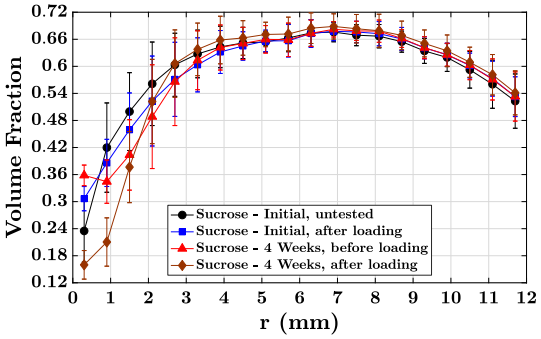

(a) 85-15-05: Sucrose (Top disc)

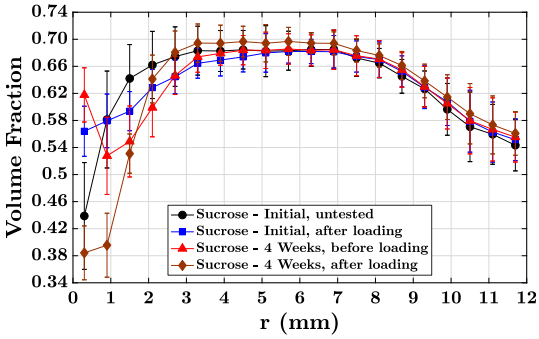

(b) 85-15-05: Sucrose (Middle disc)

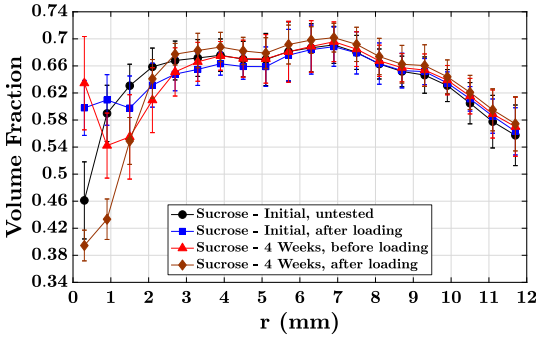

(c) 85-15-05: Sucrose (Bottom disc)

Figure 4.26. Comparison of the volume distribution of sucrose in the 85-15-05 specimen.

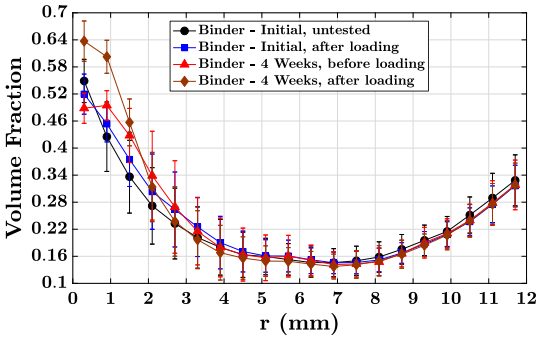

(a) 85-15-05: Binder (Top disc)

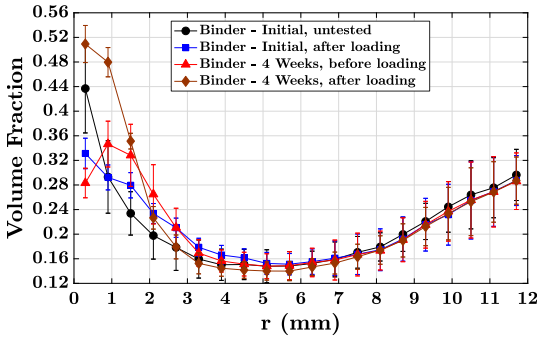

(b) 85-15-05: Binder (Middle disc)

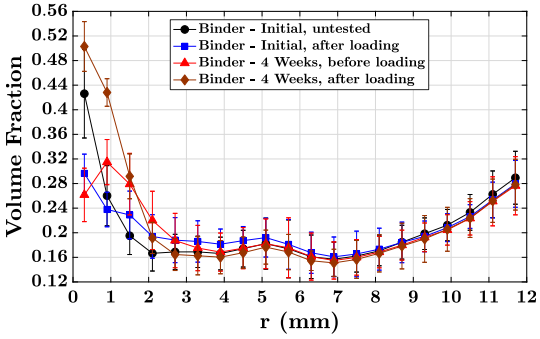

(c) 85-15-05: Binder (Bottom disc)

Figure 4.27. Comparison of the volume distribution of binder in the 85-15-05 specimen.

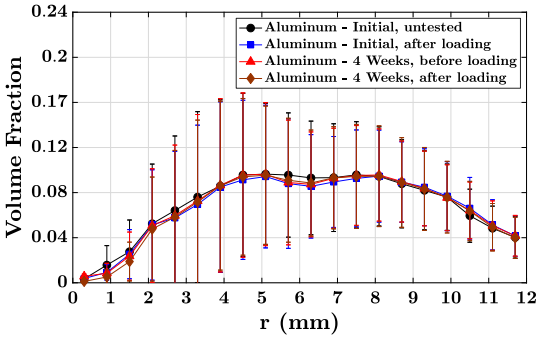

(a) 85-15-05: Aluminum (Top disc)

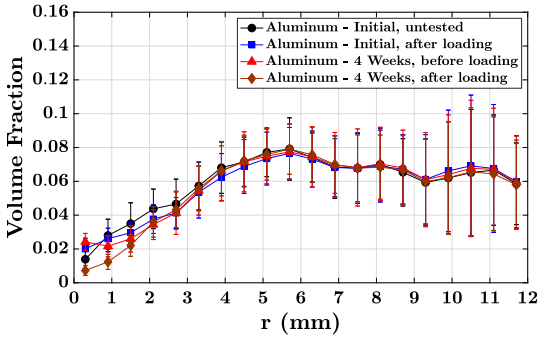

(b) 85-15-05: Aluminum (Middle disc)

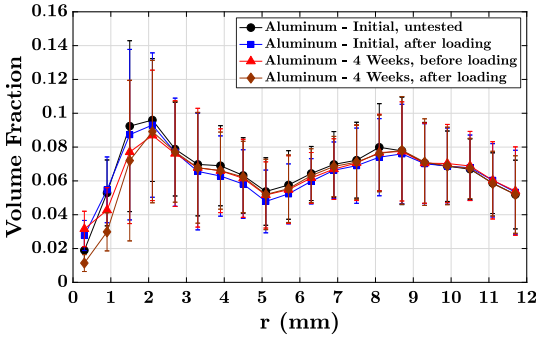

(c) 85-15-05: Aluminum (Bottom disc)

Figure 4.28. Comparison of the volume distribution of Aluminum in the 85-15-05 specimen.

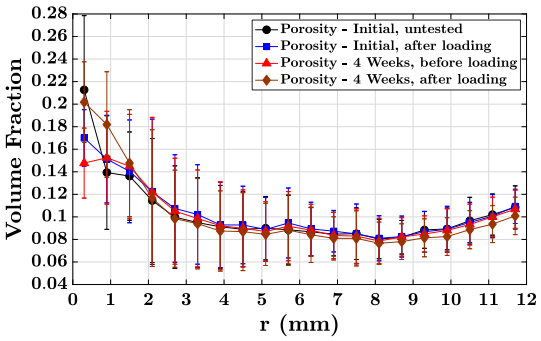

(a) 85-15-05: Porosity (Top disc)

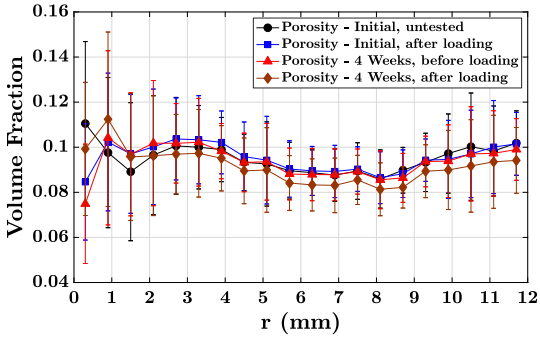

(b) 85-15-05: Porosity (Middle disc)

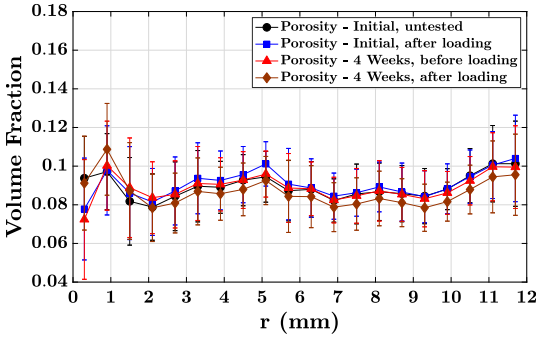

(c) 85-15-05: Porosity (Bottom disc)

Figure 4.29. Comparison of the volume distribution of porosity in the 85-15-05 specimen.

4.26-4.29). It is observed that the volume fraction of sucrose decreases near the core, while the volume fraction of the binder increases. This is the indication of an *affine* radial motion of the sucrose crystals away from the specimen core, and a *non-affine* rearrangement of the binder towards the core. A similar crystal motion has been observed previously by Manner and co-workers during *in-situ* micro-CT analysis of the uniaxial compression of a PBX formulation (ref. Manner et al. (2017) for more info on the formulation and the compression study) that undergoes ductile macroscopic plastic deformation.

In the highly aluminized 85-30 formulation (see Figures 4.22a and 4.22b; circle (black) and square (blue) plots in Figures 4.30-4.33), the prominent effects of aluminum-sucrose interactions are apparent from the first cyclic test itself, where *affine* motion of the sucrose crystals and aluminum particles (clearly observable in Figures 4.32a, 4.32b and 4.32c due to higher aluminum content) away from the specimen core, and *non-affine* rearrangement of the binder towards the core are observed. The same microstructural rearrangement continues

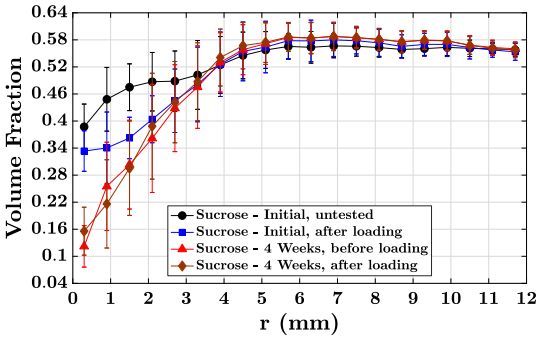

(a) 85-30-07: Sucrose (Top disc)

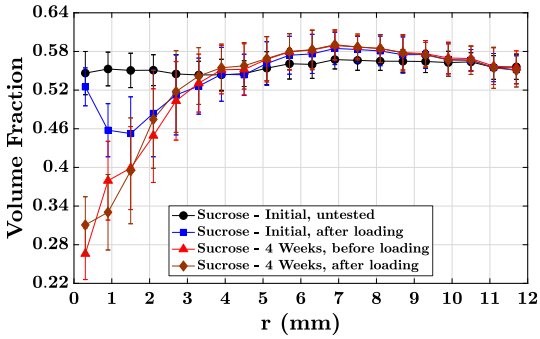

(b) 85-30-07: Sucrose (Middle disc)

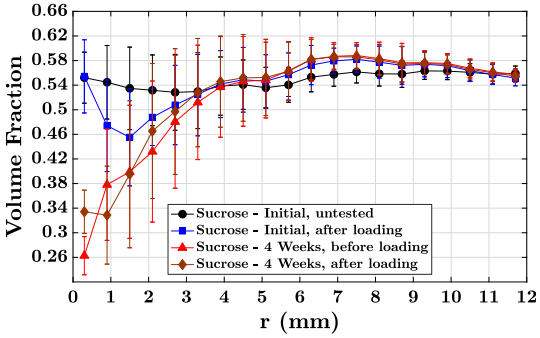

(c) 85-30-07: Sucrose (Bottom disc)

Figure 4.30. Comparison of the volume distribution of sucrose in the 85-30-07 specimen.

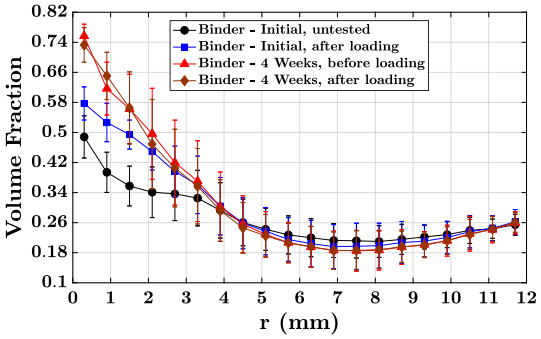

(a) 85-30-07: Binder (Top disc)

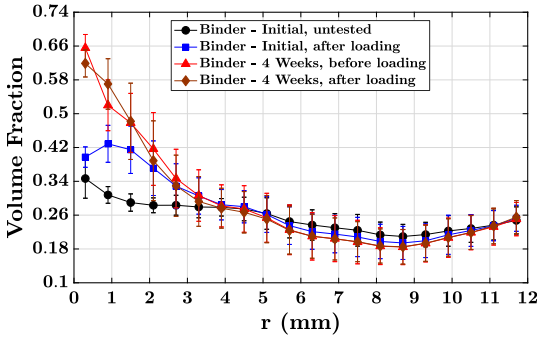

(b) 85-30-07: Binder (Middle disc)

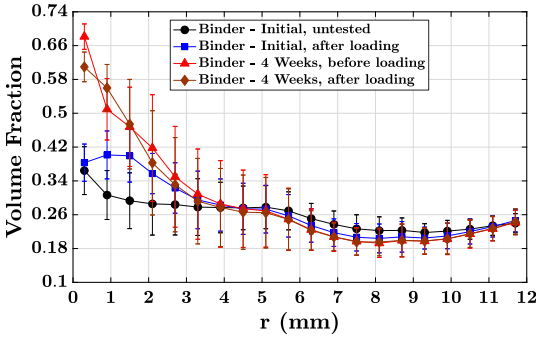

(c) 85-30-07: Binder (Bottom disc)

Figure 4.31. Comparison of the volume distribution of binder in the 85-30-07 specimen.

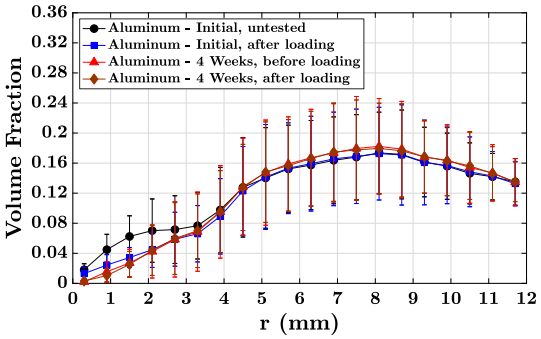

(a) 85-30-07: Aluminum (Top disc)

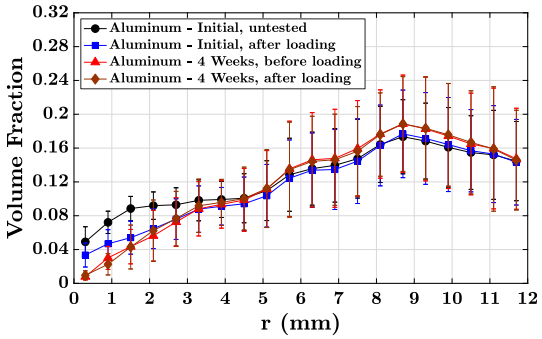

(b) 85-30-07: Aluminum (Middle disc)

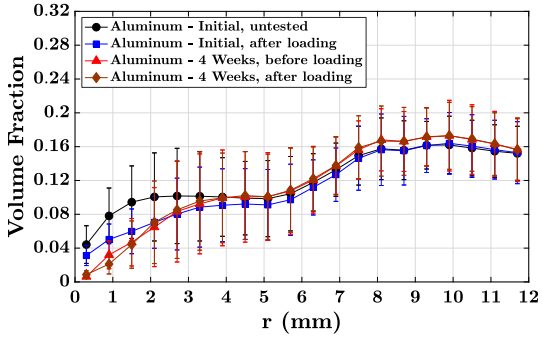

(c) 85-30-07: Aluminum (Bottom disc)

Figure 4.32. Comparison of the volume distribution of Aluminum in the 85-30-07 specimen.

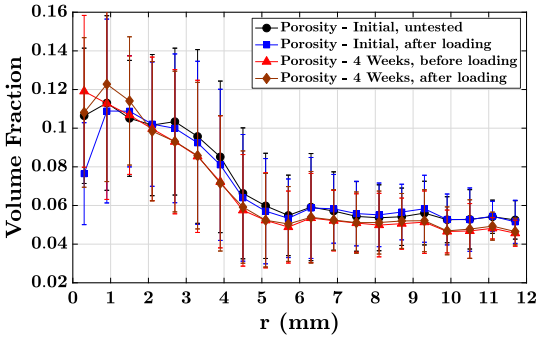

(a) 85-30-07: Porosity (Top disc)

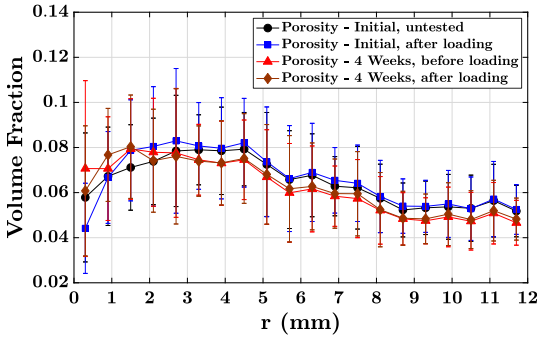

(b) 85-30-07: Porosity (Middle disc)

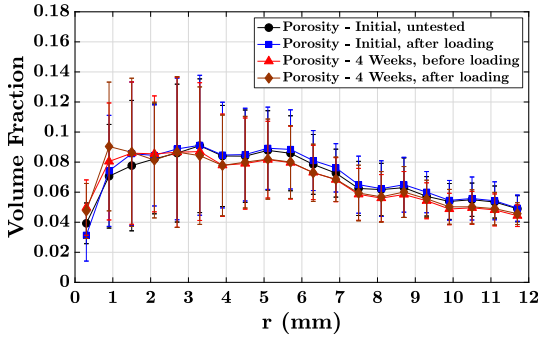

(c) 85-30-07: Porosity (Bottom disc)

Figure 4.33. Comparison of the volume distribution of porosity in the 85-30-07 specimen.

during the recovery period and during the 4-week cyclic test (see Figures 4.22c and 4.22d; triangle (red) and diamond (brown) plots in Figures 4.30-4.33).

4.7 Summary and Discussion

A systematic experimental procedure and quantitative analyses have been proposed to investigate the effects of cyclic loading and time-recovery (or aging) on the mechanical properties and microstructure of particle-binder composites. Cast cylindrical specimens of mock sugar formulations of PBXN-109 differing in the amount of aluminum content (85-00 with no aluminum, 85-15 with 12.75% w/w aluminum, 85-30 with 25.5% w/w aluminum) were subjected to quasi-static cyclic compressive loading. The microstructure of each specimen was imaged before and after cyclic loading using micro-computed tomography. This procedure was repeated after a 4-week time-recovery period. The stress-strain response of each specimen was quantified using four parameters per loading-unloading cycle, namely peak and valley stresses (related to material strength), cumulative dissipated energy density (related to cyclic hysteresis and accumulated damage), and apparent stiffness. The spatial distribution of primary components in each specimen, including pore space, was postprocessed from micro-CT images.

The cyclic compressive response of PBXN-109 mock formulations is very similar to that of filled elastomers. Namely, it exhibits a highly nonlinear elasto-plastic response without a distinct yield point, hysteresis, and progressive stress softening (or Mullins effect) with cyclic stabilization. However, in sharp contrast to filled elastomers, these mock energetic composites exhibit an initial loading path noticeably different from subsequent loading paths. This nonlinear, path-dependent behavior observed in the macroscopic response is supported by changes in the mesoscopic spatial volume distribution of formulation components (i.e., binder, sucrose, aluminum, and pore space) observed using micro-CT. The quantification of these effects, before and after cyclic loading and time-recovering, confirmed that this behavior can be attributed to mesoscale deformation and relaxation mechanisms that emerge from the presence of a hard phase (sucrose) and a soft phase (binder) in the microstructure. The soft phase becomes progressively more compliant due to accumulated damage and particle-binder

interfacial debonding. It undergoes homogeneous or *affine deformation* under compressive load, it recovers during unloading, and it relaxes over time. In sharp contrast, the hard phase experiences a collective rearrangement or *non-affine deformation* under compressive loading, and it only partially recovers during unloading and over time due to the irreversible nature of this collective rearrangement. The presence of a ductile third phase (aluminum) may significantly affect these mesoscale deformation and relaxation mechanisms by forming permanent sucrose-aluminum contacts and reducing the sucrose-binder interfacial area—i.e., by arresting interfacial debonding and thus effectively stiffening the soft phase. In all formulations, and due to the loading conditions, the majority of microstructural changes occurred near the core of the cylindrical specimens. Furthermore, in formulations with aluminum content, the non-affine nature of the deformation field appeared to be anisotropic (i.e., different longitudinal and radial behavior was observed).

To conclude, the work presented in this chapter serves as the foundation of a future study of the long-term effects of repetitive cyclic loading and time-recovery on the microstructure and mechanical properties of particle-binder composites. Such study would entail an execution of the proposed testing and recovery procedure over several months. The outcome of this study will provide compelling affirmation of the observations and analyses presented in the chapter, leading to a better understanding and characterization of the complex mechanical behavior of particle-binder composites.

CHAPTER 5. A FINITE-DEFORMATION CONSTITUTIVE MODEL OF PARTICLE-BINDER COMPOSITES INCORPORATING YIELD-SURFACE-FREE PLASTICITY

This content of this chapter has been submitted to the International Journal of Plasticity, and it is currently under review.

5.1 Introduction

Particle-binder composite materials consist of a large concentration of hard particles, called fillers, randomly dispersed in the matrix of a soft material. Generally, fillers are used to enhance the mechanical properties of the soft material. For example, filled elastomers such as carbon black and silica filled rubbers (Rattanasom et al., 2007; Omnès et al., 2008) have been shown to possess superior stiffness, strength and damping properties over natural rubber, making them suitable for application in automotive parts such as tires and bearing seals, and in structures providing vibration and shock isolation to mechanical systems.

Another class of particle-binder composites, called energetic composites or Plastic-Bonded Explosives (PBX), consists of explosive crystals and, in some formulations, metal fuel powder, embedded in a binder composed mainly of a soft polymer and a plasticizer. Since their initial development at Los Alamos National Laboratory in 1947, PBXs have been commonly used as ammunition in defense applications. Examples of explosives used include cyclotrimethylenetrinitramine (RDX) and cyclotetra-minetetranitramine (HMX), while the binder composition includes polymers like hydroxyl-terminated polybutadiene (HTPB) and Estane, and plasticizers like Dioctyl adipate (DOA) and isodecyl pelargonate (IDP), along with smaller concentrations of various additives (Akhavan, 2011). In PBX binder, the polymer, apart from providing structural integrity to the explosive, reduces their impact and vibrational sensitivity (Palmer et al., 1993; Rae et al., 2002; Rangaswamy et al., 2010), while the plasticizer improves their mechanical properties and processability (Yılmaz et al., 2014).

The metal fuel, usually aluminum, is used to enhance the blast effects. Therefore, aluminized PBXs are typically used in naval weapons and missile warheads (Kumar et al., 2010).

Energetic composites are commonly used in applications requiring high mechanical confinement or compression (Wiegand, 2000; Wiegand & Reddingius, 2005). Additionally, these materials may be subjected to diverse loading conditions, ranging from low to high strain-rate cyclic, vibrational and impact loading during transport, storage and handling over their operational life. Since PBXs are designed to detonate under specific external energy stimulus, such loading conditions may alter their mechanical response, rendering them unpredictable and unsafe (Drodge & Williamson, 2016). Therefore, understanding and predicting the mechanical response of PBX under different loading conditions is of particular interest to the defense and propulsion community.

Earlier experimental studies on the mechanical behavior of PBX under uniaxial load have shown strong dependence on strain rate and temperature (Idar et al., 2002; Thompson et al., 2002; Williamson et al., 2008). Several constitutive models in the context of small and large deformation mechanics have been developed to model their rate and temperature-dependent behavior. For instance, Bardenhagen et al. (1998) proposed a large deformation viscoelastic model for PBX binder materials using Blatz-Ko hyperelasticity formulation and a Maxwell element. Clements & Mas (2001) proposed a viscoelastic constitutive theory for filled polymers using Boltzmann superposition principle, where the filler particles were modeled as randomly positioned elastic ellipsoidal particles. Composite stress relaxation functions were developed with their prony series coefficients dependent on filler concentration, ellipsoidal aspect ratio and polymer moduli. The visco-elastic cracking constitutive model developed by Bennett et al. (1998) combined a linear viscoelastic Maxwell's model with an isotropic damage model by Addessio & Johnson (1990). It was based on the mechanism of micro-cracking and derived from the statistical crack mechanics approach proposed by Dienes (1996) for brittle materials. The model was developed to predict the nonlinear stress-strain response of the material, as well as the strain-softening and nonlinearity observed due to extensive cracking at larger deformations. The model has since been extensively implemented in finite element analyses and used to predict the thermo-mechanical behavior of PBX and study hotspot generation (Rangaswamy et al., 2010; Buechler & Luscher, 2014). In the

context of PBX undergoing low-frequency vibrational loading, nonlinear viscoelastic models for a mass-material system undergoing base excitation were proposed by Paripovic & Davies (2013, 2016).

While most of the constitutive formulations proposed for PBX model the material as viscoelastic due to the rubbery nature of the polymer binder, it has been shown that they can exhibit considerable plastic deformation with increasing confinement. Uniaxial confined compression tests carried out on inert mock sugar-based specimens for PBX 9501 (Wiegand, 2000; Wiegand & Reddingius, 2005) under different confining pressures revealed increasing plastic deformation and strain hardening with increasing pressure. Recently, Agarwal & Gonzalez (2020) conducted unconfined compression tests at room temperature and low strain rate (10^{-3}/s) on cylindrical specimens of three mock explosive formulations based on PBXN-109 (Lochert et al., 2002), with sugar as a substitute for the explosive HMX crystals. All three formulations contained 85% w/w of solids (sugar and aluminum), but differed from each other by the amount of aluminum content in the solids-composition, namely 85-00 (0% Al in solids, 0% in total), 85-15 (15% Al in solids, 12.75% in total) and 85-30 (30% additive in solids, 25.5% in total). The stress-strain response of the 85-00 specimens exhibited a quasi-brittle behavior (Pijaudier-Cabot et al., 1999), with an initial nonlinear increase in stress until a peak stress level at around 10-11% strain, followed by strain-softening due to evolution of microcracks into larger transgranular fracture leading to a loss of strength. Such behavior has been recorded and studied extensively for many non-aluminized PBX formulations (Idar et al., 1998, 2002; Rangaswamy et al., 2010). However, the aluminized specimens (i.e., 85-15 and 85-30 specimens) exhibited a more ductile plastic flow behavior with strain hardening, indicating that the presence of aluminum could cause the material to deform plastically even in the absence of confinement.

Additionally, plastic deformation and damage in PBX have been shown to be associated with hotspot mechanisms (Trumel, H. et al., 2012; Keyhani et al., 2019), thus directly impacting their ignition characteristics. Therefore, the development of a constitutive model capable of characterizing the plastic behavior of explosives is extremely important for proper modeling and prediction of their mechanical behavior. Constitutive models for PBX incorporating plasticity have been proposed for cyclic deformation (Le et al., 2010) and mild

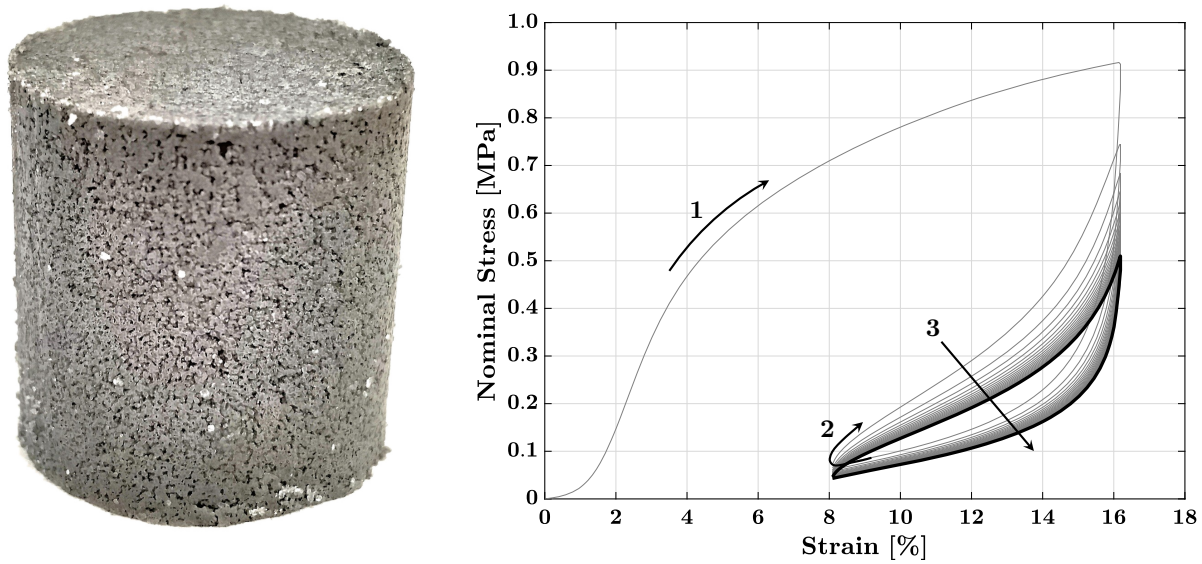

(a) (b)

Figure 5.1. (a) Aluminized mock sugar-based PBX specimen 85-15, and (b) the nominal stress-strain response under strain-controlled unconfined uniaxial compressive cyclic loading of the specimen. The response until the attainment of stable cyclic loop is shown in gray, while the stable cyclic loop is shown in black. Observable response attributes (labeled in the figure) include: (1) highly nonlinear stress-strain response without a distinctive yield point, (2) hysteresis, and (3) cyclic stress softening with eventual stabilization.

impact (Yang et al., 2018). However, the models have been developed using small deformation theory, and, therefore, are inapplicable to large deformation mechanical behavior of explosives.

Lastly, Agarwal & Gonzalez (2020) also conducted large deformation, unconfined cyclic compression tests of cylindrical sugar-based mock PBX specimens at room temperature and low strain rate (10^{-3}/s). Figure 5.1b shows the cyclic response of the 85-15 formulation. The strain-controlled, cyclic compression test was carried out by initially loading the specimen to 16% strain, and thereafter partially unloading-reloading between 8% and 16% strain. Observable response attributes (indicated in the figure) include: (1) a non-linear, continuous elasto-plastic response without apparent yield, (2) hysteresis, and (3) cyclic stress-softening with eventual stabilization. It is also worth noting that the curvature of the initial loading path is different from those of subsequent reloading paths. The former is convex and the latter are concave, indicating irreversible changes in the material behavior during the initial

loading itself. This behavior has also been previously observed for cyclic compression of aluminized RDX-based PBX in HTPB binder (Tang et al., 2016).

The mechanical response of filled elastomers and PBX specimens exhibit similar characteristics at large deformations. Constitutive models of filled elastomers have been proposed adopting both phenomenological (see, e.g., Laiarinandrasana et al. (2003); Ayoub et al. (2014); Österlöf et al. (2016); Guo et al. (2018a,b)) and micromechanical (see, e.g., Dargazany et al. (2014); Raghunath et al. (2016); Plagge & Klppel (2017)) frameworks. Ayoub et al. (2014) proposed a zener-type visco-hyperelastic constitutive model of rubber-like materials that accounts for Mullins effect (Mullins, 1948, 1969), continuous stress-softening and permanent residual strains, utilizing the network alteration theory (Marckmann et al., 2002; Chagnon et al., 2006). Raghunath et al. (2016) extended the micromechanical dynamic flocculation model developed by Klüppel (2003) to include time-dependent effects typical of filled elastomers. The majority of these models attribute the observed hysteresis, and other inelastic phenomena, to time-dependent viscous overstress in the rubber matrix. In contrast, only a limited number of models consider these phenomena as time-independent plastic deformation mechanisms. A case in point is the phenomenological elasto-plastic constitutive model proposed by Kaliske & Rothert (1998) that captures the rate-independent process of internal material friction due to irreversible polymer slippage on the filler surface and plastic deformation of the filler particles. This multi-yield-surface rheological model is comprised of a finite number of elasto-plastic Prandtl elements arranged in parallel with an elastic member. More recently, yield-surface-free endochronic plasticity (Valanis, 1970) was utilized by Netzker et al. (2010) to model the smooth and hysteretic cyclic stress-strain response of carbon-black filled rubbers, with higher computational efficiency and less parameters.

In this chapter, an elasto-plastic constitutive formulation with isotropic damage is presented, which is capable of modeling the cyclic response of mock energetic composite materials. Specifically, a Lagrangian finite-deformation formulation based on additive decomposition of strain energy (Simo, 1987; Govindjee & Simo, 1991; Holzapfel & Simo, 1996; Holzapfel, 1996, 2002) into elastic and plastic parts is adopted. The formulation uses Ogden's hyperelastic model (Ogden, 1972a,b) to predict the rubber-like nonlinear elastic response of the polymeric binder, and a hereditary (path-dependent) yield-surface-free endochronic plastic-

ity theory (Valanis, 1970), based on the concept of internal state variables (Horstemeyer & Bammann, 2010), to account for irreversible deformations. A discontinuous isotropic damage model (Kachanov, 1986; Lemaitre et al., 1985) is utilized to model the stress-softening that occurs during unloading, and an endochronic material scale function (Valanis, 1970; Wu & Yip, 1981; Yeh, 1995; Lin et al., 2007) is utilized to model progressive cyclic stress softening and attainment of stable cyclic response. The number of model parameters is a function of the number of active Ogden terms and endochronic branches, and therefore a significant number of parameters may need to be identified. Therefore, we develop a parameter identification method based on a nonlinear multivariate least-squares problem, which is expected to be non-convex and affected by multiple local optima. The range of behavior predicted by the proposed model is demonstrated by calibrating parameters for the 85-15 formulation under cyclic compression (Agarwal & Gonzalez, 2020). Finally, to gain a better insight into the dependence of material response on model parameters, the analysis is concluded by studying the sensitivity of the cyclic compressive response to variations in the estimated values of endochronic and isotropic damage parameters.

The chapter is organized as follows. The constitutive model is presented in Section 5.2, followed by Section 5.3 which provides a discrete numerical procedure to solve for stresses along a loading path. Section 5.4 presents the model parameter identification procedure and the calibrated material properties of the 85-15 mock PBX formulation. Section 5.5 shows a detailed sensitivity analysis of the yield-surface-free endochronic plasticity and the isotropic damage model. Finally, a summary and concluding remarks are presented in Section 5.6.

5.2 Constitutive model

5.2.1 General framework

The finite-deformation constitutive law is based on an additive decomposition of the Helmholtz free energy density function (Simo, 1987; Govindjee & Simo, 1991; Holzapfel & Simo, 1996; Holzapfel, 1996, 2002) into elastic and plastic parts and it employs a local multiplicative decomposition of the deformation gradient into isochoric and volumetric contributions. This approach is in contrast to the constitutive formulations based on multi-

plicative elastic-plastic decomposition of the deformation gradient (Kröner, 1959; Lee & Liu, 1967; Lee, 1969; Gurtin & Anand, 2005) or additive decomposition of the rate of deformation tensor (Hill, 1950, 1958; Prager, 1961).

For an isothermal elasto-plastic deformation process, the free energy density function Ψ is given by

$$\Psi(\mathbf{C}, \boldsymbol{\zeta}_1, \ldots, \boldsymbol{\zeta}_N) = \Psi^{\mathrm{e}}_{\mathrm{vol}}(J) + \Psi^{\mathrm{e}}_{\mathrm{iso}}(\bar{\mathbf{C}}) + \sum_{j=1}^{N} \Gamma^{\mathrm{i}}_j(\mathbf{C}, \boldsymbol{\zeta}_j) \tag{5.1}$$

where $\Psi^{\mathrm{e}}_{\mathrm{vol}}(J)$ and $\Psi^{\mathrm{e}}_{\mathrm{iso}}(\bar{\mathbf{C}})$ are the volumetric and isochoric elastic strain energy density functions, dependent respectively on the Jacobian of the deformation $J = \det(\mathbf{F})$ and on the isochoric right Cauchy-Green deformation tensor $\bar{\mathbf{C}} = \bar{\mathbf{F}}^T\bar{\mathbf{F}}$ (where $\bar{\mathbf{F}} = J^{-1/3}\mathbf{F}$). The inelastic strain energy $\sum_{j=1}^{N} \Gamma^{\mathrm{i}}_j(\mathbf{C}, \boldsymbol{\zeta}_j)$ is a set of configurational free energy functions Γ^{i}_j ($j = 1, \ldots, N$) that characterizes the inelastic deformation behavior, namely irreversible slip at particle-particle and particle-binder contacts, plastic deformation and fracture of particles, among other dissipative mechanisms typical of particle-binder composites. The path-dependent dissipative potential dependents on the right Cauchy-Green deformation tensor $\mathbf{C}$ and a set of inelastic strain-like second-order tensorial internal variables $\boldsymbol{\zeta}_j$ ($j = 1, \ldots, N$) that represent the inelastic deformation history of the material.

A discontinuous isotropic damage model is utilized to model the stress-softening that occurs during the unloading of particle-binder composites. For rubber or other polymeric materials, this phenomenon is known as Mullins effect (Mullins, 1948, 1969), and it has been phenomenologically described by applying a reduction factor of $(1 - D)$ to the stress of a hypothetical, undamaged material, where $D \in (0, 1]$ is the scalar damage variable (Kachanov, 1986; Lemaitre et al., 1985). Therefore, the second law of thermodynamics, in the form of the Clausius-Duhem inequality for an isothermal process, is given by

$$\begin{aligned} \mathcal{D}_{\mathrm{int}} &:= \frac{1}{2}\frac{\mathbf{S}}{1-D} : \dot{\mathbf{C}} - \dot{\Psi} \\ &= \frac{1}{2}\left[\frac{\mathbf{S}}{1-D} - 2\frac{\partial \Psi(\mathbf{C}, \boldsymbol{\zeta}_1, \ldots, \boldsymbol{\zeta}_N)}{\partial \mathbf{C}}\right] : \dot{\mathbf{C}} - \sum_{j=1}^{N} \frac{\partial \Gamma^{\mathrm{i}}_j(\mathbf{C}, \boldsymbol{\zeta}_j)}{\partial \boldsymbol{\zeta}_j} : \dot{\boldsymbol{\zeta}}_j \geq 0 \end{aligned} \tag{5.2}$$

From standard arguments (Coleman & Noll, 1963; Coleman & Gurtin, 1967), the first term yields the definition of the second Piola-Kirchhoff stress, that is

$$\mathbf{S} = (1-D)\, 2\frac{\partial \Psi(\mathbf{C}, \boldsymbol{\zeta}_1, \ldots, \boldsymbol{\zeta}_N)}{\partial \mathbf{C}} = (1-D)\left[\mathbf{S}^{\mathrm{e}}_{\mathrm{vol}} + \mathbf{S}^{\mathrm{e}}_{\mathrm{iso}} + \sum_{j=1}^{N} \mathbf{S}^{\mathrm{i}}_{j}\right] \tag{5.3}$$

and the second term results in a condition for each Γ^{i}_{j}, that is

$$\tilde{\mathbf{S}}^{\mathrm{i}}_{j} : \dot{\boldsymbol{\zeta}}_j \geq 0 \tag{5.4}$$

where the volumetric elastic stress $\mathbf{S}^{\mathrm{e}}_{\mathrm{vol}}$, the isochoric elastic stress $\mathbf{S}^{\mathrm{e}}_{\mathrm{iso}}$, the inelastic stress $\sum_{j=1}^{N} \mathbf{S}^{\mathrm{i}}_{j}$, and the stress-like internal variables $\tilde{\mathbf{S}}^{\mathrm{i}}_{j}$ (thermodynamically conjugate to $\boldsymbol{\zeta}_j$) are given by

$$\mathbf{S}^{\mathrm{e}}_{\mathrm{vol}} = J\frac{\mathrm{d}\Psi^{\mathrm{e}}_{\mathrm{vol}}(J)}{\mathrm{d}J}\mathbf{C}^{-1} \tag{5.5}$$

$$\mathbf{S}^{\mathrm{e}}_{\mathrm{iso}} = J^{-2/3}\mathrm{DEV}\left\{2\frac{\partial \Psi^{\mathrm{e}}_{\mathrm{iso}}(\bar{\mathbf{C}})}{\partial \bar{\mathbf{C}}}\right\} \tag{5.6}$$

$$\sum_{j=1}^{N} \mathbf{S}^{\mathrm{i}}_{j} = 2\sum_{j=1}^{N} \frac{\partial \Gamma^{\mathrm{i}}_{j}(\mathbf{C}, \boldsymbol{\zeta}_j)}{\partial \mathbf{C}} \tag{5.7}$$

$$\tilde{\mathbf{S}}^{\mathrm{i}}_{j} = -\frac{\partial \Psi}{\partial \boldsymbol{\zeta}_j} = -\frac{\partial \Gamma^{\mathrm{i}}_{j}(\mathbf{C}, \boldsymbol{\zeta}_j)}{\partial \boldsymbol{\zeta}_j} \qquad (j = 1, \ldots, N) \tag{5.8}$$

In the above equations, $\mathrm{DEV}\{\cdot\} = \{\cdot\} - (1/3)[\{\cdot\} : \mathbf{C}]\mathbf{C}^{-1}$ provides the deviator of a tensor in the reference configuration. It is worth noting that inequality (5.4) is satisfied by an evolution equation of the following form

$$\dot{\boldsymbol{\zeta}}_j = \mathbb{B}_j(\mathbf{C}, \boldsymbol{\zeta}_j) : \tilde{\mathbf{S}}^{\mathrm{i}}_{j} \tag{5.9}$$

where $\mathbb{B}_j$ is a positive definite fourth-order tensor (Holzapfel, 1996).

5.2.2 Elastic strain energy

The nonlinear elastic constitutive behavior of rubber-like materials, such as the binder in the application studied here, is commonly described through hyperelastic material models (see, e.g., the finite-deformations formulation presented by Mooney (1940); Rivlin (1948); Ogden (1972a,b); Boyce & Arruda (2000)). Ogden's hyperelastic model (Ogden, 1972a,b) is one of the most extensively used models for describing complex nonlinear responses, mainly due to its flexible series representation with the capability to introduce several model parameters. Specifically, the isochoric elastic strain energy density $\Psi^{\mathrm{e}}_{\mathrm{iso}}$ is given by

$$\Psi^{\mathrm{e}}_{\mathrm{iso}}(\bar{\mathbf{C}}) = \sum_{k=1}^{M} \frac{\mu_k}{\alpha_k}(\bar{\lambda}_1^{\alpha_k} + \bar{\lambda}_2^{\alpha_k} + \bar{\lambda}_3^{\alpha_k} - 3) \tag{5.10}$$

where the isochoric principle stretches are given by $\bar{\lambda}_a = J^{-1/3}\lambda_a$ $(a = 1, 2, 3)$ for principal stretches λ_a $(a = 1, 2, 3)$. Constants μ_k and α_k $(k = 1, \ldots, M)$ are material parameters that satisfy the following inequality to enforce stability in the material response

$$\mu_k \alpha_k > 0 \quad \forall\, k \in [1, M] \ , \tag{5.11}$$

From consistency conditions with respect to linear elasticity at small-strain (Ogden, 1984), the reference (ground-state) shear modulus of the material is given by

$$\mu = \sum_{k=1}^{M} \frac{\mu_k \alpha_k}{2} \tag{5.12}$$

5.2.3 Discontinuous isotropic damage

A discontinuous isotropic damage model (Kachanov, 1986; Lemaitre et al., 1985) is utilized to model the stress-softening that occurs during unloading, i.e., Mullins effect (Mullins, 1948, 1969) for polymeric materials, with scalar damage variable $D \in (0, 1]$. In the spirit of the damage function proposed by Zúñiga & Beatty (2002) and pseudoelastic damage func-

tions proposed by Ogden & Roxburgh (1999) and Dorfmann & Ogden (2003), we specifically define the scalar damage variable as follows

$$D(\mathbf{C}, \phi^{\max}) = \tanh^{p}\left(\frac{\phi^{\max} - \phi(|\mathbf{C}|)}{m}\right) \tag{5.13}$$

where $\phi(|\mathbf{C}|)$ is the measure of deformation proposed by Beatty and co-workers (Beatty & Krishnaswamy, 2000; Zúñiga & Beatty, 2002) given by

$$\phi(|\mathbf{C}|) = |\mathbf{C}| = \sqrt{\mathbf{C} : \mathbf{C}} \tag{5.14}$$

and where $\phi^{\max}$ is the maximum deformation level given by

$$\phi^{\max}(t) = \max_{\tau \in [-\infty, t]} \phi(|\mathbf{C}(\tau)|) \tag{5.15}$$

The scalar damage variable is then a monotonic function of the deformation measure in the interval $\phi \in [\sqrt{3}, \phi^{\max}]$, with positive damage parameters m and p.

5.2.4 Yield-surface-free endochronic plasticity and evolution equation

As explained previously, particle-binder composites, specifically Plastic-Bonded Explosives (PBX), exhibit a non-linear elasto-plastic response without apparent yield. Classical plasticity theories require a yield surface and thus their applicability is limited for modeling these composites. In this study, we follow the work of Holzapfel & Simo (1996) and assume a quadratic relationship between free energy functions $\Gamma^{\mathrm{i}}_{j}(\mathbf{C}, \boldsymbol{\zeta}_j)$ and the internal variables $\boldsymbol{\zeta}_j$, i.e.

$$\frac{\partial \Gamma^{\mathrm{i}}_{j}}{\partial \boldsymbol{\zeta}_j \boldsymbol{\zeta}_k} = 2\mu_j \delta_{jk} \mathbb{I} \quad (j \text{ not summed}) \tag{5.16}$$

where μ_j are the reference (ground state) shear moduli related to j inelastic processes, δ_{mn} is the Kronecker delta and $\mathbb{I}$ is the fourth-order identity tensor.

By integrating Equation (5.16) twice, the following inelastic strain energy functions are obtained

$$\Gamma^{\mathrm{i}}_j(\mathbf{C},\boldsymbol{\zeta}_j) = \mu_j|\boldsymbol{\zeta}_j|^2 + \mathbf{S}^*_j(\mathbf{C}) : \boldsymbol{\zeta}_j + \Psi^*_j(\mathbf{C}) \qquad (j = 1,\ldots,N) \tag{5.17}$$

where $\mathbf{S}^*(\mathbf{C})$ and $\Psi^*(\mathbf{C})$ are unknown tensor and scalar-valued functions, respectively. Similarly, an evolution or rate equation for the stress-like internal variables is obtained from Equations (5.8), (5.9) and (5.17), and it is given by

$$\dot{\tilde{\mathbf{S}}}^{\mathrm{i}}_j + 2\mu_j\, \mathbb{B}_j(\mathbf{C},\boldsymbol{\zeta}_j) : \tilde{\mathbf{S}}^{\mathrm{i}}_j = -\dot{\mathbf{S}}^*(\mathbf{C}) \qquad (j = 1,\ldots,N) \tag{5.18}$$

The inelastic strain energy without apparent yield is realized by adopting the endochronic plasticity theory developed by Valanis (1970). This theory is strain path-dependent in nature and it does not require the definition of a yield surface. This theory has been applied successfully to develop both infinitesimal-strain and finite-deformation plastic formulations to describe many metals and alloys (Wu & Yip, 1981; Valanis & Lee, 1984; Guo et al., 2016), concrete (Valanis & Read, 1986), powder compaction (Bakhshiani et al., 2002; Khoei et al., 2003; Khoei & Bakhshiani, 2004) and, more recently, filled elastomers (Netzker et al., 2010; Chen et al., 2018). In this work, we specifically assume

$$\mathbb{B}_j(\mathbf{C},\boldsymbol{\zeta}_j) = \frac{\dot{z}(|\dot{\mathbf{C}}|)}{2\mu_j\gamma_j}\mathbb{I} \qquad (j = 1,\ldots,N) \tag{5.19}$$

where the intrinsic time scale z is a monotonically increasing measure of the deformation history, and the memory kernel is given by a set of positive dimensionless material parameters γ_j $(j = 1,\ldots,N)$ (see, for reference, Hsu et al. (1991) and Khoei et al. (2003)) that defines the path-dependent behavior of the formulation. It is worth noting that $\mu_j\gamma_j \geq 0$ for $\mathbb{B}_j$ to be a positive definite tensor. In addition, we assume

$$\mathbf{S}^*_j(\mathbf{C}) = -\mathbf{S}^{\mathrm{e}}_{\mathrm{iso},j}(\mathbf{C}) = -J^{-2/3}\mathrm{DEV}\left\{2\frac{\partial\Psi^{\mathrm{e}}_{\mathrm{iso},j}(\bar{\mathbf{C}})}{\partial\bar{\mathbf{C}}}\right\} \qquad (j = 1,\ldots,N) \tag{5.20}$$

where $\Psi^{\mathrm{e}}_{\mathrm{iso},j}$ are a set of isochoric elastic strain energy functions defined according to the Ogden's model as

$$\Psi^{\mathrm{e}}_{\mathrm{iso},j} = \sum_{i=1}^{P} \frac{\mu_{ij}}{\alpha_{ij}} (\bar{\lambda}_1^{\alpha_{ij}} + \bar{\lambda}_2^{\alpha_{ij}} + \bar{\lambda}_3^{\alpha_{ij}} - 3) \qquad (j = 1, \ldots, N) \tag{5.21}$$

with constants μ_{ij} and α_{ij} such that $\mu_{ij}\alpha_{ij} > 0$ (cf. Equation (5.11)). It is worth noting that after substituting $\mathbb{B}_j$ and $\mathbf{S}^*_j$ according to Equations (5.20) and (5.21) respectively, the evolution or rate equation (5.18) simplifies to

$$\dot{\tilde{\mathbf{S}}}^{\mathrm{i}}_j + \frac{\dot{z}(|\dot{\mathbf{C}}|)}{\gamma_j} \tilde{\mathbf{S}}^{\mathrm{i}}_j = \dot{\mathbf{S}}^{\mathrm{e}}_{\mathrm{iso},j} \qquad (j = 1, \ldots, N) \tag{5.22}$$

which can be regarded as the nonlinear extension of the one-dimensional isothermal evolution equation for a standard linear solid proposed by Valanis (1972) (see section 6 of the reference). Furthermore, by eliminating time dependence on both sides of differential equation and integrating with respect to the intrinsic time scale z, the classical hereditary or convolution form is recovered, that is

$$\tilde{\mathbf{S}}^{\mathrm{i}}_j = \tilde{\mathbf{S}}^{\mathrm{i}}_{j,0} + \int_0^z \dot{\mathbf{S}}^{\mathrm{e}}_{\mathrm{iso},j} \, \mathrm{e}^{-\frac{z-z'}{\gamma_j}} \, \mathrm{d}z' \qquad (j = 1, \ldots, N) \tag{5.23}$$

with $\tilde{\mathbf{S}}^{\mathrm{i}}_j(z = 0) = \tilde{\mathbf{S}}^{\mathrm{i}}_{j,0}$. Finally, for completeness, we set $\Psi^*_j(\mathbf{C}) = \Psi^{\mathrm{e}}_{\mathrm{iso},j}(\bar{\mathbf{C}})$ and, therefore, the reference shear moduli μ_j in (5.16) are given by

$$\mu_j = \sum_{i=1}^{P} \frac{\mu_{ij}\alpha_{ij}}{2} > 0 \qquad (j = 1, \ldots, N) \tag{5.24}$$

5.2.5 Intrinsic time scale and material scale function

The intrinsic time scale z, used in the evolution or rate equation (5.22) for internal variables $\tilde{\mathbf{S}}^{\mathrm{i}}_j$, is defined as

$$\dot{z}(|\dot{\mathbf{C}}|) = \frac{|\dot{\mathbf{C}}|}{f(z)} \tag{5.25}$$

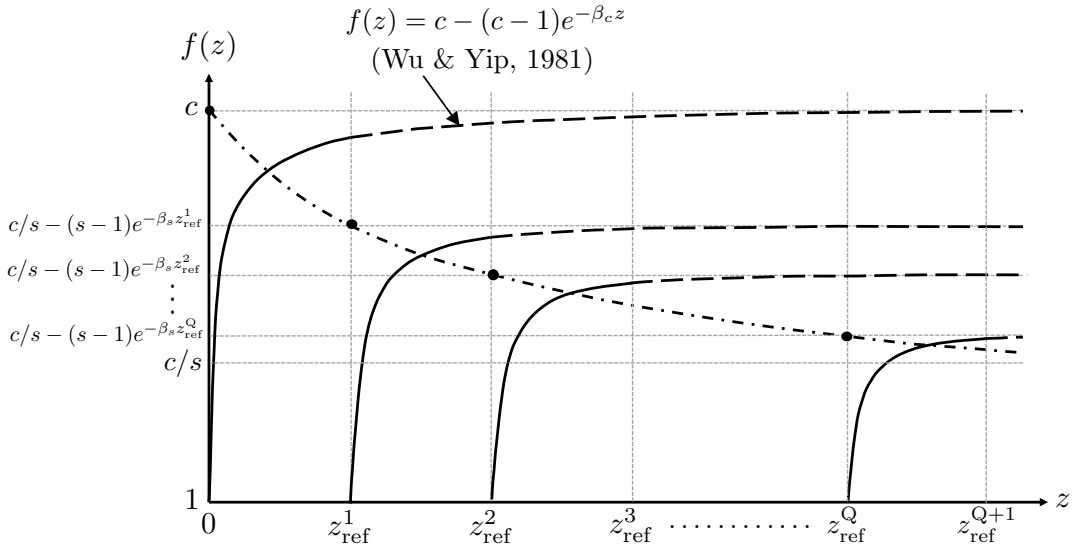

Figure 5.2. Schematic representation of the evolution of material scale function $f(z)$.

where $f(z)$ is a material scale function that represents the transient cyclic behavior of the material until attainment of a stable response. In its simplest form, $f(z)$ is a monotonically increasing function for cyclic hardening materials, and a monotonically decreasing function for cyclic softening materials, that is asymptotic to a saturation value at steady state. A simple scale function proposed by Wu & Yip (1981) is given by

$$f(z) = c - (c-1)\mathrm{e}^{-\beta_c z} \tag{5.26}$$

where β_c controls the rate of evolution, and the value at steady state is $c > 1$, for hardening materials, and $c < 1$, for softening materials. Yeh (1995) and Lin et al. (2007) proposed the following improvements to the scale function

$$f(z) = \frac{c}{s-(s-1)\mathrm{e}^{-\beta_s z_{\rm ref}}} - \left(\frac{c}{s-(s-1)\mathrm{e}^{-\beta_s z_{\rm ref}}} - 1\right)\mathrm{e}^{-\beta_c (z - z_{\rm ref})} \tag{5.27}$$

In the above improved scale function, the additional parameter $z_{\rm ref}$, defined as the value of z at which the last reversal of the strain path occurred, adds the capability to model "fading memory" effects exhibited by materials with memory (Coleman, 1964). In turn, the saturation value at steady state depends on the reference time scale $z_{\rm ref}$. It is equal to c for $z_{\rm ref} = 0$, i.e., before the first reversal, and approaches c/s for $z_{\rm ref} \to \infty$, i.e., at

cyclic stabilization. It is worth noting that for $c > s > 1$, the initial saturation value c is greater than the saturation value c/s at cyclic stabilization, i.e., the scale function describes the progressive cyclic softening typically observed in particle-binder composites. Figure 5.2 shows a schematic representation of the scale function proposed by Lin et al. (2007). It is evident from the figure that the rate of evolution of the material scale function is controlled by β_c, whereas the rate of evolution of the saturation value is controlled by β_s.

5.2.6 Inelastic stress

The inelastic stress $\mathbf{S}^{\mathrm{i}}_j$ is determined by using Equation (5.7) with the inelastic strain energy function defined by Equation (5.17) and by expressing the internal variable $\boldsymbol{\zeta}_j$ in terms of its conjugate $\tilde{\mathbf{S}}^{\mathrm{i}}_j$, i.e., using Equation (5.8). The result of this mathematical manipulation is given by

$$\mathbf{S}^{\mathrm{i}}_j = \mathbf{S}^{\mathrm{e}}_{\mathrm{iso},j} - \frac{1}{\mu_j}\frac{\partial \mathbf{S}^{\mathrm{e}}_{\mathrm{iso},j}}{\partial \mathbf{C}} : \left(\mathbf{S}^{\mathrm{e}}_{\mathrm{iso},j} - \tilde{\mathbf{S}}^{\mathrm{i}}_j\right) \tag{5.28}$$

where the internal variable $\tilde{\mathbf{S}}^{\mathrm{i}}_j$ is determined using the evolution or rate equation (5.22).

5.3 Incremental solution procedure

The constitutive model presented in the previous section is integrated by using an incremental solution procedure with time or loading intervals $[n, n+1]$. We assume that the state of the material, $\mathbf{C}_n$, $\tilde{\mathbf{S}}^{\mathrm{i}}_{j,n}$, z_n, $z_{\mathrm{ref},n}$, $\phi^{\max}_n$, is known at loading step n, and that $\mathbf{C}_{n+1}$ at loading step $n+1$ is given. The problem is then to determine $\tilde{\mathbf{S}}^{\mathrm{i}}_{j,n+1}$, z_{n+1}, $z_{\mathrm{ref},n+1}$, $\phi^{\max}_{n+1}$ at loading step $n+1$, and the value of the second Piola-Kirchhoff stress $\mathbf{S}_{n+1}$ which is given by

$$\begin{aligned}\mathbf{S}_{n+1} = (1 - D_{n+1}) \Bigg[& \mathbf{S}^{\mathrm{e}}_{\mathrm{vol},n+1} + \mathbf{S}^{\mathrm{e}}_{\mathrm{iso},n+1} + \sum_{j=1}^{N} \mathbf{S}^{\mathrm{e}}_{\mathrm{iso},j,n+1} \\ & - \sum_{j=1}^{N} \frac{1}{2\mu_j} \bar{\mathbb{C}}_{j,n+1} : \left(\mathbf{S}^{\mathrm{e}}_{\mathrm{iso},j,n+1} - \tilde{\mathbf{S}}^{\mathrm{i}}_{j,n+1}\right) \Bigg]\end{aligned} \tag{5.29}$$

where

$$\bar{\mathbb{C}}_{j,n+1} = 2\left[\frac{\partial \mathbf{S}^{\mathrm{e}}_{\mathrm{iso},j}}{\partial \mathbf{C}}\right]_{n+1} \tag{5.30}$$

and

$$\tilde{\mathbf{S}}^{\mathrm{i}}_{j,n+1} = \frac{\left(1-\Delta z/2\gamma_j\right)\tilde{\mathbf{S}}^{\mathrm{i}}_{j,n} + \mathbf{S}^{\mathrm{e}}_{\mathrm{iso},j,n+1} - \mathbf{S}^{\mathrm{e}}_{\mathrm{iso},j,n}}{\left(1+\Delta z/2\gamma_j\right)} \tag{5.31}$$

In the above equations, all quantities other than D_{n+1} and Δz are either known or depend on the right Cauchy-Green deformation tensor through equations (5.5), (5.6), and (5.20). The scalar damage variable D_{n+1} is computed after updating $\phi^{\max}_{n+1}$ using equation (5.15). The internal variable $\tilde{\mathbf{S}}^{\mathrm{i}}_{j,n+1}$ defined by Equation (5.31) above is obtained by using a midpoint rule to discretize the evolution or rate equation (5.22), i.e., from

$$\tilde{\mathbf{S}}^{\mathrm{i}}_{j,n+1} - \tilde{\mathbf{S}}^{\mathrm{i}}_{j,n} + \left(\frac{\Delta z}{\gamma_j}\right)\left(\tilde{\mathbf{S}}^{\mathrm{i}}_{j,n} + \frac{\tilde{\mathbf{S}}^{\mathrm{i}}_{j,n+1} - \tilde{\mathbf{S}}^{\mathrm{i}}_{j,n}}{2}\right) = \mathbf{S}^{\mathrm{e}}_{\mathrm{iso},j,n+1} - \mathbf{S}^{\mathrm{e}}_{\mathrm{iso},j,n} \tag{5.32}$$

The value of intrinsic time scale increment, Δz, is obtained by using a midpoint rule to discretize (5.25) together with (5.27), i.e., from

$$\begin{aligned}\Delta z\left[\frac{c}{s-(s-1)\mathrm{e}^{-\beta_s z_{\mathrm{ref},n+1}}} - \left\{\frac{c}{s-(s-1)\mathrm{e}^{-\beta_s z_{\mathrm{ref},n+1}}} - 1\right\}\mathrm{e}^{-\beta_c\left(z_n+\frac{\Delta z}{2}-z_{\mathrm{ref},n+1}\right)}\right] \\ - \left|\bar{\mathbf{C}}_{n+1} - \bar{\mathbf{C}}_n\right| = 0\end{aligned} \tag{5.33}$$

with $z_{n+1} = z_n + \Delta z$ and

$$z_{\mathrm{ref},n+1} = \begin{cases} z_n & \text{if} \quad (\phi_{n+1}-\phi_n)\cdot(\phi_n-\phi_{n-1}) < 0 \\ z_{\mathrm{ref},n} & \text{otherwise} \end{cases} \tag{5.34}$$

The above nonlinear equation is solved numerically using a Newton-Raphson method.

5.4 Model parameter identification of mock PBX

The range of behavior predicted by the proposed constitutive model is demonstrated by calibrating parameters for the 85-15 mock PBX formulation under cyclic compression (Agarwal & Gonzalez, 2020). Therefore, section 5.4.1 presents the incremental procedure for uniaxial cyclic loading under unconfined lateral conditions and incompressible material assumptions. Section 5.4.2 presents a parameter identification procedure based on a nonlinear multivariate minimization problem and the least-squares principle. Finally, sections 5.4.3 and 5.4.4 show the results of the parameter identification and the validation of the model, respectively.

5.4.1 Incremental procedure for uniaxial cyclic loading

The material is assumed to be incompressible, i.e., $J_n = 1$ and thus $\bar{\mathbf{C}}_n = \mathbf{C}_n$, due to the rubber-like behavior of the particle-binder composite. The cylindrical mock PBX specimen is loading along its axial direction which is coincidental with the $\mathbf{e}_3$ of a Cartesian coordinate system $\mathbf{e}_I$, with $I = 1, 2, 3$. Therefore, the right Cauchy-Green deformation tensor has principle stretches λ_I are related by

$$\lambda_{1,n} = \lambda_{2,n} = \frac{1}{\sqrt{\lambda_{3,n}}} \tag{5.35}$$

and principal directions aligned with the Cartesian axes, i.e., $\mathbf{C}_n = \sum_{I=1}^{3} \lambda_{I,n}^2 \mathbf{e}_I \otimes \mathbf{e}_I$. The specimen is laterally unconfined and the platens that apply the load are frictionless. Therefore, the only component of second Piola-Kirchhoff stress that is different from zero is $S_{33,n}$.

The elastic strain energy functions involved in the formulation reduce to

$$\begin{aligned}
\Psi^{\mathrm{e}}(\lambda_1, \lambda_2, \lambda_3) &= \sum_{k=1}^{M} \frac{\mu_k}{\alpha_k} (\lambda_1^{\alpha_k} + \lambda_2^{\alpha_k} + \lambda_3^{\alpha_k} - 3) \\
\Psi_j^{\mathrm{e}}(\lambda_1, \lambda_2, \lambda_3) &= \sum_{i=1}^{P} \frac{\mu_{ij}}{\alpha_{ij}} (\lambda_1^{\alpha_{ij}} + \lambda_2^{\alpha_{ij}} + \lambda_3^{\alpha_{ij}} - 3) \qquad (j = 1, \ldots, N) \\
\Psi_{\mathrm{vol}}^{\mathrm{e}}(J) &= -p_o(J - 1)
\end{aligned} \tag{5.36}$$

where the last term augments energy density and enforces the material internal or kinematic constraint imposed by incompressibility, i.e., $J = 1$, with p_o being the hydrostatic pressure.

Following the incremental procedure in section 5.3, we assume that the state of the material, $\mathbf{C}_n$, $\tilde{\mathbf{S}}^{\mathrm{i}}_{j,n}$, z_n, $z_{\mathrm{ref},n}$, $\phi^{\max}_n$, is known at loading step n, and that $\mathbf{C}_{n+1}$ at loading step $n+1$ is given. The maximum deformation $\phi^{\max}_{n+1}$ is determined from (5.14) and (5.15) using

$$\phi_{n+1} = \sqrt{\lambda^4_{3,n+1} + \frac{2}{\lambda^2_{3,n+1}}} \tag{5.37}$$

The intrinsic time scale increment Δz is obtained using (5.33) with

$$|\bar{\mathbf{C}}_{n+1} - \bar{\mathbf{C}}_n| = \sqrt{2\left(\lambda^{-1}_{3,n+1} - \lambda^{-1}_{3,n}\right)^2 + \left(\lambda^2_{3,n+1} - \lambda^2_{3,n}\right)^2} \tag{5.38}$$

and $z_{\mathrm{ref},n+1}$ is updated using (5.34) and $z_{n+1} = z_n + \Delta z$. The stress components in (5.29) simplify to

$$\begin{aligned}
&S^{\mathrm{e}}_{11,\mathrm{iso},n+1} = S^{\mathrm{e}}_{22,\mathrm{iso},n+1} = \sum_{k=1}^{M} \mu_k \lambda^{1-\alpha_k/2}_{3,n+1} && ; S^{\mathrm{e}}_{33,\mathrm{iso},n+1} = \sum_{k=1}^{M} \mu_k \lambda^{\alpha_k-2}_{3,n+1} \\
&S^{\mathrm{e}}_{11,\mathrm{vol},n+1} = S^{\mathrm{e}}_{22,\mathrm{vol},n+1} = -p_{o,n+1}\lambda_{3,n+1} && ; S^{\mathrm{e}}_{33,\mathrm{vol},n+1} = -p_{o,n+1}\lambda^{-2}_{3,n+1} \\
&S^{\mathrm{e}}_{11,\mathrm{iso},j,n+1} = S^{\mathrm{e}}_{22,\mathrm{iso},j,n+1} = \sum_{i=1}^{P} \mu_{ij} \lambda^{1-\alpha_{ij}/2}_{3,n+1} && ; S^{\mathrm{e}}_{33,\mathrm{iso},j,n+1} = \sum_{i=1}^{P} \mu_{ij} \lambda^{\alpha_{ij}-2}_{3,n+1} \\
&\bar{\mathbb{C}}_{1111,j,n+1} = \bar{\mathbb{C}}_{2222,j,n+1} = \sum_{i=1}^{P} \mu_{ij}(\alpha_{ij}-2)\lambda^{2-\alpha_{ij}/2}_{3,n+1} && ; \bar{\mathbb{C}}_{3333,j,n+1} = \sum_{i=1}^{P} \mu_{ij}(\alpha_{ij}-2)\lambda^{\alpha_{ij}-4}_{3,n+1}
\end{aligned} \tag{5.39}$$

where the hydrostatic pressure $p_{o,n+1}$ is obtained from the traction free boundary condition, i.e., from $S_{11,n+1} = S_{22,n+1} = 0$, using

$$\begin{aligned}
p_{o,n+1} = \frac{1}{\lambda_{3,n+1}} \Bigg[& S^{\mathrm{e}}_{11,\mathrm{iso},n+1} + \sum_{j=1}^{N} S^{\mathrm{e}}_{11,\mathrm{iso},j,n+1} \\
& - \sum_{j=1}^{N} \frac{1}{2\mu_j} \bar{\mathbb{C}}_{1111,j,n+1} : \left(S^{\mathrm{e}}_{11,\mathrm{iso},j,n+1} - \tilde{S}^{\mathrm{i}}_{11,j,n+1} \right) \Bigg]
\end{aligned} \tag{5.40}$$

and the internal variable $\tilde{\mathbf{S}}^{\mathrm{i}}_{j,n+1}$ is readily computed using Equation (5.31).

5.4.2 Parameter identification method

We have developed a parameter identification method based on a nonlinear multivariate minimization problem. The proposed constitutive model has $2M + 2P \times N + N + 6$ material parameters, namely

- $2M$ parameters in the elastic branch: μ_k and α_k $(k = 1, \ldots, M)$.
- $2P \times N$ elastic parameters in the yield-surface-free endochronic branches: μ_{ij} and α_{ij} $(i = 1, \ldots, P;\ j = 1, \ldots, N)$.
- N kernel parameters in the yield-surface-free endochronic branches: γ_j $(j = 1, \ldots, N)$.
- 4 material scale function parameters: c, s, β_c and β_s.
- 2 isotropic damage parameters: m and p.

The method is based on the least-squares principle, for $\mathcal{N}$ experimental nominal stress values T_n^{exp} and corresponding model first Piola-Kirchhoff stress values $\lambda_{3,n} S_{33,n}$, and it is given by

$$
\begin{aligned}
\min_{\mathbf{v} \in \mathbb{R}^{2M+2P\times N+N+6}, \epsilon_o} \quad & \frac{1}{\mathcal{N}} \sum_{n=1}^{\mathcal{N}} \left[T_n^{\text{exp}} - \lambda_{3,n} S_{33,n} \right]^2 \\
\text{subject to} \quad & -\mu_k \alpha_k \leq 0 \quad \text{for} \quad k = 1, \ldots, M \\
& -\mu_{ij} \alpha_{ij} \leq 0 \quad \text{for} \quad i = 1, \ldots, P;\ j = 1, \ldots, N \\
& s - c \leq 0 \\
& \mathbf{v} \in [\mathbf{v}^{\min}, \mathbf{v}^{\max}]
\end{aligned}
\tag{5.41}
$$

where the inequality constraints come from Ogden's stability conditions (e.g., from equation (5.11) for the elastic branch), and from the requirement of progressive cyclic softening. Since the nonlinear optimization problem is expected to be non-convex and affected by multiple local optima, appropriate bounds are applied on the set of material parameters $\mathbf{v}$. Lastly, the experimental response of the mock PBX specimen suggests that the initial loading response is affected by machine/specimen mismatch (Figure 5.1b). Therefore, the initial part of the response is omitted from the parameter estimation by applying a strain offset ϵ_o to the experimental data and setting stresses for the initial mismatch to be zero.

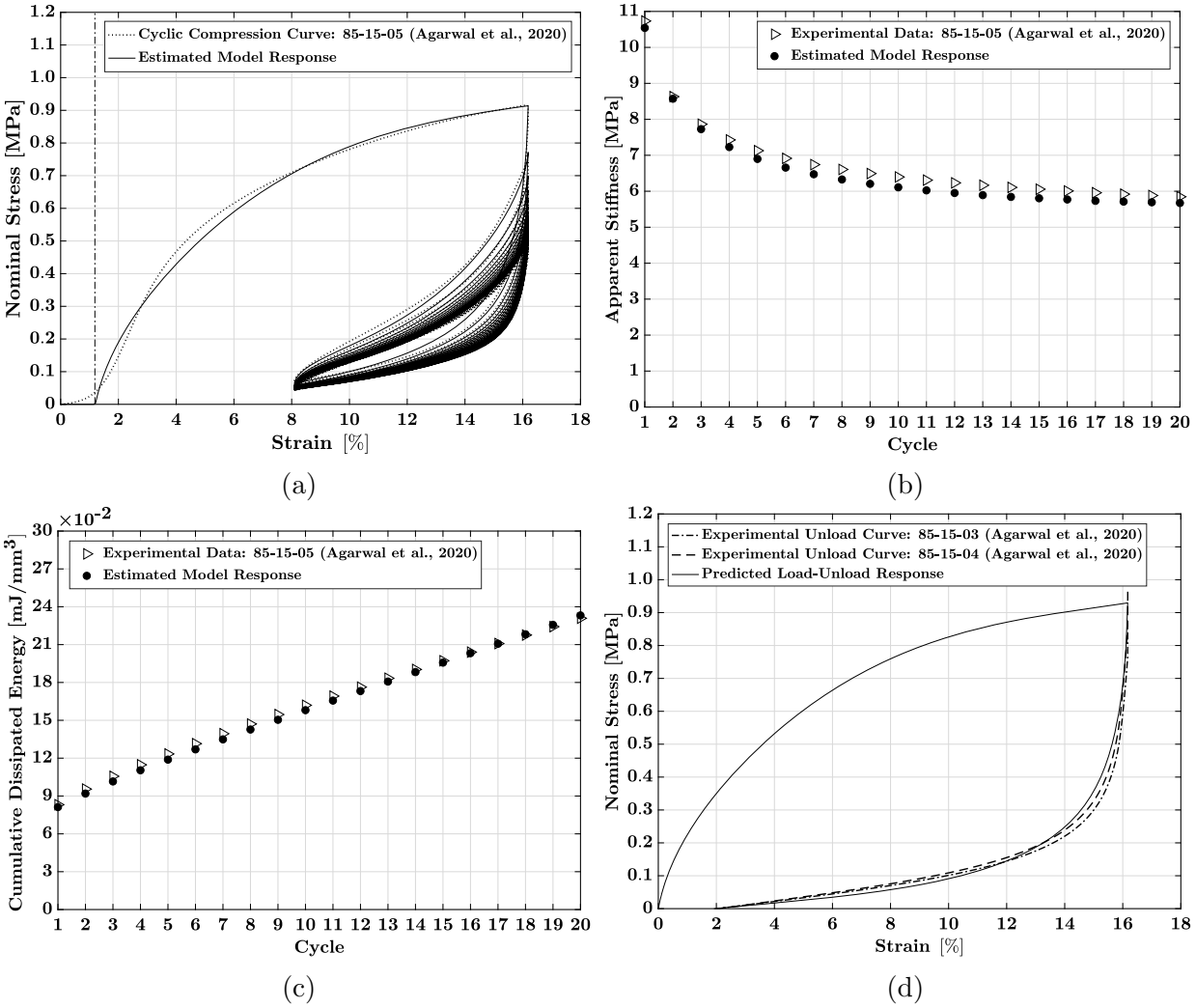

Figure 5.3. Experimental data and estimated model response for cyclic compression of the 85-15-05 PBX mock specimen, showing the (a) cyclic stress-strain curve, (b) evolution of apparent stiffness, and (c) cumulative energy dissipation with cyclic loading, and (d) the experimental and predicted model response of the unloading of specimens 85-15-03 and 85-15-04 from a strain level of 16%. The dashed-dotted line in (a) represents the value of machine/specimen mismatch offset ϵ_o.

5.4.3 Parameter identification of mock PBX

The nonlinear multivariate problem presented above was solved in MATLAB®, Version 9.4.0 (2018a) using the constrained optimization function *fmincon* with the default interior-point algorithm. The resulting estimated stress-strain curve, compared with the experimentally obtained response for the 85-15-05 specimen (ref. Agarwal & Gonzalez (2020) for the

Table 5.1. Material properties of the 85-15 mock PBX formulation with three yield-surface-free endochronic branches ($N = 3$).

Material properties of the 85-15 mock PBX formulation
Elastic branch ($M = 1$)
$\mu_1 = 1.4474$ MPa $\quad \alpha_1 = 10.4933$
Initial (ground-state) shear modulus $\mu^{\mathrm{e}} = \sum_{k=1}^{M} \mu_k \alpha_k / 2 = 7.5939$ MPa
Yield-surface-free endochronic branch 1 ($P = 1$)
$\mu_{11} = 13.5898$ MPa $\quad \alpha_{11} = 1.0454 \quad \gamma_1 = 0.0018$
Initial (ground-state) shear modulus $\mu_1^{\mathrm{i}} = \sum_{i=1}^{P} \mu_{i1} \alpha_{i1} / 2 = 7.1034$ MPa
Yield-surface-free endochronic branch 2 ($P = 1$)
$\mu_{12} = 1.2238$ MPa $\quad \alpha_{12} = 1.2841 \quad \gamma_2 = 0.0541$
Initial (ground-state) shear modulus $\mu_2^{\mathrm{i}} = \sum_{i=1}^{P} \mu_{i2} \alpha_{i2} / 2 = 0.7857$ MPa
Yield-surface-free endochronic branch 3 ($P = 1$)
$\mu_{13} = 0.5774$ MPa $\quad \alpha_{13} = 1.1829 \quad \gamma_3 = 0.4634$
Initial (ground-state) shear modulus $\mu_3^{\mathrm{i}} = \sum_{i=1}^{P} \mu_{i3} \alpha_{i3} / 2 = 0.3415$ MPa
Material scale function
$c = 11.1679 \quad s = 1.8178 \quad \beta_c = 423.9661 \quad \beta_s = 5.5234$
Isotropic damage
$m = 0.0764 \quad p = 0.6429$

specific naming convention of the tested mock PBX specimens) is presented in Figure 5.3a, along with the experimental and model-estimated values of the apparent stiffness (Figure 5.3b) and of the cumulative energy dissipation (Figure 5.3c). The apparent stiffness is calculated as the slope of the line connecting peak and valley stresses in each cycle, while the cyclic energy dissipation is calculated as the difference between the energy supplied to the material (i.e., the area under the loading path) and the energy recovered after a cycle (i.e., the area under the unloading path). It is interesting to note that an excellent agreement between the experimental data and the model response is achieved with $M = 1$, $N = 3$ and $P = 1$. Therefore, the 85-15 mock formulation is well characterized by a total of 17 material

parameters, listed in Table 5.1, with $\epsilon_o = 1.2\%$—shown in Figure 5.3a by a dashed-dotted vertical line.

5.4.4 Validation

A simple validation of the calibrated constitutive law under axial loading is performed using the unloading experimental response from a strain level of 16% to a stress-free state. Figure 5.3d shows very good agreement between the experimental unloading curves of specimens 85-15-03 and 85-15-04 (Agarwal & Gonzalez, 2020) and the model predictions. It is worth noting that while the unloading response remains fairly consistent from specimen-to-specimen, the loading response from a virgin state could vary considerably and, thus, it is not shown in the figure.

5.5 Sensitivity analysis of the yield-surface-free endochronic plasticity and the isotropic damage model

A sensitivity analysis of the cyclic stress-strain response to material properties of the yield-surface-free endochronic and the isotropic damage models is presented in this section. Specifically, we investigate the contribution of these material properties while keeping all other parameter values constant and equal to those obtained for the 85-15-05 mock PBX specimen.

5.5.1 Yield-surface-free endochronic plasticity

Figure 5.4 presents the influence of initial or ground-state shear moduli, i.e., μ_1 (Figure 5.4a), μ_2 (Figure 5.4c) and μ_3 (Figure 5.4e), and of kernel parameters, i.e., threshold strains γ_1 (Figure 5.4b), γ_2 (Figure 5.4d) and γ_3 (Figure 5.4f), on the stable cyclic response of the 85-15-05 mock PBX specimen. Solid curves correspond to the response calibrated to experimental data, dashed-dotted curves show the effect of reduction in the parameter values, while dashed curves show the effect of increase in the parameter values. It is evident from the figures that increase (decrease) in the shear moduli μ_j significantly increases (decreases)

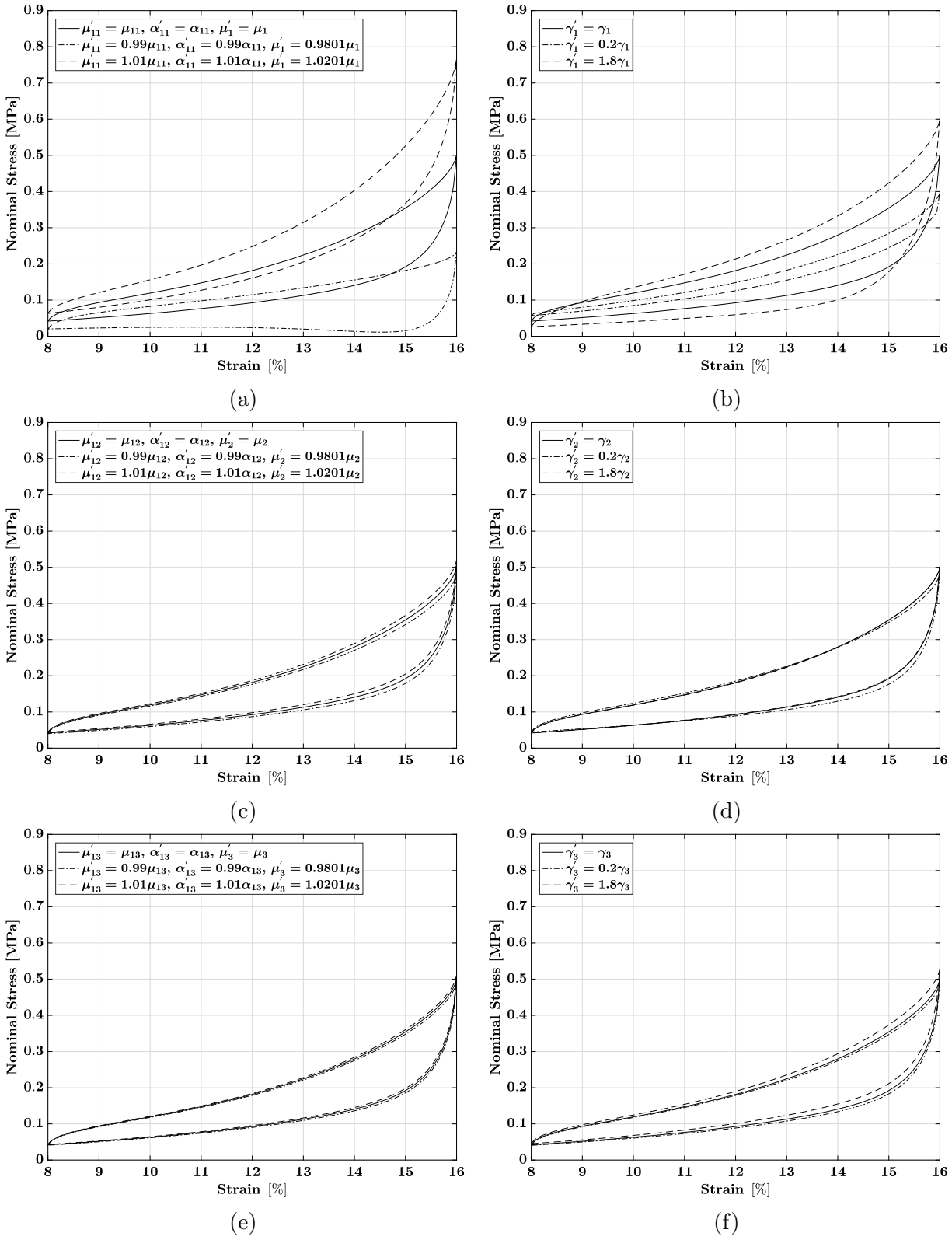

Figure 5.4. Stable cyclic response of the 85-15 mock PBX formulation for variations in yield-surface-free endochronic parameters (a) μ_1, (b) γ_1, (c) μ_2, (d) γ_2, (e) μ_3 and (f) γ_3.

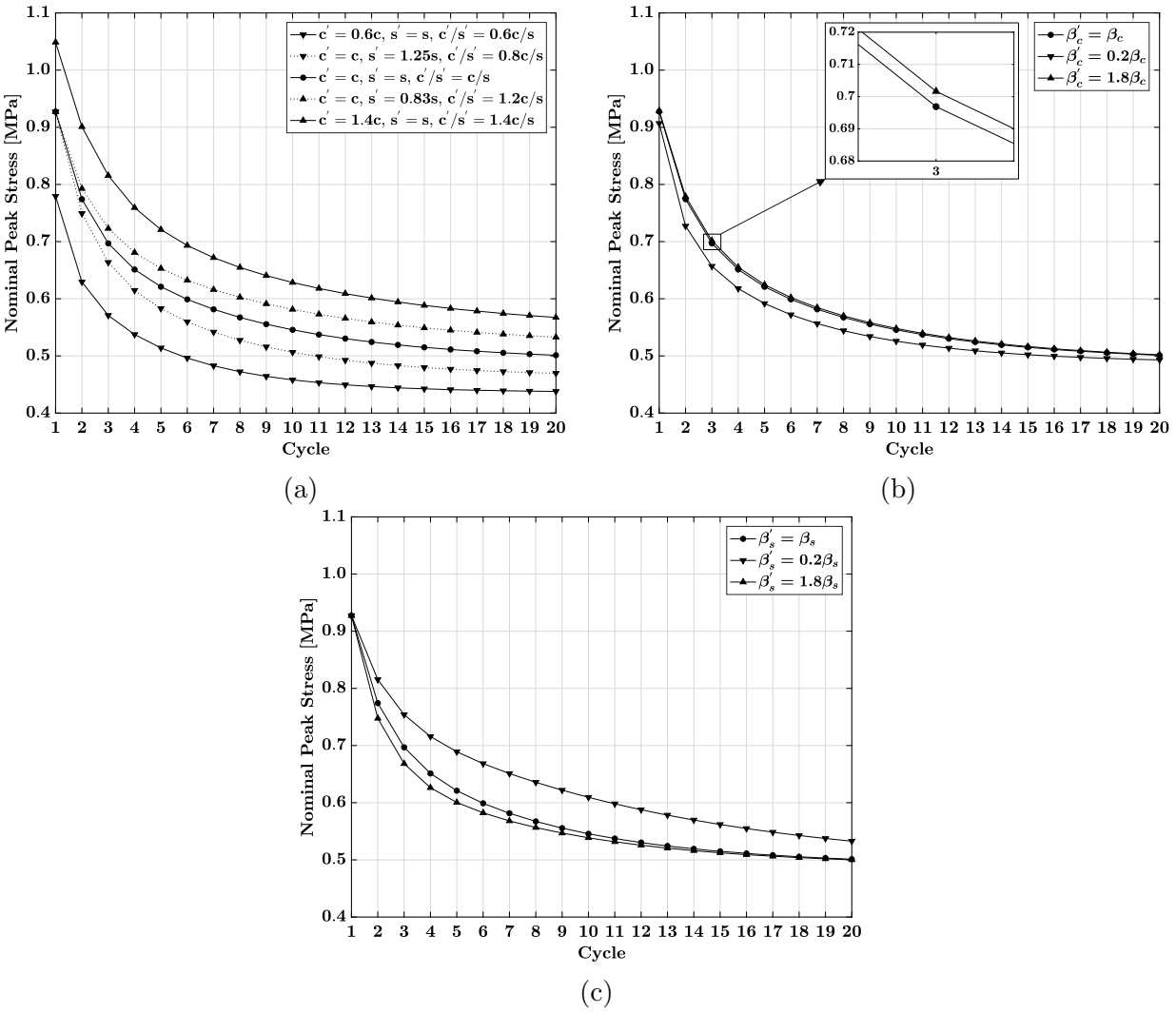

Figure 5.5. Cyclic peak stress of the 85-15 mock PBX formulation for variations in the material scale function parameters (a) c and s, (b) β_c and (c) β_s.

the stiffness of the stress-strain response, while increase (decrease) in the threshold strains γ_j increases (decreases) the cyclic hysteresis energy. Additionally, the dominant contribution to these effects is from the first yield-surface-free endochronic branch, i.e., from parameters μ_1 and γ_1.

Figure 5.5 presents the influence of material scale function parameters c and s on the evolution of peak stress with cyclic compression of the 85-15 mock PBX specimen. It is evident from Figure 5.5a that variation in c results in almost proportional change in the magnitude of the peak stress of each cycle (see $f(z) \approx c$ and $f(z) \to c/s$ in figure 5.2). In

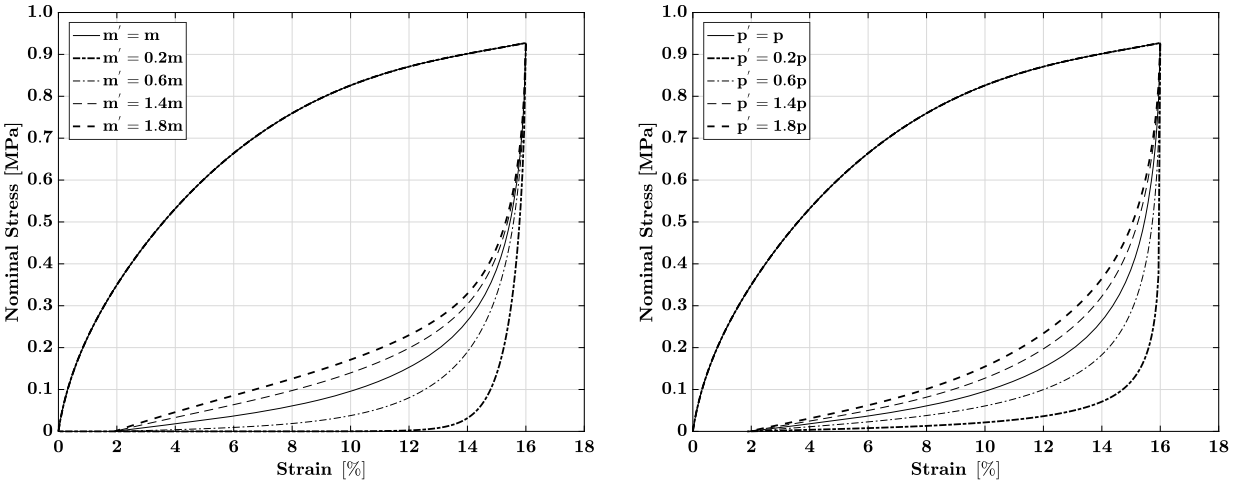

Figure 5.6. Loading-unloading response of the 85-15 mock PBX formulation for variations in the isotropic damage parameters (a) m and (b) p.

contrast, variation in s does not change the peak stress for the first cycle but it has an almost inverse proportional effect on the magnitude of the peak stress upon cyclic stabilization. Similarly, figures 5.5b and 5.5c present the influence of material scale function parameters β_c and β_s on the evolution of peak stress. The main effect of increase (decrease) in the value of β_c is to increase (decrease) the magnitude of the peak stress of each cycle in a nonlinear fashion. In contrast, the main effect of increase (decrease) in the value of β_s is to decrease (increase) the magnitude of the peak stress upon cyclic stabilization in a nonlinear fashion. These nonlinearities result from the exponential term in equation (5.27).

5.5.2 Isotropic damage model

Figure 5.6 presents the influence of isotropic damage parameters m and p on the loading-unloading stress-strain response of the 85-15 mock PBX specimen. Both parameters control the stress-softening behavior during unloading. Specifically, an increase (decrease) in the values of m and p results in decreasing (increasing) softening. Specifically, the parameter m exerts a more significant influence on the amount of softening at low strain levels, while p has greater control over the softening at moderate-to-high strain levels.

5.6 Summary and discussion

A quasi-static constitutive model for particle-binder composites is presented, which accounts for finite-deformation kinematics, non-linear elasto-plasticity without apparent yield, cyclic hysteresis and progressive stress-softening before the attainment of stable cyclic response. The model is based on an additive decomposition of strain energy into elastic and inelastic parts, where the elastic response is modeled using Ogden hyperelasticity while the inelastic response is described using yield-surface free endochronic plasticity based on the concepts of internal variables and of evolution or rate equations. Stress-softening is modeled using two approaches; a discontinuous isotropic damage model to appropriately describe the overall softening between loading and unloading responses, and a material scale function to describe the progressive cyclic softening until attainment of stable response. The constitutive model is then based on the deformation mechanisms experimentally observed during cyclic compression of mock PBX at large strain.

Furthermore, a discrete numerical procedure to solve for stresses along a loading path is proposed. To determine material properties from experimental cyclic compression data, a parameter identification method based on a nonlinear multivariate minimization problem is developed. Specifically, cyclic data for 85-15 mock PBX (Agarwal & Gonzalez, 2020) is used to demonstrate the range of behavior predicted by the proposed constitutive model and the effectiveness of the parameter identification method. The capability of the model is established from the remarkable model calibration results and validation against the unloading response from a strain level of 16% to a stress-free state. Finally, a sensitivity analysis of the cyclic stress-strain response to material properties of the yield-surface-free endochronic and the isotropic damage models is conducted to establish their influence on the mechanical response of the studied material.

To conclude, it is suitable to discuss some limitations of the proposed approach and possible directions for the future extension of the presented analysis. First, the present work restricts attention to quasi-static, i.e., low strain-rate behavior of particle-binder composites, thereby neglecting any strain-rate dependent effects in the constitutive model. However, it is well-known that viscous effects become dominant in these materials at moderate to high

strain rates. Second, the proposed constitutive model carries an assumption of elasto-plastic incompressibility, which limits the analysis to particle-binder composites with moderate levels of compressibility. Therefore, the extension of the model to rate-dependent viscous effects and compressible behavior is a worthwhile direction of future research.

CHAPTER 6. ANALYSIS OF THE LARGE DEFORMATION CONSTITUTIVE BEHAVIOR OF PARTICLE-BINDER COMPOSITES

6.1 Introduction

In this chapter, the large deformation constitutive model presented in chapter 5 is utilized to estimate the mechanical properties and model the stress-strain behavior of the three mock energetic composite formulations studied in chapter 4. For parameter identification, cyclic and monotonic compressive experimental data for cylindrical specimens of the three mock formulations of PBXN-109, namely 85-00, 85-15 and 85-30 is used. A comparative analysis of the three specimen formulations is then presented, where a correlation between the estimated mechanical properties and the mechanical behavior as well as composition of the specimens is identified and detailed.

6.2 Parameter Identification and Comparative Analysis of mock PBX specimens

The constitutive model and parameter identification method presented in Chapter 5 were used to calibrate the virgin cyclic (ref. Figures 4.12a, 4.12c and 4.12e) and monotonic (ref. Figure 4.6) compressive response of 85-00, 85-15 and 85-30 mock PBX cylindrical specimens. The calibration results are presented in Figure 6.1, and the estimated material parameters for each specimen formulation are listed in Table 6.1. As evident from the figure, an excellent agreement between the experimental data and model response is obtained for all three formulations. It is important to mention here that the parameter estimation for 85-15 specimen presented in Chapter 5 considered only the cyclic compressive response, while both cyclic and monotonic compression data is utilized here for determination of material properties. Consequently, the material properties for 85-15 listed in Table 6.1 provide a more accurate representation of the constitutive behavior of the material. Consideration of an even

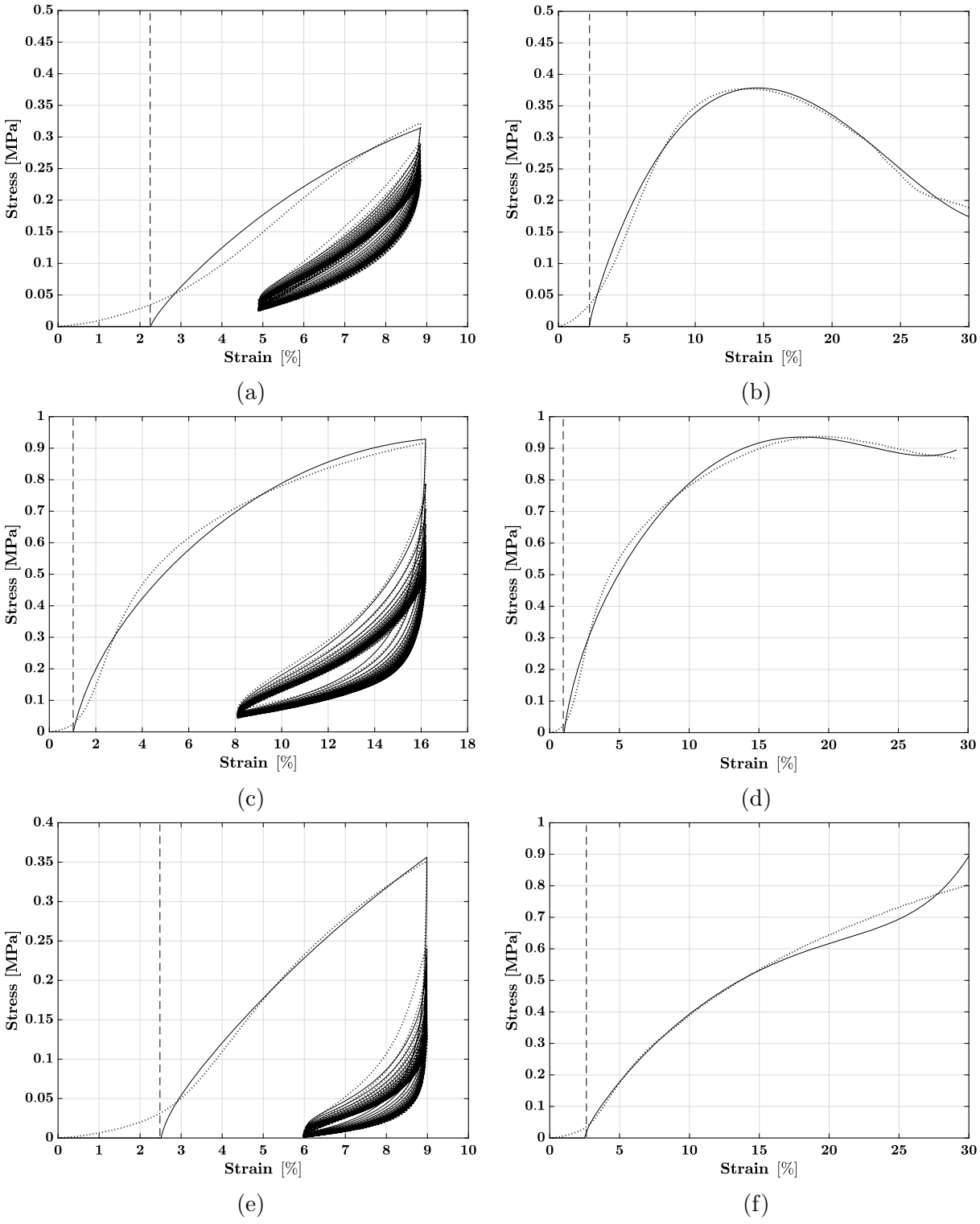

Figure 6.1. Comparison of experimental data (dotted) and estimated model response (solid) of cyclic and monotonic compressive tests conducted on virgin (a and b) 85-00, (c and d) 85-15, and (e and f) 85-30 mock PBX specimens. The omitted initial loading response attributed to machine/specimen mismatch is designated by a dashed line.

Table 6.1. Material properties of 85-00, 85-15 and 85-30 mock energetic formulations estimated from their virgin cyclic and monotonic compressive response.

Material Parameters	**85-00**	**85-15**	**85-30**
Elastic branch ($M = 1$)			
μ_1 (MPa)	1.1252	0.7483	0.0808
α_1	9.2293	10.8969	17.4232
Initial shear modulus $\mu^{\mathrm{e}} = \sum_{k=1}^{M} \mu_k \alpha_k / 2$ (MPa)	5.1922	4.0768	0.7037
Yield-surface-free endochronic branch 1 ($P = 1$)			
μ_{11} (MPa)	0.0432	5.6465	12.1770
α_{11}	0.0519	0.8418	1.1832
Initial shear modulus $\mu_1^{\mathrm{i}} = \sum_{i=1}^{P} \mu_{i1} \alpha_{i1} / 2$ (MPa)	0.0011	2.3766	7.2038
γ_1	0.0017	0.0010	0.0018
Yield-surface-free endochronic branch 2 ($P = 1$)			
μ_{12} (MPa)	0.0068	2.8725	0.0039
α_{12}	0.0661	1.5255	0.0543
Initial shear modulus $\mu_2^{\mathrm{i}} = \sum_{i=1}^{P} \mu_{i2} \alpha_{i2} / 2$ (MPa)	0.0002	2.1910	0.0001
γ_2	0.1723	0.0358	0.0622
Yield-surface-free endochronic branch 3 ($P = 1$)			
μ_{13} (MPa)	-	4.3973	0.6204
α_{13}	-	1.6687	1.2223
Initial shear modulus $\mu_3^{\mathrm{i}} = \sum_{i=1}^{P} \mu_{i3} \alpha_{i3} / 2$ (MPa)	-	3.6688	0.3792
γ_3	-	0.3413	0.2388
Material scale function			
c	14.9879	29.5182	591.1894
s	1.2592	2.0384	5.9671
β_c	125.3399	944.2924	2.0906
β_s	212.6798	16.7109	5.7283
Isotropic damage			
m	0.0247	0.0863	0.0195
p	0.7619	0.5769	0.3208

larger variety of experimental stress-strain datasets (e.g. shear tests, tensile tests) would assuredly result in higher accuracy of parameter estimation, however, it may add excessive complexity to the nonlinear multivariate problem which may lead to non-convergence of the solution.

From the observation of calibrated properties of mock PBX specimens in Table 6.1, it is possible to identify the correlation between the property values and the unique mechanical behavior of each specimen, and therefore, establish the relationship between material properties and material composition. For instance, the 85-00 specimen is accurately modeled by 2 endochronic branches, while 85-15 and 85-30 specimens require 3 endochronic branches to fully represent their mechanical response, which signifies the higher material non-linearity and more extensive inelastic behavior of the aluminized specimens. Specific trends in individual property values are also observed, which are discussed in detail below.

6.2.1 Elastic and Endochronic Branches

In the context of representing the deformation mechanics of energetic materials by a rheological model with respect to the constitutive formulation presented in Chapter 5, the elastic branch can be seen as a spring of stiffness μ^{e} acting in parallel with endochronic branches, each of which consist of a spring of stiffness μ_j^{i} and a friction element with threshold strain γ_j, where $j = 1, \ldots, N$ is the j^{th} of a total of N branches. The total stiffness μ of the material is represented by a sum of the elastic and endochronic moduli, i.e., $\mu = \mu^{\mathrm{e}} + \sum_{j=1}^{N} \mu_j^{\mathrm{i}}$, while the threshold strains represent the macroscopic strains at which the inelastic processes, such irreversible slipping of binder molecular chains on the filler (solid) surface and plastic deformation of the filler, start to occur (Kaliske & Rothert, 1998; Netzker et al., 2010).

From the calibrated parameter values listed in Table 6.1, the total stiffness of 85-00, 85-15 and 85-30 specimens is found to be 5.1941 MPa, 12.3132 MPa and 8.2868 MPa respectively. This suggests that the addition of aluminum in the PBX composition increases material stiffness, however, the stiffness starts to reduce with an increase in the amount of aluminum in the composition. This postulation is also supported by the evolution of apparent stiffness during virgin cyclic loading of the three compositions, presented in Chapter 4 (ref. Figures 4.14b, 4.14d and 4.14f). The figures show that the apparent stiffness of the cyclic loops range between 5-7 MPa for 85-00, 6-11 MPa for 85-15 and 4-11 MPa for 85-30, and therefore, the experimentally determined average stiffness follows the same order as the modeled stiffness with respect to the material composition. Another interesting observation lies in the con-

tribution to the total stiffness by the endochronic branches, which from Table 6.1 is 0.0013 MPa (0.025%) for 85-00, 8.2364 MPa (66.89%) for 85-15 and 7.5831 MPa (91.51%) for 85-30. Therefore, it is evident that with the activation of inelastic deformation mechanisms, the elastic material stiffness decreases with increasing aluminization, which is consistent with the observation of predominantly nonlinear mechanical response and ductile plastic flow to larger strain levels during monotonic compression in 85-15 and 85-30 as compared to 85-00 (ref. Figures 6.1b, 6.1d and 6.1f).

With regard to the threshold strains γ_j, the value of strain in the first endochronic branch (γ_1) is very small and comparable in magnitude for all PBX compositions (0.0017 for 85-00, 0.001 for 85-15 and 0.0018 for 85-30), suggesting that all three specimens start exhibiting inelastic behavior from almost the beginning of the loading process. However, the value of threshold strain in the second endochronic branch (γ_2) is much larger for 85-00 (0.1723) as compared to 85-15 (0.0358) and 85-30 (0.0622), indicating that more extensive inelastic processes start occurring at smaller macroscopic strains in the aluminized specimens. When comparing 85-15 and 85-30 specimens, we observe that although the second threshold strain is smaller for 85-15, the threshold strain in the third branch is smaller for 85-30 (0.2388) as compared to 85-15 (0.3413). Therefore, it can be concluded that higher aluminization leads to the material exhibiting predominant inelastic deformations at a smaller strain. This conclusion is also supported by observations of higher residual strain in 85-30 ($\sim$2%) as compared to 85-15 ($\sim$1.57%) after the recovery period following the virgin cyclic loading tests as presented in Chapter 4.

6.2.2 Material Scale Function

As explained in Chapter 5, the material scale function $f(z)$, which is a function of the intrinsic time scale z, is used in the constitutive model to represent the progressive cyclic stress-softening behavior observed during cyclic compression of mock PBX specimens. The function is given by Equation (5.27) and consists of four material parameters, namely c, s, β_c and β_s. The parameter c is the saturation value of the function during initial loading from zero deformation, when the reference intrinsic time scale z_{ref} is equal to zero. If the loading

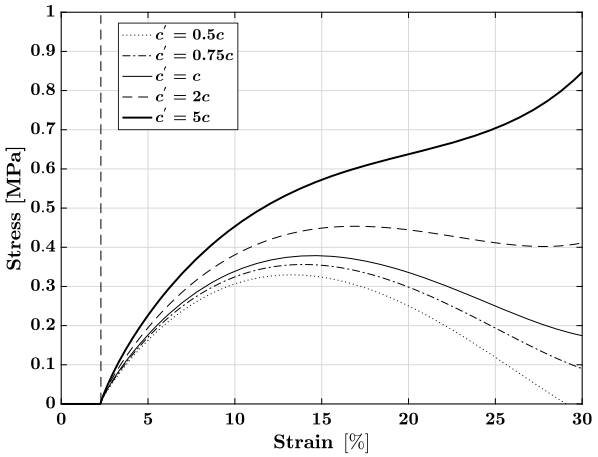

Figure 6.2. Influence of variation in the value of material scale function parameter c on the predicted monotonic compressive response of 85-00 formulation.

remains monotonic, the simpler scale function proposed by Wu & Yip (1981) and given by Equation (5.26) is recovered. According to this simpler function, the value of $f(z)$ evolves from 1 as z increases, and approaches c as $z \to \infty$, with the rate of evolution governed by β_c. If $c > 1$, then $f(z) \geq 1$. Therefore, during a loading step, the increment in intrinsic time scale z is greater than the increment in deformation measure $|\mathbf{C}|$ according to Equation (5.25), which produces a strain-hardening behavior. Conversely, if $c < 1$, then a strain-softening response is obtained. This is also true during cyclic loading-unloading, however, the saturation value evolves from c as z_{ref} increases, and approaches c/s as $z_{ref} \to \infty$ at cyclic stabilization. If $c/s < c$, then a progressive stress-softening response is obtained, which, as already stated, is one of the primary observed deformation mechanisms of mock PBX.

The value of parameter c for the studied mock PBX specimens is seen to increase with increasing aluminum content in the composition. Specifically, it is much higher for 85-30 as compared to 85-00 and 85-15 specimens. The reason for this difference lies in the monotonic compression response of the specimens. Figure 6.2 shows the influence of variation in c from its estimated value on the monotonic compression response of 85-00 specimen. It is evident that c controls the occurrence of maximum or ultimate stress in the response, as well as the magnitude of the ultimate stress, which stems from its representative role as the magnitude of strain hardening in the material. An ultimate stress is observed in the monotonic response of 85-00 and 85-15 specimens, with the value of the stress and the strain at which it occurs

being higher for 85-15 as compared to 85-00. Therefore, the estimated value of parameter c for 85-15 is comparatively higher than 85-00. However, the 85-30 specimen does not show an ultimate stress and continues to harden until the maximum applied deformation of 30%; hence, in accordance with Figure 6.2, the estimated value of c for 85-30 is much higher than both 85-00 and 85-15. With regard to parameter β_c, a correlation between the estimated values and PBX aluminum content is not observed; rather, the values are closely related to the evolution of the scale function during monotonic loading and the estimated values of c. Figure 6.3 shows the influence of variation in β_c on the monotonic compression response as well as the evolution of scale function $f(z)$ with intrinsic time z for the three specimens. It is evident that for 85-00 and 85-15 specimens, the scale function $f(z)$ reaches its saturation value c during the monotonic loading process, while the same does not occur for the 85-30 specimen as the material continues to harden beyond the maximum applied strain. For 85-15 (Figures 6.3c and 6.3d), the saturation value is reached much before the attainment of ultimate stress, and therefore, any variation in β_c has only a slight influence on the loading response at small strains ($\sim$1%-5%). For 85-00 (Figures 6.3a and 6.3b), the saturation value is reached near the end of the loading process, and therefore, the influence of variation in β_c on the stress-strain response is comparatively larger than 85-15. For 85-30 (Figures 6.3e and 6.3f), however, any variation in β_c has a significant impact on the stress-strain response. It is specifically observed that β_c controls only the evolution of stress, with the stress at any strain increasing with increasing β_c and vice versa. With regard to the magnitude of β_c, a higher value of β_c increases the rate of evolution of $f(z)$ and therefore the rate of attainment of the saturation value. Hence, 85-15 has the highest value of β_c (944.2924), followed by 85-00 (125.3399), while 85-30 assumes a much lower value (2.0906).

As discussed before, the role of parameters s and β_s in the context of PBX material is to reduce the saturation value of the scale function $f(z)$ from c to c/s during the cyclic loading process in order to achieve progressive stress-softening until cyclic stabilization. While s primarily controls the magnitude of the softening, β_s controls the softening rate or the rate of attainment of cyclic stabilization. From the estimated values of s for the three specimens, the value of c/s is obtained as 11.9027, 14.4811 and 99.0748 for 85-00, 85-15 and 85-30 respectively, resulting in a reduction of 20.58%, 50.94% and 83.24% in their respective

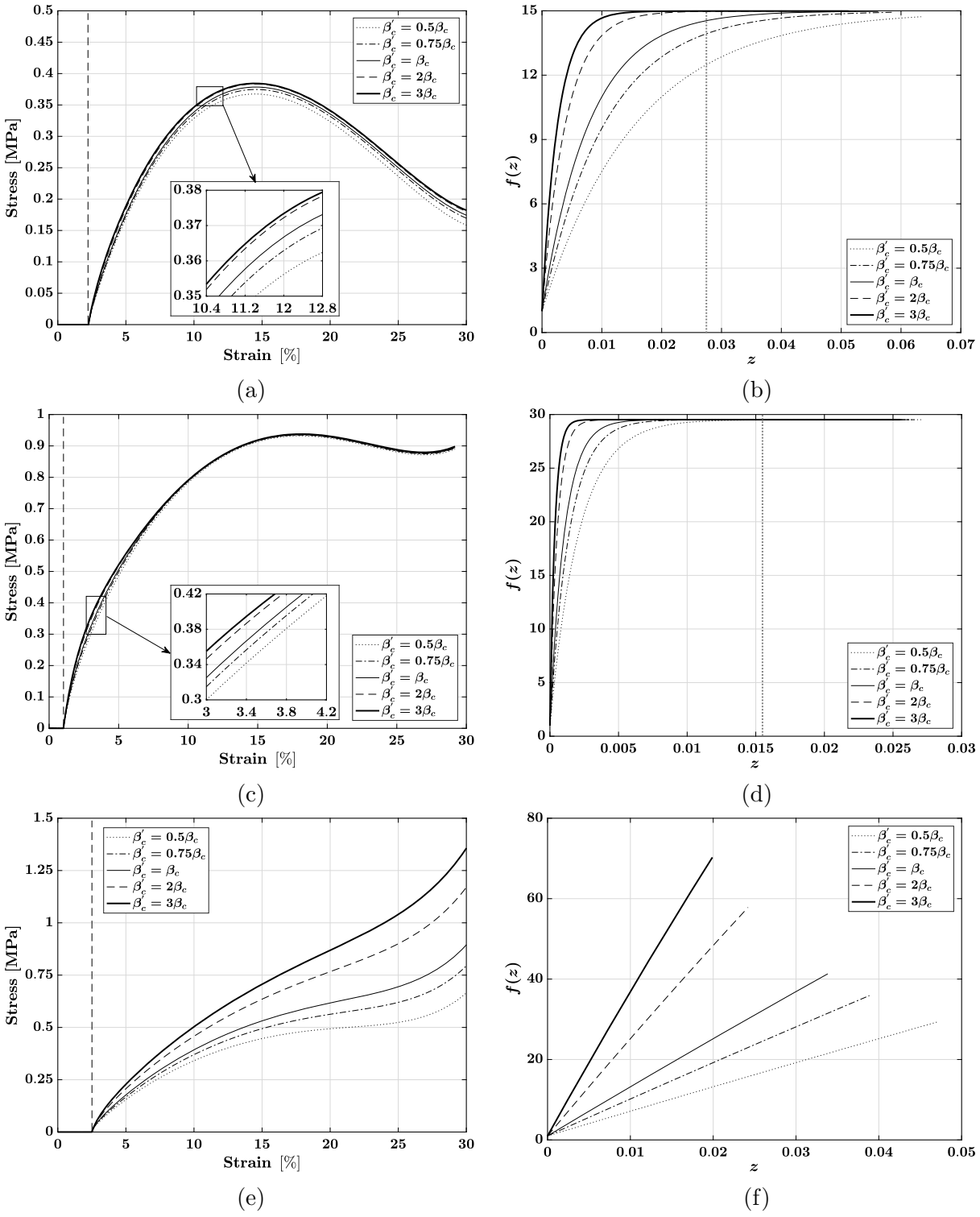

Figure 6.3. Influence of variation in the value of material scale function parameter β_c on the monotonic compressive response and the corresponding evolution of the material scale function $f(z)$ with intrinsic time z, for (a and b) 85-00, (c and d) 85-15, and (e and f) 85-30 mock formulations. The occurrence of ultimate stress in 85-00 and 85-15 is designated in their respective $f(z)$ evolution plots by a dotted line.

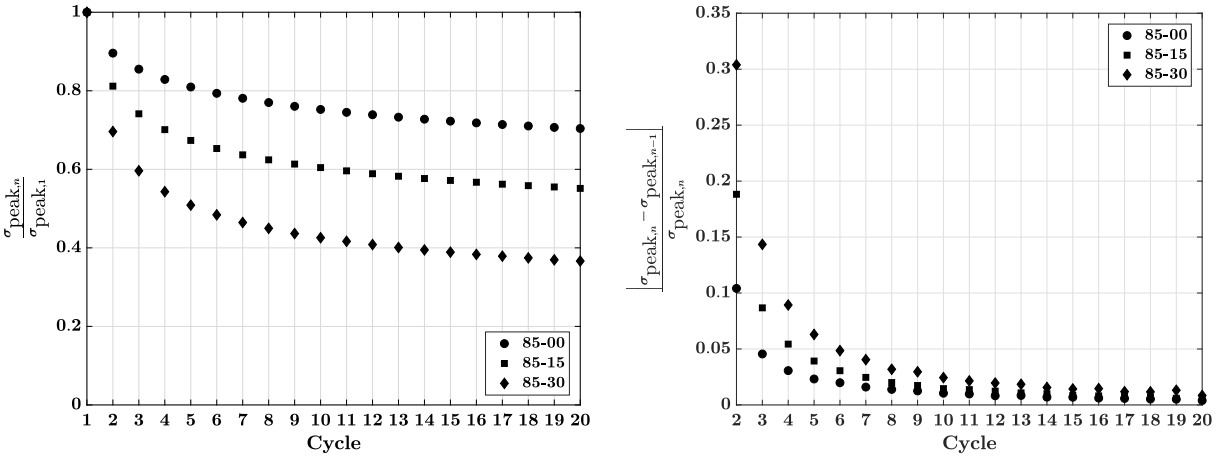

(a) (b)

Figure 6.4. Plots depicting evolution of (a) the ratio of peak stress for each cycle with respect to peak stress for the first cycle, and (b) fractional change in peak stress for a cycle with respect to peak stress for the previous cycle, for cyclic compressive experimental data of 85-00, 85-15 and 85-30 specimens.

saturation values at cyclic stabilization as compared to c. This implies that the magnitude of softening is the highest for 85-30, followed by 85-15, and the least for 85-00. Concurrently, the estimated values of β_s for the three specimens indicate the highest rate of stabilization for 85-00 (212.6798), followed by 85-15 (16.7109), and the lowest for 85-30 (5.7283). These findings with reference to the model parameters are in agreement with the experimental data, as seen in Figure 6.4, where the ratio of cyclic peak stresses with respect to the first peak stress (Figure 6.4a) drops the highest for 85-30, followed by 85-15 and then 85-00, while the change in peak stress with each cycle (Figure 6.4b) approaches zero (i.e., cyclic stabilization) fastest for 85-00, followed by 85-15 and then 85-30.

6.2.3 Isotropic Damage

It is shown in Chapter 5 that the primary function of the isotropic damage model is to represent the overall softening between loading and unloading responses during cyclic loading of particle-binder composites. The model consists of parameters m and p, each of which have been shown to increase (decrease) the softening effect as their values decrease (increase). From the sensitivity analysis of the two parameters on the unloading response of

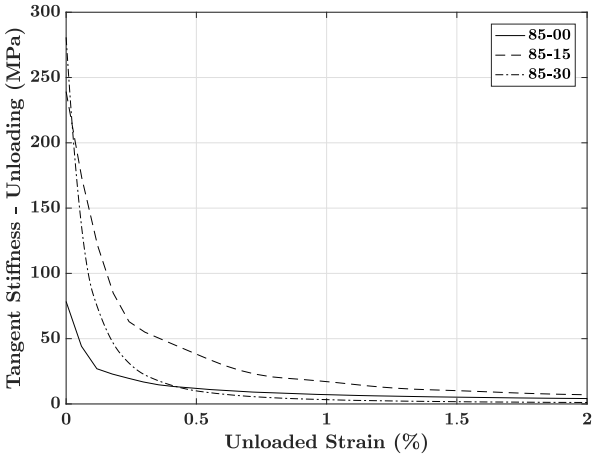

Figure 6.5. Plot depicting the slope or tangent stiffness of the experimental unloading stress-strain curve during the first cycle with respect to the unloaded strain for the three mock PBX compositions.

85-15 presented in chapter 5, it was found that p predominantly affects the softening rate at higher strains, more specifically, near the beginning of unloading. On the contrary, m exerts a predominant control at lower strain levels. A closer observation of Figure 5.6 indicates that the effects of p are dominant during the initial rapid softening ($\sim$15%-16% strain in the figure), while the influence of m predominates thereafter, when the softening rate decreases. Figure 6.5 shows the evolution of slope of the first cyclic unloading curve for the cyclic compressive response of the three mock PBX specimens. The slope is plotted for first 2% strain after the start of unloading, since it is seen that within this range the unloading curves of all three specimens begin to curve and the softening rate declines. Therefore, the effects of both m and p can be studied within this range for the three specimen compositions. From the figure, it is evident that the 85-30 specimen begins unloading with the highest slope, and therefore exhibits the highest rate of initial softening, followed by 85-15 and then 85-00. This is in agreement with the decreasing trend of the estimated p values in Table 6.1 with increasing aluminum content. With further unloading, the slope of the stress-strain curve drops rapidly for all specimens and then approaches a stable value, indicating a more linear stress-strain response beyond $\sim$0.5% unloaded strain. In this region, the influence of parameter m is predominant and a lower slope indicates a higher softening effect (ref. Figure 5.6a). Therefore, 85-30 again experiences the highest softening in this strain range since it

has the lowest slope. However, the slope of 85-00 is lower than 85-15 in this range, and therefore exhibits a higher softening. This is again in agreement with the estimated values of m in Table 6.1, which is the highest for 85-15, followed by 85-00 and lowest for 85-30.

6.3 Summary

The constitutive behavior and mechanical properties of the three mock sugar formulations of PBXN-109 are determined by utilizing the large deformation elasto-plastic constitutive model and the parameter identification method presented in Chapter 5. An excellent agreement between the cyclic and monotonic compression experimental data and the model response is obtained for all three formulations, which confirms the accuracy and versatility of the estimated mechanical properties. Correlation between the mechanical properties and the unique stress-strain response of each specimen is identified, which contributes towards establishing and validating specific trends observed in the property values with respect to the specimen composition, specifically, the amount of aluminum in the mock PBX. Finally, it is concluded that each of the estimated material parameters are more than mere numbers and have a significant contribution towards establishment of the highly complex and nonlinear mechanical behavior of particle-binder composites under finite strain.

CHAPTER 7. SUMMARY AND FUTURE WORK

This thesis presents computational and experimental tools and techniques to predict and understand the microstructural evolution and large deformation mechanical behavior of confined particulate composites, specifically, compacted powders and particle-binder composites. This work is of particular interest to a broad range of industries that manufacture powder compaction-based products, such as pharmaceutical, food, construction and powder metallurgy, and to the defense and energy sector with the ever-growing need to predict the performance and safety of energetic composite materials. The challenges of estimating the macroscopic response of these significantly heterogeneous and non-linear materials are addressed on both meso (particle) and continuum scale by developing accurate and predictive experimental, particle mechanics and constitutive models.

Particle mechanics strategies for compacted powder systems employ a contact formulation to predict the evolution of force-deformation behavior at the individual particle-particle contacts during the compaction process. In chapter 2, the nonlocal contact formulation for elastic confined granular systems pioneered by Gonzalez & Cuitiño (2012) was extended to account for both local and nonlocal contributions to the deformation at inter-particle contact boundaries (i.e., the contact area) due to other multiple contact forces acting on the pair of contacting particles in a confined environment. Additionally, the original contact formulation was corrected to include higher-order terms in the traditional one-term Taylor series representation of the undeformed profiles of the contacting surfaces. From the investigation of different symmetric and non-symmetric loading conditions on single elastic spherical particles to simulate mesoscale compaction conditions, it was established that the contact radius and curvature corrections enhance the range of applicability of the nonlocal contact formulation, providing accurate and fast predictions of the high-density inter-particle contact behavior up to the analytical limit of contact impingement. These findings were corroborated by an excellent agreement obtained between the analytical predictions and data collected from single-particle experiments and Finite Element simulation results.

While the corrected nonlocal contact formulation is an efficient and effective analytical tool for understanding the microstructural evolution of confined granular systems, it is currently limited in application to elastically deforming particles. However, a majority of compacted granular materials, for instance, pharmaceutical and metal powders, exhibit permanent plastic deformations during compaction to produce the final product. To diversify the application of this research and pave the way towards the development of a nonlocal contact formulation for elasto-plastic confined granular systems, semi-mechanistic contact laws for uniaxial and triaxial compression of elastic-perfectly plastic spherical particles were developed and presented in Chapter 3. A salient feature of these contact laws is that they are both material and loading-condition dependent, which is also a unique aspect of the elastic nonlocal contact formulation that makes it predictive at high compaction densities. Nonlinear contact pressure-deformation and contact radius-deformation relationships were developed from a sufficiently large set of finite element simulations of three symmetric loading configurations, namely simple (unconfined uniaxial) compression, die (confined triaxial with rigid lateral walls) compaction and hydrostatic (isostatic axisymmetric) compaction of single spherical particles. The accuracy and predictive capabilities of these contact laws were demonstrated with the attainment of an excellent agreement between analytical predictions and FE results for the three loading configurations within a wide range of elasto-plastic mechanical properties.

For the second class of confined particulate systems studied in this work, i.e. particle-binder composites, experimental mechanical testing and 3D imaging methods were developed and presented in Chapter 4 to understand and quantify the changes in the complex mesoscale microstructure and macroscopic mechanical response of these materials with repeated cyclic loading followed by an extended period of recovery. The specific materials of interest are Plastic Bonded Explosives (PBX), which consist of a heavy concentration of explosive crystals embedded in a polymeric binder. Inch-sized cast cylindrical mock sugar specimens of PBXN-109 formulation with three compositions differing in the amount of aluminum content (85-00 with no aluminum, 85-15 with 12.75% w/w aluminum, 85-30 with 25.5% w/w aluminum) were studied. The specimens were subjected to large quasi-static cyclic compressive loading before being allowed a time-recovery period of 4 weeks, following which the test was

repeated. Three dimensional images of the specimen's microstructure were obtained from micro-Computed Tomography before and after each loading test, which were post-processed to quantify the spatial distribution of the specimen's porosity and its primary components, namely sucrose (sugar), binder and aluminum. The mechanical response of the mock PBX specimens was found to be highly nonlinear and exhibiting several inelastic deformation mechanisms. More interesting observations were made when the same specimens were cyclically loaded again. With respect to the stress-strain response exhibited during the first test, the 85-00 specimen showed considerable increase in strength and stiffness, while the 85-15 and 85-30 specimens showed a small reduction in the overall strength and stiffness and exhibited a permanent change in their initial loading stress-strain curve, which became similar to the cyclic reloading curves. These differing changes in the mechanical response of the specimens with and without aluminum were correlated with the microstructural rearrangement observed in the specimens before and after the tests and during the recovery period using post-processed micro-CT data. It was concluded that with cyclic loading, the soft phase (binder) becomes progressively compliant due accumulated damage and particle-binder interfacial debonding, causing it to exhibit *affine* deformations in the radial direction, away from the specimen's core. On the contrary, the hard phase (sucrose) exhibits a collective *non-affine* rearrangement near the specimen's core to form a stronger inter-particle contact network, effectively increasing the load bearing capacity of the material. However, the presence of a ductile third phase (aluminum) alters these mesoscale deformation mechanisms by reducing the sucrose-binder interfacial area and arresting interfacial debonding, thereby causing a more ductile plastic material flow and inelastic material memory effects.

To complement the experimental efforts and identify a reliable method to quantify and predict the large deformation macroscopic mechanical behavior of PBX, a constitutive model based on nonlinear elasticity and the hereditary yield-surface-free endochronic plasticity was developed and presented in Chapter 5. While the model was developed on the basis of observed deformation characteristics of mock PBX, it is also applicable to the the rate-independent constitutive behavior of similar particle-binder composites such as filled elastomers. A discrete numerical procedure was proposed for solving model equations and efficiently calculating stresses along the loading path, along with a reliable parameter identi-

fication method based on a nonlinear multivariate optimization problem. Finally, in Chapter 6, the model was shown to accurately estimate the large deformation cyclic and monotonic compressive behavior of the three mock PBX formulations. A reliable correlation between the estimated mechanical properties and the distinct mechanical response of each specimen was established to demonstrate the significance of each property value and their role in uniquely identifying the material composition.

To conclude the work presented in this thesis, it is suitable to identify and mention possible avenues of extending the work and directions of future research studies.

With regard to confined granular systems, the contact formulation presented in Chapter 3 is limited to elastic-perfectly plastic material behavior. It is, therefore, desirable to extend the formulation to include strain hardening material behavior. Additionally, the loading-condition dependence of the formulation is limited to the three symmetric loading conditions (i.e., simple, die and hydrostatic), whereas a truly nonlocal contact formulation is capable of predicting contact behavior under any general loading configuration. Therefore, a systematic semi-mechanistic treatment of the nonlocal plastic contributions through extensive finite-element simulation studies is envisioned to take the next step forward in the development of a closed-form nonlocal contact formulation for plastically deforming particles.

With regard to particle-binder composites, as noted in Chapter 4, future work should be focused on utilizing the proposed experimental and post-processing procedures to study long-term effects of repetitive loading and recovery over several months on the microstructure and mechanical properties of the studied energetic materials. Additionally, as noted in Chapter 5, future work with respect to the large deformation constitutive model should be focused on extending the model to include rate-dependent viscous effects to characterize the moderate-to-high strain-rate behavior of these materials. Such a study would of course be supported by an extensive experimental campaign, including high strain-rate loading and stress-relaxation studies. Future work on including other recovery effects in the model, such as the recovery of transient cyclic response observed during the subsequent reloading of the mock specimens is also desirable and recommended.

REFERENCES

Addessio, F. L., & Johnson, J. N. (1990). A constitutive model for the dynamic response of brittle materials. *Journal of Applied Physics*, *67*, 3275–3286. doi:10.1063/1.346090.

Agarwal, A., & Gonzalez, M. (2018). Contact radius and curvature corrections to the nonlocal contact formulation accounting for multi-particle interactions in elastic confined granular systems. *International Journal of Engineering Science*, *133*, 26 – 46. doi:10.1016/j.ijengsci.2018.08.006.

Agarwal, A., & Gonzalez, M. (2020). Effects of cyclic loading and time-recovery on microstructure and mechanical properties of particle-binder composites. *Journal of Applied Mechanics*, *87*, 101008. doi:10.1115/1.4047038.

Akhavan, J. (2011). *Chemistry of Explosives*. (3rd ed.). Cambridge, UK: Royal Society of Chemistry.

Al-Raoush, R., & Papadopoulos, A. (2010). Representative elementary volume analysis of porous media using x-ray computed tomography. *Powder Technology*, *200*, 69 – 77. doi:10.1016/j.powtec.2010.02.011.

Almanstötter, J. (2015). A modified druckerprager cap model for finite element simulation of doped tungsten powder compaction. *International Journal of Refractory Metals and Hard Materials*, *50*, 290 – 297. doi:10.1016/j.ijrmhm.2015.02.005.

Argatov, I., Kachanov, M., & Mishuris, G. (2017). On the concept of far points in Hertz-contact problems. *International Journal of Engineering Science*, *113*, 20 – 36. doi:10.1016/j.ijengsci.2016.11.009.

Aurenhammer, F. (1987). Power diagrams: Properties, algorithms and applications. *SIAM Journal on Computing*, *16*, 78 – 96. doi:10.1137/0216006.

Aydin, İ., Briscoe, B. J., & Şanlitürk, K. Y. (1996). The internal form of compacted ceramic components: a comparison of a finite element modelling with experiment. *Powder Technology*, *89*, 239 – 254. doi:10.1016/S0032-5910(96)03188-9.

Ayoub, G., Zaïri, F., Naït-Abdelaziz, M., Gloaguen, J., & Kridli, G. (2014). A visco-hyperelastic damage model for cyclic stress-softening, hysteresis and permanent set in rubber using the network alteration theory. *International Journal of Plasticity*, *54*, 19–33. doi:10.1016/j.ijplas.2013.08.001.

Baker, C., & Gonzalez, M. (2020). Particle-scale modeling of particle-binder composites under weak impact loads. Manuscript in preparation.

Bakhshiani, A., Khoei, A., & Mofid, M. (2002). An endochronic plasticity model for powder compaction processes. *Journal of materials processing technology*, *125*, 138–143. doi:10.1016/S0924-0136(02)00360-6.

Bakhshiani, A., Khoei, A. R., & Mofid, M. (2004). A density-dependent endochronic plasticity for powder compaction processes. *Computational Mechanics*, *34*, 53–66. doi:10.1007/s00466-004-0553-5.

Bardenhagen, S., Harstad, E., Maudlin, P., Gray, G., & Foster Jr, J. (1998). Viscoelastic models for explosive binder materials. In *AIP Conference Proceedings* (pp. 281–284). AIP volume 429. doi:10.1063/1.55647.

Barua, A., & Zhou, M. (2011). A lagrangian framework for analyzing microstructural level response of polymer-bonded explosives. *Modelling and Simulation in Materials Science and Engineering*, *19*, 055001. doi:10.1088/0965-0393/19/5/055001.

Bay, B. K., Smith, T. S., Fyhrie, D. P., & Saad, M. (1999). Digital volume correlation: three-dimensional strain mapping using x-ray tomography. *Experimental mechanics*, *39*, 217–226. doi:10.1007/BF02323555.

Beatty, M. F., & Krishnaswamy, S. (2000). A theory of stress-softening in incompressible isotropic materials. *Journal of the Mechanics and Physics of Solids*, *48*, 1931–1965. doi:10.1016/S0022-5096(99)00085-X.

Belheine, N., Plassiard, J.-P., Donzé, F.-V., Darve, F., & Seridi, A. (2009). Numerical simulation of drained triaxial test using 3D discrete element modeling. *Computers and Geotechnics*, *36*, 320 – 331. doi:10.1016/j.compgeo.2008.02.003.

Bennett, J. G., Haberman, K. S., Johnson, J. N., & Asay, B. W. (1998). A constitutive model for the non-shock ignition and mechanical response of high explosives. *Journal of the Mechanics and Physics of Solids*, *46*, 2303–2322. doi:10.1016/S0022-5096(98)00011-8.

Bergström, J., & Boyce, M. (1998). Constitutive modeling of the large strain time-dependent behavior of elastomers. *Journal of the Mechanics and Physics of Solids*, *46*, 931–954. doi:10.1016/S0022-5096(97)00075-6.

Biwa, S., & Storåkers, B. (1995). An analysis of fully plastic Brinell indentation. *Journal of the Mechanics and Physics of Solids*, *43*, 1303 – 1333. doi:10.1016/0022-5096(95)00031-D.

Blair, D. L., Mueggenburg, N. W., Marshall, A. H., Jaeger, H. M., & Nagel, S. R. (2001). Force distributions in three-dimensional granular assemblies: effects of packing order and interparticle friction. *Physical review. E, Statistical, nonlinear, and soft matter physics*, *63*, 041304. doi:10.1103/PhysRevE.63.041304.

Blanchard, A., & Parkinson, D. (1952). Breakage of carbon-rubber networks by applied stress. *Industrial and Engineering Chemistry*, *44*, 799–812. doi:10.1021/ie50508a034.

Bommireddy, Y., Agarwal, A., Yettella, V., Tomar, V., & Gonzalez, M. (2019). Loading-unloading contact law for micro-crystalline cellulose particles under large deformations. *Mechanics Research Communications*, *99*, 22 – 31. doi:https://doi.org/10.1016/j.mechrescom.2019.06.004.

Boyce, M. C., & Arruda, E. M. (2000). Constitutive models of rubber elasticity: a review. *Rubber chemistry and technology*, *73*, 504–523. doi:10.5254/1.3547602.

Brake, M. (2012). An analytical elastic-perfectly plastic contact model. *International Journal of Solids and Structures*, *49*, 3129 – 3141. doi:10.1016/j.ijsolstr.2012.06.013.

Brake, M. (2015). An analytical elastic plastic contact model with strain hardening and frictional effects for normal and oblique impacts. *International Journal of Solids and Structures*, *62*, 104 – 123. doi:10.1016/j.ijsolstr.2015.02.018.

Brinell, J. (1900). Way of determining the hardness of bodies and some applications of the same. *Teknisk Tidskrift*, *5*, 69.

Bruck, H., McNeill, S., Sutton, M. A., & Peters, W. (1989). Digital image correlation using newton-raphson method of partial differential correction. *Experimental mechanics*, *29*, 261–267. doi:10.1007/BF02321405.

Buechler, M. A., & Luscher, D. J. (2014). A semi-implicit integration scheme for a combined viscoelastic-damage model of plastic bonded explosives. *International Journal for Numerical Methods in Engineering*, *99*, 54–78. doi:10.1002/nme.4672.

Burns, S. J., Piiroinen, P. T., & Hanley, K. J. (2019). Critical time step for DEM simulations of dynamic systems using a hertzian contact model. *International Journal for Numerical Methods in Engineering*, *119*, 432–451. doi:10.1002/nme.6056.

Cattaneo, C. (1947). Teoria del contatto elastico in seconds approssimazione. *Rendicontidi Mathematica e delle Sue Applicazioni, Serie V*, *6*, 504–512.

Chagnon, G., Verron, E., Marckmann, G., & Gornet, L. (2006). Development of new constitutive equations for the mullins effect in rubber using the network alteration theory. *International Journal of Solids and Structures*, *43*, 6817 – 6831. doi:https://doi.org/10.1016/j.ijsolstr.2006.02.011.

Chan, S., & Ngan, A. (2005). Statistical distribution of contact forces in packings of deformable spheres. *Mechanics of Materials*, *37*, 493 – 506. doi:10.1016/j.mechmat.2004.04.002.

Chen, L., Han, D., Bai, S.-L., Zhao, F., & Chen, J.-K. (2017). Compressive behavior and damage evaluation of a PBX substitute material. *Mechanics of Advanced Materials and Structures*, *24*, 737–744. doi:10.1080/15376494.2016.1196779.

Chen, Y., Imbault, D., & Dorémus, P. (2007). Numerical simulation of cold compaction of 3D granular packings. In *Progress in Powder Metallurgy* (pp. 301–304). Trans Tech Publications Ltd volume 534-536 of *Materials Science Forum*. doi:10.4028/www.scientific.net/MSF.534-536.301.

Chen, Y., Kang, G., Yuan, J., & Yu, C. (2018). Uniaxial ratchetting of filled rubber: Experiments and damage-coupled hyper-viscoelastic-plastic constitutive model. *Journal of Applied Mechanics*, *85*, 061013–061013–9. doi:10.1115/1.4039814.

Chtourou, H., Guillot, M., & Gakwaya, A. (2002). Modeling of the metal powder compaction process using the cap model. part i. experimental material characterization and validation. *International Journal of Solids and Structures*, *39*, 1059 – 1075. doi:10.1016/S0020-7683(01)00255-4.

Clements, B. E., & Mas, E. M. (2001). Dynamic mechanical behavior of filled polymers. I. Theoretical developments. *Journal of Applied Physics*, *90*, 5522–5534. doi:10.1063/1.1412843.

Coleman, B. D. (1964). Thermodynamics of materials with memory. *Archive for Rational Mechanics and Analysis*, *17*, 1–46. doi:10.1007/978-3-7091-2951-7.

Coleman, B. D., & Gurtin, M. E. (1967). Thermodynamics with internal state variables. *The Journal of Chemical Physics*, *47*, 597–613. doi:10.1063/1.1711937.

Coleman, B. D., & Noll, W. (1963). The thermodynamics of elastic materials with heat conduction and viscosity. *Archive for Rational Mechanics and Analysis*, *13*, 167–178. doi:10.1007/BF01262690.

Coleman, T., & Li, Y. (1996). An interior trust region approach for nonlinear minimization subject to bounds. *SIAM Journal on Optimization*, *6*, 418–445. doi:10.1137/0806023.

Conn, A. R., Gould, N. I., & Toint, P. L. (2000). *Trust region methods* volume 1. Society for Industrial and Applied Mathematics. doi:10.1137/1.9780898719857.

Coube, O., & Riedel, H. (2000). Numerical simulation of metal powder die compaction with special consideration of cracking. *Powder Metallurgy*, *43*, 123–131. doi:10.1179/003258900665871.

Cundall, P. A., & Strack, O. D. L. (1979). A discrete numerical model for granular assemblies. *Géotechnique*, *29*, 47–65. doi:10.1680/geot.1979.29.1.47.

Cunningham, J. C., Sinka, I. C., & Zavaliangos, A. (2004). Analysis of tablet compaction. I. characterization of mechanical behavior of powder and powder/tooling friction. *Journal of Pharmaceutical Sciences*, *93*, 2022 – 2039. doi:10.1002/jps.20110.

Daniel, M. A. (2006). *Polyurethane binder systems for polymer bonded explosives*. Technical Report DSTO-GD-0492 Defence Science and Technology Organisation Weapons Systems DIV Edinburgh, Australia.

Dargazany, R., Khiêm, V. N., & Itskov, M. (2014). A generalized network decomposition model for the quasi-static inelastic behavior of filled elastomers. *International Journal of Plasticity*, *63*, 94–109. doi:10.1016/j.ijplas.2013.12.004.

Diani, J., Fayolle, B., & Gilormini, P. (2009). A review on the mullins effect. *European Polymer Journal*, *45*, 601 – 612. doi:10.1016/j.eurpolymj.2008.11.017.

Dienes, J. K. (1996). A unified theory of flow, hot spots, and fragmentation with an application to explosive sensitivity. In L. Davison, D. E. Grady, & M. Shahinpoor (Eds.), *High-Pressure Shock Compression of Solids II: Dynamic Fracture and Fragmentation* (pp. 366–398). New York (NY), USA: Springer. doi:10.1007/978-1-4612-2320-7_14.

DiMaggio, F. L., & Sandler, I. S. (1971). Material model for granular soils. *Journal of the Engineering Mechanics Division, ASCE*, *97*, 935–951.

Dorfmann, A., & Ogden, R. (2003). A pseudo-elastic model for loading, partial unloading and reloading of particle-reinforced rubber. *International Journal of Solids and Structures*, *40*, 2699–2714. doi:10.1016/S0020-7683(03)00089-1.

Drodge, D. R., & Williamson, D. M. (2016). Understanding damage in polymer-bonded explosive composites. *Journal of Materials Science*, *51*, 668–679. doi:10.1007/s10853-013-7378-6.

Drucker, D. C., Gibson, R. E., & Henkel, D. J. (1957). Soil mechanics and work hardening theories of plasticity. *Transactions of the American Society of Civil Engineers*, *122*, 338 – 346.

Drucker, D. C., & Prager, W. (1952). Soil mechanics and plastic analysis or limit design. *Quarterly of Applied Mathematics*, *10*, 157–165. Accessed from http://www.jstor.org/stable/43633942.

Dummit, D. S. (1991). Solving solvable quintics. *Mathematics of Computation*, *57*, 387–401. doi:10.1090/S0025-5718-1991-1079014-X.

Egholm, R. D., Christensen, S. F., & Szabo, P. (2006). Stress-strain behavior in uniaxial compression of polymer gel beads. *Journal of Applied Polymer Science*, *102*, 3037–3047.

Fischmeister, H. F., & Arzt, E. (1983). Densification of powders by particle deformation. *Powder Metallurgy*, *26*, 82–88. doi:10.1179/pom.1983.26.2.82.

Frenning, G. (2008). An efficient finite/discrete element procedure for simulating compression of 3d particle assemblies. *Computer Methods in Applied Mechanics and Engineering*, *197*, 4266 – 4272. doi:10.1016/j.cma.2008.05.002.

Frenning, G. (2013). Towards a mechanistic model for the interaction between plastically deforming particles under confined conditions: A numerical and analytical analysis. *Materials Letters*, *92*, 365 – 368. doi:10.1016/j.matlet.2012.10.118.

Frenning, G. (2015). Towards a mechanistic contact model for elastoplastic particles at high relative densities. *Finite Elements in Analysis and Design*, *104*, 56 – 60. doi:10.1016/j.finel.2015.06.002.

Funk, D. J., Laabs, G. W., Peterson, P. D., & Asay, B. W. (1996). Measurement of the stress/strain response of energetic materials as a function of strain rate and temperature: PBX 9501 and mock 9501. In *AIP Conference Proceedings* (pp. 145–148). AIP volume 370. doi:10.1063/1.50735.

Gao, X.-L., Jing, X., & Subhash, G. (2006). Two new expanding cavity models for indentation deformations of elastic strain-hardening materials. *International Journal of Solids and Structures*, *43*, 2193 – 2208. doi:10.1016/j.ijsolstr.2005.03.062.

Gellatly, B., & Finney, J. (1982). Characterisation of models of multicomponent amorphous metals: The radical alternative to the voronoi polyhedron. *Journal of Non-Crystalline Solids*, *50*, 313 – 329. doi:https://doi.org/10.1016/0022-3093(82)90093-X.

Gethin, D. T., Lewis, R. W., & Ransing, R. S. (2002). A discrete deformable element approach for the compaction of powder systems. *Modelling and Simulation in Materials Science and Engineering*, *11*, 101–114. doi:10.1088/0965-0393/11/1/308.

Ghaednia, H., Wang, X., Saha, S., Xu, Y., Sharma, A., & Jackson, R. L. (2017). A review of elastic-plastic contact mechanics. *Applied Mechanics Reviews*, *69:060804*. doi:10.1115/1.4038187.

Goldrein, H., Rae, P., Palmer, S., & Lewis, A. (2001). Ageing effects on the mechanical properties of a polymer bonded explosive. In *Ageing Studies and Lifetime Extension of Materials* (pp. 129–136). Springer. doi:10.1007/978-1-4615-1215-8_13.

Gonzalez, M. (2019). Generalized loading-unloading contact laws for elasto-plastic spheres with bonding strength. *Journal of the Mechanics and Physics of Solids*, *122*, 633 – 656. doi:10.1016/j.jmps.2018.09.023.

Gonzalez, M., & Cuitiño, A. M. (2012). A nonlocal contact formulation for confined granular systems. *Journal of the Mechanics and Physics of Solids*, *60*, 333–350. doi:10.1016/j.jmps.2011.10.004.

Gonzalez, M., & Cuitiño, A. M. (2016). Microstructure evolution of compressible granular systems under large deformations. *Journal of the Mechanics and Physics of Solids*, *93*, 44–56. doi:10.1016/j.jmps.2016.03.024.

Gonzalez, M., Poorsolhjouy, P., Thomas, A., Liu, J., & Balakrishnan, K. (2018). Statistical characterization of microstructure evolution during compaction of granular systems composed of spheres with hardening plastic behavior. *Mechanics Research Communications*, *92*, 131 – 136. doi:10.1016/j.mechrescom.2018.08.010.

Govindjee, S., & Simo, J. (1991). A micro-mechanically based continuum damage model for carbon black-filled rubbers incorporating mullins' effect. *Journal of the Mechanics and Physics of Solids*, *39*, 87–112. doi:10.1016/0022-5096(91)90032-J.

Grantham, S., Siviour, C., Proud, W., & Field, J. (2004). High-strain rate brazilian testing of an explosive simulant using speckle metrology. *Measurement Science and Technology*, *15*, 1867. doi:10.1088/0957-0233/15/9/025.

Guo, J., Wu, L., Yang, X., & Zhong, S. (2016). Elastic-plastic endochronic constitutive model of 0Crl7Ni4Cu4Nb stainless steels. *Mathematical Problems in Engineering*, *2016*. doi:10.1155/2016/4396296.

Guo, Q., Zari, F., & Guo, X. (2018a). A thermo-viscoelastic-damage constitutive model for cyclically loaded rubbers. Part I: Model formulation and numerical examples. *International Journal of Plasticity*, *101*, 106 – 124. doi:https://doi.org/10.1016/j.ijplas.2017.10.011.

Guo, Q., Zari, F., & Guo, X. (2018b). A thermo-viscoelastic-damage constitutive model for cyclically loaded rubbers. Part II: Experimental studies and parameter identification. *International Journal of Plasticity*, *101*, 58 – 73. doi:https://doi.org/10.1016/j.ijplas.2017.10.009.

Gurtin, M. E., & Anand, L. (2005). The decomposition $F=F^eF^p$, material symmetry, and plastic irrotationality for solids that are isotropic-viscoplastic or amorphous. *International Journal of Plasticity*, *21*, 1686–1719. doi:10.1016/j.ijplas.2004.11.007.

Häggblad, H.-Å. (1991). Constitutive models for powder materials. *Powder Technology*, *67*, 127 – 137. doi:10.1016/0032-5910(91)80149-D.

Han, L. H., Elliott, J. A., Bentham, A. C., Mills, A., Amidon, G. E., & Hancock, B. C. (2008). A modified Drucker-Prager Cap model for die compaction simulation of pharmaceutical powders. *International Journal of Solids and Structures*, *45*, 3088 – 3106. doi:10.1016/j.ijsolstr.2008.01.024.

Hancock, B. C., Colvin, J. T., Mullarney, M. P., & Zinchuk, A. V. (2003). The relative densities of pharmaceutical powders, blends, dry granulations, and immediate-release tablets. *Pharmaceutical technology*, *27*, 64–80. Accessed from http://www.pharmtech.com/node/243786.

Hardy, C., Baronet, C. N., & Tordion, G. V. (1971). The elasto-plastic indentation of a half-space by a rigid sphere. *International Journal for Numerical Methods in Engineering*, *3*, 451–462. doi:10.1002/nme.1620030402.

Harthong, B., Jérier, J.-F., Dorémus, P., Imbault, D., & Donzé, F.-V. (2009). Modeling of high-density compaction of granular materials by the discrete element method. *International Journal of Solids and Structures*, *46*, 3357–3364. doi:10.1016/j.ijsolstr.2009.05.008.

Harthong, B., Jérier, J.-F., Richefeu, V., Chareyre, B., Dorémus, P., Imbault, D., & Donzé, F.-V. (2012). Contact impingement in packings of elasticplastic spheres, application to powder compaction. *International Journal of Mechanical Sciences*, *61*, 32 – 43. doi:https://doi.org/10.1016/j.ijmecsci.2012.04.013.

He, Y.-j., Mote, J., & Lange, D. A. (2013). Characterization of microstructure evolution of cement paste by micro computed tomography. *Journal of Central South University*, *20*, 1115–1121. doi:10.1007/s11771-013-1592-x.

Hertz, H. (1882). Ueber die berührung fester elastischer körper. *Journal für die reine und angewandte Mathematik*, *1882*, 156–171.

Hill, R. (1950). *The mathematical theory of plasticity*. Oxford engineering science series. Oxford, England: Clarendon Press.

Hill, R. (1958). A general theory of uniqueness and stability in elastic-plastic solids. *Journal of the Mechanics and Physics of Solids*, *6*, 236–249. doi:10.1016/0022-5096(58)90029-2.

Hill, R., Storåkers, B., & Zdunek, A. B. (1989). A theoretical study of the brinell hardness test. *Proceedings of the Royal Society of London. A. Mathematical and Physical Sciences*, *423*, 301–330. doi:10.1098/rspa.1989.0056.

Hollomon, J. H. (1945). Tensile deformation. *Transactions of American Institute of Mining and Metallurgical Engineers*, *162*, 268–290. Accessed from http://www.aimehq.org/doc library-assets/books/Metals%20Technology%201945%20Volume%20XII/T.P.%201879.pdf.

Holzapfel, G. A. (1996). On large strain viscoelasticity: Continuum formulation and finite element applications to elastomeric structures. *International Journal for Numerical Methods in Engineering*, *39*, 3903–3926. doi:10.1002/(SICI)1097-0207(19961130)39:22<3903::AID-NME34>3.0.CO;2-C.

Holzapfel, G. A. (2002). Nonlinear solid mechanics: A continuum approach for engineering science. *Meccanica*, *37*, 489–490. doi:10.1023/A:1020843529530.

Holzapfel, G. A., & Simo, J. C. (1996). A new viscoelastic constitutive model for continuous media at finite thermomechanical changes. *International Journal of Solids and Structures*, *33*, 3019–3034. doi:10.1016/0020-7683(95)00263-4.

Horstemeyer, M. F., & Bammann, D. J. (2010). Historical review of internal state variable theory for inelasticity. *International Journal of Plasticity*, *26*, 1310–1334. doi:10.1016/j.ijplas.2010.06.005. Special Issue In Honor of David L. McDowell.

Houwink, R. (1956). Slipping of molecules during the deformation of reinforced rubber. *Rubber Chemistry and Technology*, *29*, 888–893. doi:10.5254/1.3542602.

Hsu, S. Y., Jain, S. K., & Griffin, O. H. (1991). Verification of endochronic theory for nonproportional loading paths. *Journal of Engineering Mechanics*, *117*, 110–131. doi:10.1061/(ASCE)0733-9399(1991)117:1(110).

Hu, Z., Luo, H., Bardenhagen, S., Siviour, C., Armstrong, R., & Lu, H. (2015). Internal deformation measurement of polymer bonded sugar in compression by digital volume correlation of in-situ tomography. *Experimental Mechanics*, *55*, 289–300. doi:10.1007/s11340-014-9856-4.

Hu, Z., Luo, H., Du, Y., & Lu, H. (2016). Correlation of microscale deformations to macroscopic mechanical behavior using incremental digital volume correlation of in-situ tomography. In H. Jin, S. Yoshida, L. Lamberti, & M.-T. Lin (Eds.), *Advancement of Optical Methods in Experimental Mechanics* (pp. 125–137). Springer, Cham volume 3 of *Conference Proceedings of the Society for Experimental Mechanics*. doi:10.1007/978-3-319-22446-6_16.

Hudspeth, M., Sun, T., Parab, N., Guo, Z., Fezzaa, K., Luo, S., & Chen, W. (2015). Simultaneous X-ray diffraction and phase-contrast imaging for investigating material deformation mechanisms during high-rate loading. *Journal of Synchrotron Radiation*, *22*, 49–58. doi:10.1107/S1600577514022747.

Idar, D., Peterson, P., Scott, P., & Funk, D. (1998). Low strain rate compression measurements of PBXN-9, PBX 9501, and mock 9501. In *AIP Conference Proceedings* (pp. 587–590). AIP volume 429. doi:10.1063/1.55704.

Idar, D. J., Thompson, D. G., Gray, G. T., Blumenthal, W. R., Cady, C. M., Peterson, P. D., Roemer, E. L., Wright, W. J., & Jacquez, B. J. (2002). Influence of polymer molecular weight, temperature, and strain rate on the mechanical properties of PBX 9501. In *AIP Conference Proceedings* (pp. 821–824). AIP volume 620. doi:10.1063/1.1483663.

Jackson, R. L., & Green, I. (2003). A finite element study of elasto-plastic hemispherical contact. In *Proceedings of the STLE/ASME 2003 International Joint Tribology Conference. Contact Mechanics* (pp. 65–72). Ponte Vedra Beach, Florida, USA: ASME. doi:10.1115/2003-TRIB-0268.

Jackson, R. L., & Green, I. (2006). A statistical model of elasto-plastic asperity contact between rough surfaces. *Tribology International*, *39*, 906 – 914. doi:https://doi.org/10.1016/j.triboint.2005.09.001.

Jerier, J.-F., Hathong, B., Richefeu, V., Chareyre, B., Imbault, D., Donze, F.-V., & Doremus, P. (2011). Study of cold powder compaction by using the discrete element method. *Powder Technology*, *208*, 537 – 541. doi:10.1016/j.powtec.2010.08.056.

Jiang, Y., & Sehitoglu, H. (1994). Multiaxial cyclic ratchetting under multiple step loading. *International Journal of Plasticity*, *10*, 849 – 870. doi:10.1016/0749-6419(94)90017-5.

Jiang, Y., & Zhang, J. (2008). Benchmark experiments and characteristic cyclic plasticity deformation. *International Journal of Plasticity*, *24*, 1481–1515. doi:10.1016/j.ijplas.2007.10.003.

JMP®, Version 14 (2018). SAS Institute Inc., Cary, NC.

Johnson, K. (1970). The correlation of indentation experiments. *Journal of the Mechanics and Physics of Solids*, *18*, 115 – 126. doi:10.1016/0022-5096(70)90029-3.

Johnson, K. L. (1985). *Contact mechanics*. Cambridge: Cambridge University Press. doi:10.1017/CBO9781139171731.

Jonsson, H., Gråsjö, J., & Frenning, G. (2017). Mechanical behaviour of ideal elastic-plastic particles subjected to different triaxial loading conditions. *Powder Technology*, *315*, 347 – 355. doi:10.1016/j.powtec.2017.04.005.

Jonsson, H., Gråsjö, J., Nordström, J., Johansson, N., & Frenning, G. (2015). An apparatus for confined triaxial testing of single particles. *Powder Technology*, *270*, 121–127. doi:0.1016/j.powtec.2014.10.016.

Joseph, V. R., Gul, E., & Ba, S. (2015). Maximum projection designs for computer experiments. *Biometrika*, *102*, 371–380. doi:10.1093/biomet/asv002.

Kachanov, L. M. (1986). *Introduction to continuum damage mechanics* volume 10 of *Mechanics of elastic stability*. Springer, Netherlands. doi:10.1007/978-94-017-1957-5.

Kaliske, M., & Rothert, H. (1998). Constitutive approach to rate-independent properties of filled elastomers. *International Journal of Solids and Structures*, *35*, 2057 – 2071. doi:https://doi.org/10.1016/S0020-7683(97)00182-0.

Kerschen, N., Guo, Z., Sun, T., Claus, B., Mares, J., Fezzaa, K., & Chen, W. (2017). Visualization of PBX response to impact loading. In *32nd Technical Conference of the American Society for Composites 2017* (pp. 1485–1490). DEStech Publications Inc. volume 2. doi:10.12783/asc2017/15285.

Keyhani, A., Kim, S., Horie, Y., & Zhou, M. (2019). Energy dissipation in polymer-bonded explosives with various levels of constituent plasticity and internal friction. *Computational Materials Science*, *159*, 136 – 149. doi:https://doi.org/10.1016/j.commatsci.2018.12.008.

Khoei, A., & Bakhshiani, A. (2004). A hypoelasto-plastic finite strain simulation of powder compaction processes with density-dependent endochronic model. *International journal of solids and structures*, *41*, 6081–6110. doi:10.1016/j.ijsolstr.2004.05.013.

Khoei, A., Bakhshiani, A., & Mofid, M. (2003). An endochronic plasticity model for finite strain deformation of powder forming processes. *Finite Elements in Analysis and Design*, *40*, 187–211. doi:10.1016/S0168-874X(02)00223-8.

Khoei, A., Mofid, M., & Bakhshiani, A. (2002). Modelling of powder compaction process using an endochronic plasticity model. *Journal of Materials Processing Technology*, *130-131*, 175 – 180. doi:10.1016/S0924-0136(02)00708-2. AFDM 2002 S.I.

King, R., & Bourgeois, F. (1993). Measurement of fracture energy during single-particle fracture. *Minerals Engineering*, *6*, 353 – 367. doi:10.1016/0892-6875(93)90015-F.

Klüppel, M. (2003). The role of disorder in filler reinforcement of elastomers on various length scales. In B. Capella, M. Geuss, M. Klüppel, M. Munz, E. Schulz, & H. Sturm (Eds.), *Filler-Reinforced Elastomers Scanning Force Microscopy* (pp. 1–86). Berlin, Heidelberg: Springer. doi:10.1007/b11054.

Koloushani, M., Hedayati, R., Sadighi, M., & Mohammadi-Aghdam, M. (2018). CT-based micro-mechanical approach to predict response of closed-cell porous biomaterials to low-velocity impact. *Journal of Imaging*, *4*, 49. doi:10.3390/jimaging4030049.

Kraus, G., Childers, C. W., & Rollmann, K. W. (1966). Stress softening in carbon black-reinforced vulcanizates. Strain rate and temperature effects. *Journal of Applied Polymer Science*, *10*, 229–244. doi:10.1002/app.1966.070100205.

Kröner, E. (1959). Allgemeine kontinuumstheorie der versetzungen und eigenspannungen. *Archive for Rational Mechanics and Analysis*, *4*, 273–334. doi:10.1007/BF00281393.

Kumar, A., Rao, V., Sinha, R., & Rao, A. (2010). Evaluation of plastic bonded explosive (PBX) formulations based on RDX, aluminum, and HTPB for underwater applications. *Propellants, Explosives, Pyrotechnics*, *35*, 359–364. doi:10.1002/prep.200800048.

Laiarinandrasana, L., Piques, R., & Robisson, A. (2003). Visco-hyperelastic model with internal state variable coupled with discontinuous damage concept under total lagrangian formulation. *International Journal of Plasticity*, *19*, 977–1000. doi:10.1016/S0749-6419(02)00089-X.

Le, V. D., Gratton, M., Caliez, M., Frachon, A., & Picart, D. (2010). Experimental mechanical characterization of plastic-bonded explosives. *Journal of Materials Science*, *45*, 5802–5813. doi:10.1007/s10853-010-4655-5.

Lee, E., & Liu, D. (1967). Finite-strain elastic-plastic theory with application to plane-wave analysis. *Journal of Applied Physics*, *38*, 19–27. doi:10.1063/1.1708953.

Lee, E. H. (1969). Elastic-plastic deformation at finite strains. *Journal of Applied Mechanics*, *36*, 1–6. doi:10.1115/1.3564580.

Lemaitre, J., Chaboche, J.-L., & Germain, P. (1985). *Mécanique des matériaux solides* volume 2. Paris, France: Dunod.

Li, J., Lu, F., Qin, J., Chen, R., Zhao, P., Lan, L., & Jing, S. (2012). Effects of temperature and strain rate on the dynamic responses of three polymer-bonded explosives. *The Journal of Strain Analysis for Engineering Design*, *47*, 104–112. doi:10.1177/0309324711428836.

Lin, H.-Y., Yeh, W.-C., & Lee, W.-J. (2007). A material function of endochronic theory and its application to test under axisymmetrically cyclic loading conditions. *Journal of Mechanics*, *23*, 135–148. doi:10.1017/S1727719100001167.

Liu, B., Huang, W., Wang, H., Wang, M., & Li, X. (2014a). Study on the load partition behaviors of high particle content B_4C/Al composites in compression. *Journal of Composite Materials*, *48*, 355–364. doi:10.1177/0021998312472220.

Liu, K. K., Williams, D. R., & Briscoe, B. J. (1998). The large deformation of a single micro-elastomeric sphere. *Journal of Physics D: Applied Physics*, *31*, 294–303. doi:10.1088/0022-3727/31/3/008.

Liu, L., Jia, Z., Ma, X., Fan, Y., Li, W., & Liu, H. (2014b). A spherical cavity expansion model of large elastic deformation and its application to ballistic gelatin penetration problems. *International Journal of Impact Engineering*, *71*, 106 – 116. doi:10.1016/j.ijimpeng.2014.04.007.

Lochert, I. J., Dexter, R. M., & Hamshere, B. L. (2002). *Evaluation of Australian RDX in PBXN-109*. Technical Report DSTO-TN-0440. Defence Science and Technology Organisation, Weapons Systems Division, Edinburgh (SA), Australia.

Lu, W.-M., Tung, K.-L., Hung, S.-M., Shiau, J.-S., & Hwang, K.-J. (2001). Compression of deformable gel particles. *Powder Technology*, *116*, 1–12. doi:10.1016/S0032-5910(00)00357-0.

Ludwik, P. (1909). *Elemente der technologischen Mechanik*. Springer, Berlin, Heidelberg. doi:10.1007/978-3-662-40293-1.

Luo, J.-D. (1958). A second approximation solution on the elastic contact problem. *Scientia Sinica*, *7*, 1235–1247. doi:10.1360/ya1958-7-12-1235.

Majmudar, T. S., & Behringer, R. P. (2005). Contact force measurements and stress-induced anisotropy in granular materials. *Nature*, *435*, 1079. doi:10.1038/nature03805.

Makse, Johnson, & Schwartz (2000). Packing of compressible granular materials. *Physical review letters*, *84 18*, 4160–3. doi:10.1103/PhysRevLett.84.4160.

Manner, V. W., Yeager, J. D., Patterson, B. M., Walters, D. J., Stull, J. A., Cordes, N. L., Luscher, D. J., Henderson, K. C., Schmalzer, A. M., & Tappan, B. C. (2017). In situ imaging during compression of plastic bonded explosives for damage modeling. *Materials*, *10*, 638. doi:10.3390/ma10060638.

Marckmann, G., Verron, E., Gornet, L., Chagnon, G., Charrier, P., & Fort, P. (2002). A theory of network alteration for the mullins effect. *Journal of the Mechanics and Physics of Solids*, *50*, 2011 – 2028. doi:https://doi.org/10.1016/S0022-5096(01)00136-3.

Marigo, M., Cairns, D., Bowen, J., Ingram, A., & Stitt, E. (2014). Relationship between single and bulk mechanical properties for zeolite zsm5 spray-dried particles. *Particuology*, *14*, 130 – 138. doi:10.1016/j.partic.2013.05.006.

Martin, C., & Bouvard, D. (2003). Study of the cold compaction of composite powders by the discrete element method. *Acta Materialia*, *51*, 373 – 386. doi:10.1016/S1359-6454(02)00402-0.

Martin, C., Bouvard, D., & Shima, S. (2003). Study of particle rearrangement during powder compaction by the discrete element method. *Journal of the Mechanics and Physics of Solids*, *51*, 667 – 693. doi:10.1016/S0022-5096(02)00101-1.

Martin, C. L., Bouvard, D., & Delette, G. (2006). Discrete element simulations of the compaction of aggregated ceramic powders. *Journal of the American Ceramic Society*, *89*, 3379–3387. doi:10.1111/j.1551-2916.2006.01249.x.

Mata, M., Casals, O., & Alcalá, J. (2006). The plastic zone size in indentation experiments: The analogy with the expansion of a spherical cavity. *International Journal of Solids and Structures*, *43*, 5994 – 6013. doi:10.1016/j.ijsolstr.2005.07.002.

Mathematica, Version 12.0 (2019). Wolfram Research, Inc., Champaign, IL.

MATLAB®, Version 9.4.0 (2018a). Natick, Massachusetts: The MathWorks Inc., 1984–2018.

Matouš, K., & Geubelle, P. H. (2006). Multiscale modelling of particle debonding in reinforced elastomers subjected to finite deformations. *International Journal for Numerical Methods in Engineering*, *65*, 190–223. doi:10.1002/nme.1446.

Mesarovic, S. D., & Fleck, N. A. (2000). Frictionless indentation of dissimilar elastic-plastic spheres. *International Journal of Solids and Structures*, *37*, 7071–7091. doi:10.1016/S0020-7683(99)00328-5.

Michrafy, A., Ringenbacher, D., & Tchoreloff, P. (2002). Modelling the compaction behaviour of powders: application to pharmaceutical powders. *Powder Technology*, *127*, 257 – 266. doi:10.1016/S0032-5910(02)00119-5.

Miehe, C., & Keck, J. (2000). Superimposed finite elastic–viscoelastic–plastoelastic stress response with damage in filled rubbery polymers. experiments, modelling and algorithmic implementation. *Journal of the Mechanics and Physics of Solids*, *48*, 323–365. doi:10.1016/S0022-5096(99)00017-4.

Montes, J., Cuevas, F., & Cintas, J. (2006). A new expression for the effective pressure on powders under compression. *Computational Materials Science*, *36*, 329 – 337. doi:10.1016/j.commatsci.2005.04.008.

Mooney, M. (1940). A theory of large elastic deformation. *Journal of Applied Physics*, *11*, 582–592. doi:10.1063/1.1712836.

Mukunoki, T., Miyata, Y., Mikami, K., & Shiota, E. (2016). X-ray CT analysis of pore structure in sand. *Solid Earth*, *7*, 929–942. doi:10.5194/se-7-929-2016.

Mullins, L. (1948). Effect of stretching on the properties of rubber. *Rubber Chemistry and Technology*, *21*, 281–300. doi:10.5254/1.3546914.

Mullins, L. (1969). Softening of rubber by deformation. *Rubber Chemistry and Technology*, *42*, 339–362. doi:10.5254/1.3539210.

Netzker, C., Dal, H., & Kaliske, M. (2010). An endochronic plasticity formulation for filled rubber. *International Journal of Solids and Structures*, *47*, 2371–2379. doi:10.1016/j.ijsolstr.2010.04.026.

Ogden, R. W. (1972a). Large deformation isotropic elasticity – on the correlation of theory and experiment for incompressible rubberlike solids. *Proceedings of the Royal Society of London A: Mathematical, Physical and Engineering Sciences*, *326*, 565–584. doi:10.1098/rspa.1972.0026.

Ogden, R. W. (1972b). Large deformation isotropic elasticity: on the correlation of theory and experiment for compressible rubberlike solids. *Proceedings of the Royal Society of London A: Mathematical, Physical and Engineering Sciences*, *328*, 567–583. doi:10.1098/rspa.1972.0096.

Ogden, R. W. (1984). *Non-linear Elastic Deformations*. Mineola (NY), USA: Dover Publications.

Ogden, R. W., & Roxburgh, D. G. (1999). A pseudo–elastic model for the mullins effect in filled rubber. *Proceedings of the Royal Society of London A: Mathematical, Physical and Engineering Sciences*, *455*, 2861–2877. doi:10.1098/rspa.1999.0431.

Olsson, E., & Larsson, P.-L. (2013a). On force–displacement relations at contact between elastic–plastic adhesive bodies. *Journal of the Mechanics and Physics of Solids*, *61*, 1185–1201. doi:10.1016/j.jmps.2013.01.004.

Olsson, E., & Larsson, P.-L. (2013b). On the appropriate use of representative stress quantities at correlation of spherical contact problems. *Tribology Letters*, *50*, 221–232. doi:10.1007/s11249-013-0114-1.

Olsson, E., & Larsson, P.-L. (2016). A unified model for the contact behaviour between equal and dissimilar elasticplastic spherical bodies. *International Journal of Solids and Structures*, *81*, 23 – 32. doi:10.1016/j.ijsolstr.2015.10.004.

Omnès, B., Thuillier, S., Pilvin, P., Grohens, Y., & Gillet, S. (2008). Effective properties of carbon black filled natural rubber: Experiments and modeling. *Composites Part A: Applied Science and Manufacturing*, *39*, 1141–1149. doi:10.1016/j.compositesa.2008.04.003.

Österlöf, R., Wentzel, H., & Kari, L. (2016). A finite strain viscoplastic constitutive model for rubber with reinforcing fillers. *International Journal of Plasticity*, *87*, 1 – 14. doi:https://doi.org/10.1016/j.ijplas.2016.08.008.

Palmer, S. J. P., Field, J. E., & Huntley, J. M. (1993). Deformation, strengths and strains to failure of polymer bonded explosives. *Proceedings of the Royal Society of London. Series A: Mathematical and Physical Sciences*, *440*, 399–419. doi:10.1098/rspa.1993.0023.

Parab, N. D., Roberts, Z. A., Harr, M. H., Mares, J. O., Casey, A. D., Gunduz, I. E., Hudspeth, M., Claus, B., Sun, T., Fezzaa, K., Son, S. F., & Chen, W. W. (2016). High speed X-ray phase contrast imaging of energetic composites under dynamic compression. *Applied Physics Letters*, *109*, 131903. doi:10.1063/1.4963137.

Paripovic, J., & Davies, P. (2013). Identification of the dynamic behavior of surrogate explosive materials. In *International Design Engineering Technical Conferences and Computers and Information in Engineering Conference; 22nd Reliability, Stress Analysis, and Failure Prevention Conference; 25th Conference on Mechanical Vibration and Noise* (p. V008T13A066). ASME volume 8. doi:10.1115/DETC2013-12755.

Paripovic, J., & Davies, P. (2016). A model identification technique to characterize the low frequency behaviour of surrogate explosive materials. *Journal of Physics: Conference Series*, *744*, 012124. doi:10.1088/1742-6596/744/1/012124.

Paul, S. K., Sivaprasad, S., Dhar, S., & Tarafder, S. (2011). Key issues in cyclic plastic deformation: experimentation. *Mechanics of Materials*, *43*, 705–720. doi:10.1016/j.mechmat.2011.07.011.

Pijaudier-Cabot, G., Bittnar, Z., & Gérard, B. (1999). *Mechanics of quasi-brittle materials and structures*. Paris, France: Hermes Science Publications.

Plagge, J., & Klppel, M. (2017). A physically based model of stress softening and hysteresis of filled rubber including rate- and temperature dependency. *International Journal of Plasticity*, *89*, 173 – 196. doi:https://doi.org/10.1016/j.ijplas.2016.11.010.

Poorsolhjouy, P., & Gonzalez, M. (2018). Connecting discrete particle mechanics to continuum granular micromechanics: Anisotropic continuum properties under compaction. *Mechanics Research Communications*, *92*, 21 – 27. doi:10.1016/j.mechrescom.2018.07.001.

Portnikov, D., & Kalman, H. (2014). Determination of elastic properties of particles using single particle compression test. *Powder Technology*, *268*, 244 – 252. doi:10.1016/j.powtec.2014.08.011.

Prager, W. (1961). An elementary discussion of definitions of stress rate. *Quarterly of Applied Mathematics*, *18*, 403–407. doi:10.1090/qam/116567.

Prakash, V., Phadke, V. K., Sinha, R. K., & Singh, H. (2004). Influence of aluminium on performance of HTPB-based aluminised PBXs. *Defence Science Journal*, *54*, 475–482. doi:10.14429/dsj.54.2061.

Procopio, A. T., & Zavaliangos, A. (2005). Simulation of multi-axial compaction of granular media from loose to high relative densities. *Journal of the Mechanics and Physics of Solids*, *53*, 1523 – 1551. doi:10.1016/j.jmps.2005.02.007.

Puri, V. M., Tripodi, M. A., Manbeck, H., & Messing, G. L. (1995). Constitutive model for dry cohesive powders with application to powder compaction. *KONA Powder and Particle Journal*, *13*, 135–150. doi:10.14356/kona.1995018.

Quicksall, J. J., Jackson, R. L., & Green, I. (2004). Elasto-plastic hemispherical contact models for various mechanical properties. *Proceedings of the Institution of Mechanical Engineers, Part J: Journal of Engineering Tribology*, *218*, 313–322. doi:10.1243/135065 0041762604.

Rae, P. J., Goldrein, H. T., Palmer, S. J. P., Field, J. E., & Lewis, A. L. (2002). Quasi-static studies of the deformation and failure of β-HMX based polymer bonded explosives. *Proceedings of the Royal Society of London. Series A: Mathematical, Physical and Engineering Sciences*, *458*, 743–762. doi:10.1098/rspa.2001.0894.

Raghunath, R., Juhre, D., & Klüppel, M. (2016). A physically motivated model for filled elastomers including strain rate and amplitude dependency in finite viscoelasticity. *International Journal of Plasticity*, *78*, 223–241. doi:10.1016/j.ijplas.2015.11.005.

Rangaswamy, P., Thompson, D. G., Liu, C., & Lewis, M. W. (2010). Modeling the mechanical response of PBX 9501. In *Proceedings of the 14th International Detonation Symposium* (pp. 174–183). Coeur d'Alene (ID), USA.

Range, A. R., McMindes, N. R., Tucker, J. B., & Rhoads, J. F. (2018). The influence of formulation variation and thermal boundary conditions on the near-resonant thermomechanics of mock explosives. In J. Carroll, S. Xia, A. Beese, R. Berke, & G. Pataky (Eds.), *Fracture, Fatigue, Failure and Damage Evolution, Volume 7. Conference Proceedings of the Society for Experimental Mechanics Series*. Springer, Cham. doi:10.1007/978-3-319-62831-8_7.

Rathbone, D., Marigo, M., Dini, D., & van Wachem, B. (2015). An accurate force-displacement law for the modelling of elastic-plastic contacts in discrete element simulations. *Powder Technology*, *282*, 2 – 9. doi:10.1016/j.powtec.2014.12.055. Particle Science and Technology- UK-China International Particle Technology Forum IV.

Rattanasom, N., Saowapark, T., & Deeprasertkul, C. (2007). Reinforcement of natural rubber with silica/carbon black hybrid filler. *Polymer Testing*, *26*, 369–377. doi:10.1016/j.polymertesting.2006.12.003.

Ravindran, S., Gupta, V., Tessema, A., & Kidane, A. (2019). Effect of particle mass fraction on the multiscale dynamic failure behavior of particulate polymer composites. *Experimental Mechanics*, *59*, 599–609. doi:10.1007/s11340-019-00493-4.

Rivlin, R. (1948). Large elastic deformations of isotropic materials IV. Further developments of the general theory. *Philosophical Transactions of the Royal Society A*, *241*, 379–397. doi:10.1098/rsta.1948.0024.

Rojek, J., Nosewicz, S., Jurczak, K., Chmielewski, M., Bochenek, K., & Pietrzak, K. (2016). Discrete element simulation of powder compaction in cold uniaxial pressing with low pressure. *Computational Particle Mechanics*, *3*, 513–524. doi:10.1007/s40571-015-0093-0.

Rougier, E., Munjiza, A., & John, N. W. M. (2004). Numerical comparison of some explicit time integration schemes used in DEM, FEM/DEM and molecular dynamics. *International Journal for Numerical Methods in Engineering*, *61*, 856–879. doi:10.1002/nme.1092.

Rumchik, C., & Jordan, J. (2007). Effect of aluminum particle size on the high strain rate properties of pressed aluminized explosives. In *AIP Conference Proceedings* (pp. 795–798). AIP volume 955. doi:10.1063/1.2833243.

Santner, T. J., Williams, B. J., & Notz, W. I. (2013). *The design and analysis of computer experiments*. Springer, New York, NY. doi:10.1007/978-1-4757-3799-8.

SAS Institute Inc. (2018). *JMP® Design of Experiments Guide*. SAS Institute Inc. Cary, NC.

Scarfe, W. C., & Farman, A. G. (2008). What is cone-beam CT and how does it work? *Dental Clinics of North America*, *52*, 707–730. doi:10.1016/j.cden.2008.05.005.

Schofield, A., & Wroth, P. (1968). *Critical state soil mechanics*. McGraw-hill.

Shapiro, L., & Stockman, G. (2001). *Computer Vision*. Prentice Hall.

Sheng, Y., Lawrence, C., Briscoe, B., & Thornton, C. (2004). Numerical studies of uniaxial powder compaction process by 3D DEM. *Engineering Computations*, *21*, 304–317. doi:10.1108/02644400410519802.

Sheng, Y., Lawrence, C. J., Briscoe, B. J., & Thornton, C. (2002). 3D DEM simulations of powder compaction. In *Discrete Element Methods* (pp. 305–310). doi:10.1061/40647(259)54.

Shima, S., Tatara, Y., Iio, M., Shu, C., & Lucero, C. J. (1993). Large deformations of a rubber sphere under diametral compression : Part 2 : Experiments on many rubber materials and comparisons of theories with experiments. *JSME international journal. Ser. A, Mechanics and material engineering*, *36*, 197–205. doi:10/ckbs.

Simo, J. (1987). On a fully three-dimensional finite-strain viscoelastic damage model: Formulation and computational aspects. *Computer Methods in Applied Mechanics and Engineering*, *60*, 153–173. doi:10.1016/0045-7825(87)90107-1.

Sinha, T., Curtis, J. S., Hancock, B. C., & Wassgren, C. (2010). A study on the sensitivity of Drucker-Prager Cap model parameters during the decompression phase of powder compaction simulations. *Powder Technology*, *198*, 315 – 324. doi:10.1016/j.powtec.2009.10.025.

Sinka, I., Cunningham, J., & Zavaliangos, A. (2003). The effect of wall friction in the compaction of pharmaceutical tablets with curved faces: a validation study of the druckerprager cap model. *Powder Technology*, *133*, 33 – 43. doi:10.1016/S0032-5910(03)00094-9.

Sinka, I. C., Cunningham, J. C., & Zavaliangos, A. (2004). Analysis of tablet compaction. II. finite element analysis of density distributions in convex tablets. *Journal of Pharmaceutical Sciences*, *93*, 2040 – 2053. doi:10.1002/jps.20111.

Skrinjar, O., & Larsson, P.-L. (2004). On discrete element modelling of compaction of powders with size ratio. *Computational Materials Science*, *31*, 131 – 146. doi:10.1016/j.commatsci.2004.02.005.

Spence, D. A., & Temple, G. F. J. (1968). Self similar solutions to adhesive contact problems with incremental loading. *Proceedings of the Royal Society of London. Series A. Mathematical and Physical Sciences*, *305*, 55–80. doi:10.1098/rspa.1968.0105.

Storåkers, B., Biwa, S., & Larsson, P.-L. (1997). Similarity analysis of inelastic contact. *International Journal of Solids and Structures*, *34*, 3061–3083. doi:10.1016/S0020-7683(96)00176-X.

Storåkers, B., & Larsson, P.-L. (1994). On brinell and boussinesq indentation of creeping solids. *Journal of the Mechanics and Physics of Solids*, *42*, 307 – 332. doi:10.1016/0022-5096(94)90012-4.

Stronge, W. J. (2018). *Impact Mechanics*. (2nd ed.). Cambridge University Press. doi:10.1017/9781139050227.

Studman, C. J., Moore, M. A., & Jones, S. E. (1977). On the correlation of indentation experiments. *Journal of Physics D: Applied Physics*, *10*, 949. doi:10.1088/0022-3727/10/6/019.

Sun, X.-K., & Kim, K.-T. (1997). Simulation of cold die compaction densification behaviour of iron and copper powders by camclay model. *Powder Metallurgy*, *40*, 193–195. doi:10.1179/pom.1997.40.3.193.

Sundstrom, B., & Fischmeister, H. F. (1973). Continuum mechanical model for hot and cold compaction. *Powder Metallurgy International*, *5*, 171–174.

Tabor, D. (1951). *The hardness of metals*. Clarendine Press, Oxford.

Tang, M.-f., Pang, H.-y., Lan, L.-g., Wen, M.-p., & Ming, L. (2016). Constitutive behavior of RDX-based PBX with loading-history and loading-rate effects. *Chinese Journal of Energetic Materials*, *24*, 832–837. doi:10.11943/j.issn.1006-9941.2016.09.002.

Tatara, Y. (1989). Extensive theory of force-approach relations of elastic spheres in compression and in impact. *Journal of engineering materials and technology*, *111*, 163–168. doi:10.1115/1.3226449.

Tatara, Y. (1991). On compression of rubber elastic sphere over a large range of displacements–Part 1: Theoretical study. *Journal of engineering materials and technology*, *113*, 285–291. doi:10.1115/1.2903407.

Tatara, Y., Shima, S., & Lucero, J. C. (1991). On compression of rubber elastic sphere over a large range of displacements–Part 2: Comparison of theory and experiment. *Journal of engineering materials and technology*, *113*, 292–295. doi:10.1115/1.2903408.

Thompson, D. G., Deluca, R., & Brown, G. W. (2012). Time-temperature analysis, tension and compression in PBXs. *Journal of Energetic Materials*, *30*, 299–323. doi:10.1080/07370652.2011.569831.

Thompson, D. G., Idar, D. J., Gray, G., Blumenthal, W. R., Cady, C. M., Roemer, E. L., Wright, W. J., & Peterson, P. D. (2002). Quasi-static and dynamic mechanical properties of new and virtually-aged PBX 9501 composites as a function of temperature and strain rate. In *Proceedings of the 12th International Detonation Symposium* (pp. 363–368). San Diego (CA), USA.

Thornton, C., & Ning, Z. (1998). A theoretical model for the stick/bounce behaviour of adhesive, elastic-plastic spheres. *Powder Technology*, *99*, 154 – 162. doi:10.1016/S0032-5910(98)00099-0.

Timoshenko, S. P., & Goodier, J. N. (1970). *Theory of Elasticity*. McGraw-Hill.

Topin, V., Delenne, J. Y., Radjaı, F., Brendel, L., & Mabille, F. (2007). Strength and failure of cemented granular matter. *The European Physical Journal E*, *23*, 413–429. doi:10.1140/epje/i2007-10201-9.

Topuz, F., & Okay, O. (2009). Macroporous hydrogel beads of high toughness and superfast responsivity. *Reactive and Functional Polymers*, *69*, 273–280. doi:10.1016/j.reactfunctpolym.2009.01.009.

Trott, M., & Adamchik, V. (2001). Solving the qunitic with mathematica. Wolfram Library Archive, https://library.wolfram.com/infocenter/TechNotes/158. Accessed: 2020-03-13.

Trumel, H., Lambert, P., & Biessy, M. (2012). Mechanical and microstructural characterization of a HMX-based pressed explosive: Effects of combined high pressure and strain rate. *EPJ Web of Conferences*, *26*, 02005. doi:10.1051/epjconf/20122602005.

Tsigginos, C., Strong, J., & Zavaliangos, A. (2015). On the force-displacement law of contacts between spheres pressed to high relative densities. *International Journal of Solids and Structures*, *60-61*, 17–27. doi:10.1016/j.ijsolstr.2015.01.024.

Valanis, K., & Read, H. (1986). An endochronic plasticity theory for concrete. *Mechanics of Materials*, *5*, 277–295. doi:10.1016/0167-6636(86)90024-4.

Valanis, K. C. (1970). *A theory of viscoplasticity without a yield surface part 1 - general theory*. Technical Report AFOSR-71-1765. Air Force Office of Scientific Research, Office of Aerospace Research, US Air Force, Arlington (VA), USA.

Valanis, K. C. (1972). *Irreversible thermodynamics of continuous media: internal variable theory* volume 77 of *International Centre for Mechanical Sciences book series*. Springer, Vienna. doi:10.1007/978-3-7091-2987-6.

Valanis, K. C., & Lee, C. (1984). Endochronic theory of cyclic plasticity with applications. *Journal of Applied Mechanics*, *51*, 367–374. doi:10.1115/1.3167627.

Vu-Quoc, L., Zhang, X., & Lesburg, L. (1999). A normal force-displacement model for contacting spheres accounting for plastic deformation: Force-driven formulation. *Journal of Applied Mechanics*, *67*, 363–371. doi:10.1115/1.1305334.

Wang, C., Cowen, C., Zhang, Z., & Thomas, C. (2005). High-speed compression of single alginate microspheres. *Chemical Engineering Science*, *60*, 6649–6657. doi:10.1016/j.ces.2005.05.052.

Ward Jr., J. H. (1963). Hierarchical grouping to optimize an objective function. *Journal of the American Statistical Association*, *58*, 236–244. doi:10.1080/01621459.1963.10500845.

Wellington, S. L., & Vinegar, H. J. (1987). X-ray computerized tomography. *Journal of Petroleum Technology*, *39*, 885–898. doi:10.2118/16983-PA.

Wiegand, D. A. (2000). The influence of confinement on the mechanical properties of energetic materials. In *AIP Conference Proceedings* (pp. 675–678). AIP volume 505. doi:10.1063/1.1303563.

Wiegand, D. A., & Reddingius, B. (2005). Mechanical properties of confined explosives. *Journal of Energetic Materials*, *23*, 75–98. doi:10.1080/07370650590936415.

Williamson, D. M., Palmer, S. J. P., Proud, W. G., & Govier, R. (2007). Brazilian disc testing of a UK PBX above and below the glass transition temperature. In *AIP Conference Proceedings* (pp. 803–806). volume 955. doi:10.1063/1.2833246.

Williamson, D. M., Siviour, C. R., Proud, W. G., Palmer, S. J. P., Govier, R., Ellis, K., Blackwell, P., & Leppard, C. (2008). Temperature-time response of a polymer bonded explosive in compression (EDC37). *Journal of Physics D: Applied Physics*, *41*, 085404. doi:10.1088/0022-3727/41/8/085404.

Wu, C.-Y., Ruddy, O., Bentham, A., Hancock, B., Best, S., & Elliott, J. (2005). Modelling the mechanical behaviour of pharmaceutical powders during compaction. *Powder Technology*, *152*, 107 – 117. doi:10.1016/j.powtec.2005.01.010.

Wu, H., & Yip, M. (1981). Endochronic description of cyclic hardening behavior for metallic materials. *Journal of Engineering Materials and Technology*, *103*, 212–217. doi:10.1115/1.3225003.

X. Allan Zhong, W. G. K. (2000). Effects of particle interaction and size variation on damage evolution in filled elastomers. *Mechanics of Composite Materials and Structures*, *7*, 35–53. doi:10.1080/107594100305410.

Yan, Y., Zhang, Z., Stokes, J. R., Zhou, Q. Z., Ma, G. H., & Adams, M. J. (2009). Mechanical characterization of agarose micro-particles with a narrow size distribution. *Powder Technology*, *192*, 122–130. doi:10.1016/j.powtec.2008.12.006.

hua YANG, B., xiang WU, A., xiu MIAO, X., & zhi LIU, J. (2014). 3D characterization and analysis of pore structure of packed ore particle beds based on computed tomography images. *Transactions of Nonferrous Metals Society of China*, *24*, 833 – 838. doi:10.1016/S1003-6326(14)63131-9.

Yang, K., Wu, Y., & Huang, F. (2018). Numerical simulations of microcrack-related damage and ignition behavior of mild-impacted polymer bonded explosives. *Journal of Hazardous Materials*, *356*, 34–52. doi:10.1016/j.jhazmat.2018.05.029.

Yeh, W.-C. (1995). Verification of the endochronic theory of plasticity under biaxial load. *Journal of the Chinese Institute of Engineers*, *18*, 25–34. doi:10.1080/02533839.1995.9677663.

Yermukhambetova, A., Tan, C., Daemi, S. R., Bakenov, Z., Darr, J. A., Brett, D. J., & Shearing, P. R. (2016). Exploring 3D microstructural evolution in li-sulfur battery electrodes using in-situ x-ray tomography. *Scientific reports*, *6*, 35291. doi:10.1038/srep35291.

Yılmaz, G. A., Şen, D., Kaya, Z. T., & Tinçer, T. (2014). Effect of inert plasticizers on mechanical, thermal, and sensitivity properties of polyurethane-based plastic bonded explosives. *Journal of Applied Polymer Science*, *131*. doi:10.1002/app.40907.

Yohannes, B., Gonzalez, M., Abebe, A., Sprockel, O., Nikfar, F., Kiang, S., & Cuitiño, A. (2017). Discrete particle modeling and micromechanical characterization of bilayer tablet compaction. *International Journal of Pharmaceutics*, *529*, 597 – 607. doi:10.1016/j.ijpharm.2017.07.032.

Yohannes, B., Gonzalez, M., Abebe, A., Sprockel, O., Nikfar, F., Kiang, S., & Cuitiño, A. M. (2016). Evolution of the microstructure during the process of consolidation and bonding in soft granular solids. *International journal of pharmaceutics*, *503*, 68–77. doi:10.1016/j.ijpharm.2016.02.032.

Yu, X., Peng, G., & Lu, S. (2018). Characterizing aggregate pore structure by x-ray micro-computed tomography and a network model. *Soil Science Society of America Journal*, *82*, 744–756. doi:10.2136/sssaj2017.11.0385.

Zhang, J., & Jiang, Y. (2004). A study of inhomogeneous plastic deformation of 1045 steel. *Journal of engineering materials and technology*, *126*, 164–171. doi:10.1115/1.1647125.

Zhang, Z. L., Kristiansen, H., & Liu, J. (2007). A method for determining elastic properties of micron-sized polymer particles by using flat punch test. *Computational Materials Science*, *39*, 305–314. doi:10.1016/j.commatsci.2006.06.009.

Zhong, X. A., & Knauss, W. G. (1997). Analysis of Interfacial Failure in Particle-Filled Elastomers. *Journal of Engineering Materials and Technology*, *119*, 198–204. doi:10.1115/1.2812243.

Zhu, H., Zhou, Z., Yang, R., & Yu, A. (2008). Discrete particle simulation of particulate systems: a review of major applications and findings. *Chemical Engineering Science*, *63*, 5728–5770. doi:10.1016/j.ces.2008.08.006.

Zhupanska, O. (2011). Contact problem for elastic spheres: Applicability of the hertz theory to non-small contact areas. *International Journal of Engineering Science*, *49*, 576 – 588. doi:10.1016/j.ijengsci.2011.02.003.

Zúñiga, A. E., & Beatty, M. F. (2002). A new phenomenological model for stress-softening in elastomers. *Zeitschrift für angewandte Mathematik und Physik ZAMP*, *53*, 794–814. doi:10.1007/PL00022513.

APPENDIX A. DETERMINATION OF RADIAL DISPLACEMENT OF A CONTACT BOUNDARY POINT DUE TO A SINGLE FORCE

Figure A.1 depicts a three dimensional view of a linear-elastic spherical particle under the action of a concentrated force P_i applied at the origin A of cylindrical coordinates (z, r). We consider the deformation of a spherical cap of base radius a and center C, situated at an angular distance θ_i from the force P_i, due an ellipsoidally distributed pressure given by Equation (2.1) in section 2.2. The pressure distribution is approximated by an effective force P applied at C. A point Q on the cap boundary is situated at angle ϕ from the plane defined by points A, O and C. Using vector algebra, the angle AOQ, denoted by β_Q, can be expressed as

$$\beta_Q = \cos^{-1}\left[\cos\left|\theta_i - \sin^{-1}\left(\frac{a}{R}\right)\right| - \left(\frac{a}{R}\right)(1-\cos\phi)\sin\theta_i\right] \tag{A.1}$$

The above equation implies that the angular distance between a contact force and any point on the cap boundary can be represented in terms of a constant reference angle θ_i and a variable angle ϕ. The dependency on angle ϕ vanishes for the two extreme values of θ_i, i.e. 0 and π. For $\theta_i = 0$, which corresponds to the case when $P_i = P$, Equation (A.1) reduces to

$$\beta_Q|_{\theta_i=0} = \sin^{-1}\left(\frac{a}{R}\right) \tag{A.2}$$

the above result restates the geometrical fact that the contact force P is equidistant from any point on the cap boundary, the angular distance being $\sin^{-1}(a/R)$. A similar result is obtained for $\theta_i = \pi$, which makes the force P_i equidistant from any point on the cap boundary. The angular distance in this case becomes

$$\beta_Q|_{\theta_i=\pi} = \pi - \sin^{-1}\left(\frac{a}{R}\right) \tag{A.3}$$

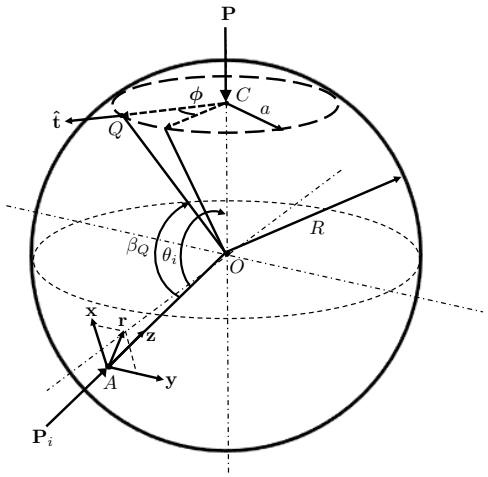

Figure A.1. A linear-elastic sphere of radius R under the action of an ellipsoidally distributed pressure, approximated by an effective force P on a spherical cap of radius a and center C, with concentrated force P_i acting normally on one of its surface points.

At point Q with coordinates $(z, r) : \big(2R\sin^2(\beta_Q/2), R\sin\beta_Q\big)$, displacements due to force P_i along the (z, r) axes, denoted by $(W_{i,Q}, U_{i,Q})$, are given by the Boussinesq solution (Johnson, 1985; Timoshenko & Goodier, 1970) and can be expressed in terms of angle β_Q as

$$W_{i,Q}(\beta_Q) = \frac{(1+\nu)P_i}{2\pi ER}\left[\frac{\sin(\beta_Q/2)}{2} + \frac{1-\nu}{\sin(\beta_Q/2)}\right] \tag{A.4}$$

$$U_{i,Q}(\beta_Q) = \frac{(1+\nu)P_i}{4\pi ER}\left[\cos(\beta_Q/2) - \frac{(1-2\nu)\cos(\beta_Q/2)}{\sin(\beta_Q/2)\,(1+\sin(\beta_Q/2))}\right] \tag{A.5}$$

Similarly, for the cap center C with coordinates $(z, r) : \big(2R\sin^2(\theta_i/2), R\sin\theta_i\big)$, displacements due to force P_i along the (z, r) axes, denoted by $(W_{i,C}, U_{i,C})$, can be expressed in terms of angle θ_i as

$$W_{i,C}(\theta_i) = \frac{(1+\nu)P_i}{2\pi ER}\left[\frac{\sin(\theta_i/2)}{2} + \frac{1-\nu}{\sin(\theta_i/2)}\right] \tag{A.6}$$

$$U_{i,C}(\theta_i) = \frac{(1+\nu)P_i}{4\pi ER}\left[\cos(\theta_i/2) - \frac{(1-2\nu)\cos(\theta_i/2)}{\sin(\theta_i/2)\,(1+\sin(\theta_i/2))}\right] \tag{A.7}$$

The displacement of point Q due to force P_i in the radial direction with respect to center C, denoted by $u_{i,Q}$, can be expressed as

$$u_{i,Q} = [(W_{i,Q} - W_{i,C})\hat{e}_z + (U_{i,Q} - U_{i,C})\hat{e}_r] \cdot \hat{t} \tag{A.8}$$

where $\hat{t}$ is a unit vector in the radial direction at Q, as shown in figure A.1. Using vector algebra, it can be proved that the vector $\hat{t}$ can be expressed in terms of (x, y, z) coordinates as

$$\hat{t} = -\cos\theta_i \cos\phi\, \hat{e}_x - \sin\phi\, \hat{e}_y - \sin\theta_i \cos\phi\, \hat{e}_z \tag{A.9}$$

which implies that $\hat{t}$ in terms of (z, r) coordinates becomes

$$\hat{t} = -\sin\theta_i \cos\phi \hat{e}_z + \left(\sqrt{1 - \sin^2\theta_i \cos^2\phi}\right) \hat{e}_r \tag{A.10}$$

Substituting $\hat{t}$ from Equation (A.10) into Equation (A.8), we get

$$u_{i,Q} = -(W_{i,Q} - W_{i,C}) \sin\theta_i \cos\phi + (U_{i,Q} - U_{i,C})\sqrt{1 - \sin^2\theta_i \cos^2\phi} \tag{A.11}$$

Equation (A.11) provides a general definition of the radial displacement of a contact boundary point on an elastic spherical particle due to a concentrated force acting on the surface of the particle. After substituting the values of $W_{i,Q}$, $U_{i,Q}$, $W_{i,C}$ and $U_{i,C}$ from Equations (A.4), (A.5), (A.6) and (A.7) respectively into Equation (A.11), the resulting final expression for $u_{i,Q}$ in terms of angles θ_i and ϕ is given by

$$\begin{aligned} u_{i,Q} = \frac{(1+\nu)P_i}{2\pi ER} \Bigg[& \frac{\sin\theta_i \cos\phi \left\{\sin(\theta_i/2) - \sin(\beta_Q(\theta_i,\phi)/2)\right\} \times \left\{\sin(\theta_i/2)\sin(\beta_Q(\theta_i,\phi)/2) - 2 + 2\nu\right\}}{2\sin(\theta_i/2)\sin(\beta_Q(\theta_i,\phi)/2)} \\ & + \sqrt{1 - \sin^2\theta_i \cos^2\phi} \Bigg[\frac{1}{2}\left(\cos(\beta_Q(\theta_i,\phi)/2) - \cos(\theta_i/2)\right) \\ & - (1-2\nu)\left\{ \frac{1 - \sin(\beta_Q(\theta_i,\phi)/2)}{\sin\beta_Q(\theta_i,\phi)} - \frac{\cos(\theta_i/2)}{2\sin(\theta_i/2)(1+\sin(\theta_i/2))} \right\} \Bigg] \Bigg] \end{aligned} \tag{A.12}$$

The above expression can be further reduced to the following form

$$u_{i,Q} = \frac{P_i}{\eta_{i,Q}} \tag{A.13}$$

where

$$\frac{1}{\eta_{i,Q}} = \frac{1+\nu}{2\pi ER}\left[\frac{\sin\theta_i\cos\phi\,\{\sin(\theta_i/2)-\sin(\beta_Q(\theta_i,\phi)/2)\}}{\times\,\{\sin(\theta_i/2)\sin(\beta_Q(\theta_i,\phi)/2)-2+2\nu\}}{2\sin(\theta_i/2)\sin(\beta_Q(\theta_i,\phi)/2)}\right.$$

$$+\sqrt{1-\sin^2\theta_i\cos^2\phi}\left[\frac{1}{2}\left(\cos(\beta_Q(\theta_i,\phi)/2)-\cos(\theta_i/2)\right)\right. \tag{A.14}$$

$$\left.\left.-(1-2\nu)\left\{\frac{1-\sin(\beta_Q(\theta_i,\phi)/2)}{\sin\beta_Q(\theta_i,\phi)}-\frac{\cos(\theta_i/2)}{2\sin(\theta_i/2)(1+\sin(\theta_i/2))}\right\}\right]\right]$$

APPENDIX B. CALCULATION OF PRESSURE DISTRIBUTION ON THE CONTACT SURFACE OF AN ELASTIC SPHERE

Considering the contact configuration presented in Figure 2.2 in Section 2.3, the contact area is circular and depicted in Figure 2.5 in Section 2.4. Based on the analysis of Luo (1958) and Cattaneo (1947), the following approximate form of pressure distribution can be assumed at a radial distance r_{ij}.

$$p_{ij}(r_{ij}) = \sum_{n=1}^{N} \rho_n \left(1 - \frac{r_{ij}^2}{a_{ij}^2}\right)^{\frac{2n-1}{2}} \tag{B.1}$$

where N corresponds to the number of Taylor series terms considered in the profile function, and ρ_n are N unknown function parameters. For an internal point A in the contact region at a radial distance r_{ij} from the contact center, we can write the following using cosine rule

$$s_{ij}^2 = r_{ij}^2 + q_{ij}^2 + 2r_{ij}q_{ij}\cos\omega_{ij} \tag{B.2}$$

Using Equations (B.1) and (B.2), the pressure distribution at elemental region $B(q_{ij}, \omega_{ij})$ can be written as

$$p_{ij}(q_{ij}, \omega_{ij}) = \sum_{n=1}^{N} \frac{\rho_n}{a_{ij}^{2n-1}} (a_{ij}^2 - r_{ij}^2 - 2r_{ij}q_{ij}\cos\omega_{ij} - q_{ij}^2)^{\frac{2n-1}{2}} \tag{B.3}$$

Let $\zeta_{ij} = \sqrt{a_{ij}^2 - r_{ij}^2}$ and $\delta_{ij} = r_{ij}\cos\omega_{ij}$. Then Equation (B.3) reduces to

$$p_{ij}(q_{ij}, \omega_{ij}) = \sum_{n=1}^{N} \frac{\rho_n}{a_{ij}^{2n-1}} (\zeta_{ij}^2 - 2\delta_{ij}q_{ij} - q_{ij}^2)^{\frac{2n-1}{2}} \tag{B.4}$$

After substituting the expression for $p_{ij}(q_{ij}, \omega_{ij})$ given by Equation (B.4) in Equation (2.22) (Section 2.4), the displacement field inside the circular region becomes

$$\begin{aligned} w_i(r_{ij}) + w_j(r_{ij}) &= \bar{u}_{iz_{ij}}(r_{ij}) + \bar{u}_{jz_{ij}}(r_{ij}) \\ &= \left(\frac{1-\nu_i^2}{\pi E_i} + \frac{1-\nu_j^2}{\pi E_j}\right) \int_0^{2\pi} d\omega_{ij} \int_0^{q_1} \left\{ \sum_{n=1}^{N} \frac{\rho_n}{a_{ij}^{2n-1}} (\zeta_{ij}^2 - 2\delta_{ij} q_{ij} - q_{ij}^2)^{\frac{2n-1}{2}} \right\} dq_{ij} \end{aligned} \tag{B.5}$$

where q_1 is the positive root of the equation (Johnson, 1985, pg. 60)

$$q_{ij}^2 + 2\delta_{ij} q_{ij} - \zeta_{ij}^2 = 0 \tag{B.6}$$

given by

$$q_1 = -\delta_{ij} + \sqrt{\zeta_{ij}^2 + \delta_{ij}^2} \tag{B.7}$$

We now consider three cases depending upon the number of Taylor series terms (N) taken in the profile function. The three cases correspond to $N = 2$, 3 and 4. We shall now calculate the pressure distribution for each of these cases.

We first calculate the displacement field for $N = 4$ and then modify the function accordingly for different cases. First, the internal integrals with respect to dq_{ij} for $n = 1$, 2, 3 and 4 are obtained and given by

$$\int_0^{q_1} (\zeta_{ij}^2 - 2\delta_{ij} q_{ij} - q_{ij}^2)^{1/2} dq_{ij} = -\frac{1}{2}\zeta_{ij}\delta_{ij} + \frac{1}{2}(\zeta_{ij}^2 + \delta_{ij}^2) \left\{ \frac{\pi}{2} - \tan^{-1}\left(\frac{\delta_{ij}}{\zeta_{ij}}\right) \right\} \tag{B.8}$$

$$\int_0^{q_1} (\zeta_{ij}^2 - 2\delta_{ij} q_{ij} - q_{ij}^2)^{3/2} dq_{ij} = -\frac{1}{8}\zeta_{ij}\delta_{ij}(5\zeta_{ij}^2 + 3\delta_{ij}^2) + \frac{3}{8}(\zeta_{ij}^2 + \delta_{ij}^2)^2 \left\{ \frac{\pi}{2} - \tan^{-1}\left(\frac{\delta_{ij}}{\zeta_{ij}}\right) \right\} \tag{B.9}$$

$$\begin{aligned} \int_0^{q_1} (\zeta_{ij}^2 - 2\delta_{ij} q_{ij} - q_{ij}^2)^{5/2} dq_{ij} &= -\frac{1}{48}\zeta_{ij}\delta_{ij}(33\zeta_{ij}^4 + 40\zeta_{ij}^2\delta_{ij}^2 + 15\delta_{ij}^4) \\ &\quad + \frac{5}{16}(\zeta_{ij}^2 + \delta_{ij}^2)^3 \left\{ \frac{\pi}{2} - \tan^{-1}\left(\frac{\delta_{ij}}{\zeta_{ij}}\right) \right\} \end{aligned} \tag{B.10}$$

$$\begin{aligned} \int_0^{q_1} (\zeta_{ij}^2 - 2\delta_{ij} q_{ij} - q_{ij}^2)^{7/2} dq_{ij} &= -\frac{1}{384}\zeta_{ij}\delta_{ij}(279\zeta_{ij}^6 + 511\zeta_{ij}^4\delta_{ij}^2 + 385\zeta_{ij}^2\delta_{ij}^4 + 105\delta_{ij}^6) \\ &\quad + \frac{35}{128}(\zeta_{ij}^2 + \delta_{ij}^2)^4 \left\{ \frac{\pi}{2} - \tan^{-1}\left(\frac{\delta_{ij}}{\zeta_{ij}}\right) \right\} \end{aligned} \tag{B.11}$$

When the resulting expression from combination of Equations (B.8), (B.9), (B.10) and (B.11) is substituted in Equation (B.5), and integrated with respect to ω_{ij} from 0 to 2π, the terms containing $\zeta_{ij}\delta_{ij}$ and $\tan^{-1}(\delta_{ij}/\zeta_{ij})$ are eliminated. The final form of Equation (B.5) re-expanded in terms of a_{ij} and r_{ij} is given by

$$\begin{aligned} w_i(r_{ij}) + w_j(r_{ij}) &= \bar{u}_{iz_{ij}}(r_{ij}) + \bar{u}_{jz_{ij}}(r_{ij}) \\ &= \left(\frac{1-\nu_i^2}{E_i} + \frac{1-\nu_j^2}{E_j}\right)\left(\frac{\pi}{4a_{ij}}\right)\left[a_{ij}^2\left(2\rho_1 + \frac{3}{2}\rho_2 + \frac{5}{4}\rho_3 + \frac{35}{32}\rho_4\right)\right. \\ &\quad -r_{ij}^2\left(\rho_1 + \frac{3}{2}\rho_2 + \frac{15}{8}\rho_3 + \frac{35}{16}\rho_4\right) + r_{ij}^4\left(\frac{9\rho_2}{16a_{ij}^2} + \frac{45\rho_3}{32a_{ij}^2} + \frac{315\rho_4}{128a_{ij}^2}\right) \\ &\quad \left.-r^6\left(\frac{25\rho_3}{64a_{ij}^4} + \frac{175\rho_4}{128a_{ij}^4}\right) + r_{ij}^8\left(\frac{1225\rho_4}{4096a_{ij}^6}\right)\right] \end{aligned} \tag{B.12}$$

We now consider the three cases individually.

B.1 Case I: Two terms (N=2)

For $N = 2$, the terms with ρ_3 and ρ_4 are eliminated from Equation (B.12). Substituting the modified equation in Equation (2.23) (Section 2.4) with two terms, we have

$$\begin{aligned} &\left(\frac{1-\nu_i^2}{E_i} + \frac{1-\nu_j^2}{E_j}\right)\left(\frac{\pi}{4a_{ij}}\right)\left[a_{ij}^2\left(2\rho_1 + \frac{3}{2}\rho_2\right) - r_{ij}^2\left(\rho_1 + \frac{3}{2}\rho_2\right) + r_{ij}^4\left(\frac{9\rho_2}{16a_{ij}^2}\right)\right] \\ &= (\gamma_{ij} + \gamma_{ij}^{\mathrm{NL}}) - \frac{r_{ij}^2\mathbb{A}_{ij}}{2} - \frac{r_{ij}^4\mathbb{B}_{ij}}{8} \end{aligned} \tag{B.13}$$

In order to satisfy Equation (B.13) for all points withing the circular contact region, coefficients of like powers of r_{ij} on both sides must be equal. Hence,

$$-\left(\frac{1-\nu_i^2}{E_i} + \frac{1-\nu_j^2}{E_j}\right)\left(\frac{9\pi\rho_2}{8a_{ij}^3}\right) = \mathbb{B}_{ij} \tag{B.14}$$

$$\left(\frac{1-\nu_i^2}{E_i} + \frac{1-\nu_j^2}{E_j}\right)\left(\frac{\pi}{2a_{ij}}\right)\left(\rho_1 + \frac{3}{2}\rho_2\right) = \mathbb{A}_{ij} \tag{B.15}$$

$$\left(\frac{1-\nu_i^2}{E_i} + \frac{1-\nu_j^2}{E_j}\right)\left(\frac{\pi a_{ij}}{4}\right)\left(2\rho_1 + \frac{3}{2}\rho_2\right) = \gamma_{ij} + \gamma_{ij}^{\mathrm{NL}} \tag{B.16}$$

Solving Equations (B.14) and (B.15) for ρ_1 and ρ_2, we get

$$\rho_1 = \frac{2a_{ij}(3\mathbb{A}_{ij} + 2a_{ij}^2\mathbb{B}_{ij})}{3\pi}\left(\frac{1-\nu_i^2}{E_i} + \frac{1-\nu_j^2}{E_j}\right)^{-1} \tag{B.17}$$

$$\rho_2 = -\frac{8a_{ij}^3\mathbb{B}_{ij}}{9\pi}\left(\frac{1-\nu_i^2}{E_i} + \frac{1-\nu_j^2}{E_j}\right)^{-1} \tag{B.18}$$

Substituting the expressions for ρ_1 and ρ_2 obtained above into Equation (B.16), we get an expression for displacement γ_{ij} in terms of contact radius a_{ij}

$$\gamma_{ij} + \gamma_{ij}^{\mathrm{NL}} = a_{ij}^2\mathbb{A}_{ij} + \frac{a_{ij}^4}{3}\mathbb{B}_{ij} \tag{B.19}$$

Also, by substituting the expressions for ρ_1 and ρ_2 in Equation (B.1) and rearranging, we obtain the pressure distribution of the form

$$p_{ij}(r_{ij}) = \frac{2a_{ij}}{\pi}\left(\frac{1-\nu_i^2}{E_i} + \frac{1-\nu_j^2}{E_j}\right)^{-1}\left(1 - \frac{r_{ij}^2}{a_{ij}^2}\right)^{1/2}\left[\mathbb{A}_{ij} + \frac{2a_{ij}^2\mathbb{B}_{ij}}{9}\left(1 + 2\frac{r_{ij}^2}{a_{ij}^2}\right)\right] \tag{B.20}$$

B.2 Case II: Three terms (N=3)

For $N = 3$, terms with ρ_4 are eliminated. Substituting the modified Equation (B.12) in Equation (2.23) with three terms, we have

$$\begin{aligned}\left(\frac{1-\nu_i^2}{E_i} + \frac{1-\nu_j^2}{E_j}\right)\left(\frac{\pi}{4a_{ij}}\right)\left[a_{ij}^2\left(2\rho_1 + \frac{3}{2}\rho_2 + \frac{5}{4}\rho_3\right) - r_{ij}^2\left(\rho_1 + \frac{3}{2}\rho_2 + \frac{15}{8}\rho_3\right)\right.\\ \left.+r_{ij}^4\left(\frac{9\rho_2}{16a_{ij}^2} + \frac{45\rho_3}{32a_{ij}^2}\right) - r_{ij}^6\left(\frac{25\rho_3}{64a_{ij}^4}\right)\right] = (\gamma_{ij} + \gamma_{ij}^{\mathrm{NL}}) - \frac{r_{ij}^2\mathbb{A}_{ij}}{2} - \frac{r_{ij}^4\mathbb{B}_{ij}}{8} - \frac{r_{ij}^6\mathbb{C}_{ij}}{16}\end{aligned} \tag{B.21}$$

Since the coefficients of like powers of r_{ij} on both sides of Equation (B.21) must be equal, we get

$$\left(\frac{1-\nu_i^2}{E_i}+\frac{1-\nu_j^2}{E_j}\right)\left(\frac{25\pi\rho_3}{16a_{ij}^5}\right)=\mathbb{C}_{ij} \tag{B.22}$$

$$-\left(\frac{1-\nu_i^2}{E_i}+\frac{1-\nu_j^2}{E_j}\right)\left(\frac{9\pi}{8a_{ij}^3}\right)\left(\rho_2+\frac{5\rho_3}{2}\right)=\mathbb{B}_{ij} \tag{B.23}$$

$$\left(\frac{1-\nu_i^2}{E_i}+\frac{1-\nu_j^2}{E_j}\right)\left(\frac{\pi}{2a_{ij}}\right)\left(\rho_1+\frac{3}{2}\rho_2+\frac{15}{8}\rho_3\right)=\mathbb{A}_{ij} \tag{B.24}$$

$$\left(\frac{1-\nu_i^2}{E_i}+\frac{1-\nu_j^2}{E_j}\right)\left(\frac{\pi a_{ij}}{4}\right)\left(2\rho_1+\frac{3}{2}\rho_2+\frac{5}{4}\rho_3\right)=\gamma_{ij}+\gamma_{ij}^{\mathrm{NL}} \tag{B.25}$$

solving Equations (B.22), (B.23) and (B.24) for ρ_1, ρ_2 and ρ_3, we get

$$\rho_1=\frac{2a_{ij}(15\mathbb{A}_{ij}+10a_{ij}^2\mathbb{B}_{ij}+9a_{ij}^4\mathbb{C}_{ij})}{15\pi}\left(\frac{1-\nu_i^2}{E_i}+\frac{1-\nu_j^2}{E_j}\right)^{-1} \tag{B.26}$$

$$\rho_2=-\frac{8a_{ij}^3(5\mathbb{B}_{ij}+9a_{ij}^2\mathbb{C}_{ij})}{45\pi}\left(\frac{1-\nu_i^2}{E_i}+\frac{1-\nu_j^2}{E_j}\right)^{-1} \tag{B.27}$$

$$\rho_3=\frac{16a_{ij}^5\mathbb{C}_{ij}}{25\pi}\left(\frac{1-\nu_i^2}{E_i}+\frac{1-\nu_j^2}{E_j}\right)^{-1} \tag{B.28}$$

By substituting the expressions for ρ_1, ρ_2 and ρ_3 obtained above into Equation (B.25), we get

$$\gamma_{ij}+\gamma_{ij}^{\mathrm{NL}}=a_{ij}^2\mathbb{A}_{ij}+\frac{a_{ij}^4}{3}\mathbb{B}_{ij}+\frac{a_{ij}^6}{5}\mathbb{C}_{ij} \tag{B.29}$$

And by substituting the expressions for ρ_1, ρ_2 and ρ_3 into Equation (B.1) and rearranging, we obtain the pressure distribution of the form

$$\begin{aligned}p_{ij}(r_{ij})=\frac{2a_{ij}}{\pi}\left(\frac{1-\nu_i^2}{E_i}+\frac{1-\nu_j^2}{E_j}\right)^{-1}\left(1-\frac{r_{ij}^2}{a_{ij}^2}\right)^{1/2}\Bigg[\mathbb{A}_{ij}+\frac{2a_{ij}^2\mathbb{B}_{ij}}{9}\left(1+2\frac{r_{ij}^2}{a_{ij}^2}\right)\\+\frac{a_{ij}^4\mathbb{C}_{ij}}{25}\left(3+4\frac{r_{ij}^2}{a_{ij}^2}+8\frac{r_{ij}^4}{a_{ij}^4}\right)\Bigg]\end{aligned} \tag{B.30}$$

B.3 Case III: Four terms (N=4)

For $N = 4$, we substitute Equation (B.12) into Equation (2.23) to get

$$\left(\frac{1-\nu_i^2}{E_i}+\frac{1-\nu_j^2}{E_j}\right)\left(\frac{\pi}{4a_{ij}}\right)\left[a_{ij}^2\left(2\rho_1+\frac{3}{2}\rho_2+\frac{5}{4}\rho_3+\frac{35}{32}\rho_4\right)-r_{ij}^2\left(\rho_1+\frac{3}{2}\rho_2\right.\right.$$
$$\left.+\frac{15}{8}\rho_3+\frac{35}{16}\rho_4\right)+r_{ij}^4\left(\frac{9\rho_2}{16a_{ij}^2}+\frac{45\rho_3}{32a_{ij}^2}+\frac{315\rho_4}{128a_{ij}^2}\right)-r_{ij}^6\left(\frac{25\rho_3}{64a_{ij}^4}+\frac{175\rho_4}{128a_{ij}^4}\right) \tag{B.31}$$
$$\left.+r_{ij}^8\left(\frac{1225\rho_4}{4096a_{ij}^6}\right)\right]=(\gamma_{ij}+\gamma_{ij}^{\mathrm{NL}})-\frac{r_{ij}^2\mathbb{A}_{ij}}{2}-\frac{r_{ij}^4\mathbb{B}_{ij}}{8}-\frac{r_{ij}^6\mathbb{C}_{ij}}{16}-\frac{5r_{ij}^8\mathbb{D}_{ij}}{128}$$

Since the coefficients of like powers of r_{ij} on both sides of Equation (B.31) must be equal, we get

$$-\left(\frac{1-\nu_i^2}{E_i}+\frac{1-\nu_j^2}{E_j}\right)\left(\frac{245\pi\rho_4}{128a_{ij}^7}\right)=\mathbb{D}_{ij} \tag{B.32}$$

$$\left(\frac{1-\nu_i^2}{E_i}+\frac{1-\nu_j^2}{E_j}\right)\left(\frac{\pi}{16a_{ij}^5}\right)\left(25\rho_3+\frac{175}{2}\rho_4\right)=\mathbb{C}_{ij} \tag{B.33}$$

$$-\left(\frac{1-\nu_i^2}{E_i}+\frac{1-\nu_j^2}{E_j}\right)\left(\frac{9\pi}{8a_{ij}^3}\right)\left(\rho_2+\frac{5\rho_3}{2}+\frac{35}{8}\rho_4\right)=\mathbb{B}_{ij} \tag{B.34}$$

$$\left(\frac{1-\nu_i^2}{E_i}+\frac{1-\nu_j^2}{E_j}\right)\left(\frac{\pi}{2a_{ij}}\right)\left(\rho_1+\frac{3}{2}\rho_2+\frac{15}{8}\rho_3+\frac{35}{16}\rho_4\right)=\mathbb{A}_{ij} \tag{B.35}$$

$$\left(\frac{1-\nu_i^2}{E_i}+\frac{1-\nu_j^2}{E_j}\right)\left(\frac{\pi a_{ij}}{4}\right)\left(2\rho_1+\frac{3}{2}\rho_2+\frac{5}{4}\rho_3+\frac{35}{32}\rho_4\right)=\gamma_{ij}+\gamma_{ij}^{\mathrm{NL}} \tag{B.36}$$

Solving Equations (B.32), (B.33), (B.34) and (B.35) for ρ_1, ρ_2, ρ_3 and ρ_4, we get

$$\rho_1=\frac{2a_{ij}(105\mathbb{A}_{ij}+70a_{ij}^2\mathbb{B}_{ij}+63a_{ij}^4\mathbb{C}_{ij}+60a_{ij}^6\mathbb{D}_{ij})}{105\pi}\left(\frac{1-\nu_i^2}{E_i}+\frac{1-\nu_j^2}{E_j}\right)^{-1} \tag{B.37}$$

$$\rho_2=-\frac{8a_{ij}^3(35\mathbb{B}_{ij}+63a_{ij}^2\mathbb{C}_{ij}+90a_{ij}^4\mathbb{D}_{ij})}{315\pi}\left(\frac{1-\nu_i^2}{E_i}+\frac{1-\nu_j^2}{E_j}\right)^{-1} \tag{B.38}$$

$$\rho_3=\frac{16a_{ij}^5(7\mathbb{C}_{ij}+20a_{ij}^2\mathbb{D}_{ij})}{175\pi}\left(\frac{1-\nu_i^2}{E_i}+\frac{1-\nu_j^2}{E_j}\right)^{-1} \tag{B.39}$$

$$\rho_4=-\frac{128a_{ij}^7\mathbb{D}_{ij}}{245\pi}\left(\frac{1-\nu_i^2}{E_i}+\frac{1-\nu_j^2}{E_j}\right)^{-1} \tag{B.40}$$

By substituting the expressions for ρ_1, ρ_2, ρ_3 and ρ_4 obtained above into Equation (B.36), we get

$$\gamma_{ij} + \gamma_{ij}^{\mathrm{NL}} = a_{ij}^2 \mathbb{A}_{ij} + \frac{a_{ij}^4}{3}\mathbb{B}_{ij} + \frac{a_{ij}^6}{5}\mathbb{C}_{ij} + \frac{a_{ij}^8}{7}\mathbb{D}_{ij} \tag{B.41}$$

And by substituting the expressions for ρ_1, ρ_2, ρ_3 and ρ_4 into Equation (B.1) and rearranging, we obtain the pressure distribution of the form

$$\begin{aligned} p_{ij}(r_{ij}) = \frac{2a_{ij}}{\pi}\left(\frac{1-\nu_i^2}{E_i} + \frac{1-\nu_j^2}{E_j}\right)^{-1}\left(1 - \frac{r_{ij}^2}{a_{ij}^2}\right)^{1/2}\Bigg[\mathbb{A}_{ij} + \frac{2a_{ij}^2\mathbb{B}_{ij}}{9}\left(1 + 2\frac{r_{ij}^2}{a_{ij}^2}\right) \\ + \frac{a_{ij}^4\mathbb{C}_{ij}}{25}\left(3 + 4\frac{r_{ij}^2}{a_{ij}^2} + 8\frac{r_{ij}^4}{a_{ij}^4}\right) + \frac{4a_{ij}^6\mathbb{D}_{ij}}{245}\left(5 + 6\frac{r_{ij}^2}{a_{ij}^2} + 8\frac{r_{ij}^4}{a_{ij}^4} + 16\frac{r_{ij}^6}{a_{ij}^6}\right)\Bigg] \end{aligned} \tag{B.42}$$

APPENDIX C. DERIVATION OF A CURVATURE CORRECTED CONTACT LAW USING SELF-SIMILAR APPROACH

Figure C.1 shows a magnified view of the contact between two spherical particles of radii R_1 and R_2, representative strengths κ_1 and κ_2, and hardening exponent m being pressed along the normal direction. A Cartesian coordinate system $\mathbf{x}_i$ $(i = 1, 2, 3)$ and a polar coordinate system $(\mathbf{z}, \mathbf{r})$ is adopted, where $(\mathbf{z}, \mathbf{x}_3)$ is the normal direction that is positive downwards, and $\mathbf{x}_1 - \mathbf{x}_2$ is the plane of contact with $r = \sqrt{x_1^2 + x_2^2}$. According to Storåkers et al. (1997), the boundary condition at the contact region is given by

$$u_3^{(1)} + u_3^{(2)} = \gamma - f_1(r) - f_2(r) \tag{C.1}$$

where $u_3^{(1)}$ and $u_3^{(2)}$ are the local displacements of any two corresponding surface points on the spheres 1 and 2 at a distance r from the contact center, γ is the total displacement of the centers of mass of the two spheres, and $f_1(r)$ and $f_2(r)$ are the profile functions of the undeformed contacting surfaces, given by $f_1(r) = R_1 - \sqrt{R_1^2 - r^2}$ and $f_2(r) = R_2 - \sqrt{R_2^2 - r^2}$. To obtain the similarity solution, the profile functions are approximated by the first term of their Taylor series expansion about $r = 0$, i.e.

$$R_l - \sqrt{R_l^2 - r^2} = \frac{r^2}{2R_l} + \mathcal{O}\left(\frac{a^4}{R_l^3}\right) \simeq \frac{r^2}{2R_l} \qquad (l = 1, 2) \tag{C.2}$$

To control the error associated with this approximation, the profile curvature can be corrected by including higher order terms of the Taylor expansion. We consider a two term expansion to approximate the profile functions as

$$R_l - \sqrt{R_l^2 - r^2} = \frac{r^2}{2R_l} + \frac{r^4}{8R_l^3} + \mathcal{O}\left(\frac{a^6}{R_l^5}\right) \simeq \frac{r^2}{2R_l} + \frac{r^4}{8R_l^3} \quad (l = 1, 2) \tag{C.3}$$

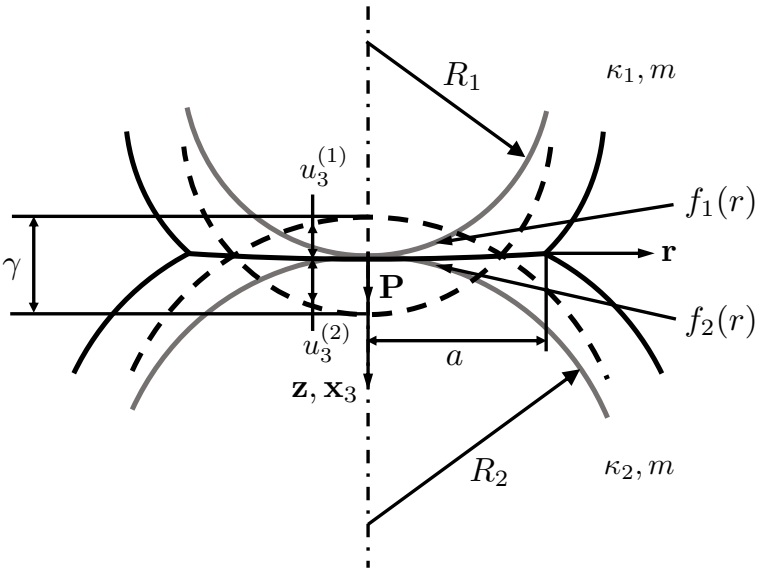

Figure C.1. Schematic of the contact between two spherical particles of radii R_1 and R_2. The total displacement γ generates a radius of contact a between the two particles.

With this correction, the boundary condition given by Equation (C.1) becomes

$$u_3^{(1)} + u_3^{(2)} = \gamma - \frac{r^2\mathbb{A}}{2} - \frac{r^4\mathbb{B}}{8} \tag{C.4}$$

where

$$\mathbb{A} = \frac{1}{R_1} + \frac{1}{R_2} \quad \text{and} \quad \mathbb{B} = \frac{1}{R_1^3} + \frac{1}{R_2^3}$$

With the consideration of small-strain kinematics, the field equations together with the boundary conditions can be summarized as:

$$\dot{\epsilon}_{ij}^{(l)} = \frac{1}{2}\left(\frac{\partial \dot{u}_i^{(l)}}{\partial x_j} + \frac{\partial \dot{u}_j^{(l)}}{\partial x_i}\right) \tag{C.5}$$

$$\frac{\partial \sigma_{ij}^{(l)}}{\partial x_j} = 0 \tag{C.6}$$

$$\sigma_e^{(l)} = \kappa_l \left(\epsilon_e^{(l)}\right)^{1/m} \tag{C.7}$$

$$\dot{u}_3^{(1)} + \dot{u}_3^{(2)} = \dot{\gamma}, \quad \sigma_{13}^{(l)} = \sigma_{23}^{(l)} = 0, \quad r \leq a \tag{C.8}$$

$$\sigma_{13}^{(l)} = \sigma_{23}^{(l)} = \sigma_{33}^{(l)} = 0, \quad r > a \tag{C.9}$$

where $l = 1, 2$ and equations (C.5), (C.6) and (C.7) correspond to compatibility, equilibrium and constitutive law respectively.

The solution to this problem can be started by first taking a basic assumption that

$$\sigma_{ij}^{(l)}(x_k) = \sigma_{ij}^{o}(x_k) \qquad (l = 1, 2) \tag{C.10}$$

in order to ensure continuity of traction at the contact region. This in turn also satisfies the local equilibrium. In addition, scaling the displacements as

$$u_i^{(l)}(x_k) = \left(\frac{\bar{\kappa}}{\kappa_l}\right)^m u_i^o(x_k) \qquad (l = 1, 2) \tag{C.11}$$

where

$$\bar{\kappa} = \left(\frac{1}{\kappa_1^m} + \frac{1}{\kappa_2^m}\right)^{-1/m} \tag{C.12}$$

satisfies the complete field equations. With these assumptions, the boundary condition, Equation (C.4) can be expressed as

$$u_3^o = \gamma - \frac{r^2\mathbb{A}}{2} - \frac{r^4\mathbb{B}}{8} \tag{C.13}$$

and the inhomogeneous rate boundary conditions (Equations (C.8) and (C.9)) can be expressed as

$$\dot{u}_3^o = \dot{\gamma}, \quad \sigma_{13}^o = \sigma_{23}^o = 0, \quad r \leq a \tag{C.14}$$

$$\sigma_{13}^o = \sigma_{23}^o = \sigma_{33}^o = 0, \quad r > a \tag{C.15}$$

The above moving boundary problem can now be converted to a stationary one by removing the dependence on indentation magnitude (contact radius) through appropriate transfor-

mations. The kinematic variables, namely particle velocities and strain rates are transformed first and expressed as

$$x_k = a\tilde{x}_k \tag{C.16}$$

$$\dot{u}_i^o(x_k, a) = \dot{\gamma}\tilde{u}_i^o(\tilde{x}_k) \tag{C.17}$$

$$\dot{\epsilon}_{ij}^o(x_k, a) = \left(\frac{\dot{\gamma}}{a}\right)\tilde{\epsilon}_{ij}^o(\tilde{x}_k) \tag{C.18}$$

With the help of the above scaling, the inhomogeneous rate boundary condition, Equation (C.14) now reduces to

$$\tilde{u}_3^o = 1, \quad \tilde{x}_3 = 0, \quad \tilde{r} \leq 1 \tag{C.19}$$

The vertical velocity field $\dot{u}_3^o$, when integrated over time, gives the total vertical displacement u_3^o which must satisfy the boundary condition given by Equation (C.13). Using the transformation given by Equation (C.17), we get

$$\int_0^t \tilde{u}_3^o \dot{\gamma}\, dt = \gamma - \frac{r^2\mathbb{A}}{2} - \frac{r^4\mathbb{B}}{8} \tag{C.20}$$

Variable transformation from t to a and the use of reduced rate boundary condition (Equation (C.19)) yields a particular Volterra integral equation for $\gamma = \gamma(a)$ given by

$$\gamma\,(r) - \int_0^r \tilde{u}_3^o(r/s)\gamma'(s)\, ds = \frac{r^2\mathbb{A}}{2} + \frac{r^4\mathbb{B}}{8}, \quad \gamma'(a) = \frac{d\gamma}{da} \tag{C.21}$$

the solution to which is given as

$$\gamma(a) = \frac{1}{c^2}\left(\frac{a^2\mathbb{A}}{2} + \frac{a^4\mathbb{B}}{8}\right) \tag{C.22}$$

with the eigenfunction c^2 given by

$$c^2 = 1 - 2\int_1^\infty \frac{\tilde{u}_3^o}{\tilde{r}^3}\, d\tilde{r} \tag{C.23}$$

Equation (C.22) is a quadratic equation in a^2, which can be solved algebraically to obtain the following $a - \gamma$ relationship

$$a = \left[\left(\frac{2}{\mathbb{B}} \right) \left\{ (\mathbb{A}^2 + 2\mathbb{B}c^2\gamma)^{1/2} - \mathbb{A} \right\} \right]^{1/2} \tag{C.24}$$

The above $a - \gamma$ relationship can be expressed as a Taylor series about $\gamma = 0$ as follows

$$a = \left(\frac{2c^2}{\mathbb{A}} \right)^{1/2} \gamma^{1/2} - \left(\frac{\mathbb{B}^{2/3}c^2}{2\mathbb{A}^{5/3}} \right)^{3/2} \gamma^{3/2} + \left(\frac{7^{2/5}\mathbb{B}^{4/5}c^2}{2^{9/5}\mathbb{A}^{9/5}} \right)^{5/2} \gamma^{5/2} + \mathcal{O}(\gamma^{7/2}) \tag{C.25}$$

where the first term of the series corresponds to the $a - \gamma$ relationship without curvature correction, proposed by Storåkers et al. (1997), while the higher order terms correspond to the applied curvature correction. Equation (C.25) serves as the motivation behind formulation of the semi-mechanistic contact radius formulation proposed in Section 3.4 of Chapter 3.

APPENDIX D. DERIVATION OF THE CONTACT DISPLACEMENT AT MINIMUM NORMALIZED HARDNESS FOR CONFINED PARTICLE LOADING CONDITIONS

According to the condition of minimum normalized hardness for confined loading configurations given by Equation (3.33), expressions for various volume and surface quantities in the equation are provided in Table 3.5 for primary contacts under die and all contacts under hydrostatic loading configurations. The particle volume is given by $V_{\text{particle}} = (4/3)\pi R^3$ and the contact area is given by $S^{\text{LC}}_{\text{contact}} = \pi a^2$ where contact radius a is given by Equation (3.17). We now proceed to derive Equation (3.33) for the two confined loading cases in terms of the unknown contact displacement at the minimum.

Die Compaction:

$$\begin{aligned}\rho_V^{\text{LC,contact}}\rho_S^{\text{LC,contact}} &= \left(\frac{V_{\text{particle}}}{V^{\text{LC}}_{\text{voro}}}\right)\left(\frac{V^{\text{LC}}_{\text{contact}}}{V^{\text{LC}}_{\text{voro}}}\right)\left(\frac{S^{\text{LC}}_{\text{contact}}}{S^{\text{LC}}_{\text{face}}}\right)\\ &= \frac{\frac{4}{3}\pi R^3}{8R^2\left(R-\frac{\gamma}{2}\right)} \times \frac{\frac{4}{3}R^2\left(R-\frac{\gamma}{2}\right)}{8R^2\left(R-\frac{\gamma}{2}\right)} \times \frac{\pi a^2}{4R^2}\\ &= \frac{\pi^2 a^2}{144R\left(R-\frac{\gamma}{2}\right)} = \Gamma\end{aligned} \tag{D.1}$$

Now, substituting a in terms of γ from Equation (3.17) with $\mathbb{A} = 1/R_1 + 1/R_2 = 2/R$ and $\mathbb{B} = 1/R_1^3 + 1/R_2^3 = 2/R^3$, rearranging and simplifying the above equation, we finally get

$$\begin{aligned}&\left(\frac{\pi^2\mathcal{D}_5^2}{32R^3}\right)\gamma^5 - \left(\frac{\pi^2\mathcal{D}_3\mathcal{D}_5}{8R^2}\right)\gamma^4 + \left(\frac{\pi^2\mathcal{D}_3^2}{8R} + \frac{\pi^2\mathcal{D}_1\mathcal{D}_5}{4R}\right)\gamma^3 - \left(\frac{\pi^2\mathcal{D}_1\mathcal{D}_3}{2}\right)\gamma^2\\ &+ \left(\frac{\pi^2\mathcal{D}_1^2 R}{2} + 72R\Gamma\right)\gamma - 144R^2\Gamma = 0\end{aligned} \tag{D.2}$$

Hydrostatic Compaction:

$$\begin{aligned}\rho_V^{\text{LC,contact}}\rho_S^{\text{LC,contact}} &= \left(\frac{V_{\text{particle}}}{V_{\text{voro}}^{\text{LC}}}\right)\left(\frac{V_{\text{contact}}^{\text{LC}}}{V_{\text{voro}}^{\text{LC}}}\right)\left(\frac{S_{\text{contact}}^{\text{LC}}}{S_{\text{face}}^{\text{LC}}}\right)\\ &= \frac{\frac{4}{3}\pi R^3}{8\left(R-\frac{\gamma}{2}\right)^3}\times\frac{\frac{4}{3}\left(R-\frac{\gamma}{2}\right)^3}{8\left(R-\frac{\gamma}{2}\right)^3}\times\frac{\pi a^2}{4\left(R-\frac{\gamma}{2}\right)^2}\\ &= \frac{\pi^2R^3a^2}{144\left(R-\frac{\gamma}{2}\right)^5} = \Gamma\end{aligned} \tag{D.3}$$

Now, substituting a in terms of γ from Equation (3.17) with $\mathbb{A} = 1/R_1 + 1/R_2 = 2/R$ and $\mathbb{B} = 1/R_1^3 + 1/R_2^3 = 2/R^3$, rearranging and simplifying the above equation, we finally get

$$\begin{aligned}&\left(\frac{\pi^2\mathcal{D}_5^2}{32}+\frac{9\Gamma}{2}\right)\gamma^5-\left(\frac{\pi^2\mathcal{D}_3\mathcal{D}_5R}{8}+45R\Gamma\right)\gamma^4\\ &+\left(\frac{\pi^2\mathcal{D}_3^2R^2}{8}+\frac{\pi^2\mathcal{D}_1\mathcal{D}_5R^2}{4}+180R^2\Gamma\right)\gamma^3-\left(\frac{\pi^2\mathcal{D}_1\mathcal{D}_3R^3}{2}+360R^3\Gamma\right)\gamma^2\\ &+\left(\frac{\pi^2\mathcal{D}_1^2R^4}{2}+360R^4\Gamma\right)\gamma-144R^5\Gamma=0\end{aligned} \tag{D.4}$$

The quintic equations in terms of the unknown γ, given by Equations (D.2) and (D.4), are solvable in radicals for given values of $\mathcal{D}_1$, $\mathcal{D}_3$, $\mathcal{D}_5$, R and Γ by the method proposed by Dummit (1991) (please ref. Trott & Adamchik (2001) for an implementation of the method in Mathematica, Version 12.0 (2019)). Although the obtained quintic functions have five roots, there is only one positive real root, the proof of which is described below.

First, we immediately observe that the limits of the quintic functions in Equations (D.2) (denoted by $g(\gamma)$) and (D.4) (denoted by $h(\gamma)$) at $x \to -\infty$ and $x \to \infty$ are $-\infty$ and ∞ respectively, which means that the functions have at least one real root. Then, we calculate the derivative of the two polynomials with respect to γ to obtain

$$g'(\gamma) = 72R\Gamma + \left[\frac{\pi^2}{32R^3}\left(\mathcal{D}_5\gamma^2-2R\mathcal{D}_3\gamma+4R^2\mathcal{D}_1\right)\left(5\mathcal{D}_5\gamma^2-6R\mathcal{D}_3\gamma+4R^2\mathcal{D}_1\right)\right] \tag{D.5}$$

$$h'(\gamma) = \frac{45}{2}\Gamma(\gamma-2R)^4 + \left[\frac{\pi^2}{32}\left(\mathcal{D}_5\gamma^2-2R\mathcal{D}_3\gamma+4R^2\mathcal{D}_1\right)\left(5\mathcal{D}_5\gamma^2-6R\mathcal{D}_3\gamma+4R^2\mathcal{D}_1\right)\right] \tag{D.6}$$

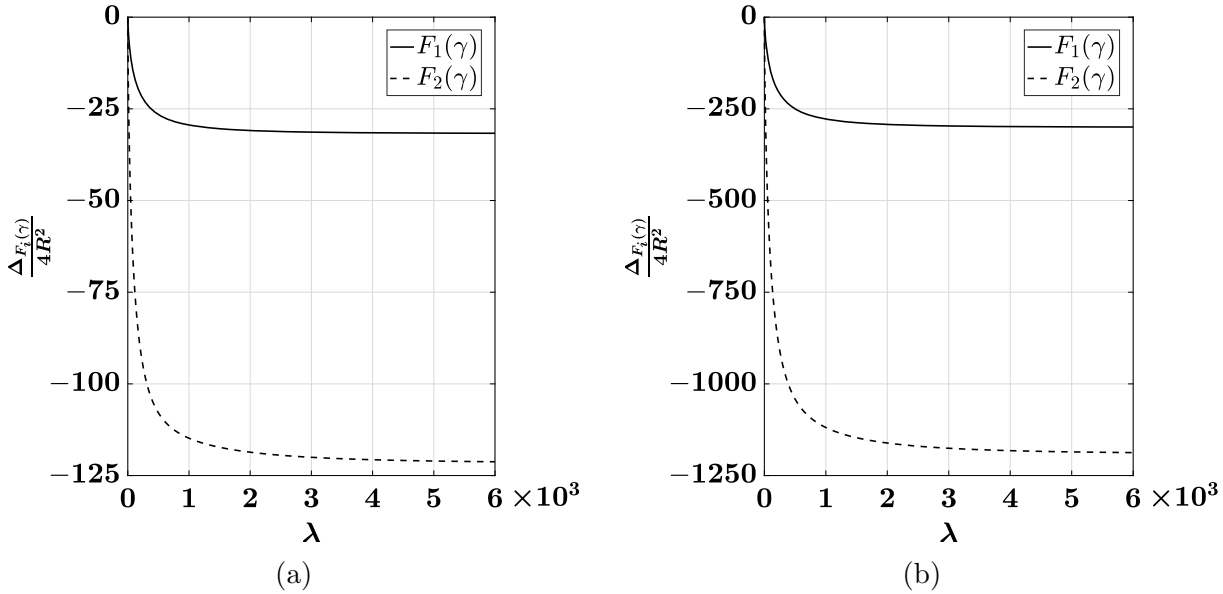

Figure D.1. Plots of $\Delta_{F_i(\gamma)}/4R^2$ $(i = 1, 2)$ against material parameter λ for (a) die and (b) hydrostatic loading configurations.

If it is proved that $g'(\gamma)$ and $h'(\gamma)$ are positive in $\mathbb{R}$, then $g(\gamma)$ and $h(\gamma)$ are monotonic in $\mathbb{R}$, meaning that they have only one real root. Both $g'(\gamma)$ and $h'(\gamma)$ include an addition of two terms, where the first term in both functions is evidently positive, while the second term contains a product of two quadratic functions in γ, given by

$$F_1(\gamma) = \mathcal{D}_5\gamma^2 - 2R\mathcal{D}_3\gamma + 4R^2\mathcal{D}_1 \tag{D.7}$$

$$F_2(\gamma) = 5\mathcal{D}_5\gamma^2 - 6R\mathcal{D}_3\gamma + 4R^2\mathcal{D}_1 \tag{D.8}$$

If these quadratic functions are both positive or negative in $\mathbb{R}$, then the derivative functions $g'(\gamma)$ and $h'(\gamma)$ are positive in $\mathbb{R}$. We thus calculate the discriminants of the two quadratic functions, given by

$$\Delta_{F_1(\gamma)} = 4R^2(\mathcal{D}_3^2 - 4\mathcal{D}_1\mathcal{D}_5) \tag{D.9}$$

$$\Delta_{F_2(\gamma)} = 4R^2(9\mathcal{D}_3^2 - 20\mathcal{D}_1\mathcal{D}_5) \tag{D.10}$$

Figure D.1 presents the plots of $\Delta_{F_i(\gamma)}/4R^2$ $(i = 1, 2)$ against material parameter λ for die (Figure D.1a) and hydrostatic (Figure D.1b) loading configurations. The plots evidently

Table D.1. Limiting values of $\Delta_{F_i(\gamma)}/4R^2$ $(i = 1, 2)$ at $\lambda \to \infty$ for die and hydrostatic loading configurations.

	DC	HC
$\lim_{\lambda\to\infty} \Delta_{F_1(\gamma)}/4R^2$	-31.76	-300.49
$\lim_{\lambda\to\infty} \Delta_{F_2(\gamma)}/4R^2$	-121.70	-1191.71

show that the discriminant values remain negative for $\lambda > 0$, with the limiting negative values at $\lambda \to \infty$ provided in Table D.1. This analysis proves that the quadratic functions $F_1(\gamma)$ and $F_2(\gamma)$ are positive in $\mathbb{R}$, and hence derivative functions $g'(\gamma)$ and $h'(\gamma)$ are monotonic in $\mathbb{R}$. Therefore, it is proved that the quintic functions $g(\gamma)$ and $h(\gamma)$ have only one real root.

Finally, we observe that $g(\gamma = 0) = -144R^2\Gamma$ and $h(\gamma = 0) = -144R^5\Gamma$. Hence, at $\gamma = 0$, both $g(\gamma)$ and $h(\gamma)$ are negative. Therefore, it is also proved that the real root of the quintic functions is a positive value.

APPENDIX E. DERIVATION OF THE CONTACT DISPLACEMENT AT MINIMUM NORMALIZED HARDNESS FOR CONFINED PARTICLE LOADING CONDITIONS

From the observation of normalized hardness ($\bar{H}$) vs. contact deformation ($\gamma/2R$) curves obtained from FEA simulations of simple (Figure 3.7a), hydrostatic (Figure 3.8a) and die (Figure 3.9a) loading configurations depicted in Chapter 3, it is evident that the curves experience a change in curvature from *concave downward* to *concave upward* during the fully plastic deformation regime. The contact deformation at the inflection point, i.e., the point of curvature change, can be obtained by setting the second derivative of $\bar{H}$ with respect to contact deformation $\gamma/(R_1+R_2)$ $(=\gamma/2R)$ equal to zero, and solving the resulting equation for the unknown deformation.

Using Equations (3.27) and (3.28) with $R_1 = R_2 = R$, the second derivative of $\bar{H}$ with respect to $\gamma/2R$ is given by

$$\begin{aligned}\frac{\partial^2 \bar{H}}{\partial \left(\frac{\gamma}{2R}\right)^2} = -p^{\mathrm{LC}} r \left[\tanh(qx)\cos\left\{x - s(\gamma^{\mathrm{LC}}|_{\bar{H}_{\min}}, q)\right\}\right]^r \Big[4q^2\mathrm{csch}^2(2qx)\left\{r - \cosh(2qx)\right\} \\ -2qr\,\mathrm{csch}(qx)\mathrm{sech}(qx)\tan\left\{x - s(\gamma^{\mathrm{LC}}|_{\bar{H}_{\min}}, q)\right\} \\ +(r-1)\tan^2\left\{x - s(\gamma^{\mathrm{LC}}|_{\bar{H}_{\min}}, q)\right\} - 1\Big]\end{aligned} \tag{E.1}$$

where

$$x = \frac{\gamma - \gamma|_{\bar{H}_{\max}}}{2R} \tag{E.2}$$

Setting $\partial^2\bar{H}/\partial\left(\frac{\gamma}{2R}\right)^2 = 0$ and simplifying the resulting equation, we get the following non-linear equation in unknown x

$$\begin{aligned}&4q^2\mathrm{csch}^2(2qx)\left\{r - \cosh(2qx)\right\} - 2qr\,\mathrm{csch}(qx)\,\mathrm{sech}(qx)\tan\left\{x - s(\gamma^{\mathrm{LC}}|_{\bar{H}_{\min}}, q)\right\} \\ &+ (r-1)\tan^2\left\{x - s(\gamma^{\mathrm{LC}}|_{\bar{H}_{\min}}, q)\right\} - 1 = 0\end{aligned} \tag{E.3}$$

Due to the high degree of non-linearity, the above equation cannot be solved analytically. However, an approximate solution for x can be obtained by reducing the equation to the first term of its Taylor series expansion at $x = 0$ ($\gamma/2R = \gamma|_{\bar{H}_{\max}}/2R$). The resulting equation is given by

$$x^2 - \frac{6r\tan\left\{s(\gamma^{\mathrm{LC}}|_{\bar{H}_{\min}}, q)\right\}}{(2q^2+3)(2r+1)+3(r+1)\tan^2\left\{s(\gamma^{\mathrm{LC}}|_{\bar{H}_{\min}}, q)\right\}}\,x - \frac{3(r-1)}{(2q^2+3)(2r+1)+3(r+1)\tan^2\left\{s(\gamma^{\mathrm{LC}}|_{\bar{H}_{\min}}, q)\right\}} = 0 \tag{E.4}$$

The two solutions to the above equation are given by

$$x = \frac{3r\tan\left\{s(\gamma^{\mathrm{LC}}|_{\bar{H}_{\min}}, q)\right\} \pm \left[3(2q^2+3)(r-1)(2r+1) + 9(2r^2-1)\tan^2\left\{s(\gamma^{\mathrm{LC}}|_{\bar{H}_{\min}}, q)\right\}\right]^{1/2}}{(2q^2+3)(2r+1)+3(r+1)\tan^2\left\{s(\gamma^{\mathrm{LC}}|_{\bar{H}_{\min}}, q)\right\}} \tag{E.5}$$

Among the two solutions, the solution involving a difference of the two terms in the numerator is always negative, since $(2r^2-1) \geq r^2$ and $3(2q^2+3)(r-1)(2r+1) > 0$. Therefore, x is given by the second, positive solution. Consequently, from Equation (E.2), $\gamma/2R$ at the inflection point, denoted by $\gamma^{\mathrm{LC}}|_{\bar{H}''=0}/2R$ is approximately given by

$$\frac{\gamma^{\mathrm{LC}}|_{\bar{H}''=0}}{2R} \simeq \frac{\gamma|_{\bar{H}_{\max}}}{2R} + \frac{3r\tan\left\{s(\gamma^{\mathrm{LC}}|_{\bar{H}_{\min}}, q)\right\} + \left[3(2q^2+3)(r-1)(2r+1) + 9(2r^2-1)\tan^2\left\{s(\gamma^{\mathrm{LC}}|_{\bar{H}_{\min}}, q)\right\}\right]^{1/2}}{(2q^2+3)(2r+1)+3(r+1)\tan^2\left\{s(\gamma^{\mathrm{LC}}|_{\bar{H}_{\min}}, q)\right\}} \tag{E.6}$$

VITA

Ankit Agarwal obtained his Bachelor's degree in Mechanical Engineering from the Indian Institute of Technology (IIT) Roorkee, India in June 2012. He worked as an Associate Engineer with Caterpillar Inc. Engineering Design Center, Chennai, India from June 2012 - July 2014 before receiving a F. N. Andrews Fellowship to pursue a direct PhD program at Purdue University. He joined Purdue as a graduate student in Fall 2014 and worked with Prof. Marcial Gonzalez at the Center for Particulate Products and Processes (CP3) in affiliation with the School of Mechanical Engineering and the Purdue Energetics Research Center (PERC) in affiliation with the Ray W. Herrick Laboratories. He is expected to obtain his PhD degree in August 2020, following which he will pursue his postdoctoral research with Prof. Gonzalez at Purdue.